UMA ABORDAGEM DE MODELAGEM FÍSICA QUALITATIVA DE RESISTÊNCIA PARA MACIÇOS ROCHOSOS

LUDGER OSWALDO SUÁREZ BURGOA

TESE DE DOUTORADO EM GEOTECNIA
DEPARTAMENTO DE ENGENHARIA CIVIL E AMBIENTAL

FACULDADE DE TECNOLOGIA

UNIVERSIDADE DE BRASÍLIA

UNIVERSIDADE DE BRASÍLIA

FACULDADE DE TECNOLOGIA

DEPARTAMENTO DE ENGENHARIA CIVIL E AMBIENTAL

UMA ABORDAGEM DE MODELAGEM FÍSICA QUALITATIVA DE RESISTÊNCIA PARA MACIÇOS ROCHOSOS

LUDGER OSWALDO SUÁREZ BURGOA

ORIENTADOR: ANDRÉ PACHECO DE ASSIS, PH.D

TESE DE DOUTORADO EM GEOTECNIA

PUBLICAÇÃO: G.TD–079/12

BRASÍLIA/DF: AGOSTO – 2012

UNIVERSIDADE DE BRASÍLIA
FACULDADE DE TECNOLOGIA
DEPARTAMENTO DE ENGENHARIA CIVIL E AMBIENTAL

UMA ABORDAGEM DE MODELAGEM FÍSICA QUALITATIVA DE RESISTÊNCIA PARA MACIÇOS ROCHOSOS

LUDGER OSWALDO SUÁREZ BURGOA

TESE SUBMETIDA AO DEPARTAMENTO DE ENGENHARIA CIVIL E AMBIENTAL DA FACULDADE DE TECNOLOGIA DA UNIVERSIDADE DE BRASÍLIA COMO PARTE DOS REQUISITOS NECESSÁRIOS PARA A OBTENÇÃO DO GRAU DE DOUTOR EM GEOTECNIA.

APROVADA POR:

ANDRÉ PACHECO DE ASSIS, PH.D (ENC–UnB)
(ORIENTADOR)

HERNÁN EDUARDO MARTINEZ CARVAJAL, DSC (ENC–UnB)
(EXAMINADOR INTERNO)

ANDRÉ LUÍS BRASIL CAVALCANTE, DSC (ENC–UnB)
(EXAMINADOR INTERNO)

JOÃO LUÍZ ARMELIN, DSC (Furnas–Electrobrás)
(EXAMINADOR EXTERNO)

CARLOS ALBERTO LAURO VARGAS, DSC (EEC–UFG)
(EXAMINADOR EXTERNO)

Brasília/DF, 31 de Agosto de 2012

FICHA CATALOGRÁFICA

SUÁREZ BURGOA, L.O., (LUDGER OSWALDO), 2012
Uma Abordagem de Modelagem Física Qualitativa de Resistência para Maciços Rochosos [Distrito Federal] 2012.
xxvii, 297 p., 32 mm, (ENC/FT/UnB, Tese, Geotecnia, 2012)
Tese de Doutorado – Universidade de Brasília, Faculdade de Tecnologia, Departamento de Engenharia Civil e Ambiental.

1. Descontinuidades	2. Mecânica das Rochas
3. Modelos Físicos	4. LASER
I. ENC/FT/UnB	II. Título (série)

REFERÊNCIA BIBLIOGRÁFICA

SUÁREZ BURGOA, L.O. (2012). Uma Abordagem de Modelagem Física Qualitativa de Resistência para Maciços Rochosos. Tese de Doutorado, Publicação G.TD–079/12, Departamento de Engenharia Civil e Ambiental, Universidade de Brasília, Brasília, DF, 324p.

CESSÃO DE DIREITOS

AUTOR: Ludger Oswaldo Suárez Burgoa
TÍTULO: Uma Abordagem de Modelagem Física Qualitativa de Resistência para Maciços Rochosos
GRAU: Doutor/ ANO: 2012

Ludger Oswaldo Suárez Burgoa
ludger.suarez.burgoa@gmail.com
Calle F. Diez de Medina # 845, Sopocachi Alto
P.O. Box 6794, La Paz – Bolivia

. . . to all the rock mechanics researchers of Latin America.

. . . a todos os pesquisadores da mecânica das rochas de América Latina.
. . . a todos los investigadores de mecánica de rocas de América Latina.

Acknowledgments

The present research was performed under the agreement signed between the University of Brasilia (UnB) and Electrobrás–Furnas company. The laboratory test campaign was supported by the Electrobrás–Furnas company, since other materials and expenses were supported by the Postgraduate Program in Geotechnics of the University of Brasilia (PPG–UnB) and the Post-Graduate and Research Dean of the University of Brasilia (DPP-UnB) in the modality of Support to the Post-Graduate Student of Doctoral Program. The living allowance during the initial three years was granted by the Brazilian Post–Graduate Agency (CAPES: *Coordenação de Aperfeiçoamento de Pessoal de Nível Superior*), under Grant Number L06BOL0280.

The author is thankful to all the institutions mentioned above, as without their collaboration, this thesis would not have been possible.

Special acknowledgments is given to a great friend: Dr. João Luíz Armelin; and to MSc. Heloisa Helena A.B. da Silva, Tech. Renato Batista, Mr. Marco Aurelio Pureza Inacio, Mr. José Donizete Piovezani, Mr. Nilvane Teixeira Porfírio, Mr. Vander Oliveira e Silva, and Mr. Reginaldo Moreira de Araujo, all of them from the Furnas Electrobrás company, for their unconditional support with the physical modeling tests.

Acknowledgment is given to Professor André P. de Assis, adviser of the actual research project and professor of the disciplines: Rock Mechanics, Underground Works, Dams Works and Geotechnical Statistics; for his supervision and clever advices. The same extensive acknowledgments are given to all professors of the Doctoral Course in Geotechnics of the University of Brasilia between the years 2009 to 2011.

A very special acknowledgments are given to the Maia–Restrepo family (Andrea, Geraldo and Sofía), Lucas Ferraz and Paula Osorio, which help me and my family in logistic during the last phase of this doctoral course; and to my colleagues: Paulo André Charbel, Robinson Giraldo, Viviana Trujillo, Gabriel Zapata, Daniel Henao, and Jaime Obando.

Important acknowledgments are given to my wife Nathalia Jiménez Laverde and my little daughter Ana Sofía, who have helped and also supported me with her love and comprehension, during all the process of the making of the doctoral course and the preparation of the thesis.

Finally, I'm thankful to my mother Rosario Burgoa Humérez and my father Milton Suárez Montero, who shown me my correct vocation and have always encouraged and supported me emotionally and economically, during my adventures in life.

Agradecimentos

A presente pesquisa foi feita sob o convênio assinado entre a Universidade de Brasília (UnB) e a companhia Electrobrás–Furnas. A campanha de testes de laboratório foi suportada por Electrobrás–Furnas, e os materiais e outras expensas foram suportados por o Programa de Pós–Graduação em Geotecnia da Universidade de Brasília (PPG–UnB) e ao Decanato de Pesquisa e Pós Graduação da Universidade de Brasília (DPP–UnB) na modalidade de Apoio ao Estudante de Pós-Graduação do Programa de Doutorado. As expensas de vivenda durante os primeiros três anos foram dadas pela Coordenação de Aperfeiçoamento de Pessoal de Nível Superior com o número L06BOL0280.

O autor está muito agradecido com todas as instituições nomeadas acima, que sem sua colaboração, esta tese não seria possível.

Agradecimentos especiais são dados a um grande amigo: Dr. João Luíz Armelin; e a MSc. Heloisa Helena A.B. da Silva, Técnico Renato Batista, Senhor Marco Aurelio Pureza Inacio, Senhor José Donizete Piovezani, Senhor Nilvane Teixeira Porfírio, Senhor Vander Oliveira e Silva, e Senhor Reginaldo Moreira de Araujo, todos eles da companhia Electrobrás–Furnas, pela sua incondicional ajuda nos ensaios dos modelos físicos.

Um agradecimento é dado ao Professor André P. de Assis, orientador do presente projeto de pesquisa e professor das disciplinas: Mecânica das Rochas, Obras Subterrâneas, Barragens e Estatística para Geotecnia; pela sua supervisão e suas sábias sugestões. Os mesmos agradecimentos extensivos são dados a todos os professores do Curso de Doutorado em Geotecnia da Universidade de Brasília entre os anos 2009 e 2011.

Também se dão os especiais agradecimentos á família Maia–Restreo (Andrea, Geraldo e Sofía), Lucas Ferraz e Paula Osorio, que ajudaram a mim e a minha família com logística durante a última fase do curso de doutorado e a tese; e a meus colegas: Paulo André Charbel, Robinson Giraldo, Viviana Trujillo, Gabriel Zapata, Daniel Henao, e Jaime Obando.

Especiais agradecimentos são dados a minha esposa Nathalia Jiménez Laverde e minha pequena filha Ana Sofía, que me ajudaram com seu amor e compreensão durante todo o processo da elaboração de minha tese e o curso de doutorado.

Finalmente, agradeço com minha mãe Rosario Burgoa Humérez e meu pai Milton Suárez Montero, que me mostraram a correta vocação e sempre me ajudaram emocionalmente e economicamente durante minhas aventuras da vida.

A Qualitative Physical Modeling Approach of Rock Mass Strength

Ludger Oswaldo Suárez Burgoa

An interesting approach for constructing and testing physical rock mass models are presented in this research as a new method, which consist in using Optical Borosilicate Crown Glass as representative of rock material and using the Sub–Surface Light Amplification by Stimulated Emission of Radiation Engraving technique as the method to put inside of the translucent material any complex total–persistent and/or un–persistent discontinuity network, without perturbing their surroundings. As a first step for other possible themes that can be studied in future researches within the proposed technique, this research concentrated in the material and discontinuities mechanical description of the model–involved–materials, and on the study of the mechanical behavior at an uniaxial compressive stresses state of a hypothetical rock mass with one set of total–persistent discontinuities, which dip at five different angles between the range of 0°and 90°. In total there were tested 42 cubical samples of around 70 mm of mean side, under a rigid frame. It is concluded from this work that this physical model approach has a good potential to be used to assess qualitatively the ultimate strength behavior phenomena of rock masses, by using scaled specimens, as shown when comparing the tested results with the analytical single–plane weakness model, as described by Jaeger (1969), which is applied effectively nowadays in rock mechanics practice for analyzing rock masses with ubiquitous secondary discontinuities.

Key Words: Discontinuities, Rock Mechanics, Physical Models, LASER.

Uma Abordagem de Modelagem Física Qualitativa de Resistência para Maciços Rochosos

Ludger Oswaldo Suárez Burgoa

Esta pesquisa apresenta uma interessante abordagem para construir e testar modelos físicos de maciços rochosos como um novo método, que consiste em usar Cristais Óticos de Borosilicato, como representante do material rochoso, e usar a técnica de Gravação Abaixo da Superfície com Luz Amplificada por Emissões Estimuladas de Radiação, com o método para colocar dentro do material translucido quaisquer rede de descontinuidades (sejam complexas ou não, persistentes ou não) sem perturbar o material circundante. Como primeiro passo, de muitos possíveis temas que se possam estudar em futuras pesquisas com esta técnica proposta, esta pesquisa se concentrou na descrição mecânica do material e das descontinuidades dos materiais que formam parte do modelo físico, e no estudo do comportamento mecânico de um maciço rochoso hipotético sob um estado de tensçes em compressão uniaxial com uma família de descontinuidades totalmente persistentes que mergulham a cinco diferentes ângulos no intervalo de 0°até 90°. No total foram testados 42 corpos de prova cúbicos com um lado médio de 70 mm em uma prensa rígida. Conclui-se deste trabalho, que esta abordagem de modelo físico tem uma alta potencialidade para avaliar os fenômenos de resistência última com corpos de prova em escala, como demonstraram os resultados dos ensaios quando comparados com o modelo analítico de um só plano de fraqueza persistente, descrito por Jaeger (1969), o que é usado de forma eficaz na atualidade na prática da mecânica das rochas para a análise de maciços rochosos com descontinuidades secundárias onipresentes e persistentes.

Palavras Chave: Descontinuidades, Mecânica das Rochas, Modelos Físicos, LASER.

Contents

List of Figures

List of Tables

List of Abbreviations and Symbols

Acronyms and Abbreviations

2D	Two Dimension(al).
3D	Three Dimension(al).
3D–CDNG	Three Dimensional Cloud Discontinuity Networks Generation.
3D–OSPM	Three Dimensional OBCG SSLE Physical Model.
3UDEC	Three Dimensional Universal Distinct Element Code.
A3DFN	Artificial 3D Fracture Network.
ALDS	Axial Load Data Signal.
ALFS	Axial Load Feedback Signal.
ALOS	Axial Load Output Signal.
ASCII	American Standard Code for Information Interchange.
ASG	Active Strain Gage(s).
ASTM	American Society of Testing Materials.
AWG	American Wire Gauge.
B	Steel Base.
BPM	Bonded Particle Model.
BQi	Basic Quality Index of rock mass.
CHALE	Continuum Homogenous Anisotropic Linear–Elastic.
CHANE	Continuum Homogenous Anisotropic Non–Elastic models.
CNL	Constant Normal Load.
CNS	Constant Normal Stiffness.
CPU	Central Processing Unit.
CRIEPI	Central Research Institute of Electric Power Industry of Japan.
DAC	Data Acquisition Card.
DAS	Data Acquisition System.

DCT.T	*Departamento de Apoio e Controle Técnico*: Department of Support and Technical Control.
DEM	Distinct Element Method.
DFN	Discrete Fracture Network.
DMR	Dam Rock Mass Rating.
DoF	Degree of Freedom.
DSG	Dummy Strain Gage.
DVD	Digital Versatile Disc.
ED	Etched Discontinuity.
F	Frame.
FLAC^{3D}	Three Dimensional Fast Lagrangian Analysis of Continua.
FT1	Force Transducer #1.
GCTS	Geotechnical Consulting and Testing Systems.
GNU	Genuinely Not Unix.
GPL	General Public License.
GSI	Geological Strength Index.
HC	Hydraulic Compressors, Servo Controls, and Intensifiers.
HE	Homogeneously Etched.
HH	Hydraulic Hose.
HJ	Servo–Controlled Hydraulic Jack for Axial Vertical Force.
HSG	Horizontal Strain Gage.
IOSMS	Input & Output Data Management System.
IP	Inferior Platen.
ISG	Inclined Strain Gage.
ISMES	*Istituto Sperimentale Modelli e Strutture*: Institute of Experimental Models and Structures.
ISRM	International Society of Rock Mechanics.
JDBC	Java Data Base Connectivity.
KDP	Potassium Dihydrogen Phosphate.
LASER	Light Amplification by Stimulated Emission of Radiation.
LBM	LASER Beam Machining.
LDT	LASER Damage Threshold.
LOWESS	Locally Weighted Scatterplot Smoothing.
LVDT	Linear Variable Differential Transformer.
M	Monitor.

MATLAB	Matrix Laboratory.
MRMR	Mining Rock Mass Rating.
NaN	Not a Number.
Nd:YAG	Neodymium–doped Yttrium Aluminium Garnet, $Y_3Al_5O_{12}$.
NED	Negative Etched Discontinuities.
NEN	North–East–Nadir coordinate system.
OBCG	Optical Borosilicate Crown Glass.
OOP	Object Oriented Programming.
PC	Personal Computer.
PDF	Portable Document Format.
PFC2D	Particle Flow Code in two dimensions.
PFC3D	Particle Flow Code in three dimensions.
PL	Plane.
PMMA	Poly–Methyl Methacrylate.
PNG	Portable Network Graphics.
PP	Procedural Programming.
R	Steel Reinforcements Plates.
RAM	Random Access Memory.
RDi	Rock mass drillability index.
REV	Representative Elementary Volume.
RMDN	Rock Mass Discontinuity Network.
RMi	Rock mass index proposed by Palmström.
RMR	Rock Mass Rating.
S	Sample.
S3	Software 3 about Data Retrieving.
S4	Software 4 about 3D–OSPM.
S5	Software 5 about Servo Controled System.
SB	Steel Beam (section H type).
SBEL	Structural Behavior Engineering Laboratories.
SC	Steel Column (section H type).
SEM	Scanning Electron Microscope.
SG	*Sin Gravación*: without engraving.
SJM	Smooth–Joint Contact Model.
SMR	Slope Rock Mass Rating.
SP	Superior Platen.

SQL	Structured Query Language.
SRM	Synthetic Rock Mass Model.
SSLE	Sub–Surface LASER Engraving.
UCS	Uniaxial Compressive Strength.
UDEC	Universal Distinct Element Code.
USA	United States of America.
VRML	Virtual Reality Modeling Language.
VSG	Vertical Strain Gage.
WB	Wiring Box.
WE	West to East.
WP	Work Package.
X3D	Extensible 3D Graphics.
XLS	Microsoft Excel spreadsheet file.

Variables in Latin Letters

$\mathbf{n}$	Normal to the discontinuity plane unit–vector.
$\mathbf{p}(\mathbf{n})$	Traction vector.
S_0	Initial state stress tensor.
S_i	Some instance after the initial state stress tensor.
$\widehat{v}_{\text{etching}}$	Mean etching velocity.
$\widehat{v}_{\text{sd},mat.}$	Mean sound propagation velocity, of the specified `material`.
$\widehat{v}_{\text{sd},sample}$	Mean of sound propagation velocity of `sample-type`.
a	Hoek–Brown empirical parameter of rock mass.
A_{BT}	Brown–Trollope strength empirical parameter dependent on discontinuities configuration.
a_{d}	Notch separation to produce notch–coupling for the discontinuities band–width.
A_{G}	Goldstein model rock mass empirical constant dependent on UCS of rock material.
A_{L}	Lama Model empirical constant of rock.
a_{mMin}	Minimum notch separation to avoid notch–coupling but to produce mechanical alteration in the modeled rock material.
A_{M}	Mogi model empirical constant of rock.
A_{ne}	Transverse section parallel to the North–East plane.
A_{Ri}	Ramamurthy model empirical parameter for rock material.

$A_{R,90}$	Ramamurthy model empirical parameter from results of rock mass physical models when β_{sd} equals 90°.
$A_{R,\beta}$	Ramamurthy model empirical parameter dependent on rock mass type.
A_R	Ramamurthy model variable obtained from the plot of deformation modulus *vs.* confining pressure of the rock material.
a_v	Minor ellipsoid half–side of notch volume–geometrical model.
A_{YP}	Yudhbir–Prinzl empirical value dependent on the rock mass quality.
b	Minor sample size.
B_{BT}	Brown–Trollope strength empirical parameter dependent on discontinuities configuration.
B_G	Goldstein model rock mass empirical constant dependent on UCS of rock material.
B_L	Lama Model empirical constant of rock.
b_{min}	Minimum minor sample size.
B_M	Mogi model empirical constant of rock.
B_{Ri}	Ramamurthy model empirical parameter for rock material.
$B_{R,90}$	Ramamurthy model empirical parameter from results of rock mass physical models when β_{sd} equals 90°.
$B_{R,\beta}$	Ramamurthy model empirical parameter dependent on rock mass type.
B_R	Ramamurthy model variable obtained from the plot of deformation modulus *vs.* confining pressure of the rock material.
B_S	Sheorey model empirical number.
b_v	Mayor ellipsoid half side of notch volume–geometrical model.
B_{YP}	Yudhbir–Prinzl empirical value dependent on the rock material.
Bq	Rock mass basic quality index used in China.
C	Confidence.
$c_{d,sample}$	Shear strength of the material across a discontinuity plane under the Coulomb–Navier model of `sample-type`.
c_d	Coulomb–Navier model shear strength of the material across a discontinuity plane.
c_i	Coulomb–Navier model shear strength of rock material.
C_{max}	Maximum confidence value to reject H_o.
c_m	Navier–Coulomb model shear strength of rock mass as an equivalent continuum, homogenous material.
$CV_{prop.}$	Coefficient of variation of the specified `property`.

d_{c}	Breakdown channel diameter of notch.
d_{fi}	i^{th} measurement of the diameter of the cross section of the foot, in the notch geometrical model.
d_{f}	Mean diameter of the cross section of the foot, in the notch geometrical model.
D_{pulse}	Pulse LASER duty.
dip_{d}	Discontinuity dip.
$dipDir_{\mathrm{d}}$	Discontinuity dip–direction.
DoF	Degree–of–freedom.
E_{i}	Rock material elastic isotropic Young Modulus.
$E_{\mathrm{max},LASER}$	LASER maximum pulse energy.
$E_{\mathrm{m},t50}$	Rock mass tangential deformation modulus at the 50% of the ultimate strength.
E_{m}	Uniaxial deformation modulus of rock mass as an equivalent continuum, homogenous material.
$E_{\mathrm{t},50\%,mat.}$	Tangential deformation modulus at the 50% of the ultimate strength of the specified `material`.
$E_{\mathrm{t},50\%,sample,5}$	Tangential vertical deformation modulus of the strain gage number five in respect the axial force of `sample-type`.
$E_{mat.}$	Young's Modulus of the specified `material`.
eV	LASER photon energy.
f	Ultimate force in uniaxial compressive stress tests.
f_{r}	Data Cutting Factor.
f_{d}	Discontinuity friction coefficient.
$F_{\mathrm{max},LASER}$	LASER maximum repetition rate.
f_{pulse}	Frequency of the pulse LASER.
$G_{s,mat.}$	Specific Gravity of the specified `material`.
H_{l}	Alternative hypothesis.
H_{o}	Null hypothesis.
$HK_{mat.}$	Knoop Hardness of the specified `material`.
$HV_{mat.}$	Vicker's Hardness of the specified `material`.
J_{f}	Joint factor.
J_{n}	Axial discontinuity factor, as the number of joints per length in the direction of the maximum compression strength.
k	Horizontal stress to the vertical stress ratio.
k_{n}	Discontinuity normal stiffness.

k_s	Discontinuity shear stiffness.
$K_{Ic,mat.}$	Fracture Toughness of the specified `material`.
L	Side of a rock mass blocky sample.
l	Discontinuity spacing.
l_{fi}	ith measurement of the longitude of the foot parallel to its axis, in the notch geometrical model.
l_f	Mean longitude of the foot parallel to its axis, in the notch geometrical model.
l_{gi}	ith measurement of the length of each finger, in the notch geometrical model.
l_g	Mean length of each finger, in the notch geometrical model.
$LDT_{1on1,mat.}$	Single Shot LASER Damage Threshold of the specified `material`.
$LDT_{Son1,mat.}$	Multiple Shot LASER Damage Threshold of the specified `material`.
m	Natural number.
m_b	Hoek–Brown empirical parameter of rock mass.
m_W	Weibull model rock material constant.
n	Natural number.
n_b	Number of cubic size blocks present in the minor dimension of the volume that represent the rock mass.
n_{d1}	Number of notches in the direction of waviness amplitude that will represent surface roughness.
n_d	Ramamurthy model inclination parameter that varies in respect to β_{sd} angle.
n_{notch}	Number of notches.
n_{O2}	Material Optical Property: non–linear refractive index.
n_{Od}	Material Optical Property: linear refractive index.
n_t	Total number of notches in a gross volume.
P_{avg}	Pulse LASER average power.
P_a	Atmospheric pressure.
P_{base}	LASER base power on a pulse plot.
P_{peak}	LASER peak power on a pulse plot.
Q	Rock mass index proposed by the Norwegian Geotechnical Institute.
R^2	Coefficient of determination.
R_1	One dimensional notch resolution.
R_3	Three dimensional notch resolution.
R_{d1}	Roughness waviness one dimensional resolution in the amplitude direction.
R_{d2}	Discontinuity two dimensional areal resolution.
R_{d3}	Discontinuity three dimensional notch resolution.

R_{dd}	Notch density in the discontinuity.
R_{dm}	Notch density in the material.
R_{d}	Notch gross density.
r_{d}	Ramamurthy model roughness parameter that characterizes discontinuities.
R_{m3}	Rock material three dimensional notch resolution.
r_{max}	Maximum radial crack of notch.
R_{rm1}	One dimensional rock mass resolution.
R_{rm3}	Rock mass three dimensional resolution.
r_{v}	Sphere radius of notch volume–geometrical model.
$R_{\sigma_{\mathrm{c}}}$	Rock mass to rock material uniaxial compressive strengths ratio.
R_E	Rock mass to rock material deformation moduli ratio.
s	Hoek–Brown empirical parameter of rock mass.
$s_{\sigma_{\mathrm{ci},mat.}}$	Standard deviation of uniaxial compressive strength of the specified `material`.
$s_{v_{\mathrm{sd},mat.}}$	Standard deviation of mean sound propagation velocity, of the specified `material`.
$s_{v_{\mathrm{sd},sample}}$	Standard deviation of sound propagation velocity of `sample-type`.
t_{etching}	Etching time.
t_{off}	Base time interval on a LASER pulse plot.
t_{on}	Peak time interval on a LASER pulse plot.
t_{s}	One–dimensional sound wave velocity propagation time.
t_σ	Stress application rate.
$T_{mat.}$	Transformation Temperature of the specified `material`.
V_n	Volume of a material.
V_{ch}	Breakdown channel volume of notch.
V_{et}	Total notch volume in a gross volume.
V_{e}	Notch volume–geometrical model volume.
V_{f}	Total damage volume of notch.
$v_{\mathrm{sd},mat.}$	Sound wave propagation velocity of a specified dry `material`.
$v_{\mathrm{sd},sample}$	Sound propagation velocity of `sample-type`.
V_{t}	Gross volume.
$w_{\mathrm{d\,min}}$	Minimum scaled discontinuity thickness.
$w_{\mathrm{d}model}$	Scaled discontinuity thickness, i.e. model discontinuity thickness.
w_{d}	Dry weight of a solid.
W_{peak}	Pulse LASER peak energy.
$s_{\mathrm{d}model}$	Scaled discontinuity spacing, i.e. model discontinuity spacing.

Variables in Greek Letters

α_{YP}	Yudhbir–Prinzl empirical constant suggested to be equal to 0.65.
$\alpha_{mat.}$	Coefficient of Thermal Expansion of the specified `material`.
$\beta_{\mathrm{g}i}$	i^{th} measurement of the relative angle between two adjacent fingers projected in a plane perpendicular to the foot axis, in the notch geometrical model.
β_{g}	Mean relative angle between two adjacent fingers projected in a plane perpendicular to the foot axis, in the notch geometrical model.
β_{sd}	Inclination of the single set discontinuity plane vector in respect to the direction of the major principal stress.
ε_1	Uniaxial strain measured at the lateral right face in a horizontal position.
ε_2	Uniaxial strain measured at the back face in a horizontal position.
ε_3	Uniaxial strain measured at the back face in a inclined 45° position.
ε_4	Uniaxial strain measured at the frontal face in a vertical position.
ε_5	Uniaxial strain measured at the lateral left face in a vertical position.
$\gamma_{\mathrm{d},mat.}$	Dry unit weight of a specified `material`.
$\gamma_{\mathrm{d},sample}$	Dry unit weight of `sample-type`.
λ_{LASER}	LASER wave length.
ν_{i}	Rock material elastic isotropic Poisson ratio.
$\nu_{mat.}$	Poisson Ratio of the specified `material`.
$\nu_{sample,5-1}$	Strain ratio of strain gage five in respect to strain gage one of `sample-type`.
$\phi_{\mathrm{d},sample}$	Internal friction angle at a discontinuity plane under the Coulomb–Navier model of `sample-type`.
ϕ_{d}	Coulomb–Navier model internal friction angle at a discontinuity plane.
ϕ_{i}	Coulomb–Navier model internal friction angle of rock material.
ϕ_{m}	Internal friction angle of rock mass as an equivalent continuum, homogenous material.
ρ_{notch}	Notch Density, number of notches in an unit volume.
$\rho_{mat.}$	Mass Density of the specified `material`.
σ_1	Principal major stress.
σ_3	Principal minor stress.
σ_{a}	Axial stress.
$\sigma_{\mathrm{c,V}}$	Uniaxial compressive strength of rock mass at a certain volume V as an equivalent continuum, homogenous material (e.g. $\sigma_{\mathrm{c,V1}}$, $\sigma_{\mathrm{c,V2}}$).
$\sigma_{\mathrm{ci},mat.}$	Uniaxial compressive strength of the specified `material`.
$\sigma_{\mathrm{ci},sample}$	Rock material uniaxial compressive strength of of `sample-type`.

σ_{ci}	Uniaxial compressive strength of rock material as an equivalent continuum, homogenous material.
$\sigma_{\mathrm{cm},150d}$	Uniaxial compressive strength of a specimen containing more than 150 secondary discontinuities.
$\sigma_{\mathrm{cm},90}$	Uniaxial compressive strength of rock mass, when β_{sd} is equal to 90°.
$\sigma_{\mathrm{cm},sample}$	Rock mass uniaxial compressive strength of of `sample-type`.
σ_{cm}	Uniaxial compressive strength of rock mass as an equivalent continuum, homogenous material.
$\sigma_{\mathrm{c},D}$	Uniaxial compressive strength of cylindrical samples with diameter D different from the reference diameter.
$\sigma_{\mathrm{c},d}$	Uniaxial compressive strength of cylindrical samples with the reference diameter d.
σ_{H}	Major horizontal natural stress magnitude.
σ_{h}	Minor horizontal natural stress magnitude.
σ_{n}	Normal stress at a plane (e.g. discontinuity).
σ_{ti}	Uniaxial traction strength of rock material as an equivalent continuum, homogenous material.
σ_{v}	Vertical natural stress magnitude.
$\sigma_{E,mat.}$	Uniaxial stress at the limit of elastic behavior of the specified `material`.
$\sigma_{x,0}$	Initial stress magnitude.
$\sigma_{x,\mathrm{f}}$	Final stress magnitude.
τ	Shear stress across a plane (e.g. discontinuity).
$\tau_{\mathrm{min},LASER}$	LASER minimum pulse length.
θ	Spherical angle that determines the orientation of a plane.
φ	Spherical angle that determines the orientation of a plane.
$\widehat{\sigma}_{\mathrm{ci},mat.}$	Mean of uniaxial compressive strength of the specified `material`.

Chapter 1

Introduction

The biosphere contamination is a problem that actually is questioning the actual survivor of the human civilization. Probably, the rock mass seems not to be an important factor for the biosphere protection, but it is known that the stresses transmitted to the underground space can accelerate the dynamic of the geological processes in the earth crust (e.g. huge civil structures —as reservoirs— alter the stress field in the rock mass and can induce short seismic events).

For that reason, rock mass at the earth crustal could also constitute the last defense line of the biosphere, and at the same time the last place to maintain the superficial environment in an acceptable sustainability.

When the rock mass will be invaded more intensively in deep than in the past (e.g. deeper petroleum boreholes and deeper storage chambers), it is important to have a clear understanding of the mechanical behavior of it, which is different in respect to the superficial behavior. For all these reasons, the mechanical behavior understanding of the rock mass is one of the most concerns in the geological engineering.

One of the principal problems of the Rock Mass Discipline (i.e. now still Rock Mechanics) is the rock mass understanding as a mechanical material (i.e. a deformable and strengthen material), is that it has natural defects called in general discontinuities. This singular characteristic of rock mass —represented by the so called geometrical properties of the discontinuities— makes rock mass as a complex mechanical material, situation that comes mainly from two sources:

- there is the problem of the geometrical and mechanical representation of discontinuities;

- depending upon the scale of interest, a discontinuous rock mass may exhibit behavior extending from that of an intact rock to that of a near–homogeneous highly discontinuous medium.

These two facts originated that rock engineering is being nowadays a different discipline from the soil mechanics and solid mechanics.

The assessment of the mechanical properties of rock masses (i.e. strengths and deformations) under a specified chosen model, is at the core of rock mechanics research, and a reliable estimate of these properties is required for almost any form of analysis used in rock engineering (Brown, 2008).

The term discontinuity groups any discontinuous feature within the rock mass, say: fractures, fissures, joints, faults, bedding planes, cleavage planes, foliations etc. More specifically a discontinuity may classified in two main groups:

- primary discontinuities, those features that appears in rock mass occasionally and erracticly (e.g. fault, shear and altered zones) which can be represented deterministically;
- secondary discontinuities, those features that are distributed in the rock mass almost uniformly and mainly under a certain probability rule (e.g. joints, schistosity) which ca be represented probabilistically.

From the rock engineering point of view, rarely an intact rock mass is encountered (i.e. a rock mass without any discontinuity). In almost all rock masses at middle level depth (i.e. from 200 m to 500 m), they have totally persistent or un–persistent secondary discontinuities and some scarce primary ones, this last depending on the geological condition.

Primary discontinuities —in contrast to secondary discontinuities— are treated as individual discontinuities[1]; but the conceptualization of secondary discontinuities has been always a problem.

Until now, neither a consistent theory nor a systematic method exists in order to estimate rock mass mechanical behavior by considering the three dimensional character of persistent and un–persistent secondary discontinuities in rock mass. Not either, a technique for physical modeling of this kind of rock masses was possible to define.

By simplicity and unavailability of solvent theories, continuous mechanics (e.g. elastic and plastic mechanics) was in the beginning an useful tool. But with the advent of the computers

[1] Primary discontinuities: the influence of primary discontinuities is also of great concern, but from this point and after, this will not studied here.

revolution, one of the solution that engineering has found was the use of numerical models. Nowadays, the rock mechanics discipline —by the hand of computational tools— has developed more accurate but more complex numerical models, which take into account the influence of secondary discontinuities, say: under the discontinuous mechanics and under fracture mechanics, both improving our knowledge to simulate secondary discontinuous rock mass with apparently great exactitude.

By fortune, the technology is also at the level to collect —in a comprehensive manner— the fully geometrical properties of secondary discontinuities at rock masses, with the help of stochastic models called Discrete Fracture Network (DFN) models, which defines the so called Synthetic Rock Mass Models (SRM). But, one should be conscious, that even though these theories and tools helped to better understand mechanically the common rock mass, enough experimental evidence does not exist. And it is of great concern to have a more fundamentally–based approach to explicitly consider the factors that are influencing the mechanical responses of rock masses.

Despite the fact that numerical models are a fantastic engineering product of a high human intelligence development of present days, the use of complicated and cumbersome numerical models is a cheap abstract model fashion for unskilled users, that lead them unfortunately to apply that models as a cook–book or a black–box. And the major disservice of these model–users is that they led to a generalized decreasing interest to perform laboratory and *in situ* tests for a better understanding of rock masses.

Rock mass physical modeling decreased when numerical modeling increased to solve the discipline questions; this because high investments have been required to attain physical modeling (e.g. a high level research laboratory), while lower investments are been required to deal with numerical modeling.

Actual laboratory standard test equipments are frequently not large and powered enough to deal with rock masses, and the use of small samples of the rock mass they want to represent often involve uncertainties related to the control of their boundary conditions and problems with scale effects.

Cook (1981) expressed the important need for laboratory testing on a scale of the same order as that of the *in situ* tests, because there are fundamental differences in the problems faced by reduced laboratory testing and *in situ* testings, this last which are tedious and expensive tasks.

With the objective to reduce the conceptual and procedural limitations of numerical and actual physical models, and by the absence of real–scale laboratory tests and huge *in situ* tests in rock masses, the actual research proposal wants to elucidate a possible new approach to simulate rock mass mechanical behavior through reduced physical models using an unpopular method to create discontinuity sets inside a transparent solid material by the use of Light Amplification by Stimulated Emission of Radiation (LASER).

Therefore —this time and as a first step— this research studied the mechanical behavior at ultimate Uniaxial Compressive Strength (UCS) of one set of total persistent discontinuities, dipping at five different angles, created inside Optical Borosilicate Crown Glasses (OBCG) by the Sub-Surface LASER Engraving (SSLE) technique; as a possible representative scaled physical mechanical model of one of the most basic rock mass types present in practice: a single set of total–persistent unfilled discontinuities at a hard and brittle rock material.

The results obtained in this research —may be one of the firsts of its type– were really interesting and useful, because among others techniques it was observed that discontinuities can be easy created inside a solid, and that this physical model so obtained behaves mechanically similar to some particular real rock masses.

Because it is a new proposal of doing something: not all the questions were answered in this research; instead, more questions emerged. It is wished that this work may be the starting point of further research.

1.1 Motivation

Since the advents of the rock mechanics discipline (fifty years ago), researchers were involved in rock mass mechanical behavior. The most principal difficulty of this task was in most all the times to know the influence of secondary discontinuities in rock mass mechanical behavior. Physical models were ever a good choice in trying to model this problem, but even though all model improving attempts, difficulties in preparing samples were —and is still been— a cumbersome problem.

All of these reduced to solve the following question: How can be possible to introduce any secondary discontinuity inside the rock mass model, without disturbing the rock material?

In the eventual case one could have in hand a methodology and a technique which permits

to create any shape, size and sets of secondary discontinuities inside the rock mass without perturbing it, one should think:

- how can be improved actual rock mass mechanical predictions?
- how much time and how many resources can be earned if one could reproduce hundred or thousands of cubic meters of complex structured rock mass in a reduced model, submitted under its real stress regime?

In the following three figures it is shown fictitious laboratory arranges by using the present physical model approach, for studying the mechanical behavior of rock mass under three different common applications in civil, mining and petroleum engineering:

- the excavation process of a circular tunnel inside a rock mass with one set of secondary discontinuities with dip–direction parallel to the tunnel axis and dip equal to 60° submitted into a biaxial natural stress state (Figure 1.1);
- the excavation process of a circular–conical open pit mine inside a rock mass with one set of secondary discontinuities dipping 60° submitted into a biaxial natural stress state (Figure 1.2);
- the drilling process of a deep petroleum borehole inside a rock mass with one set of secondary discontinuities dipping 60° submitted into a biaxial natural stress state and under fluid pressure inside the borehole (Figure 1.3).

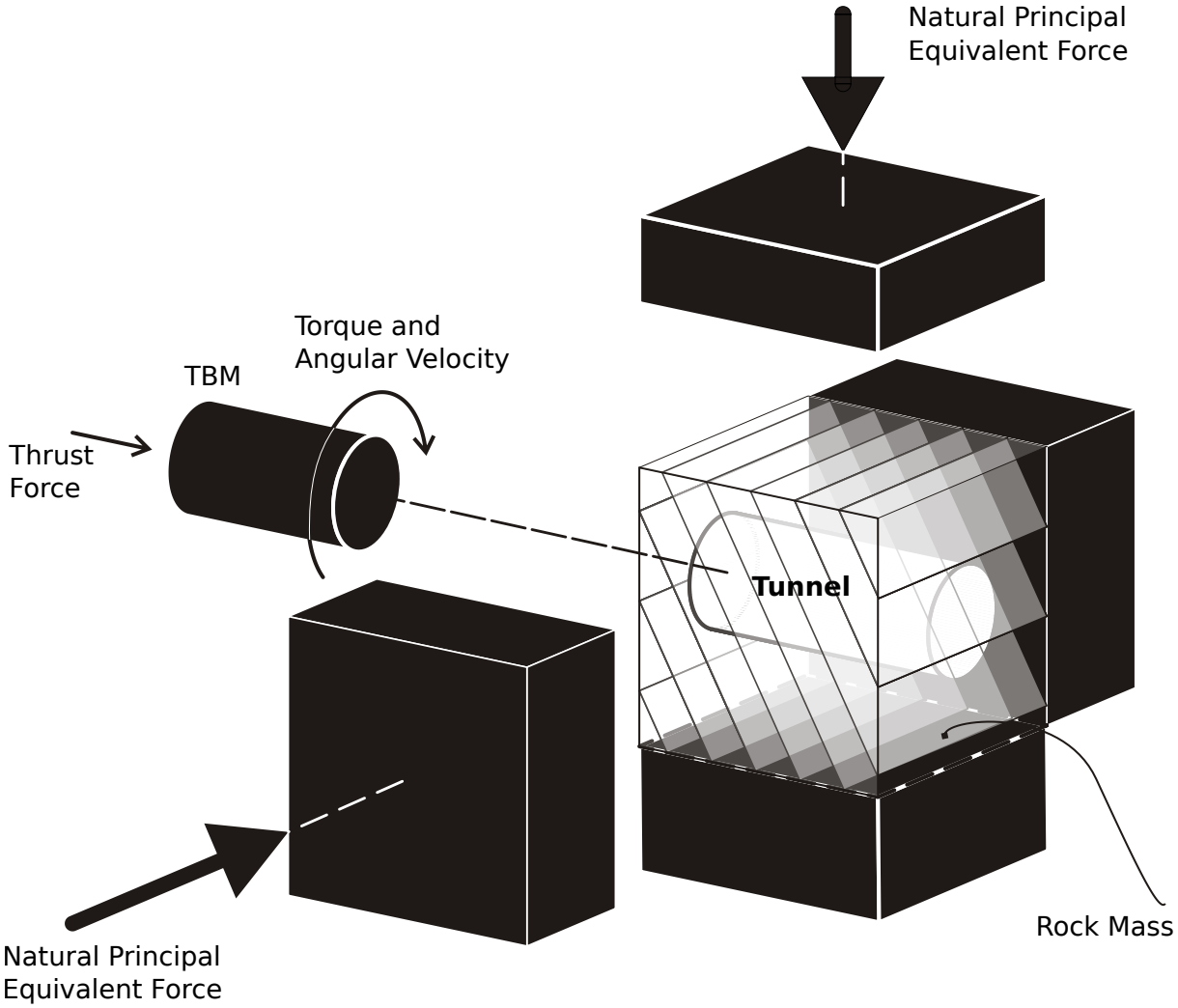

FIGURE 1.1: Tunnel excavation process modeling through reduced physical models.

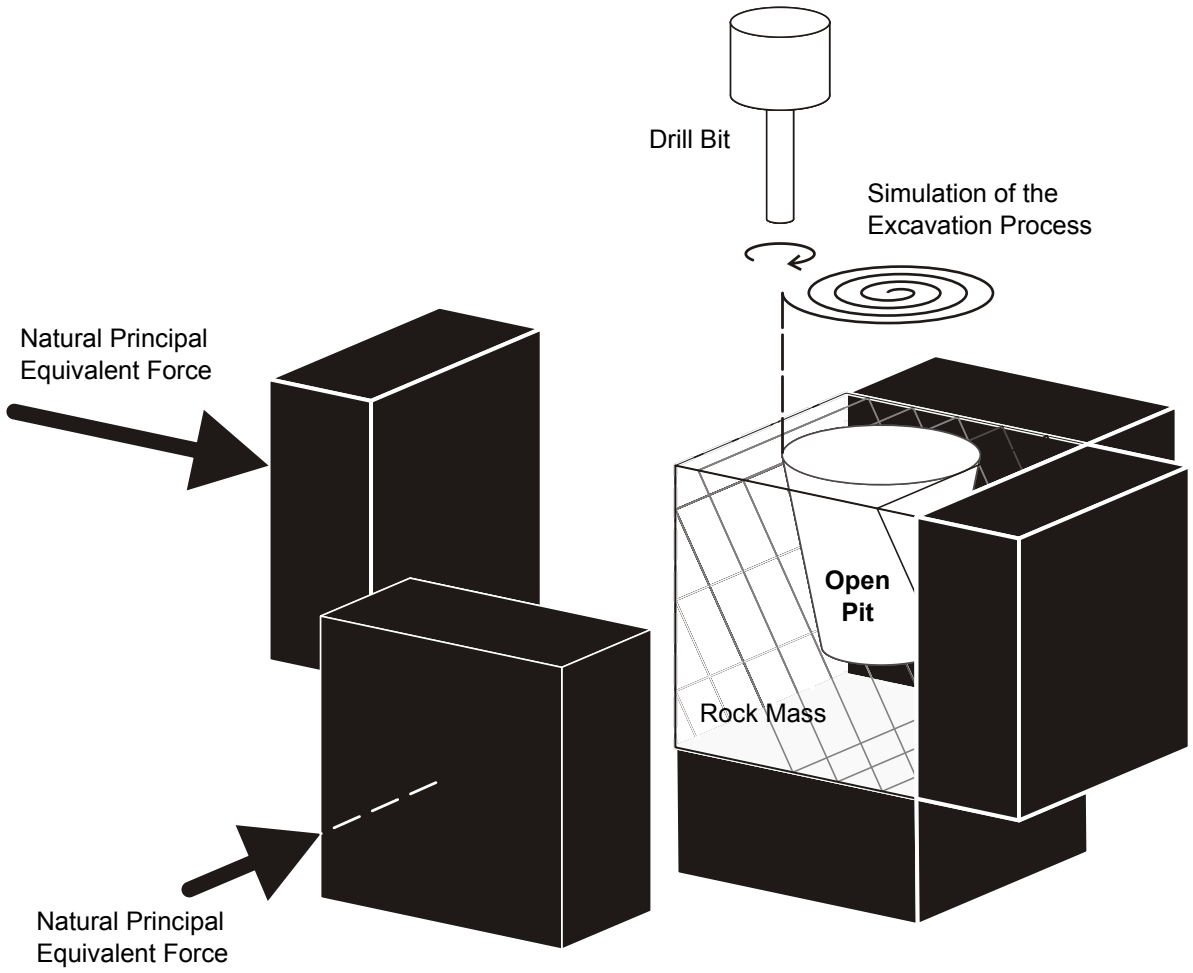

FIGURE 1.2: Open pit excavation process modeling through reduced physical models.

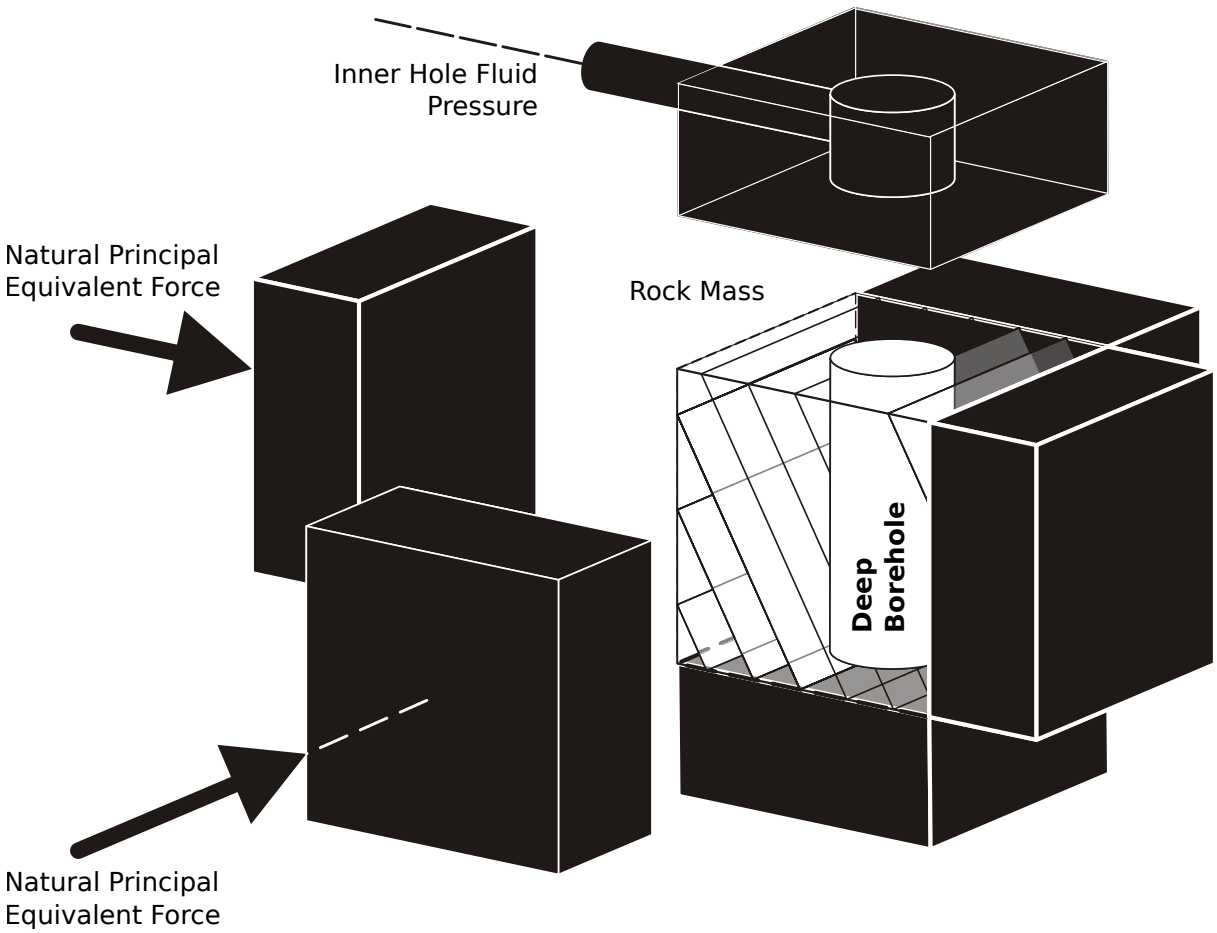

FIGURE 1.3: Deep borehole drilling process modeling through reduced physical models.

In the mentioned figures, and for simplification of them, the shape of the structure, the orientation, the size, the shape and the number of the secondary discontinuity sets, as also the orientation of the principal stresses were set in a convenient simple manner. But the grade of difficulty of those variables should not be a limitation, because in the case one can introduce any secondary discontinuity inside the rock mass model, without disturbing the rock material; one can put inside the model: any arrangement and number of any type of secondary discontinuity sets, any additional primary discontinuity (by cutting the material in two or more parts) and under any stress state. Therefore, all of these will be limited by the size and shape of the sample and the equipment used to apply the forces to generate the desired stress state.

These three examples may open the mind to question about: how more answers one can have in hand? if in addition one can use in the model the real–time monitoring equipments available nowadays (e.g. strain gauges, acoustic emission sensors, bender elements, force cells, displacement transducers) and methods (e.g. electronic speckle pattern interferometry (e.g. Jones and Wykes, 1989), three dimensional photo–elasticity (e.g. Wijerathne et al., 2008), shearography[2]), which are well implemented in specialized laboratories.

The fact to probably have in hand the tail of the answers of the questions mentioned above, was by far the main motivation of this research.

1.2 Main Objective and Hypotheses

Even though the main motivation of this research aims within the methodology of creating any secondary discontinuity inside solid —which was solved in this research when using the OBCG and the SSLE technique— this is not the main objective of this research. The main goal of this research is to demonstrate if any model resulted by this new construction method behaves mechanically similar as the material it is wanted to represent (i.e. the rock mass).

But, there are plenty of mechanical behaviors can be studied (e.g. a deformational static process, a dynamic cyclic process, a degradational process, an ultimate strength process). Therefore, in the present research attention was focused only in the ultimate strength under uniaxial compressive stress and for only one set of discontinuities dipping from 0° to 90°.

The resulting hypotheses of this research was proposed here as a positive affirmation:

[2] Shearography is an interferometric method which allows full–field observation of surface displacement derivatives.

the mechanical behavior about the ultimate strength under uniaxial compressive stress of brittle rock masses, with a totally persistent unfilled secondary discontinuities set, can be efficiently modeled with reduced physical models of Optical Borosilicate Crown Glass prepared with the Sub–Surface Laser Engraving technique.

1.3 Secondary Objectives

To attain the main objective, the following two specific objectives were necessary to accomplish:

- characterize the model materials (i.e. the material that represent the discontinuities and the material that represent the rock material itself);
- validate the models tests results with a common used analytical model.

1.4 Organization of this Document

This document was structured to provide an easy, fast, but clear understanding of the work performed to attain the principal and the two secondary objectives, and to validate or refuse the hypotheses. Therefore, it is comprised on seven chapters followed by a list of references and three appendixes, as described as follows:

- Chapter 1 (this chapter) exposes the necessity and the motivation of the resulting research, and outlines the motivation, the main and the secondary objectives, the hypotheses, and introduces in the topics in summary form;
- in the literature review of Chapter 2 are presented the common popular analytical, empirical, numerical and physical rock mass models; here the section of analytical models is explained in more detail, because it will be used to validate this research results, explained further in Chapter 6;
- Chapter 3 is devoted to describe the fundamentals of the proposed model construction technique (referred here as the OBCG–SSLE technique), which is a combination of the use of the SSLE technique in OBCG;
- in Chapter 4 it is explained the work performed in this research to accomplish the first secondary objective, which was to characterize the model materials (i.e. the material that represent the discontinuities and the material that represent the rock material itself);

- the experimental program of this research (i.e. procedures, materials, equipments and tests performed) is described in Chapter 5, in where also those tests results are presented and discussed;
- in Chapter 6, the results obtained in the above chapter are validated through a common used analytical model, in where findings are discussed by comparing the theoretical results with those obtained in the experimental program; all of these in order to accomplish the second and last secondary objective of this research;
- finally, in Chapter 7, the principal findings that have been drawn on the basis of this research are presented; the conclusions exposed here highlight the benefits of this work, establishes a new approach to rock mass mechanical assessment and outlines recommendations for future work to encourage further research in this field.

In the appendixes of this document it is presented:

- photographs and plots of the data measured during this research experimental program (Appendix A);
- the structured query language (SQL) statements to create the initial data processing from rough measured data (Appendix B).
- the auxiliary codes, scripts, macros and batch files developed in order to facilitate calculations in data pre–processing and post–processing (Appendix C);

In this research all model input parameters as also all reading data are included, in order to be verifiable with same or other models approach. Therefore, in addition to this document —as a complementary electronic material of this research– a single Digital Versatile Disc (DVD) is offered:

- this document in portable document format (PDF);
- the MATLAB® source code of the 3D–CDNG software;
- the POSTGRESQL® script to create the database of all the data acquired in the experimental program;
- the auxiliary source codes and script files here developed;
- the MATLAB® source code of the 3D–OSPM software;
- the cloud–point files of each specimens types.

Hope this research be useful to rock mass mechanics discipline all over the world!

Chapter 2

Literature Review

The present review deals about analytical, empirical, numerical and physical rock mass models. The first one —about analytical models— is discussed exhaustively with formulas and examples, because one of these models will be used as the primer model to validate the physical modeling campaign done in this research. The empirical and numerical models will be discussed superficially because both themes are so interesting but large to deal. Finally, this review ends with a review about physical models used for rock masses.

The review about rock mass physical models is the principal theme of this research, which was focused on the period from the around 1960s of last century to the present. This main review draws mainly on English–language written publications at peer–review and international congress articles, but has also an outlook to publications developed in Latin America, written in Spanish and Portuguese languages. Research documents about this theme in other languages (e.g. German, French, Russian, Japanese and Chinese) were not possible to be consulted.

Non–comprehensive rock mass mechanical models, which is the nowadays state–of–the–art in rock mechanics, can deal only with rock mass deformation at pre–failure and the identification of the maximum failure threshold, all those under three dimensional geometric approach under any three dimensional monotonic stress state path. Researches are being performed in order to have in hand models that can consider pre–failure material damage thresholds —known as critical thresholds (i.e. crack compression, crack initiation, crack damage, and coalescence thresholds; Shen, 1993)— and post–failure deformation; and under a three–dimensional geometric approach, and under any three–dimensional non–monotonic stress state path.

In order to model rock mass, it is imperative to make an outstanding and complete rock mass field–campaign for its description (e.g. Kemeny and Post, 2003; Fouché and Diebolt, 2004; Zhang and Einstein, 1998; Mauldon, 1998; Ferrero et al., 2007; Song, 2006), characterization, and classification (e.g. Henry et al., 2001) and geometrical representation (e.g. Meyer and Einstein, 2002; Starzec and Andersson, 2002; Wu and Wang, 2002); those of them which are interesting research fields in rock mechanics that in the resent years have solved most of their questions, and made it easy to apply; all with the help of electronic equipments and computational calculations. These interesting research fields will not be explained here, but it may be important to say that no rock mass model can be ascertained if a bad rock mass geometrical representation is made.

In the following sections, it will be shown some of the common known rock mass models used in practice.

2.1 Rock Mass Analytical Models

In order to understand the mechanical behavior of rock mass during its deformation until its rupture (or perhaps beyond its rupture), it is necessary to understand separately two concepts:

- the mechanical behavior of the rock material, which is that rock without discontinuities or fractures under the scale selected as appropriate to the engineering problem; and
- the mechanical behavior of the secondary discontinuities by self.

Rock material is the basic constituent responsible for strength of rock mass; while, discontinuities perturbs the rock material modifying the stress media, and it strongly influences the rock mass type of deformation and failure. Sometimes, in each secondary discontinuity, negligible stiffness is present compared with the stiffness of the surrounding material, creating a mismatch between adjacent surfaces. Other times, each secondary discontinuity creates a coalescence process in rock material around it. Also, stresses acting on each of the secondary discontinuity plane creates different stress magnitudes and directions, modifying the stress field around it, and in the overall rock mass.

Similar behavior is present in primary discontinuities, with the difference that they act in a broader scale and are not present in certain Representative Elementary Volumes (REV). This research does not concerns about this kind of discontinuities.

In the rock mechanics discipline, conceptual models were developed in order to describe those two behaviors separately, that of discontinuities and that of rock material. Then, by the appropriate combination of them, it is possible to have an approximate understanding of the entire rock mass.

Oversimplified analytical approaches for predicting the strength of a rock mass with a determined joint pattern of discontinuities exist since at least the sixties of last century (e.g. Jaeger, 1969; Lajtai, 1969). These analytical solutions are still been the fundamental basis for engineering structures analysis at rock masses with a single set of ubiquitous total–persistent and unfilled discontinuities.

Even though, they are good predictors for this special case or rock mass, they often leads to erroneous conclusions in complex rock masses, because it is not possible to ascertain the structural relationships, stress and strength distribution in the complex rock mass structure. This is largely responsible for the slow progress in the development of rational approaches to design engineering structures in rock mass.

Another, more realistic but more complex approach, is to study the rock mass mechanical behavior as a whole unit, without separating the influence of rock material and the secondary discontinuities. At the beginning, in order to approach rock mass mechanical behavior as a whole, empirical approaches as also tests, and large–scale tests were a step forward. Nowadays, with the advent of numerical computation programs, particle stochastic models are a good choice to make similar analysis; but they have lack verifications with real situations, because not always it is possible to have data to compare them.

2.1.1 Rock mass with one total–persistent secondary discontinuities set

The analytical model for one total–persistent secondary discontinuities set is based on the Coulomb–Navier[1] model with the conceptual considerations done by Jaeger (1969) (also see Jaeger and Cook, 1979; Jaeger et al., 2007). This rock mass model was presented for rock masses in the presence of one plane of weakness (i.e. primary discontinuity), but was extensible for the case of a single set of secondary discontinuities within the rock mass. It is called single–plane weakness model, if it is considered as a discontinuous model of one plane within

[1] Coulomb–Navier, in this document it will be used the name of Coulomb–Navier to the model that in most of the references are known as the Mohr–Coulomb model.

the rock mass; ubiquitous model, if it is considered a discontinuity set being a continuum equivalent model; or simply Jaeger Model for rock mechanics practitioners.

The criterion is based on find out those conditions under which ultimate strength will reach in those discontinuities present in rock mass. The principal requisite is that the discontinuities should be weaker than the rock material (e.g. does not apply for the case of a rock mass with a set of strong quartz veins inside a phillite rock material). This analysis was made for the two–dimensional case, where the principal middle stress (σ_2) is equal to the principal minor stress (σ_3).

If σ_n and τ are respectively the normal and shear stresses across the secondary discontinuity planes, the assumption of a Coulomb–Navier model gives the following known expression:

$$|\tau| = c_d + \sigma_n \tan\phi_d \tag{2.1}$$

where c_d is the shear strength of the material in the discontinuity(ies) plane(s) and $\tan\phi_d$ is the coefficient of internal friction for it(them).

Knowing that it is a two–dimensional case, the discontinuity planes can be represented only by the dip angle, and knowing that the plane is inclined β_{sd} grades to the direction of the major principal stress (σ_1), the following equations are resulted:

$$\sigma_n = \frac{1}{2}(\sigma_1 + \sigma_3) + \frac{1}{2}(\sigma_1 - \sigma_3)\cos 2\beta_{sd} \tag{2.2a}$$

$$\tau = \frac{1}{2}(\sigma_1 - \sigma_3)\sin 2\beta_{sd} \tag{2.2b}$$

By substituting Eq. 2.2 in Eq. 2.1 the criterion results as follows, which is known as the Coulomb–Navier criterion:

$$\frac{1}{2}(\sigma_1 - \sigma_3) = \left(\frac{1}{2}(\sigma_1 + \sigma_3) + c_d \cot\phi_d\right)\tan\delta \tag{2.3a}$$

$$\tan\delta = \sin\phi_d \csc(2\beta_{sd} + \phi_d) \tag{2.3b}$$

Another manner to express the above equations is as follows, which was proposed by Jaeger (1969):

$$\sigma_1[\sin(2\beta_{sd} + \phi_d) - \sin\phi_d] - \sigma_3[\sin(2\beta_{sd} + \phi_d) + \sin\phi_d] = 2c_d\cos\phi_d \tag{2.4}$$

Equations 2.1, 2.3 and 2.4 are the fundamental formulae and it should be understood that they apply to the state in failure and in the plane(s) as described above. It will be also noted, that the same condition for failure can be represented in three possible terms, related to the mentioned fundamental equations:

- stresses σ_n and τ across the plane(s) present in rock mass (Eq. 2.1);
- mean normal stress $\frac{1}{2}(\sigma_1 + \sigma_3)$ and maximum shear stress $\frac{1}{2}(\sigma_1 - \sigma_3)$ on rock mass (Eq. 2.2);
- principal stresses, σ_1 and σ_3, on rock mass (Eq. 2.3 or Eq. 2.4).

From these three alternatives, the relation that gives information about the failure of discontinuities in the rock mass is the third one.

Now, suppose the principal stresses on rock mass are $\sigma_1 = 14,5\,\text{MPa}$ and $\sigma_3 = 4,35\,\text{MPa}$ corresponding to the Mohr circle as shown in Figure 2.1.

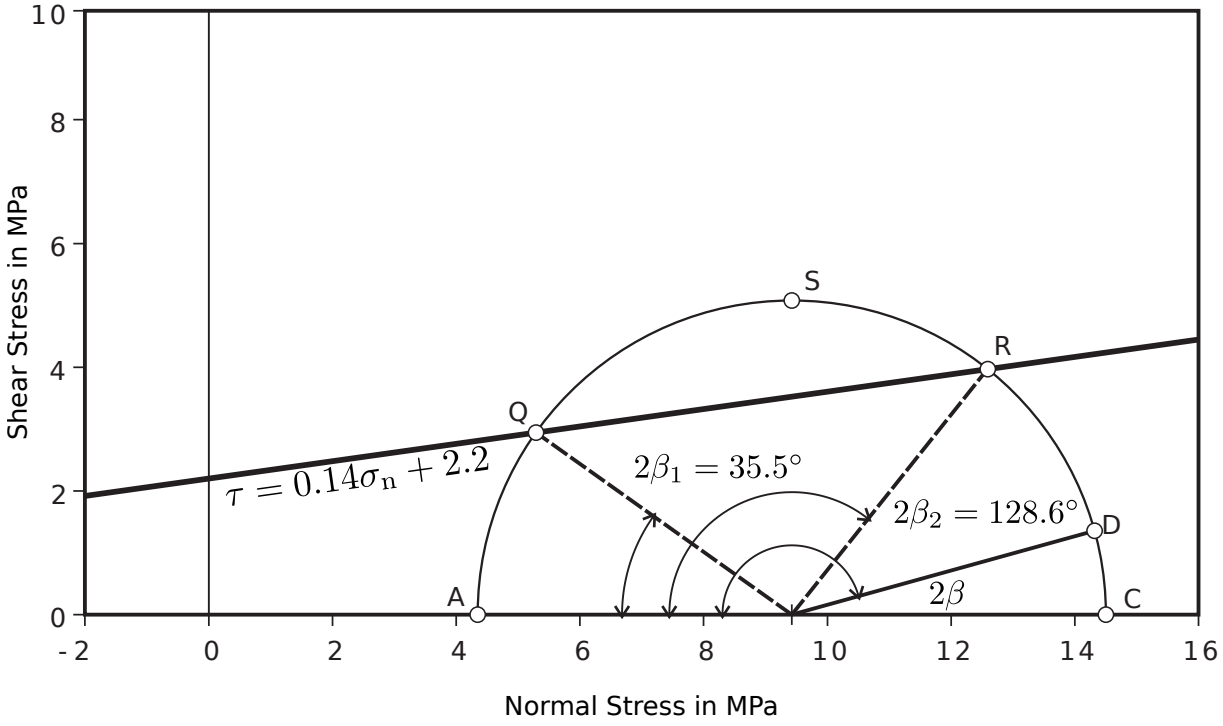

FIGURE 2.1: The Mohr representation for failure in a plane of weakness in rock mass (after: Jaeger, 1969).

For any discontinuity–set plane inclination β_{sd}, the values of σ_n and $|\tau|$ across all the discontinuities of the set will be the coordinates of a point D on the Mohr circle. If this point lies in either of arcs $\widehat{AQ}$ or $\widehat{RC}$, the stresses on rock mass will not cause failure through the discontinuity planes; but if this point D lies in the arc $\widehat{QSR}$, failure will occur through those planes.

In the same rock mass, rock material ultimate strength around discontinuities may be possible to represent under a Coulomb–Navier model, as follows:

$$|\tau| = c_{\mathrm{i}} + \sigma_{\mathrm{n}} \tan \phi_{\mathrm{i}} \tag{2.5}$$

where c_{i} is the shear strength of the rock material in the plane when it fails, and $\tan \phi_{\mathrm{i}}$ is the coefficient of internal friction for it.

In Figure 2.2 the line $\widehat{\mathrm{DE}}$ represents the condition of Equation 2.5 (for a rock material with uniaxial compressive strength σ_{ci} of 6,7 MPa and uniaxial traction strength σ_{ti} of -3,4 MPa) and the semicircle $\widehat{\mathrm{AC}}$ the stress state at failure of that rock material.

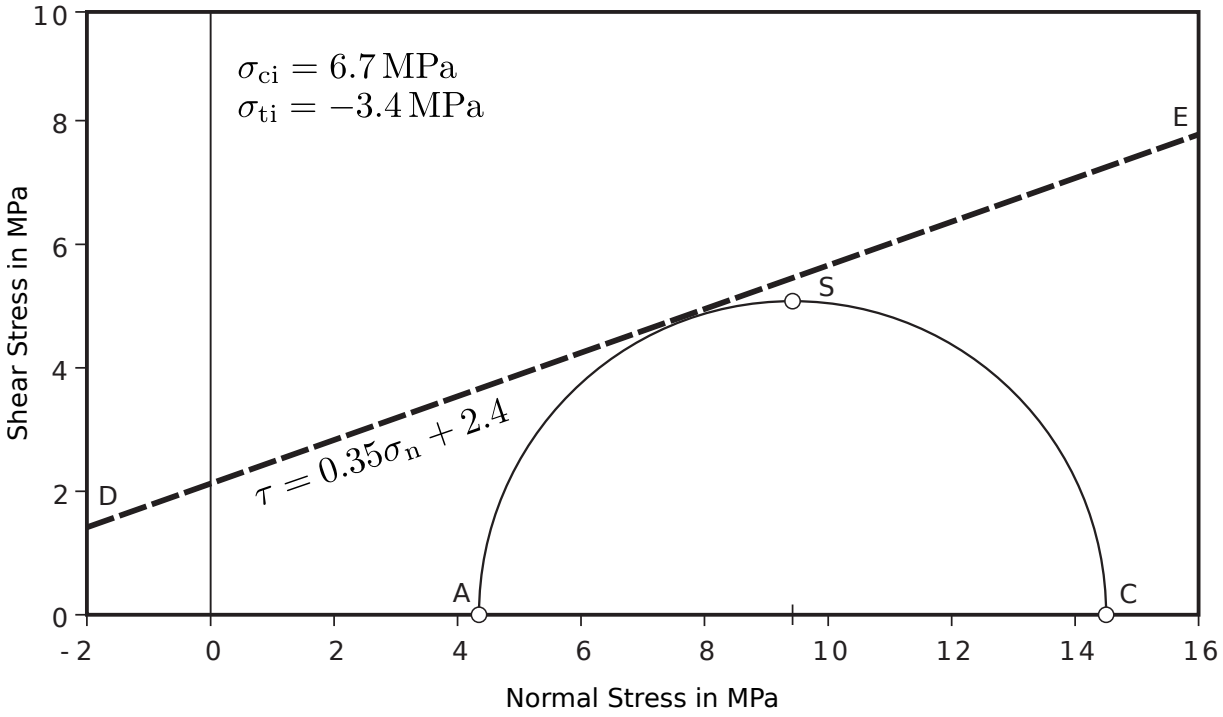

FIGURE 2.2: The Mohr representation for failure of rock material in rock mass (after: Jaeger, 1969).

Now, suppose that from an initial natural stress condition $\sigma_{1,0} = 12\,\mathrm{MPa}$ and $\sigma_{3,0} = 4,35\,\mathrm{MPa}$ of rock mass, where it is stable (i.e. rock material stable + discontinuities stable = rock mass stable), the stress condition changes to $\sigma_{1,f} = 14,5\,\mathrm{MPa}$ and $\sigma_{3,f} = 4,35\,\mathrm{MPa}$. There will be one moment that rock material fails or that discontinuities fail; therefore, both failure envelopes must be analyzed together as shown in Figure 2.3.

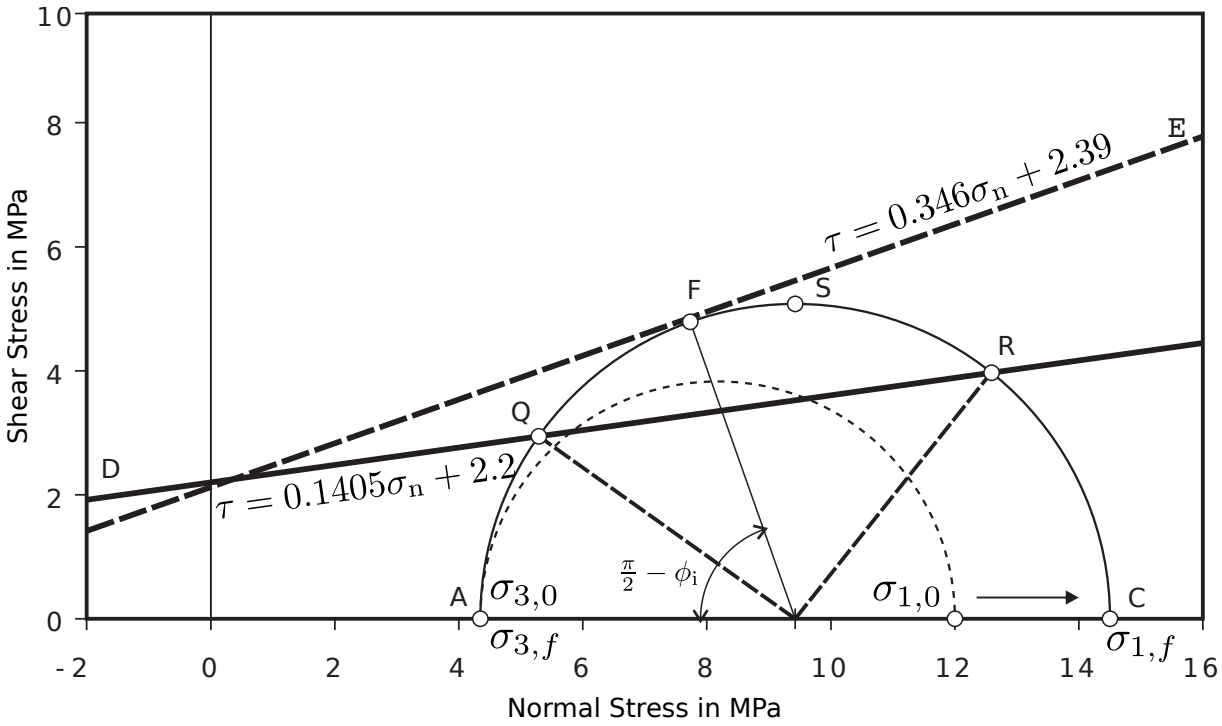

FIGURE 2.3: The Mohr representation for failure of weakness plane and rock material in rock mass (after: Jaeger, 1969).

First, it may be expected that the combination of c_i and $\tan\phi_i$ in Eq. 2.5 will be much larger in strength than the combination of c_d and $\tan\phi_d$ in Eq. 2.1, in order to accomplish the condition that discontinuities be weaker than the rock material; therefore, the line representing the rock material failure must be steeper than the corresponding of discontinuities.

In the case of $2\beta_{sd}$ lies in the arcs $\widehat{AQ}$ or $\widehat{RC}$ and σ_1 increases until the Mohr circle touches the rock material linear envelope; failure may take place through the rock material at the Coulomb–Navier angle of $(\pi/4 - 1/2\phi_i)$ until this fracture plane intersects the discontinuity planes.

In the other case when $2\beta_{sd}$ lies in the arc $\widehat{QFR}$, failure will be present through discontinuity planes before σ_1 creates a Mohr circle that touches the rock material envelope. Similar cases may be possible for a decrement of σ_3, or any unfavorable variations of σ_1 and σ_3.

2.1.2 Rock mass with more than one total–persistent secondary discontinuities sets

In the case in which a rock mass has more than one total–persistent secondary discontinuities sets, the previous consideration for a single set is now possible to consider for each of the sets present in the rock mass. In the analysis, one should select the most unfavorable discontinuity set for the considered stress state. This extension was made by Bray (1967) based on the superposition principle, under the assumption that the failure by slip occurs only in one discontinuity set at time. Therefore, the method will fail when the discontinuities sets increase, because now the interaction among the different discontinuity sets will be not negligible (Amadei, 1988).

Figure 2.4 shows how useful can be the previous considerations, in the case where more than one discontinuity sets are present in rock mass. This figure shows a case of the strength stability analysis of an underground mine, whose WE section extends large to the Northern direction. This mine, is excavated by the stope benching method at 500 m below the surface, and the far natural stress regime is of distension with a factor $k = {}^{\sigma_h}/_{\sigma_v}$ equal to 0.3 and equal horizontal stresses (i.e. the intermediate natural stress [σ_H] is equal to minor [σ_h]).

All three discontinuity sets have the same dip–direction pointing to the East, but variable dip angles and strength parameters as shown in Table 2.1. Mean rock mass unit weight is 29 kN m^{-3}, and uniaxial compressive and extensional strengths of rock material are respectively 15.4 MPa and -7.8 MPa.

TABLE 2.1: Discontinuities Strength Parameters.

Discontinuity Set	$dipDir_d$ in °	dip_d in °	f_d	ϕ_d in °	c_d in MPa
1	090	5	0.158	9	0.8
2	090	55	0.105	6	4.4
3	090	75	0.141	8	2.2

Note. $dipDir_d$ is discontinuity dip direction; dip_d is discontinuity dip; f_d is discontinuity friction coefficient; ϕ_d is discontinuity friction angle; and c_d is discontinuity cohesion.

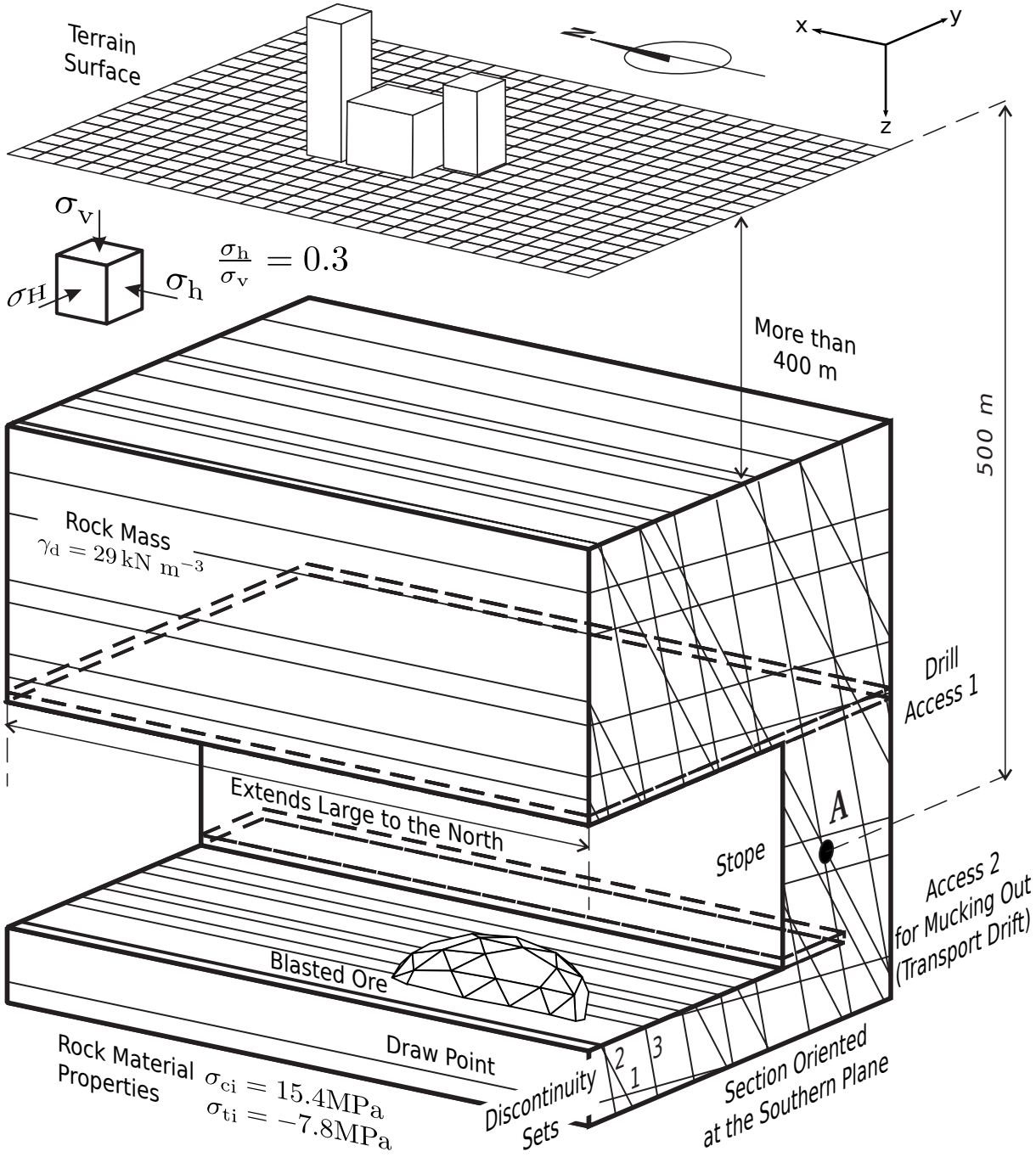

FIGURE 2.4: Rock Mass with Three Discontinuity Sets in a Stressed Stope Mine.

As the excavation will advance, there will be a change of stress state in point A of Figure 2.4, from the initial S_0 to any S_i (Here it is assumed a North–East–Nadir coordinate system [NEN]):

$$S_0 = \begin{vmatrix} \sigma_H & 0 & 0 \\ 0 & \sigma_h & 0 \\ 0 & 0 & \sigma_v \end{vmatrix} \tag{2.6}$$

If it is assumed, for simplification of this example, that stabilization and excavations measures where added to rock mass at point A in order to reduce simultaneously the two horizontal stresses in magnitude and in the same proportion, but without varying their directions; there will be a stress state where the rock mass fails through the discontinuity number 2, as shown in Figure 2.5.

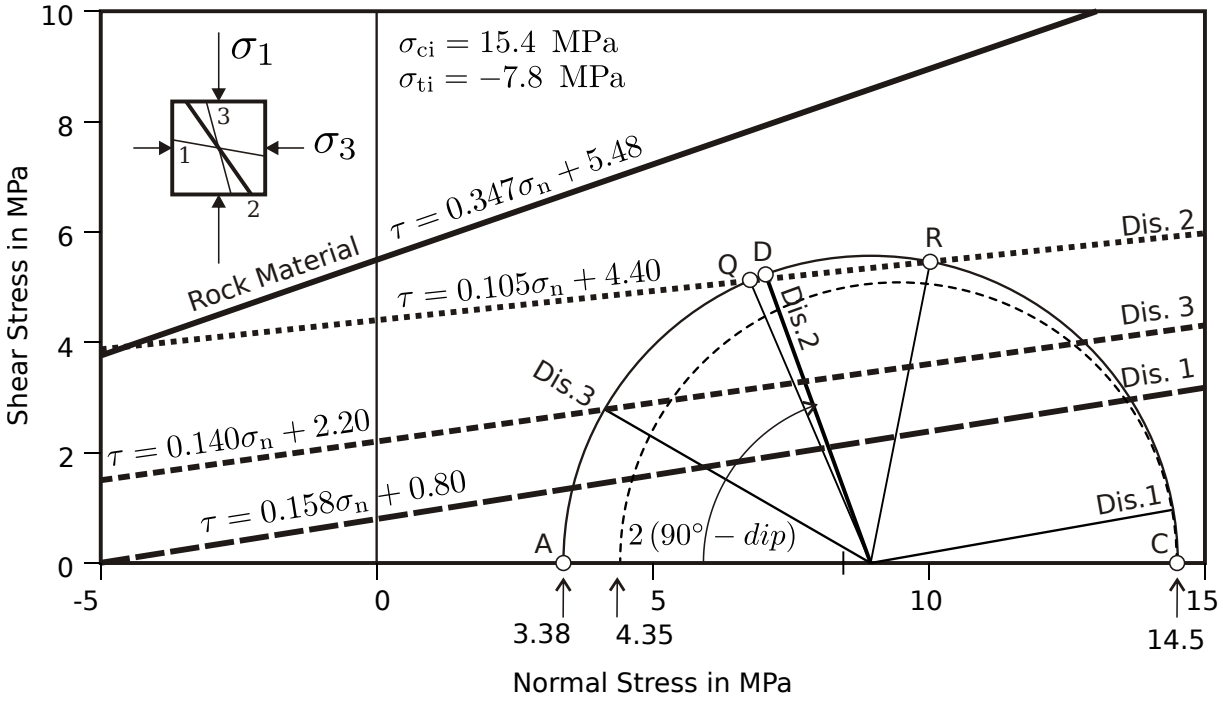

FIGURE 2.5: Stress Condition where Rock Mass Fails.

One can observe with this example, that rock mass is more frequently to fail through one of their discontinuity sets, which are weaker than rock material; but that is not a rule. Also, one can see that in most of the cases, it is not a guarantee to have a strong–to–shear–stresses discontinuity set if it is bad oriented. In Table 2.1 it is shown that the discontinuity number two is the strongest among the other two, but in Figure 2.5 it is observed that this discontinuity is the first to fail for that stress path, because it is bad oriented in respect to the principal stresses orientations

and magnitudes. Therefore, when dealing with rock masses, it is same important to assess the discontinuity strength parameters as also the discontinuity orientation, for all the possible stress state rock mass will pass.

2.1.3 Extension to three dimensions

Only in special cases: in rock slopes at their surface, and in tunnel faces; bi–dimensional stress state conditions are possible at rock masses in common human projects. Instead —specially at deep depths in the rock mass— rock slopes, foundations, galleries and caverns experience all polyaxial conditions.

In the Section 2.1.2 example, we could appreciate that performing a two–dimension analysis is very restrictive, and perhaps no real cases can be analyzed with this approach, but academic cases. Restrictions of a two–dimension analysis require to accomplish the following conditions:

- discontinuity sets all should have the same dip–direction pointing perpendicular to the analysis plane;
- analysis plane should be perpendicular to the intermediate principal stress;
- major principal stress always should be major during all the stress path;
- minor principal stress always should be minor during all the stress path;
- stress path should be monotonic.

By extending the above special two–dimensional case of analyzing rock mass to three dimensions, it is possible to at least ignore the two first conditions described above. The challenge here is to find out the direction cosines of the normals to the discontinuity planes in which slip cannot take place at a given stress state.

This is obtained first by calculating the two shear stresses and the normal stress magnitudes and directions in the discontinuity set plane, by projecting the traction vector $\mathbf{p}(\mathbf{n})$ into the discontinuities set plane given by its unit normal vector $\mathbf{n}$:

$$\begin{aligned} \mathbf{p}(\mathbf{n}) &= \tau^T \mathbf{n} \\ &= \begin{vmatrix} \tau_{xx} & \tau_{yx} & \tau_{zx} \\ \tau_{xy} & \tau_{yy} & \tau_{zy} \\ \tau_{xz} & \tau_{yz} & \tau_{zz} \end{vmatrix} \begin{vmatrix} n_x \\ n_y \\ n_z \end{vmatrix} \end{aligned} \tag{2.7}$$

Then, it is necessary to analyze if the traction vector —which shows a stress state on the plane— fails under the assumed discontinuity shear failure criterion.

By following the previous example of Figure 2.4 in Section 2.1.2, we can now assume that during excavation of the stopes, stabilization measures where added to rock mass at point A in order to maintain invariable in magnitude and direction one of the horizontal stresses, and reduce the other horizontal stress in magnitude until rock mass fails.

For the Discontinuity Set 2 that in the previous example of Section 2.1.2 failed, one can expect that for a similar stress state in where the minor principal stress is equal to 3.38 MPa a failure may occur. Figure 2.6 shows the stress state where this case is analyzed in a Mohr diagram representation. Here the angles θ and φ in the black shaded area, determine in space the orientations of planes that fail.

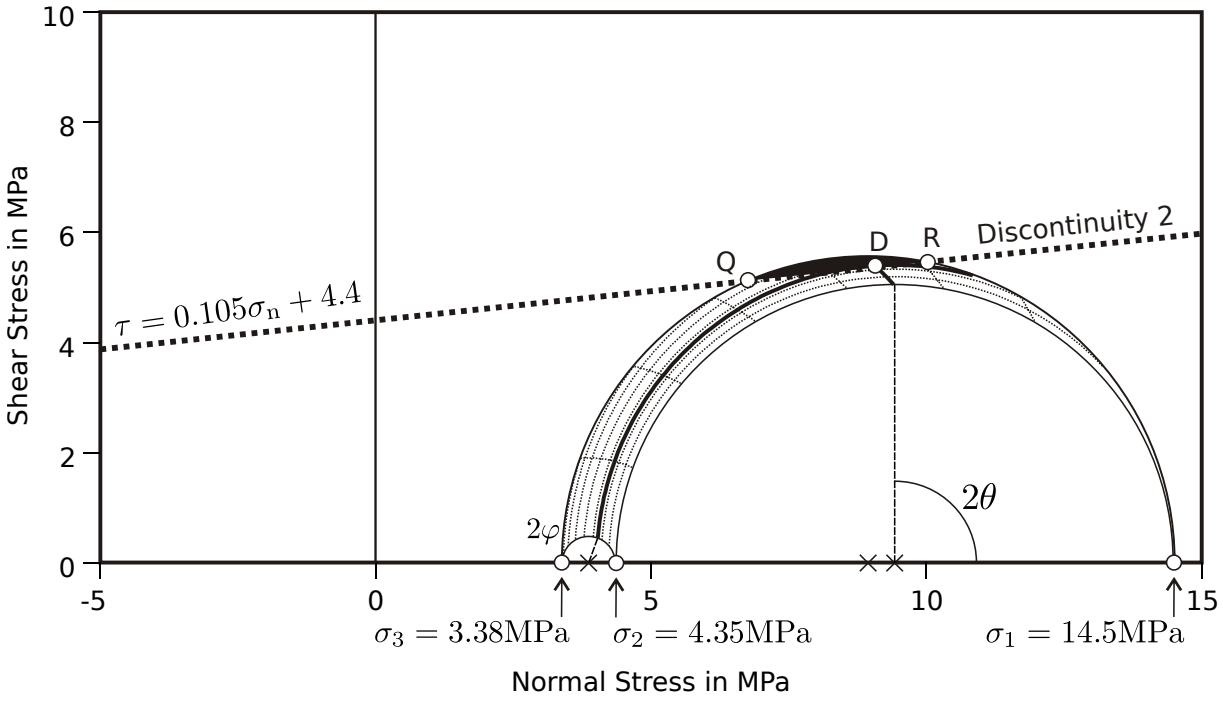

FIGURE 2.6: Stress 3D Condition where Rock Mass Fails.

If it is analyzed for all possible plane orientations, one can see in a stereographic projection plot —where planes are represented by their poles— those regions where plane orientations will fail for the given stress state (see Figure 2.7, the black dashed regions).

Because the pole corresponding to the Discontinuity Set 2 (oriented 270/35) is outside the black regions, it is concluded that failure does not occur through that discontinuity set.

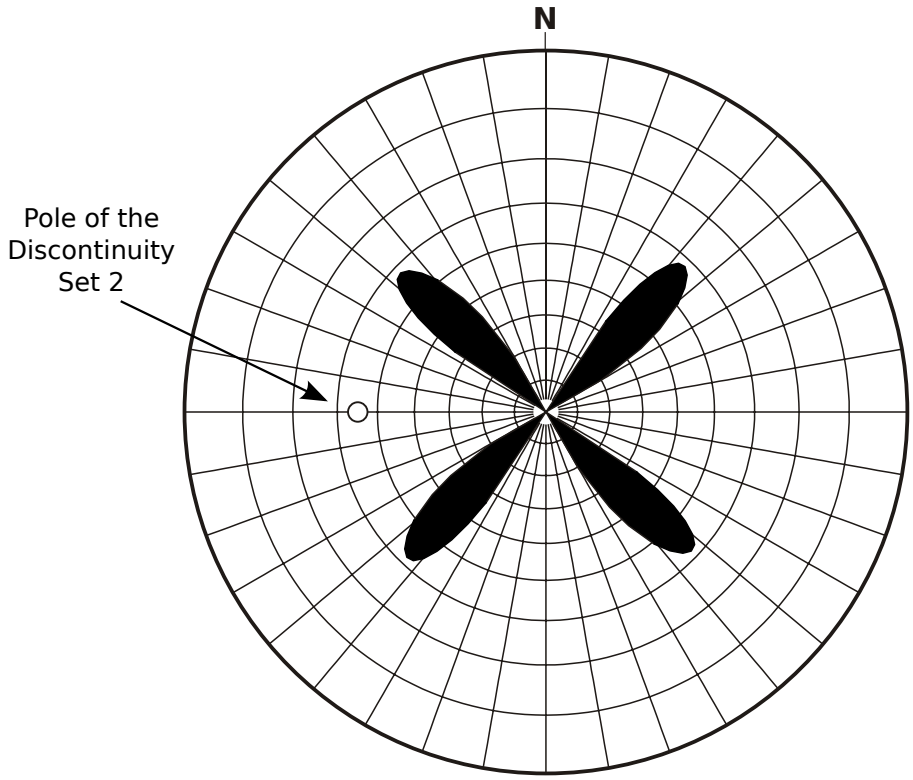

FIGURE 2.7: Stereographic projection of plane orientations that will fail under the stress state given in Figure 2.6.

2.1.4 Rock mass with plenty total-persistent discontinuity sets

By using the same Coulomb–Navier criterion for plenty discontinuity sets in any orientations and for rock material, it is possible to analyze the failure condition of rock mass as shown above.

But there will be a limiting number of discontinuity sets, in which the orientation of them is no more relevant. Therefore, rock mass can be treated as a equivalent continuum, where the weakest failure plane will be present at the angle $(\pi/4 - 1/2\phi_m)$, where $\tan\phi_m$ is the friction coefficient of the rock mass, considered as a continuum.

By this consideration, Eq. 2.5 becomes now:

$$\tau_m = c_m + \sigma_m \tan\phi_m \tag{2.8}$$

where c_m is the shear strength of the rock mass considered as a continuum.

Also, Eq. 2.4 becomes:

$$\sigma_1 = 2c_{\mathrm{m}} \tan\left(\frac{\pi}{4} - \frac{1}{2}\phi_{\mathrm{m}}\right) + \sigma_2 \tan^2\left(\frac{\pi}{4} - \frac{1}{2}\phi_{\mathrm{m}}\right) \tag{2.9}$$

This provides the possible justification for treating some rock masses as an equivalent continuum material. But the questions that still arises for any user are:

- how many is plenty number of discontinuity sets?
- upon how many discontinuity sets one can consider an equivalent continuum material?
- how dispersed should be oriented each of the discontinuity sets in respect to the others, in order to have an equivalent continuum material?
- how spaced should be each of the discontinuity sets, in order to have an equivalent continuum material?

A common practice rule tell that an equivalent continuum approach for rock mass can be possible when the least dimension of the representative elementary volume is at least an order of magnitude larger than the discontinuities average spacing. But the problem of this rule is that in order to assess the REV for each particular rock mass, one should perform that rock mass mechanical assessments for a variety volume sizes, therefore the rule turns to the chicken or the egg causality dilemma.

Therefore it is clear, that the above questions are still unanswered in rock mechanics discipline, and that for that reason there are many controversies when one adopts rock mass as an equivalent continuum material, only for simplicity, economy or availability of a tool to assess it (e.g. a computational program).

2.1.5 Generalization of analytical models

In the above sections it was shown, how rock mass behavior can be modeled by assigning a special an independent failure criterion to the rock material and to the discontinuities set. In the case described above (about the Coulomb–Navier model for rock mass), for convenience and simplicity it was chosen the same model type for rock material and for discontinuities, but differentiating clearly among the parameters for both cases (i.e. rock material and discontinuities).

But, adopting the Coulomb–Navier models in that manner, is not compulsory. If one wants to use more sophisticated and different models for rock material and discontinuity sets, is under

its entire freedom, specially in the presence of many analytical and empirical models developed up to date in rock mechanics discipline.

2.1.6 Parameters estimation for analytical models

The general approach to estimate the parameters of the desired analytical model is to obtain the strength parameters of rock material, and the corresponding for each discontinuity set, separately; by analyzing various stress states. But here emerges at least two other problems when studding the entire rock mass, and when it is wanted to perform laboratory tests on rock material and discontinuities, separately:

- when performing the laboratory tests on rock material, how can one differentiate and mechanically separate between rock material and rock mass?
- when performing the laboratory tests on the discontinuities, how can one isolate the behavior of any secondary discontinuity set from the rock material and/or other discontinuities sets?

In order to solve these two questions, it is necessary to consider a determined scale of analysis, which in most of the cases result in testing huge samples in relation to the human size.

But the major limitation of performing tests, both in samples and discontinuities —in the case of there exist a manner to solve the above questions— is that the standard tests (i.e. uniaxial compressive, triaxial axis–symmetric compressive, indirect traction, direct uniaxial traction, direct shear) do not cover the complete possible stress states the materials can have. For rock material and discontinuity testing, one should submit the sample under true–triaxial tests and not to axial–axis–symmetric or direct stresses, for example.

But, because nowadays standard tests are still the norm for almost all the laboratories; parameters estimation for rock masses is only possible for the special case of two dimensional stress conditions. Therefore and in practice, the Coulomb–Navier analytical model presented above for rock material and discontinuities can be used with reliability, even though it is the simplest model available.

The potential of analytical models for rock masses with a reliable parameter estimation campaign can be shown with the following motivational example.

By considering the Coulomb–Navier analytical model —for both rock material and discontinuities, and for a rock mass with an unique discontinuity set— it was developed a method to

assess the rock mass model parameters with the standard testing methods. For that, one need to perform at least three triaxial–axisymmetric compressive strength tests; or two of them and one uniaxial compressive strength[2] for a total range of discontinuity dips (i.e. from 0° to 90°), for example a set of $\{0, 30, 45, 60, 75, 90\}[^\circ]$. Table 2.2 shows the results of a laboratory campaign of 21 triaxial–axis–symmetric compressive strength tests performed in a fractured Sandstone (Horino and Ellikson, 1970) on straight cylindrical samples, in order to obtain the complete parameters of rock mass model.

TABLE 2.2: Triaxial–Axis–Symmetric Compressive Strength Tests in a Rock Mass with one Discontinuity Set (Horino and Ellikson, 1970).

σ_3 in MPa	dip_d in °	σ_{1f} in MPa	β_{sd} in °
27.6	0	380.3	90
	15	204.1	75
	21	178.1	69
	30	179.1	60
	45	239.5	45
	60	327.8	30
	90	395.0	0
13.8	0	289.2	90
	15	161.0	75
	21	120.3	69
	30	103.0	60
	45	182.1	45
	60	287.1	30
	90	313.5	0
3.5	0	181.0	90
	15	70.8	75
	21	45.6	69
	30	45.6	60
	45	105.4	45
	60	112.4	30
	90	219.5	0

Note. σ_{1f} is the major principal stress at failure; β_{sd} is the acute angle between the discontinuity set plane and the direction of the major principal stress, which is equal to $(90^\circ - dip_d)$ for the special case of the standard uniaxial compressive laboratory test.

Here, because the discontinuities where not possible to isolate from rock material, and rock material could no be possible to isolate from rock mass; it was not possible to perform separately

[2] The uniaxial compressive strength test is considered a special case of the triaxial–axis–symmetric compressive strength test, where the radial stresses are zero.

tests on discontinuities (e.g. direct shear tests) and test on rock material (e.g. uniaxial and triaxial axis–symmetric tests). But, by applying the Jaeger analytical model for the case of one discontinuity set and for a two–dimensional stress state condition, it was possible to find out the rock material and the discontinuities set strength parameters.

To obtain this, it is necessary to assume that the compressive strength of rock material is similar in value to the compressive strength of rock mass when the discontinuities set have an angle to the major principal stress (β_{sd}) of 0° and 90°. Doing so, one can obtain the rock material failure envelope parameters with the test results of those samples that have dip angles of 0° and 90°; and the discontinuity failure envelope parameters from test results of samples that have dip angles different than 0° and 90°. For the last failure envelope parameters, it is necessary to take into account the discontinuity set inclination with respect to the major principal stress (i.e. the β_{sd} angle). Figure 2.8 and Figure 2.9 show the resulted parameters obtained with the data of Table 2.2.

After obtaining the model parameters of both rock material and discontinuities, one can present the rock mass failure model in a graphic, where abscissas are the β_{sd} angle, the ordinates are the σ_{1f} and in the iso–lines the σ_3 stresses; as shown for this example in Figure 2.10.

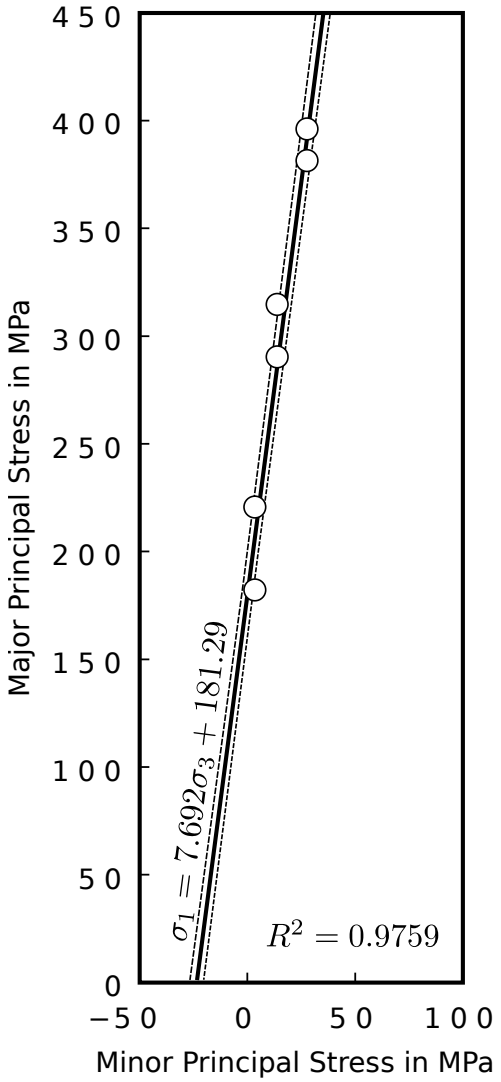

FIGURE 2.8: Rock material failure envelope under the Coulomb–Navier criterion obtained with data of Table 2.2.

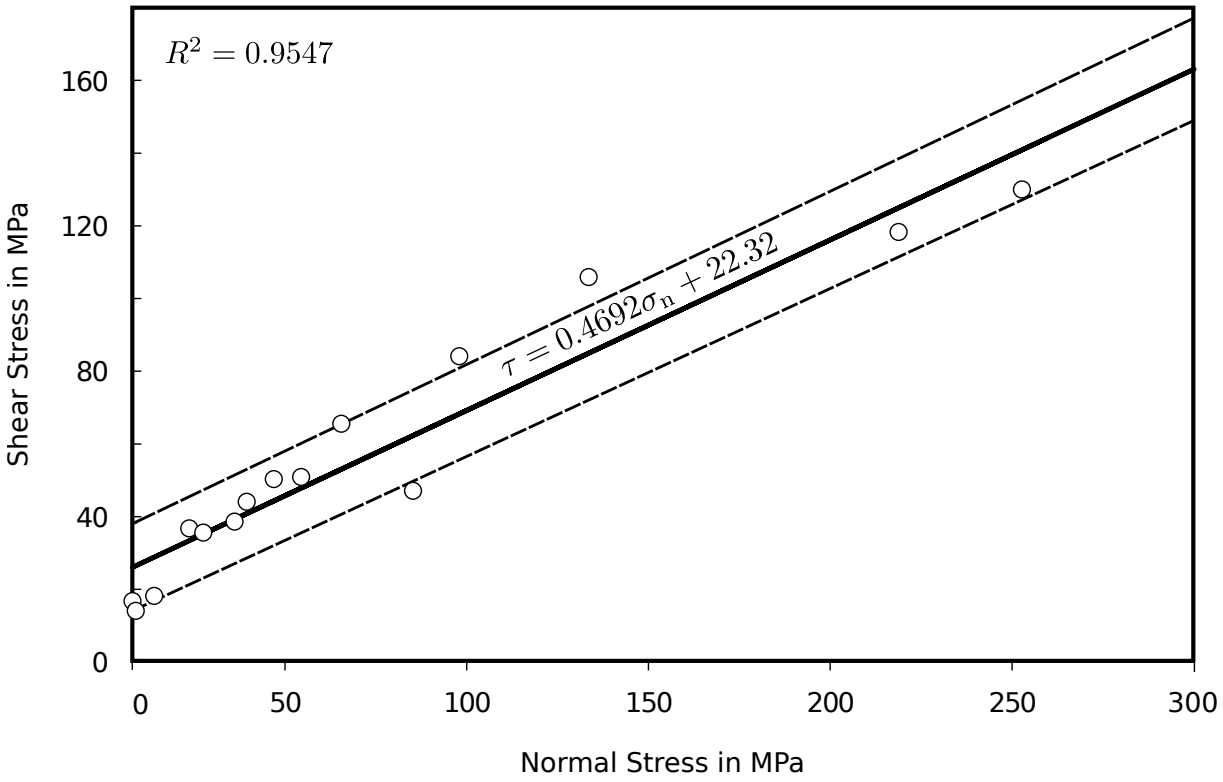

FIGURE 2.9: Discontinuities set failure envelope under the Coulomb–Navier criterion obtained with data of Table 2.2.

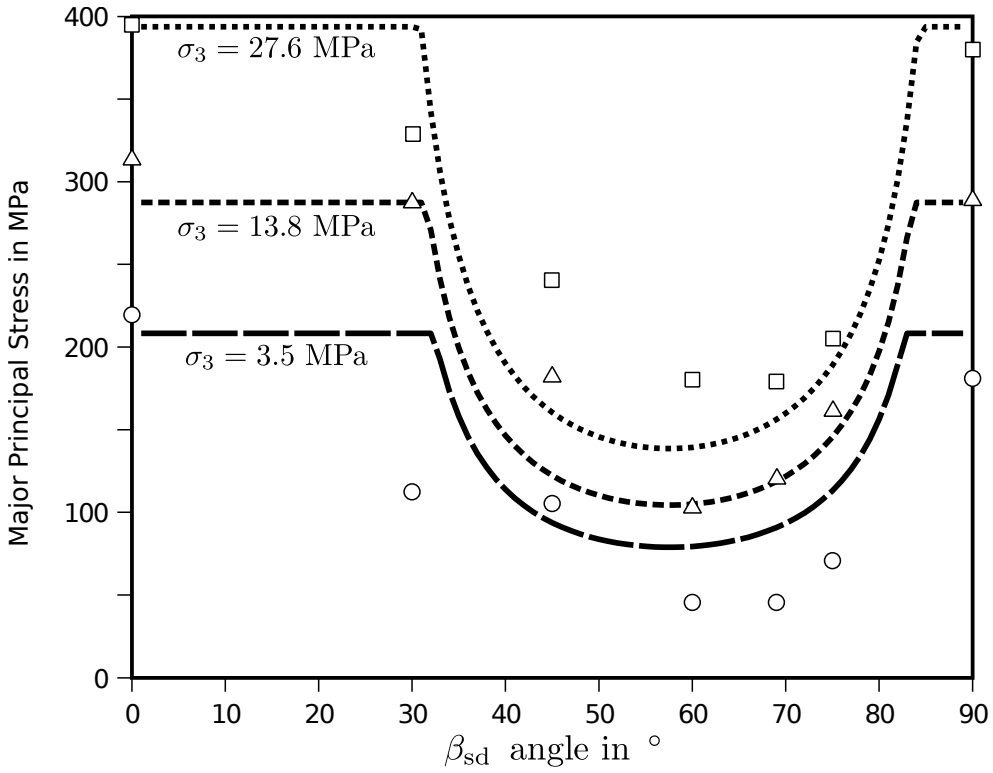

FIGURE 2.10: Rock mass failure envelope under the Coulomb–Navier criterion obtained with data of Table 2.2.

The envelope shown in Figure 2.10 can be drawn by the theoretical basis of the sliding–on–a–plane–of–weakness model, explained in Section 2.1.1, with the following re–arranged equation:

$$(\sigma_1 - \sigma_3) = \frac{2(c_\mathrm{d} + \sigma_3 tan\phi_\mathrm{d})}{(1 - tan\phi_\mathrm{d}\, cot\beta_\mathrm{sd})\, sin(2\beta_\mathrm{sd})} \tag{2.10}$$

where σ_3 is the axis–symmetric minimum stress (i.e. confining stress), β_sd is the inclination of the single set discontinuity plane vector in respect to the direction of the major principal stress σ_1, and ϕ_d and c_d the instantaneous friction angle and instantaneous cohesion of discontinuity under the Coulomb–Navier model.

The failure envelope shown in the mentioned figure is best called an analytical rigid perfectly plastic rock mass model, applied to a triaxial axis–symmetric stress field for a single un–filled discontinuity set surrounded by rock material, and is more representative for low normals stresses at un–filled, near plane and smooth discontinuities that permit shearing under Constant Normal Load (CNL) conditions (i.e. free normal displacement during shear). Similar results were obtained for Slate (McLamore and Gray, 1967) and a physical model (Ladanyi and Archambault, 1972).

Also, similar approach can be applied by using other failure models for discontinuities under high normal stresses at rough waving discontinuities, where shearing is under Constant Normal Stiffness (CNS) conditions, creating dilatation during shear. Also, the rock material failure threshold criteria may be different. But perhaps, their solution will not remain being closed and analytical.

2.1.7 Applications

The use of the analytical models still remains as the principal and first tool to use when dealing rock masses with few secondary discontinuities. For example, Prakoso et al. (2004) resumes exhaustively the procedure to obtain the lower bound bearing capacity of strip footings on jointed rock masses for maximum two discontinuity sets. Here, rock material as also discontinuities where considered to behave in failure within the Coulomb–Navier model.

2.2 Rock Mass Empirical Models

Rock mass empirical models emerged from those empirical expressions —authors proposed in the first steps– to show the scale effect observed at rock material tests when submitted rock mass to uniaxial compressive stresses.

At the beginning rock mass as also rock material was wanted to be modeled as a Continuum Homogenous Anisotropic Linear–Elastic (CHALE) solid, but in the way more tests where performed on small rock samples (i.e. straight cylinders of approximate 50 mm of diameter and height to diameter ratio more than two), more clearly was the necessity to differentiate rock material with rock mass. Therefore the REV concept emerged.

Probably, one of the first possible proposal used an empirical approach to asses rock mass failure —at an uniaxial compressive stress state— was present by Weibull (1939) under the following logarithmic expression:

$$m_{\mathrm{W}} \lg\left(\frac{\sigma_{\mathrm{c},V_1}}{\sigma_{\mathrm{c},V_2}}\right) = \lg\frac{V_1}{V_2} \tag{2.11}$$

where V_1 and V_2 are two different volumes of rock masses, and m_{W} is a constant that depends on the rock material. The last value can vary from 12 for a Granite (Lundborg, 1967) up to 12 for Coal (Bieniawski, 1968).

Twenty years later, Mogi (1962) found out another empirical expression:

$$\sigma_{\mathrm{c},D} = A_{\mathrm{M}}\, d^{B_{\mathrm{M}}} \tag{2.12}$$

where $\sigma_{\mathrm{c},D}$ is the uniaxial compressive strength of cylindrical samples of diameter D greater than the reference sample of diameter d, and A_{M} and B_{M} are empirical constants for each rock type.

From this proposal, some researches found different values of these two empirical constants, as can be shown in Table 2.3.

TABLE 2.3: Empirical Constants for the Mogi Equation about the Scale Effect.

Rock Material	Values		Units		Reference
	A_M	B_M	A_M	B_M	
Marl & Concr.	1.0	-0.092	kg cm^{-2}	mm	Mogi (1962)
Coal	5718	-0.5	psi	inch	Hustrulid (1976)
Qz. Diorite*	60.04	-0.17	MPa	mm	Abou-Sayed and Brechtel (1976)
Maffic Basalt*	6025	-0.85	MPa	mm	Kramadibrata and Jones (1993)
Porphid*	2630	-0.58	MPa	mm	Kramadibrata and Jones (1993)
Au in Dol.*	513 to 603	-0.29	MPa	mm	Kramadibrata and Jones (1993)

Note. Concr. stands for concrete, Qz. for quartz, Dol. for dolerite, and Au for Gold Ore.
*For samples with $d < 150$ mm.

Later, Goldstein et al. (1966) reported laboratory tests results of equivalent continuum models. They proposed an empirical equation for the relation of rock mass to rock material uniaxial strengths (i.e. σ_{cm} and σ_{ci}, respectively) and the relation of rock mass block sample side (L) to discontinuity spacing (l), for the case of three orthogonal sets of total persistent discontinuities, as follows:

$$\frac{\sigma_{cm}}{\sigma_{ci}} = A_G + (1 - A_G)\left(\frac{L}{l}\right)^{B_G} \tag{2.13}$$

where A_G and B_G are empirical values to be dependent on rock material uniaxial strength.

Also, Kostak and Bielenstein (1971) proposed another logarithmic expression:

$$\lg \sigma_{c,V} = 4.7 - 0.06 \lg V \quad \text{stresses in psi and lengths in inches} \tag{2.14}$$

where V is the volume of rock mass and $\sigma_{c,V}$ their uniaxial compressive strength.

Lama (1974) proposed two similar empirical equations for uniaxial compressive strength (σ_{cm}) and uniaxial deformation modulus (E_m) of rock mass. These equations take into account the differences in the mechanical properties related to the size of rock mass cubic specimens (Sridevi and Sitharam, 2003), as it is shown in the following equations:

$$\sigma_{cm} = \sigma_{cm150d} + \left(\frac{L}{l}\right)^{A_L} \tag{2.15a}$$

$$E_m = \sigma_{cm150d} + \left(\frac{L}{l}\right)^{B_L} \tag{2.15b}$$

where $\sigma_{cm,150d}$ is the strength of a specimen containing more than 150 secondary discontinuities, l is the side of a cubic block element that forms the rock mass, L is the side of the cubic rock mass specimen, and A_L and B_L are empiric constants.

Even though these models give the user a numerical result of the ultimate strength of rock mass, this first proposals do not had success because there was no method available to assess the uniaxial compressive strength of rock mass without performing laboratory tests on rock mass samples, therefore no other studies were encountered about the use of these empirical models.

More than 30 years after the first empirical proposal of Weibull (Eq. 2.11), Bieniawski (1975) proposed the Rock Mass Rating (RMR) system, which has introduced a new tendency of rock mass mechanical behavior prediction. Even though the RMR–system is not directly a rock mass strength empirical model, it was the first time that users had in hand a method to give a number to rock mass strength and to indirectly asses numerically at least the uniaxial compressive strength of it. The RMR system has been modified several times since their first proposal, in the measure more rock masses were described with it. Based on the RMR system, surged other particular systems: the Mining RMR (MRMR) —originally proposed by Laubscher (1990); the Slope RMR (SMR); and the Dam RMR (DMR), both last proposed by Romana (e.g. Romana, 2003).

Almost parallel to the Bieniwaski proposal and since that to present, surged in 35 years as many as 21 rock mass indexes. The most common used are the Q index (Barton et al., 1974), the Rmi (Palmström, 1996), and the Geological Strength Index (GSI) (Hoek and Brown, 1980). In Edelbro et al. (2006) it was resumed the mentioned 21 rock mass indexes, under the name of classification or characterization systems. But these authors do not account the for example: Japanese scheme for rock mass description of the Central Research Institute of Electric Power Industry (CRIEPI) (Tanaka, 1964; Kikuchi et al., 1982), the American Society of Testing Materials (ASTM) recommendations for rock mass description (ASTM D5878-08, 2008), the Rock Drill–ability Index (Rdi) (Hoseinie et al., 2008), the rock mass basic quality index (Bq) also called the Chinese BQ Index (Lin, 1998; Feng and Hudson, 2011), or the local academic and industry proposals each country or group of users can propose (e.g. Patiño-Henao, 2005). For that reason, it is very probable that in the world the engineering community is driving as many rock mass indexes we can found, or at least one rock–mass–index proposal each two years.

Rock mechanics discipline has been used all these rock mass indexes for almost 50 years, and the major advantage of this was that they permitted to overcome human projects at rock masses with the use of empirical rock mass models. But researches should grasp the new tendencies of rock mechanical behavior assessment, which basically are the use of:

- complete rock mass description techniques;
- stochastic models to describe secondary discontinuities;
- numerical non–continuous models;
- physical models.

In the following sections, one will shown some rock mass mechanical empirical models — perhaps the most known models— which are dependent by the above mentioned rock mass classification systems. In literature are reported more empirical models than those explained here (e.g. the Franklin (1971), the Amadei (1988), Haimson and Chang (2000) and Kulatilake et al. (2003) models) which also are suitable only for certain types of rock masses configurations and stress states as also stress magnitude levels.

2.2.1 Brown–Trollope empirical model

Brown and Trollope (1970) after conducting physical models of rock masses finally proposed the following rock mass strength model:

$$\left(\frac{\tau - c_{\mathrm{m}}}{\sigma_{\mathrm{ci}}}\right) = A_{\mathrm{BT}}\,\sigma_{\mathrm{ci}}^{(B_{\mathrm{BT}}-1)}\left(\frac{\sigma_{\mathrm{n}}}{\sigma_{\mathrm{cm}}}\right)^{B_{\mathrm{BT}}} \tag{2.16}$$

where c_{m} is the rock mass cohesion, σ_{ci} is the uniaxial compressive strength of rock material, and A_{BT} and B_{BT} are strength empirical parameters which are dependent from the discontinuities configurations. For the particular physical tests campaign performed by the authors, the two parameters c_{m} and σ_{ci} are respectively 3.1 MPa and 20.7 MPa, and parameters A_{BT} and B_{BT} are listed in Table 2.4.

TABLE 2.4: Empirical Constants for the Brown–Trollope Equation about Rock Mass Strength.

Rock Mass	A_{BT}	B_{BT}
Without Discontinuities	39	0.50
Discontinuities Set that Dip 0°	66	0.47
Discontinuities Set that Dip 15°	6.3	0.75
Discontinuities Set that Dip 30°	0.84	1.0
Discontinuities Set that Dip 45°	2.54	0.86

One should be aware that the parameters shown in Table 2.4 only are valid for samples of the same sizes the authors tested (i.e. 102 mm $\times$ 102 mm $\times$ 204 mm), and the same discontinuities configurations (i.e. an arrangement of cubic blocks whose one of its sides dips i°). Therefore, if someone wants to find others parameters for their special rock mass of configuration, it should be performed a similar test campaign, and one should verify if the suggested rock mass strength model applies to that particular case. In conclusion, this empirical model is not universal.

2.2.2 Yudhbir–Prinzl empirical model

The Yudhbir–Prinzl empirical model for rock masses (Yudhbir et al., 1983) practically is the application of the Bieniawski (1974) rock material model applied to soft rock masses. The authors tested samples of Diatomite with discontinuities filled with Gypsum. The expression of this model is as follows:

$$\sigma_1 = A_{\mathrm{YP}}\sigma_{\mathrm{cm}} + B_{\mathrm{YP}}\sigma_{\mathrm{cm}}\left(\frac{\sigma_3}{\sigma_{\mathrm{cm}}}\right)^{\alpha_{\mathrm{YP}}} \tag{2.17}$$

where A_{YP} is a dimensionless parameter whose numerical value depends on the rock mass quality and may vary from 0 —when is rock material— to 1 —when is a disintegrated rock mass (i.e. failure–like material); B_{YP} is a constant dependent on the rock material, with low values for soft rock materials (e.g. 3 for Siltstone) and high values for hard rock materials (i.e. 4.5 for Quartzite); and α_{YP} an empirical constant suggested to be equal to 0.65, because authors shown that is independent of rock material and rock mass quality.

The uniaxial compressive strength of the evaluated rock mass is suggested to be assessed through the *Rmr* index, as follows:

$$\sigma_{\mathrm{cm}} = \sigma_{\mathrm{ci}} \exp\left[7.65\left(\frac{Rmr - 100}{100}\right)\right] \tag{2.18}$$

This empirical failure criterion was developed based on 20 samples tests submitted under triaxial axis–symmetric compressive stresses. The same model was wanted to encompass rock materials as also rock masses, as also to be used indifferently for ductile and brittle rock masses.

2.2.3 Sheorey empirical model

This rock mass model was more properly applied to coal rock masses. The Sheorey empirical model (Sheorey et al., 1989) is resumed to the following expression:

$$\sigma_1 = \sigma_{cm}\left(1+\frac{\sigma_3}{\sigma_{tm}}\right)^{B_S} \tag{2.19}$$

where B_S is an empirical value.

The criterion, as any empiric rock mass model, is dependent on a rock mass index. In this case, first it was dependent on the Q–system, and later the author changed its dependency to the RMR–system.

2.2.4 Hoek–Brown empirical model

The concept of homogenization has already conveyed in the famous Hoek–Brown failure criterion. Apart from this main restriction of this criterion, one should empathize the empirical character of it. Hoek (1983) commented that the process used to derive that empirical criterion was one of pure trial and error, and that apart from the conceptual starting point provided by Griffith theory, there is no fundamental relationship between the empirical constants included in the criterion and any physical characteristics of the rock.

Since the appearance of the empirical model until present, this criterion has been applied in many rock masses worldwide. But it is erroneously treated as an universal rock mass criterion. The same co–author of this criterion Brown (2008) manifested that he is concerned that some of the developments of that criterion —in the past 20 years— may overlook the original purpose of it, its basis and its fundamentally empirical nature. He exposes the uses and abuses of the model and commented on other methods that have been used in engineering practice for estimating the mechanical properties of rock masses. Among those other methods, the physical models were considered one of the important ones.

The generalized Hoek–Brown criterion for rock mass is as expressed as follows:

$$\sigma_1 = \sigma_3 + \sigma_{ci}\left(m_b\frac{\sigma_3}{\sigma_{ci}}+s\right)^a \tag{2.20}$$

where m_b, s, a are parameters for the rock mass, and σ_{ci} is the uniaxial compressive strength of rock material.

Under this model, rock mass can be considered to fail under yielding–ductile manner or brittle manner. There are plenty of publications —in manuals, conference articles, academic and technical books, and research articles (e.g. Cai et al., 2004)— that describes the procedures to obtain the rock mass model parameters from rock material tests, and an outstanding rock mass description, calculations, criticism or generalizations; therefore in this literature review this empirical model will be not more extended in detail.

2.2.5 Ramamurthy empirical model

The PhD theses of Yaji (1984), Rao (1984), Arora (1987), Behrestaghi (1992) and Roy (1993) were the basis in order to define the Rammamurthy rock mass empirical model. In these researches were conducted consistent physical model campaigns.

In the Yaji (1984) research, the researcher did not propose a rock mass strength envelope, but he proposed an expression of the rock mass tangential deformation modulus at the 50% of the ultimate strength $E_{m,t50}$, this related to the confining pressure σ_3 and two numerical values — A_R and B_R —obtained from the plots of deformation modulus *vs.* confining pressure of the rock material, as follows.

$$E_{m,t50} = A_R P_a \left(\frac{\sigma_3}{P_a} \right)^{B_R} \tag{2.21}$$

where P_a is the atmospheric pressure.

In the Arora (1987) research, models were also performed. There, some real rock material —as the Jamarani and Agra Sandstones (in Sridevi and Sitharam, 2003)— were submitted under triaxial–axis–symmetric compression tests. From this thesis the Joint Factor (J_f) concept emerged:

$$J_f = \frac{J_n}{n_d \, r_d} \tag{2.22}$$

where J_n is the axial discontinuity factor calculated as the number of joints per length in the direction of the maximum compression strength, n_d is the inclination parameter that varies in

respect the β_{sd} angle —as used in the above analytical expressions it is the angle between the maximum compression stress direction and the discontinuity plane— and r_d is the roughness parameter that characterizes the discontinuities. Both two last parameters are given by the authors, which proposed them for different rock masses.

The Ramamurthy empirical strength model equations are therefore as follows:

$$\frac{\sigma_1}{\sigma_3} = 1 + B_{R,\beta}\left(\frac{\sigma_{cm}}{\sigma_3}\right)^{A_{R,\beta}} \tag{2.23a}$$

$$\frac{A_{R,\beta}}{A_{R,90}} = \left(\frac{\sigma_{cj}}{\sigma_{cm,90}}\right)^{\left(1-A_{R,90}\right)} \tag{2.23b}$$

$$\frac{B_{R,\beta}}{B_{R,90}} = \left(\frac{A_{R,90}}{A_{R,\beta}}\right)^{0.5} \tag{2.23c}$$

where σ_{cm} is the uniaxial compressive strength of the rock mass as per the Coulomb–Navier criterion, $B_{R,\beta}$ and $A_{R,\beta}$ are empirical model parameters that is rock mass type dependent and should be obtained from a physical model campaign.

In order to obtain the special values of $\sigma_{cm,90}$, $A_{R,90}$ and $B_{R,90}$ —which are the results of the physical models on rock mass when β_{sd} is equal to 90° (i.e. the discontinuities are perpendicular to the major principal compression stress direction)— at least three tests should be analyzed.

In the impossibility to make physical models on rock mass, the author suggest the following empirical equations, in order to assess the parameters of the rock mass model from rock material tests and the J_f variable:

$$\frac{\sigma_{cm}}{\sigma_{ci}} = \exp\left(-0.008 J_f\right) \tag{2.24a}$$

$$\frac{B_{Ri}}{B_{R,\beta}} = 0.13 \exp\left[2.037\left(\frac{\sigma_{cm}}{\sigma_{ci}}\right)^{0.5}\right] \tag{2.24b}$$

$$\frac{A_{R,\beta}}{A_{Ri}} = \left(\frac{\sigma_{cm}}{\sigma_{ci}}\right)^{0.5} \tag{2.24c}$$

where B_{Ri}, A_{Ri} are the Ramamurthy model empirical parameters for rock material.

The variable A_{Ri} is the slope of the plot between $(\sigma_1 - \sigma_3)/\sigma_3$ *vs.* σ_{ci}/σ_3, and B_{Ri} can vary between 1.8 to 3.0.

Rock material strength model can be obtained with the upper parameters with the following equation, (Sridevi and Sitharam, 2000):

$$\frac{\sigma_1}{\sigma_3} = 1 + B_{\mathrm{Ri}} \left(\frac{\sigma_{\mathrm{ci}}}{\sigma_3} \right)^{A_{\mathrm{Ri}}} \tag{2.25}$$

The Ramamurthy also created the theoretical frame in order to have within the J_{f} —a rock mass classification system— which is dependent on the uniaxial compressive strength ratio $R_{\sigma_{\mathrm{c}}}$ and the deformation modulus ratio R_E, ratios of the same property for the case of rock mass and rock material at the uniaxial compressive stress state:

$$R_{\sigma_{\mathrm{c}}} = \frac{\sigma_{\mathrm{cm}}}{\sigma_{\mathrm{ci}}} \tag{2.26a}$$

$$R_E = \frac{E_{\mathrm{m}}}{E_{\mathrm{i}}} \tag{2.26b}$$

In Ramamurthy (2004), the author presented empirical correlations of σ_{cr} and R_E with the most common rock mass indexes (i.e. RMR, Q and GSI). Some of these equations were obtained with the results of the research of Roy (1993). Also, in Sridevi and Sitharam (2003) there are tabulated ten empirical equations that relate R_E with J_{f} for uniaxial a triaxial–axisymetric stress states.

The joint factor is a pertinent concept for rock mass mechanical description, because it is based on many outstanding physical models of similar type. But J_{f} can be near to be exact only for those rock masses which have only one discontinuities set at triaxial–axis–symmetric in compression stress states; and it can fail for polyaxial stress states, or be less exact for rock masses with more discontinuity sets at triaxial–axis–symmetric stress states.

Also, the idea to express a model parameter in respect to the same property for the case of rock mass and rock material at the uniaxial compressive stress state —as in Equation 2.26– is useful, because in the case it is possible to asses these ratios without performing tests or physical models on rock masses, one can obtain these important mechanical values by simply multiplying the ratios with their corresponding values of rock material, they which are obtained by standard tests. As it will be read in the following chapters of this research document, the physical model campaign made here will give the possibility to obtain the uniaxial compressive strength ratio

(R_{σ_c}) —as expressed in Equation 2.26— but not the rock mass uniaxial compressive strength. It is for this reason that the modeling approach gives only a qualitative answer.

2.2.6 Dimensional homogeneity in empirical equations

In this section, it will discussed why some empirical equations given to express some mechanic behavior of rock masses are not properly useful. Major of the described here was obtained from the Chapter 6 of the book Applied Dimensional Analysis and Modelling (Szirtes, 2007). If someone wants to explore more in deep the message it is wanted to transmit in this section, it is recommended that refers to the mentioned book.

Any equation, including empirical equations, to meaningfully express properties of the physical world must fulfill two criteria:

- its two sides must have numerical equality;
- its two sides must have dimensional homogeneity.

In order a expression have dimensional homogeneity, five basic rules should be accomplished— as described by Szirtes (2007). But, most of the empirical equations fails in the first one, which claims: "In any derived equation, both sides of the equation must have identical dimensions. All numbers appearing in this equation must be dimensionless constants (i.e. they must have the dimension of one)".

If any user starts to put in practice the five rules Szirtes (2007) exposed to determine the equal homogeneity of equations used in rock mechanics, one will find out that most of them are not equal homogeneous. Therefore, researches should avoid empirical equations because most of them violate the dimensional homogeneity of an equality.

Finally, the five rules Szirtes (2007) exposed to analyze this matter may also be useful to determine if any equality is analytical or not. An analytical equality should necessary accomplish all the equal homogeneity rules.

2.3 Rock Mass Numerical Models

A numerical model of rock mass consider together the mechanical interaction of the two different types of solids rock mass has: the rock material, and the discontinuities. Therefore, the following paragraphs will not talk about numerical models and constitutive models that tends to simulate rock material or discontinuities separately (e.g. Wang et al., 2003), this because the bibliographic revision can be extensive, and specially because is common to occur that constitutive models for separate material types can simulate correctly a real behavior, but they fail in the moment they are implemented together in a combined type material model, as is rock mass. Perhaps, this is the major overcome of rock mass numerical modeling, and therefore not too much constitutive models exist for rock masses.

2.3.1 Continuous Models

Continuum homogenized media models consist in treating the discontinuous rock mass as a continuum, with equivalent material properties, where the effect of the discontinuities is implicit accounted for. This approach is only valid if a REV was verified to the rock mass to be analyzed. Basic assumptions in order to be possible an homogenization approach are:

- discontinuities are idealized as flat planes;
- discontinuities thickness is negligible when compared to the discontinuity spacing;
- discontinuities are long enough to cut through the REV boundaries;
- REV are bigger enough than the Perturbation Volume (e.g. that volume that an excavation or a foundation will perturb).

In Maghous et al. (2008) it is described in detail the discontinuity density and scale conditions that rock mass should have in respect to the perturbation volume, in order to apply correctly the homogenization model. In general terms, one should assume that the average stresses are distributed throughout the rock mas and the overall strains are contributed by both the rock material and discontinuities; therefore, the expressions for the overall moduli or compliances should be found.

The numerical continuum models approach for rock masses are well applicable for equivalent continuous rock masses, because they can use the constitutive models of solids. Perhaps the best application of continuum models for rock masses appears when one simulates those rock

masses with ubiquitous discontinuities, because one can use a continuous anisotropic constitutive model. This approach is known as the equivalent modeling method or the analytical decomposition technique which puts the influences of discontinuities into the constitutive relation but takes no regard of their exact positions.

For example, Sainsbury et al. (2008) used a three dimensional continuum model to simulate rock mass with one equal–spaced total–persistent discontinuity set, by using the method of finite differences with the aid of the commercial program FLAC^{3D} (this software incorporates the ubiquitous discontinuities model). Rock material as also discontinuities were considered to behave as an elastic isotropic material with Coulomb–Navier failure models. Volumes of the models tested by these authors varied from the hand–sample size to some cubic meters.

Other technique is the use of a consistent theoretical frame with the use of the Discontinuities Tensor concept. The discontinuities tensor concept was introduced for the continuum model approach by the necessity to represent the influence of discontinuities on the global anisotropic response of rock masses, in both deformations and ultimate strength. In literature, the discontinuities tensor name is very little used; instead, the concept is better known as Fracture Tensor or Crack Tensor. Basically the name depends in which material this concept is used and at which scale level is worked on. Also, it was named Damage Tensor, because the applicability it was given to develop damage models under the fracture–mechanics. In this document, it will maintained the broad concept of the discontinuity tensor for generalization.

The strength and the deformability of rock masses considered as an equivalent continuum material may be represented with a second order tensor, which to some extent can capture the anisotropic and scale dependent behavior of rock mass. Discontinuities tensors are obtained from the geometrical properties of discontinuities (i.e. orientation, shape, size, intensity), but it is necessary to guarantee that rock mass attain small displacements before the failure of discontinuities, and that the analysis be applied for at a minimum of one REV.

Unfortunately, the constitutive models resulted with this concept are complicated to manage and operate, and need much input parameters obtained from exhaustive laboratory and field experimental campaigns in order to carry out the analysis. A complete example of how this works is presented by Cai and Horii (1993). Refer to Kulatilake et al. (1993) in order to have a methodology to relate the discontinuities geometrical properties with the discontinuities tensor, and to relate the discontinuities tensor with the rock mass deformability parameters.

In the need for a simpler technique, where the equivalent continuum method can capture sufficiently well the behavior of a discontinuous rock mass using minimal inputs, most of the users turned their attention in apply numerical models under the continuum theoretical frame with rock mass empirical strength models (see Section 2.2) and some continuum deformation model that possibilities consider anisotropic deformation behavior. The deficiency of the inaccuracy of empirical models are compensated with statistical analysis. Under this last methodology, Sitharam et al. (2001) —for example— used the Ramamurthy empirical model (Section 2.2.5) for rock mass strength and a non–linear elastic formulation for deformations dependent from the confining stresses, in where it was possible to admit a small grade of tension. This methodology was used to assess the mechanical response of the Shiobara power station underground opening, located in Japan, which was modeled in two dimensions.

In the other extreme, continuum models can be applicable for rock masses with scarce, but notable in respect to them, primary discontinuities (e.g. a large fracture, thick shear zone, geological fault). Primary discontinuities in rock masses, can be simulated by the numerical continuous approach, by given to that region other model properties values to special and different designed constitutive models and elements from those models for rock materials. This approach is named the explicit modeling method or the numerical decomposition technique because it takes regard of the exact position and dimension of the discontinuities.

For that it should be the necessary to create interface elements or slide–lines between the continuum material, which enable them to model a discontinuous material to some extend. However, their formulation is usually restricted in the following ways:

- the logic may break down when many intersecting interfaces are used;
- there may not be an automatic scheme for recognizing new contacts;
- the formulation may be limited to small displacements and/or rotations.

In the extent of the possibilities and limitations, one can use a combination of both methods: the equivalent modeling method for rock mass with ubiquitous secondary discontinuities, and the explicit modeling method for primary discontinuities.

But, the use of the explicit modeling method for the simulation of rock masses with secondary discontinuities result in a tedious task and imperfect way to deal with. This because it will require to consider each of the hundreds or thousands of discontinuities the rock mass may have. Therefore, continuous numerical models are not the right decision for rock masses with only secondary discontinuities.

Even though the mentioned shortcomings, there were several researches that have analyzed the mechanical influence of secondary discontinuities in rock mass with continuum models. This was possible by reducing the rock mass volume in order to analyze only few discontinuities. For this reason, nowadays there exist some interesting but academic constitutive continuum formulations for special rock masses, which allowed the understanding of the mechanical response of rock masses at all.

For example, Chen (1989) proposed a bi–dimensional constitutive formulation for rock masses with two orthogonal discontinuity sets. The author separated the strain formulation for rock material and for discontinuities, and was solved trough the finite element method by using an academic program. Rock material was assumed to behave linear elastic during deformation and discontinuities assumed to behave no–linear elastic during normal and shear deformation. Maximum strength was assumed to be governed by the Coulomb–Navier criterion, for both rock material and discontinuities.

In Chen and Qiang (2004) it is described in detail how explicit modeling method for rock masses can be used much easier with composite elements. They developed an algorithm for that, but it requires to assume that: there is a small deformation within the rock mass; there is no large–scale shearing and opening along discontinuities; and there is no detachment of sub–elements from the parent elements.

Wang and Huang (2009) set out a constitutive formulation to be used for the simulation a rock mass with a one set of ubiquitous discontinuities. Here, a Coulomb–Navier failure criterion for rock material and the empirical Barton–Choubey failure criterion for discontinuities were considered. The model can simulate pre–failure and post–failure deformations, after differentiate the failure state of rock mass. Pre–failure deformation was by considering an elastic continuum material of rock mass and discontinuities, while post–failure deformation was solved under an empirical formulation according to experimental reported in literature.

Wang et al. (2011) used the Coulomb–Navier shear model to simulate the failure of rock material and secondary discontinuities, and the elastic model to simulate their deformability by using the finite element method with the commercial program Abaqus. In order to understand the mechanical behavior of secondary discontinuities in rock mass, the researchers selected five possible discontinuities planes combinations to analyze exhaustively. They also simulate the scale effect of discontinuity size within the rock mass.

Some tools as the dual boundary element method and the automatic crack growth simulation technique, under the concept of continuity, have provided also powerful techniques to predict the influence of primary discontinuities. Later, they were extended to academic assessment of the influence of secondary discontinuities. For example, Adey and Pusch (1999), uses the Boundary Element Method (BEM) with dual boundary elements to asses the scale dependency in rock mass strength when it has secondary discontinuities. The model consider the linear fracture mechanics approach, but it only considers a two–dimensional case.

Also, Martynyuk and Sher (2002) analyzed in two dimensions the influence of two un–persistent discontinuity traces when submitted under a biaxial compressive stress state. They found a relation between the principal stresses ratio and the orientation of the discontinuity traces.

One interesting continuum approach for treating rock masses with their secondary discontinuities —inclusive un–persistent discontinuities— was reported by Pariseau et al. (2008), by using effectively the representative area element concept for two–dimensions analysis, and the representative volume element concept for three–dimensions analysis. The method suggest account explicitly rock material and secondary discontinuities parameters for elements that are equal or less in size than the REV; and to account them explicitly for those elements that are greater in size than the REV. This method reduces the times considerably in the numerical models solving process.

Finally, it is necessary comment, that even though all the shortcomings the numerical methods under the continuum approach has, they still retain a dominant position in engineering practice.

2.3.2 Discrete Models

Many computer programs based upon a continuum mechanics formulation can simulate the variability in material types and non–linear constitutive behavior, typically associated with a rock mass. But internal distribution of stresses within a rock mass can be highly complex in the measure it has many discontinuity sets, therefore the representation of discontinuities and solving approach requires a discrete–based formulation.

Discrete element methods characterizes in allowing finite displacements and rotations of discrete bodies, including complete detachment, and recognize new contacts automatically as the calculation progresses.

A discontinuous medium is distinguished from a continuous medium by the existence of interfaces or contacts between the discrete bodies that comprise the system. The discrete model is the one of the most straightforward ways of mechanically dealing with the discontinuous rock mass. Some methods related to this kind of discrete approaches have been developed, such as: the block theory, the distinct element method (DEM), the rigid body–spring element method, the discontinuous deformation analysis method, the block element method, the manifold method, and the element–free Galerkin method (Chen and Qiang, 2004).

Among the above mentioned methods, it is the DEM who has been accepted better by rock mechanics users, because it does not require the formulation of complex constitutive models, but requires extensive calibration with measured macro–scale results (i.e. laboratory tests) in order to assess their elementary parameters. One can differentiate between two types used for rock mass mechanics: those DEM which uses systems composed of many polyhedral blocks; and those DEM which uses systems composed of many spheres.

DEM with polyhedral blocks has been converted in a powerful technique to perform stress analysis in rock masses formed by total–persistent discontinuities only (i.e. blocky rock masses), because the model considers an assemblage of rigid or deformable rock material blocks, and discontinuities are considered as boundary interactions among these blocks. But, even though this method solves strictly rock masses with total–persistent discontinuities, now one have in hand a suggested technique to perform analyzes in rock masses with non–persistent secondary discontinuities (Kulatilake et al., 1993).

The most known commercial software used to solve blocky rock masses under the DEM are: the UDEC, for two–dimensions analysis; and the 3DEC for three dimensions analysis. Both are extremely costly programs, even though to the mining and petroleum industry of Latin America. Therefore, the DEM models were widely used in research, when research conveniences are possible to find between the commercial developers and the research institution; and good results were obtained.

The DEM with spherical particles has been used in the last 10 years and is substituting progressively the DEM with polyhedral blocks, because can analyze broad types of materials, including the geological materials as any soil, rock material and rock masses.

DEM with spherical particles used for rock mass models can have two particular methods: the Bonded Particle Model (BPM) (e.g Potyondy and Cundall, 2004; Cho et al., 2007; Wang and Tonon, 2009), which has been used to represent rock material; and the Smooth–Joint Contact

Model (SJM) (e.g. Ivars et al., 2008), which has been used successfully to represent the discontinuities in rock masses at both large and small scales, because particle pairs adjacent to the discontinuity plane are jointed by a smooth–joint contact that may overlap and slide past each other instead of being forced to move around one other, creating a sliding process through the plane.

The most known commercial software used with spherical particles in rock mechanics are the PFC2D and PFC3D, for two and three dimensions, respectively. But these are not unique, an GNU/GPL open source project provide the YADE code, which has similar performance analysis than the three–dimensional commercial program.

DEM models have also their limitations in representing with accuracy complex processes, because small changes in initial conditions may result in large differences in response. Also, there exist computational constraints and inadequate understanding of correct physical response of complex media under complex loading conditions.

2.3.3 Synthetic Models

It is a waste of effort to construct a very large and complicated model with the up–to–date discontinuous methods. For this reason, the synthetic model approach is being used in order to improve the capabilities of sophisticated calculations with those versatile ones.

Synthetic modeling is defined here to the action of create a non- *in situ* and non–huge–laboratory model (i.e. create a numerical model) in where basic standard and well know tests are reproduced (e.g. uniaxial compressive, triaxial axis–symmetric, and poly–axial tests) with the most economically possible but with the highest detail and with most possible exact approach, in order to extract the common, representative, continuum, homogeneous, parameters of the material as a unit whole (i.e. CHALE: Continuum Homogenous Anisotropic Linear-Elastic or CHANE: Continuum Homogenous Anisotropic Non-Elastic models). The parameters resulted by this approach is then applied in simpler material constitutive models, where one can now concentrate attention in the general complexities of a particular problem, like in–homogenities, geometrical features, stress variations etc. This model procedure applied to common laboratory tests, are therefore referred as Synthetic Rock Mass Testing, where samples can vary from 10^3 m^3 up to 100^3 m^3 of volume.

Because non *in situ* and non–laboratory models are mainly analytic–numeric models, this approach is commonly directly related to numerical modeling. But the concept of synthetic model does not discard the possibility to create a physical model which accomplishes the objectives responsible for its creation. Also, because it was shown that a most economically possible with the highest detail and with most possible exact approach is possible efficiently performed under the parallel use of the Bonded Particle Model (BPM) and Smooth–Joint Contact Model (SJM), the synthetic model concept is commonly related to them. But again, this situation does not discard that under some circumstances other simplest/complex analytical–numerical model(s) may be used to create synthetics models.

Common models to create synthetic models may be:

- discontinuous models; and
- particle models.

In synthetic rock mass models the main inputs are rock material properties, discontinuities properties and the discrete fracture network. This approach is proposed as an appealing method for better understanding and prediction of rock mass behavior.

2.4 Rock Mass Physical Models

Rock mass testing may not be only unpractical, but impossible in certain cases, therefore difficult–to–understand phenomena —as are rock masses— were necessarily supported by physical models. Physical model tests are the laboratory simulation of natural processes at a proportionally reduced scale. When the processes to be studied are so complex that a mathematical representation is not easy, physical models are often necessary to identify the key mechanisms, and are an instrument for validation and calibration of numerical models. The greatest benefits of using models occurs in cases when the analytic expression of the sought–after characteristics or variables are not available or only inaccurately known.

Physical unfailingly is an elegant method that provides reliable results, achieved with astonishing speed and little effort, when tackled correctly with the dimensional method.

Numerical models were implemented to enlarge the analysis capabilities of analytical solutions. But, in certain situations the results of numerical models —especially in those involving discontinuous materials— can be extremely sensitive to very small changes in initial conditions or

trivial changes in loading sequence. This situation may seem unsatisfactory and may be taken as a reason to mistrust numerical models. For these reasons, physical models are still being used to model complex problems, as is rock mass mechanical modeling.

Referring to the studies with physical models, it was observed that since the advent of the rock mechanics discipline, most of the research was conducted by considering rock mass as a unit material, even though these was not enough to obtain a good comprehension of rock mass mechanical behavior.

2.4.1 Physical models for rock masses

Research and specific studies on rock masses where performed by Goldstein et al. (1966) resulted in the perhaps the first rock mass empirical model, as shown in Equation 2.13. The researches studied the strength of discontinuities with physical models composed by two cubic halves of 2 cm of side made from Paris plaster with sand. In order to attain different discontinuities strengths, they vary the sand to Paris plaster proportions ratios. Goldstein and coworkers research results contributed also to the so called Patton bi–linear discontinuity strength envelope, which is still applicable for initial estimations of discontinuity strength.

Hayashi (1966), evidenced by physical models submitted to uniaxial compressive strength, that the strength of rock mass decreased with increasing number of secondary discontinuities; nowadays it is just a dogma in rock mass mechanics discipline, but in that days was a novelty. This author modeled rock masses with one set of joints with in–plane and un–persistent discontinuities. He used Plaster as the model material, and discontinuities were simulated by replacing them with Wax papers during the casting. He used four arrangements for a global discontinuity inclination of 30°, 45°, and 60°. Each arrangement used twelve same samples, testing a total of 144 samples. With these tests, it was evidenced that parallel un–persistent discontinuities influences negatively to the rock mass strength.

Krsmanovic et al. (1966) intended to satisfy the law of similarity of models when they modeled a dam foundation. But they did not achieve that. Also they mentioned that the detail precision of the geometrical details of the model should be at least 0.1 mm, which also was impossible to accomplish in their model. This problem is still present nowadays, because it is difficult to obtain a model material with deformation and strength values at the same time proportional to the real material, and also a model material that permits the construction of surfaces at the detail of at least 0.1 mm.

It was Brown (1970) —one among others in the past as Einstein et al. (1969)— that performs conventional triaxial tests (i.e. axis symmetric triaxial tests) on physical models of rock mass prismatic specimens of dimensions 102 mm × 102 mm × 204 mm. The confining pressure (σ_3) was increased from 0 MPa to 14 MPa in four un–equal steps. The rock mass was constructed by the assembly of cubic elements of 25 mm side of Gypsum plaster, arranging therefore a rock mass of three equal spaced discontinuity sets. Even though important results were obtained as for example defined seven zones of failure mechanisms, a global behavior of rock mass was not recognized. Similar investigation was reported in Brown and Trollope (1970). In this last publication, the typical relationship between ultimate uniaxial strength of rock mass to the discontinuity set dip were presented roughly because the absence of more tests in the range from 45° to 90° of dip. The results of those physical models originated the proposal of the Brown–Trollope rock mass empirical model for ultimate strength (Section 2.2.1).

Later, Einstein and Hirschfield (1973) (see also Einstein et al., 1969) reported results when submitting cylindrical rock mass specimens also under triaxial axis–symmetric loads. They also used artificially made jointed specimens of Gypsum plaster. The main goal of the study was to again find out some rational explanation of the effect of discontinuities orientation, spacing, and number of sets on the rock mass. They found that the upper limit of the relation between shear strength and normal stress of the rock mass can be defined by the Coulomb–Navier envelope for the rock material, and the lower limit can be defined by also a Coulomb–Navier envelope but for sliding along the smooth discontinuity surface. Also, they observed that at high stress confining pressures, the influence of discontinuities strength as weaker material is low, and the global rock mass failure mode is of ductile behavior, while at low confining pressures the discontinuities strength influence great in the global rock mass strength and its failure mode is brittle.

Lama (1974) in Sridevi and Sitharam (2003) conducted extensive tests by using model materials of different strengths to determine the influence of the number of horizontal and vertical secondary discontinuities on both deformation moduli and strength. He proposes empirical relations which takes into account the scale effect of rock mass (see Equation 2.15).

The lecture given by Hoek (1983) is considered of importance because it resumes the results of past researches (some of them explained in the preceding paragraphs) and explains the effects of discontinuity sets on the deformability and strength of a rock mass. At the end of the lecture, the author resumes rock mass mechanical strength behavior in an empirical equation, which will be the basis of the today known Hoek–Brown rock mass model.

This lecture describes the highest milestone relating rock mass mechanical behavior and it was

the beginning of the empirical models; but at the same time it was the beginning of the end of rock mass physical models. Since the development of the Hoek–Brown rock mass empirical model, the interest in obtaining answers of the generalized mechanical behavior of rock masses by mean of physical models drops down, drastically. And until now, there is no theoretical model and nor physical model approaches that can compete with the Hoek–Brown rock mass empirical model, even though the last model was developed from knowledge coming from physical models; and it has its deficiencies related to dimensional homogeneity as short exposed in Section 2.2.6.

Parallel to the formalization process of the Hoek–Brown empirical rock mass model, many other researches based on rock mass physical models were performed.

In the eighties decade of the past century, five researches —students of Professor T.N. Ramamurthy (India)— permitted to tests many physical models, with the objective to finally obtain the so called Ramamurthy model —as explained in Section 2.2.5. In the physical model campaigns of these researches, specimens were submitted under triaxial–axis–symmetric tests. Materials used for the specimens were plaster of Paris, Gypsum plaster, Sandstones and Granites. Specimens had a single and multiple discontinuities sets, with or without infilling. Similar as the previous researches, observations where reported about the mode of rock mass failures that are dependent on the magnitude of the confining pressure and orientations of the discontinuities.

All of the above mentioned physical models, were developed in rock masses with totally persistent and orthogonal discontinuities, or with regular block assemblies; and under bi–axial or axis–symmetric stress conditions. Reik and Zacas (1978) made perhaps the hugest rock mass models, by constructing a giant true–triaxial cell for polyaxial stress states; which was a great improvement in the research field of rock mass physical modeling. These authors used physical specimens of 600 mm $\times$ 600 mm $\times$ 1 300 mm which were assemblies of cubic elements of 50 mm $\times$ 75 mm $\times$ 100 mm (case 1) and elements of 40 mm $\times$ 60 mm $\times$ 100 mm (case 2). Case 1 elements were cut in dry from a pre–fabricated German commercial light–weight concrete, while case 2 elements were casted. Also, elements were oriented in order to have one of its planes with a dip angle, which vary in each group of samples according to the set $\{0, 15, 30, 45, 60, 75\}[^\circ]$. Even though 19 tests were performed, they did not report any generalized rock mass behavior.

Only thirty years after, another rock mass physical model campaign were performed under true–triaxial stress states by the Ramamurthy research group (Tiwari and Rao, 2004, 2007). This time, authors used cubic specimens of size 150 mm of side, which were an assembly of

small cube elements of 25 mm side. They arranged the elements in order to have one of their planes dipping at $\{0, 20, 40, 60, 80, 90\}[^\circ]$, and an interlocking of 5 mm at one of their other planes. They performed nine true–triaxial tests and proposed an empirical strength model in the pattern of the generalized Drucker–Prager criterion (Drucker and Prager, 1952). This last research concluded the goals that Reik and Zacas (1978) were searching for.

Further more, in the nineties of last century, Yang and Huang (1995) used also physical models to study the effect of discontinuities sets on the anisotropic behavior of rock masses. They used prismatic physical models of 125 mm $\times$ 100 mm $\times$ 1 300 mm with two discontinuities configurations: one with a two discontinuities sets, dipping at 90° and $\{0$, 15, 30, 40, 45, 50, 60, $90\}[^\circ]$; and the other with three discontinuities sets, in where another inclined set was added with a dip–direction oriented 180° more the second discontinuity set of the first configuration. Each set, in both configurations, had four parallel discontinuities. The researchers tested 26 specimens of the first configuration and 8 specimens of the second one. The main result of this model campaign was that it was observed that the strength of the discontinuities sets can be added or deduct to the strength of rock material only when it is guaranteed that the rock mass has a fracture mode of sliding. They did not proposed any rock mass strength model.

Recent studies were performed by Lin and Ku (2006) and Sainsbury et al. (2008), for example. These studies can be considered a new generation of rock mass analysis because they use the actual numerical models capabilities, allowing perform plenty of computations in short times and permitting be exhaustive in details. With this new analysis tool, researches try to understand rock mass mechanical behavior by describing the micro–mechanics of discontinuities and rock material, establishing their relations, and characterizing with a certain high grade of details. But the great upward of this interesting approach is that they lack of real verification, situation that can only solved with huge in-situ tests, or more easy and economically with physical models.

Tien et al. (2006) prepared physical models of artificial banded rock material. But their experience gave a new approach to construct banded rock–like materials. Their experimental campaign was corroborated with the Jaeger analytical model (see Section 2.1.1) by using the Hoek–Brown strength model for the strong rock material, and the Coulomb–Navier strength model for the weak rock material. Later, they corroborated better with the Imperfect Bonded Interface Constitutive Model (Lai et al., 1997), which assumed that the interfaces among the two materials are partially bonded.

Mughieda and Alzo'ubi (2004) studied the crack coalescence of rock masses with two un–persistent parallel discontinuities submitted to a series of uniaxial compressive stresses by using

physical models. For that challenge they used specimens of size 635 mm × 279 mm × 203 mm, where rock material was replaced with a so called rock–like material, and discontinuities where replaced by solid plates during the material curing in order to obtain a clean space when dried. Even tough the research attempts to elucidate the secondary discontinuities influence in rock mass —because there where analyzed only two un–persistent discontinuities— the research results limited only to show the mechanical behavior around discontinuities. Later, the same research group (Mughieda and Karasneh, 2006) reported their results of the crack coalescence of rock masses with two un–persistent parallel discontinuities; this time under a biaxial compression stress state. They also used the same physical model specimens as those in the past and the discontinuities were all inclined at 45°, but the variation was in the angle between the plane of the discontinuity and the line that connects the two inner tips of the discontinuities, which varied from 0° to 90° with an increment of 15°.

In order to give continuity to the research initiated by Ramamurthy in the eighties of last century, and now under the direction of Professor Roy (Teja, 2008) performed physical tests under uniaxial compressive stress on specimens of Paris Plaster: one group, with only one discontinuity with a β_{sd} angle varying from 0° to 90° with an interval of 10°; and other group, with two parallel discontinuities of a same set with a β_{sd} angle of $\{60, 70, 80, 90\}[^\circ]$.

Also from the same research group, Singh et al. (2002) (see also Singh and Rao, 2005; Singh and Singh, 2008) performed physical modeling in three basic types of cubic–in–shape rock mass specimens with a side of 150 mm, formed from also cubical elements of side 25 mm.

Just in all physical models of this research group, similar characteristics are found:

- in the experimentation of the rock mass specimens, axial deformation is assessed by measuring in four points the global axial shortness through the axial platens, and transverse deformation was assessed by measuring the lateral extension at the center of each vertical face;
- specimens are submitted under a constant rate controlled by the axial deformation;
- axial vertical load is applied through a hydraulic jack which transmitted the force first to a rigid platen with a spherical seat, then to a Teflon sheet smeared with silicon grease, and finally to the rock mass face;
- in order to hold the elements in place during the testing, the specimens are rounded by eight rubber bands of low stiffness;
- deformations are continued be registered until the load decreased to about ½ to ⅔ the peak load;
- block elements arrangement and specimens size are similar.

With the physical modeling tests results, authors tried to differentiate the rock mass failure among always four different modes:

- rotation, in where elements rotates before splitting or shearing mechanism;
- sliding, in where a relative displacement occurred trough the elements planes;
- splitting, in where rock material of elements fail due to tensile stresses without any sign of shearing;
- shearing, in where the contact of the elements planes formed the principal rock mass shearing plane;

All physical model programs performed by this research group were outstanding, therefore the rock mass strength and deformation models they are promoting are clear, supported with many tests over more than thirty years of experience, and are in continuum improving in their techniques. Is for this reasons that one can be more comfortable with the Ramamurthy model rather than the Hoek–Brown model, when a decision about empirical rock mass models is required.

In Latin America, physical models on rock masses were also performed. Bortolucci (1993) used physical models to investigate rock material with cracks mechanical phenomena rather than rock mass mechanical phenomena. But his experience on physical modeling is shown here as an interesting contribution for the region. This author validated a probabilistic failure criterion of brittle rocks under compression —based on the linear elastic fracture mechanics— with physical models of different sizes. Their principal goal was to introduce in his model the scale–effect of the samples. For that reason, he prepared specimens of different sizes with a proportional–to–the–sample crack inside (analogous to a single un–persistent discontinuity). He used plaster to simulate the rock–like material and polyester film strips to introduce the cracks. The physical tests proved that the proposed probabilistic model can be used to predict the scale–effect on the strength of brittle materials, without the necessity to tests specimens of different sizes.

Later, Gaitán-Oliva (2005) of the same research group of Bortolucci, performed a physical model campaign which consisted in submitting 22 rock–like specimens of plaster into a biaxial compressive stress field. This time, the specimens had all 15 un–persistent discontinuities of the same set —arranged in a constant manner— for all the experimental campaign, and was the roughness —under the Joint Roughness Coefficient concept— which varied in each experimental set. The specimens were slabs of 300 mm $\times$ 600 mm $\times$ 132 mm where rock–material was simulated with Plaster and discontinuities by putting poliester film strips. The author verified

that the discontinuities roughness influence the geometrical and mechanical manner of their own propagation when submitted to the tested stress field.

Similar to the Gaitan–Oliva research, Prudencio-Salcedo (2009) (see also Prudencio and Van Sint Jan, 2007) analyzed the mechanical behavior of rock masses with un–persistent discontinuities when submitted to a biaxial stress state. They observed three basic failure modes: failure through a planar surface, stepped failure, and failure by rotation of new formed blocks; after failing eleven samples of 300 mm $\times$ 150 mm $\times$ 50 mm slabs. The stresses were introduced to the slabs through cylindrical hydraulic jacks, as follows: two adjacent sides of the sample were directly in contact to the frame trough steel plates, and the other two opposite adjacent sides of the sample against the jacks through other steel platens, where these last reacts also at the same rigid steel frame. One of the eleven samples doesn't have any discontinuity set, while the others have one discontinuity set in where variation among them where present in discontinuities dip, discontinuities persistence trace length and discontinuities spacing.

2.4.2 Physical models on rock discontinuities

Physical modeling was not only used to study the mechanical behavior of rock masses as a whole, it also contributed to the understanding of the complex phenomenon of discontinuity strength and deformation under direct shear or triaxial stress fields.

For example, Lajtai (1969) proposed a strength model for coplanar un–persistent discontinuities by testing physical models under direct shear. This author studied discontinuous rock masses by using models of plaster of Paris and mixtures of it with Kaolin in cubical samples of 76 mm of side and prismatic samples of the same cubical section but with a height to side ratio of two. In order to create the closed discontinuities between the contact surfaces, he introduced a sheet of tin. Even though Lajtai was conscious of the global mechanical behavior of rock mass, their study limited for that special case of discontinuities and that stress state (i.e. one coplanar un–persistent discontinuity set submitted to shear stress).

Later Ladanyi and Archambault (1970) (see also Ladanyi and Archambault, 1972, 1977) proposed another discontinuities strength empirical model. This model is famous, and common used in practice after the known model of Barton and Choubey (1977). The failure criterion was developed upon physical tests. Even though —with this criterion— interesting discontinuity behavioral answers were obtained, no further researchers using this model were found in literature; therefore, there are no evidence of the universal character of the model.

Later, Xie et al. (1997) prepared six two–dimensional physical models in a polycarbonate material —suitable to be used in photo–elasticity— in order to verify the fractal effects of surface roughness on the mechanical behavior of rock discontinuities. The plates had a side size of 120 mm $\times$ 120 mm and a thickness of 5 mm. The specimens were loaded under uniaxial compression and direct shear. By making use of photo–elastic methods, the contact states and the stress fields close to the discontinuities were assessed.

Also, the Brazilian researcher Fleury (2001) used a similar methodology (i.e. using the photo–elastic method in physical models) to study the stress distribution around discontinuities in rock, when they are submitted under a direct–shear stress field. The specimen dimensions were 190 mm $\times$ 140 mm $\times$ 14.5 mm.

In Colombia, Camacho Tauta et al. (2009) created cylindrical specimens of two rock–like material with different strengths, for three different types of pre–determined roughness at a single discontinuity plane (i.e. planes dipping at 60°). The specimens were prepared with cement mortar (i.e. cement, sand and water). The specimens had 51 mm of diameter and a height–to–diameter ratio of 2.7 . Then, the specimens were submitted under triaxial axis–symmetric stresses, with variable chamber pressures of 2 MPa, 6 MPa and 10 MPa, in order to find out the mechanical strength against failure of the discontinuities. Axial desviator stress was submitted under a rate of 0.07 MPa s^{-1}. With this experimental campaign, the researches verified that for low rock material mechanical strengths, the shear strength of discontinuities are less influencing to the global rock mass resistance. They obtained also the discontinuities parameters under the Coulomb–Navier model.

2.4.3 Physical models for geotechnical structures

Research concerning specialized physical models of geotechnical structures in rock masses (e.g. foundations, underground cavities), were available since at least second half of the 20^{th} century (Krsmanovic et al. (1965) in Brown and Trollope (1970)).

Most experience on physical models for geotechnical structures at rock masses have been developed by the Institute of Experimental Models and Structures (ISMES: *Istituto Sperimentale Modelli e Strutture*) by the hand of Professor Emanuele Fumagalli at Italy[3]. Interesting physical modeling of geotechnical structures performed by this institution were for example: the Rapel

[3] Actually the ISMES is the Institute of Experimental Geotechnical Models *Istituto Sperimentale Modelli Geotecnici* (ISMGEO).

Dam at Chile, the Itaipú Dam at the Paraná River between Brazil and Paraguay, the Agua del Toro Dam at Argentina, the Grancarevo Dam model at Yugoslavia, and the Canelles Dam at Spain.

Bakhtar (1997) reported an intersecting physical modeling campaign —of five experiments— that studied the influence of rock mass integrity surrounding underground structures (i.e. tunnels) when they submitted to a ammunition arsenal explosion. The models tried to reproduce rock mass geometrical and mechanical characteristics at a testing acceleration of 1 g, therefore a scaled model was designed (i.e. scale 1:20) where material similitude was accomplished.

Recently Zhu et al. (2011) (also see: Zhu et al., 2010) performed a two dimensional physical model to simulate the rock mass reaction against the construction of an underground electric power generator chamber system. The scale reduction was 1:150 and the global dimensions of the model (width $\times$ height $\times$ thickness) were 2.5 m $\times$ 2.0 m $\times$ 0.5 m. The intersecting parts of this model were: the implementation of the real–time measuring systems consisted on high–accuracy mini multi–point displacement measuring systems and a mini convergence measuring system consisted of an adaption of an endoscope; the creation and simulation of mini rock bolts and pre–stresses cables; and the excavation simulation. Results of the physical model were compared with those obtained by a finite difference numerical model, which were very similar.

2.4.4 Construction of Physical Models

The benefits one has in using artificial rock–like materials for physical models instead of real ones, is the possibility to: reproduce them many times; obtain a wide range of mechanical properties; and obtain specimens with different discontinuities conformations.

In the section of Specimen Preparation of the research article of Mughieda and Alzo'ubi (2004), they began with the phrase: "Many investigators concluded that, it was very difficult to have a model material that simulates rock material in their properties". And at the end, they cited at least five references. This phrase show clearly, that construct physical rock mass models were the major difficulty for the researches.

In the past, materials used for rock mass modeling were in general casting material mixtures with granular or non–granular ingredients, however non–granular materials do not show the frictional properties which are of interest for geologic materials as rock, therefore mixtures with granular materials were more often used for that purpose. Those granular materials can

be natural silica sand to artificial glass beads. Also, additives such as bentonite, limestone, litharge and barite can be used to improve cohesion or unit weight to the mixture. In casting materials, water proportions are important to define, because can define air proportions in the final cured material, and an excess of even capillary voids greatly reduces the strength of the material. Also, excessive water usually enhances viscosity and plasticity. Therefore, it is better to prepare strongly compressed materials containing little proportions of water.

Paris plaster with sand was used by Goldstein et al. (1966) and Patton (1966), and a not detailed specified plaster by Hayashi (1966). Compressed concrete was used by Ladanyi and Archambault (1970) which argued that this material has rock–like properties and could be obtained in convenient shape and reproductively uniform quality. Brown and Trollope (1970) used a some type of plaster as a substitute rock material, arguing that this material can be readily and accurately casted and machined to almost any desired shape. Later, in Brown (1970) it was specified that the plaster used in that experience was a high strength Gypsum plaster. Einstein and Hirschfield (1973) used a mixture of Gypsum plaster (Hydrocal B-11), diatomaceous earth (Celite) and water, with weight ratios of Hydrocal B-11:Water and Celite:Water of 2.22 and 0.312, respectively; as model material for their research. A light weight concrete G75 of Hebel Company (Germany) mixed with a high strength plaster (Hebör Hartformengips), sand and water in proportion 1:4:0,24 by weight was used by Reik and Zacas (1978). Yang and Huang (1995) used a mixture of plaster: sand of the I-Lan River, and water in the proportions of 1:0.25:0.92 by weight; which were cured at 25°C and at a relative humidity between 50% and 70% for maximum six days.

In Singh et al. (2002), Tiwari and Rao (2004) and Singh and Singh (2008) it is reported the use of a so called Sand-lime Brick, a manufactured material of U.P. Minerals Products Ltd. located in Meerut India, as model material for the authors' rock mass physical testing program. This material is a mixture of hydrated lime, fine sand and water in the proportion of 1:4:0,20 by weight. In Singh and Rao (2005) same material is reported as a lime silica material.

Similarly, Gaitán-Oliva (2005) used a mixture of Portland cement, fine sand and water in two proportions of 0.4:1:0.21 and 0.2:1:0.18 for the rock material representation. In the reported researches of Mughieda and Karasneh (2006) and Mughieda and Alzo'ubi (2004) a mixture of silica sand, ordinary Portland cement type 1 and water in a proportion in weight of 0.72:0.76:0.12, respectively.

Two material proportions of a mixture of cement, kaolinite and water, as possible model material for rock was used in Tien et al. (2006). The proportions of cement, kaolinite and water specified

in that research were 4:1:1,2 and 1:1:0,6. Previous experiences made by the same research group (Tien and Tsao, 2000), reported the use of two similar materials: a mixture of cement, Otawa sand and micro–silica in a ratio of 6:5:1, and a mixture of cement mixed with kaolinite in a ratio of 4:1.

For a two materials inter–layered transversely isotropic physical model, Tien and Tsao (2000) used cement, Ottawa sand, some kaolinite and microsilica. For the first material the proportions in weight they used were of 6:5:1 for cement, sand and microsilica, respectively; while for the second material the proportions in weight were of 4:1, for only cement and kaolinite. Both materials were mixed first in dry and then compacted in layers of 2 mm by adding a static load of 20 kN inside molds by adding water with spray —for each 96 g of material they added 10 g. Finally the materials were cured for three days in a chamber at 75°C and then for 28 days at a temperature of 25°C and humidity above 98%.

Also Tiwari and Rao (2007) used a mixture in weight proportions of: 22% of hydrated lime and 78% of sand —passing the 600 µm sieve– mixed with 22% of water of hardness less than 330 g m^{-3}. Prudencio and Van Sint Jan (2007) used a mixture of fine sand, common cement (i.e. Portland) and distilled water; then, they mixed in a proportion of 4:1:1.3 by weight. Vacek et al. (2008) used Araldite material to model rock–bursting phenomenon in coal.

These casting materials have their limitations, they have low resistances comparing them with hard rock materials, their resistance is curing time dependent, and the texture has trapped air in pores. Also models made with these materials behave like sedimentary rocks and can not reproduce a brittle behavior like many metamorphic and igneous rocks. The process of constructing models with casting materials need a rigorous quality control, where controlled ambient conditions should be maintained uniform during the curing of all pieces.

By using these materials, rock mass models resulted typically huge in volume and in consequence too heavy to carry on. They occupy sometimes a room for their preparation and there exist the necessity to develop and construct special machines and cells for their testing, which incremented enormously the research budget constraining their main objectives.

Other reduced models were synthetic polycarbonate materials, many of them patented materials with particular trademarks. These materials were used specially in solid mechanics in order to model fracture propagation phenomena. For example Sinha and Singh (2000) used Poly–Methyl Methacrylate (PMMA) material in order to simulate the rock material of discontinuous

models with, where discontinuities had infilled clay material. A PMMA is high resistant (reporting UCS on the order of 120 MPa), homogeneous, and porous–less; which permits the modeling of hard rock materials.

Also, Fleury (2001) used Epoxi resin with a proper lining to model rock material in their research of the stress distributions around discontinuity planes trough the photo–elasticity method.

The advantage of these polycarbonate materials is that they emit acoustic emissions during crack propagation permitting events monitoring, as is now performed in brittle rock material tests (e.g. Chang and Lee, 2004; Eberhardt et al., 1999; Cai et al., 2007).

In regards to the discontinuities construction in rock mass physical models, it was observed that putting the discontinuities inside the material was another difficult phase during the rock mass model construction; and it was found only two possible methods:

- inserting a medium (e.g. steel, cardboard sheets) between the two opposing surfaces that provided a lower friction angle in relation to the friction angle of the rock material (the solid phase of the model); and
- assembling individual small blocks in a specific shape to form a large mass containing total–persistent or non–persistent discontinuities.

For example, Bortolucci (1993), Mughieda and Karasneh (2006), Gaitán-Oliva (2005), and Prudencio and Van Sint Jan (2007) adopted to use the first method; while Brown and Trollope (1970), Ladanyi and Archambault (1970), and Reik and Zacas (1978) adopted to use the second method.

The second method has the shortcoming to prevail the existence of imperfect matching and closure of rock material blocks. These blocks also experiences rotation and non–uniformity; all creating un–desired and un–determined load concentrations of stresses in rock material. The first method avoids many of the above mentioned problems, but it is still restricted to few discontinuities, and it increases in difficulty when more than two discontinuity sets are wanted to consider in the physical model.

Some investigations reported —exhaustively in single articles— the procedures to create artificially rock–like materials for physical modeling. Tien and Tsao (2000) described the procedure for the preparation of transversely–isotropic inter–layered rock–like materials.

2.4.5 The Need for Other Materials and Techniques

As pointed out above, most of physical model material used in the past consisted in casting materials. This selection has its limitations: they have low mechanical resistance when comparing them with hard rock materials (i.e. from 20 MPa to 50 MPa of uniaxial compressive strength); strength is dependent on the curing time which introduces to the material variability; and strength is dependent on the resulting texture which is variable because has uncontrolled air trapped in the material pores.

Also, models made with these materials tend to behave in an transverse isotropy manner, like sedimentary rocks, because of the preparation process; and cannot reproduce a brittle behavior like many metamorphic and igneous massifs present in the nature. The process of constructing physical models with these methods needs a rigorous quality control, where controlled environmental conditions should be kept uniform during the curing of all pieces, in order to have homogeneity. This takes us to the question of: how reproducible can these kind of model materials be?

By using these materials, rock mass models resulted typically huge in volume and in consequence too heavy to carry on (i.e. volumes of $3.37\times10^{-3}\,\mathrm{m}^3$ to $0.47\,\mathrm{m}^3$, that weight from 8.2 kg to 1 150 kg). Sometimes, they occupied a room for their preparation, another room for curing and a considerable volume of waste after testing.

Also special machines, cells or frames for the specimens testing had to built and developed, which enormously increase the research budget, constraining their main objectives. For example: the cell of the physical models of Reik and Zacas (1978) was bell–shaped with a diameter of 1.6 m and ≈ 3.2 m of height, the hydraulic compressor needed to maintain a chamber pressure of 2.2 MPa, the axial load jack of 5 000 kN, internal flat jacks for lateral stresses with a capacity of 12 kN, among other giant accessories as the internal four–walled steel reaction frame; or the biaxial frame of at least $0.2\,\mathrm{m}^2$ and 300 kN of capacity of the physical model test campaign of Rao and Tiwari (2008) which should be mounted to a frame of 5 MN of capacity; or the Prudencio-Salcedo (2009) biaxial frame of $1.3\,\mathrm{m}^2$ in order to support more than 50 kN in each direction.

In addition, the time of curing of these models can vary from weeks to months, which requires controlled temperature and humidity rooms; these also translated into special logistic needs which at large are costly. For example, Tiwari and Rao (2007) cured their specimens in casts

under an axial pressure of 40 MPa for four hours at 180°C in an autoclave and then at room environment for three weeks; and Teja (2008) keep their specimens for 15 days inside desiccators containing sulphuric acid in order to maintain a relative humidity in the range of 40%–60%.

When using the second method of constructing the discontinuities as described in the preceding section —that method that requires to insert a medium in the mold— it was observed variations in the resulted discontinuity thickness with the time the medium is retired from the mold. For example, Prudencio and Van Sint Jan (2007) obtained discontinuities thickness of less than 0.1 mm when they removed the steel sheets after two hours of curing, and discontinuities thickness of more than 0.1 mm when they removed after 24 hours of curing; even though they used the same steel sheets —of 0.1 mm thickness— as separation material for creating the discontinuities.

In recent physical models, interesting materials were added to resines instead of plasters. For example, Zhu et al. (2011) used a mixture of Rosin (grade 1) —a resin obtained from conifers— and alcohol, with added powders of iron, barite and quartz. Here, the alcohol was used only for mixing the material, because it evaporates and leaves the Rosin be the binder.

Also, other model materials were used specially in solid mechanics to model fracture propagation phenomena. These were synthetic polycarbonate materials; many of them patented materials with particular trademarks, which allowed reducing the size of the models. For example, Sinha and Singh (2000) used PMMA material in order to simulate the rock material of discontinuity models with infilled clay material. Fleury (2001) used Epoxi resin with a photo–elastic lining to model rock material in their research of the stress distributions around discontinuity planes.

Also, there were reported new materials that can be used for rock material physical modeling called IBSCM and NIOS (refer Zhu et al., 2011, for example).

These kind of homogeneous and transparent materials have high resistance (e.g. an uniaxial compressive strength on the order of hundreds of mega pascals), is porous–less, generates acoustic emissions and have brittle behavior; which permits the modeling of hard rock materials by permitting the identification of crack propagation thresholds, useful to limit the stress field in the sample.

2.5 Final Comments

In this literature review one could observe that analytical methods of mechanical strength are useful for some rock masses present in nature, (i.e. those with ubiquitous discontinuities); and for a limited stress state paths (i.e. triaxial monotonic). But, in the case one can use those analytical models, it was observed that these models are robust and reliable, therefore they are mostly used to validate numerical or physical models.

But, in order to deal with a broader types of rock masses, one should look for numerical methods. Among those numerical methods used to analyze stress–strain behavior of rock masses one can consider the rock mass as a continuum or as a blocky rock mass, which requires to consider numerical continuous or discrete models, respectively. If continuum numerical models are selected, one can opt to use empirical rock mass models; and if discrete models are selected, one should have to implement for their special case: a software, which can consume some financial and time efforts. Independently one decide to use any numerical method, it should be necessary —or recommendable— to test physical models for parameters definition and/or for results validation of them.

After being awarded of the importance of physical models, in the last section of this literature review it was told all the research outcomes users had with the physical model researches since their beginning. It can be expressed that with physical models research, just all the empiric models for rock masses has been proposed, and many rock material, discontinuities and rock masses process were understood.

Therefore, in order to go forward in the rock mass mechanical behavior understanding, it is necessary to look for a consistent and robust Rock Mass Physical Modeling Approach. Is that the reason, that the present research made emphasis in developing such physical model approach, which by the moment is only qualitative.

In the following chapters, one will read: a methodology to create physical models with the OBCG–SSLE technique; the materials involved in this type of models and its characterization; the methodology used in this research to built a special case of rock masses and its validation with an analytical model; and the results and findings this research had.

Chapter 3

Creation of the Physical Models

In this chapter it is presented the basis of this thesis proposed technique (referred here as the OBCG–SSLE technique) for the creation of rock mass physical model samples, which is a combination of the use of the Sub–Surface LASER Engraving (SSLE) technique in Optical Borosilicate Crown Glass (OBCG).

3.1 The SSLE Technique

The sub–surface LASER engraving (SSLE) technique is that methodology process of engraving an image below the surface of a solid transparent material by pulsed Light Amplification by Stimulated Emission of Radiation (LASER). The transparent material is usually a high quality laserable glass (e.g. Crystal BK7 grade A) that provides optical clarity in order to minimize distortion of the LASER beam during the engraving process. This idea was presented by Russian inventors as early as 1970 (Agadshanow et al., s.d.; refer Lenk and Witke, 1998). The commercial application of these results began in the late 1990s, and since then SSLE has become more cost effective and machines became more available around the world (e.g. Russia, China, USA, England, Germany, Mexico, Brazil).

Also, different patents were applied for this technique but for different materials (e.g. Goldfarb, 1996; Menard, 1978). It can be said that SSLE is part of the LASER Beam Machining (LBM) technology.

The SSLE technique, as it is nowadays known, is an application turned in favor of an unwanted phenomenon called LASER Induced Damage. The study of this last phenomenon was motivated by the development of LASER systems with short and ultra–short pulse capabilities at high pulse energies (e.g. Stuart et al. (1996), Du et al. (1994)). Researchers working with LASER in optical materials had the problem of damaging the optical material with high energy LASER beams. At that time, the research was focused in avoiding this LASER induced damage. In the process of years, it was obtained a list of material compositions that provided good transparency with minimal head absorption and LASER damage (Doty, 2000), and another list of materials that did not. Then, engineers began to study the manner to control the LASER and the manner to place the beam inside those materials that presented damage by the LASER beam, a so called etching process.

To etch, is the process of having a LASER pump beam (e.g. with an intensity around 400 GW cm^{-2} pulsed at 2.5 Hz) penetrating a crystal to create tiny cracks (points or dots), one by one, inside the glass. This is carried out by focusing a LASER light onto the target point with a single but a properly–special convex lens (e.g. F–Theta Lens) within the transparent material for a split second (e.g. nano seconds [ns] to fempto seconds [fs]) which creates a damage point (i.e. a tiny spot within the crystal) which changes visibly. The lens changes the focal length which enables in–progress intensity changes. The time needed to complete this step varies depending on the LASER engraving machine velocity. The small damage shape obtained by the etching process has been named a notch.

One material that responds well to the etching process is the Optical Borosilicate Crown Glass (OBCG). An experimental investigation on the induced damage into this material by accumulative pulses generated by a Neodymium–doped Yttrium Aluminium Garnet LASER (Nd:YAG) was reported in Navarrete et al. (2003), for example.

The resulting images upon this technique appear to be suspended within the crystal. The 3D composition is obtained point by point in the crystal by programming relative motion between the LASER beam and the target, a process that is nowadays controlled by computer software.

Usually two kinds of software for engraving is needed: the point–cloud converting software and the etching control software (also known as engraving control software). The first software, the Point–Cloud Converting Software, transforms the 3D model image information (e.g. a layered sequence of 2D images of PNG format) or 3D vector file format (e.g. VRML, X3D) to the special image file format which consists on abundant small points, named point–cloud format. The second software, the Engraving Control Software, is used for controlling the synchronizing

output of the LASER beam with the variable lens focus, and the movement in space of the x, y and z axes of the target object. Figure 3.1 shows a subsurface engraving machine scheme and the etching process.

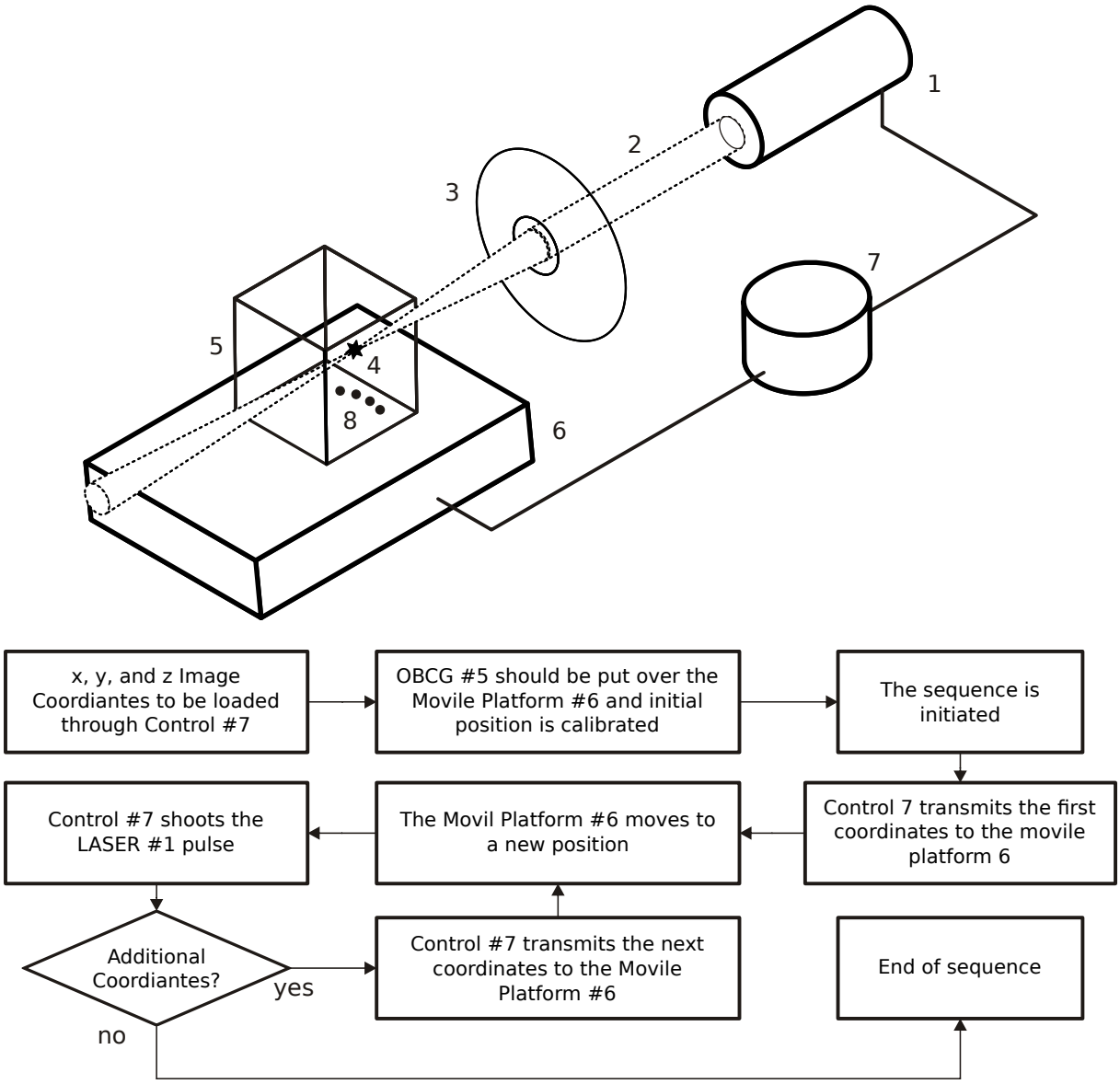

FIGURE 3.1: Scheme of a subsurface laser engraving machine and the etching process (US Patent# 5575936 Goldfarb, 1996); *1* short pulse laser, *2* beam, *3* focusing lens, *4* focused point, *5* OBCG, *6* mobile platform, *7* controlling system, *8* notches.

In the etching process, high–energy LASER beams, known as coherent light, are used to produce a phenomenon known as Multi–Photon Absorption within optically perfect crystal. The LASER beam creates an electric field greater than 10^6 V cm^{-1}. When it is focused within the

interior of the subject crystal, the energy creates unattached electrons also known as free electrons. These free electrons, accelerated by the electric field created by the LASER beam cause the high energy electrons to collide with atoms and ions in the focus area. This is possible because glass, as other materials, exhibit strong absorptions in the infrared, and LASER photons are absorbed rapidly. As the process continues, it causes a chain reaction and produces about one million trillion free electrons per cubic centimeter in about one trillionth of a second, resulting in excitation of vibrational modes in the material. Therefore, the LASER produces a tiny micro–crack, because the thermal expansion exceeds the bonding forces of the crystal. Because the LASER generates power densities of 10 billion watts per square centimeter, the surface of the crystal is not damaged due to the highly transparent nature of optically perfect crystal. In resume, phenomena as plasma formation and subsequent micro cracking occur during the etching process.

In engineering terms, in order to etch a material, the LASER beam should be operated at the single–pulse damage energy threshold of it. The single–pulse damage energy threshold is considered nowadays a material property for this purpose. Most transparent materials can be etched with this technique, such as: crystal, glass or acrylic glass as Polymethyl Methacrylate Plastic (PMMA), among others. But for best and economical solution in arts, the OBCG crystal is recommended.

Points generated by the LASER are relatively small, usually 0.1 mm and slightly egg shaped. For the artistic use, the engraved points are spaced typically no closer than 1.5 times their size across the tree orthogonal x, y and z planes. This is due largely by the fact that the entire lasered image is held together by the internal stress of the glass itself, where tighter spacing increases the probability of creating a fissure between points, resulting in damaging the crystal and/or the desired 3D image.

3.2 Machines for the SSLE technique

The machines used to perform the SSLE technique can be divided into two categories, accordingly with the difference of the LASER medium, those with:

- diode pump LASER (i.e. those that uses red or green LASER light); and
- Xe–lamp Yag–rod LASER.

Table 3.1 shows two commercial LASER engraving machines. The quality of the output from a machine depends on at least three factors: point size, point density, and point layering. Other issues that maybe of concern include total burn time, the number of cubes which can be burnt simultaneously, and cost.

TABLE 3.1: Example of Commercial LASER Engraving Machines.

Specification	TJDP–522A*	TJYAG–505B*
LASER Medium and Head	1 Diode Pump	3 Xe–lamp YAG Rod
Engraving Range in mm	$290 \times 190 \times 80$	$280 \times 280 \times 90$
Engraving Speed in dots s^{-1}	2 000	200
Cooling System Type	Air	Water
Overall Dimensions in mm	$850 \times 730 \times 650$	$850 \times 730 \times 1\,348$
Weight in kg	140	270

*Manufactured by Tianjun China.

The main criteria to be aware of, are: LASER speed (the time it takes to burn a cube); LASER diameter (this affects the size of the notch and how close they can be together, and therefore a small diameter gives more detailed images); and the size and number of crystal samples the equipment can continuously burn.

Typically a machine with a red LASER burns with a slightly larger point size, and consequently point density comes down leaving a sparser and slightly fuzzy image. Machines with green LASER can burn smaller point sizes than those with red LASER, allowing higher point density within the cube and giving the impression of a more focused image. Within this machines, it is also possible to layer point clouds which add an extra depth to the 3D image and enhancing the presence of the final output.

The SSLE machines require expensive cooling attachments, and the maintenance and calibration must be frequently and at high costs, for proper use. The primary component being to replace after some limited hours of use is the LASER diodes, which can easily cost one third of the machine cost itself.

3.3 LASER for the SSLE technique

A LASER is an electromagnetic wave in the visible or not range of human eye. LASER can be of the following possible characteristics:

- monochromatic LASER, which consists of one single wavelength or a very narrow spectral range that gives an extremely pure light;
- multiple wavelength LASER;
- directional LASER, where the beam is well collimated and travels over long distances with very little spread;
- coherent LASER, because all the individual waves of light moves precisely together through time and space (i.e. they are in phase).

To be used in SSLE technique, LASER must have sufficient power, so this reduces to a select solid crystalline state LASERs, as for example the Ruby Cr:Al2O3 (Chromium doped Aluminum Oxide), CO_2, Nd:YAG (Neodymium doped Yttrium Aluminum Garnet [$Y_3Al_5O_{12}$]), Nd:YVO4 (Neodymium–doped Yttrium Ortho Vanadate) or Nd:Glass (Amorphous Glass) LASER. Among these LASERs, ruby–LASER is no longer used because of its low efficiency, and Nd:glass LASER have low thermal conductivity which limits pulse repetition.

Any LASER, may be electronically or optically pumped. In a LASER pumped optically, one or more flashlamps are used (e.g. Xenon Flashlamp [Xe–lamp]). Whereas, in a LASER pumped electronically (i.e. diode pumped), the excitation is done by one or more infra–red LASER diodes. Operations of these two types, permit to produce up to several hundred watts in continuous mode, and even more higher powers in the pulsed mode (i.e. short and ultra–short pulsed modes). In the pulsed mode, the basic energy of the LASER is increased through the Q–switching technique; sometimes known as giant pulse formation. For the SSLE technique, the short pulsed mode is generally used.

A short pulse LASER, as the name specifies, emits its power in short intervals, around 50 kHz, of peaks power values spaced by other longer intervals of base power values. A typical diagram of the power variation through the time of this type of LASER, named the pulse shape, is shown in Figure 3.2.

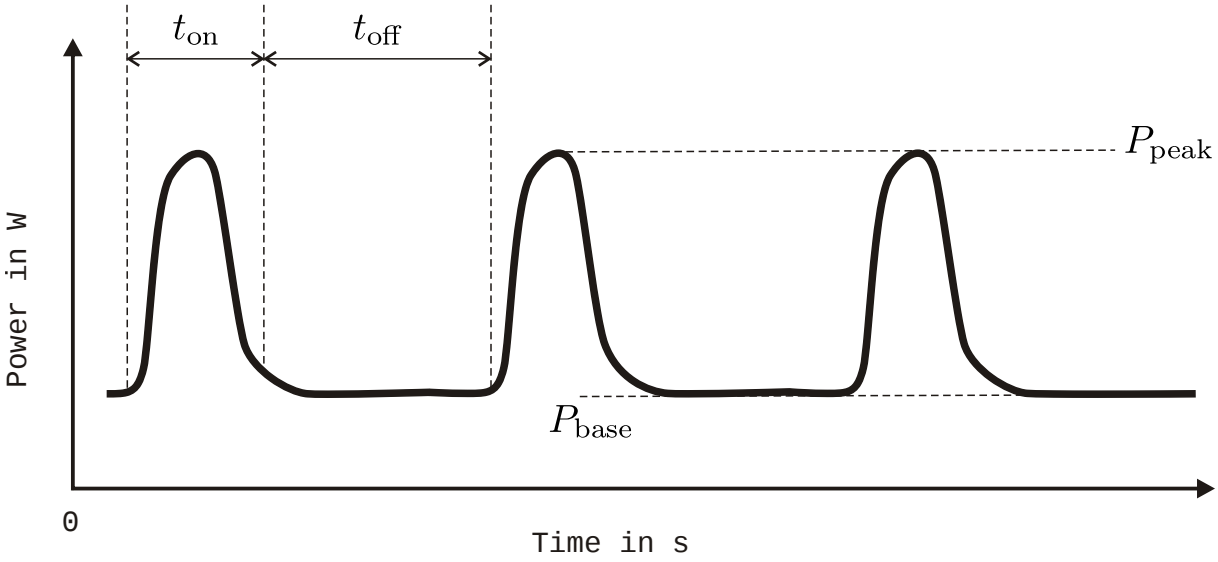

FIGURE 3.2: LASER pulse shape.

From this pulse shape, it is possible to recognize the LASER peak and base–power values, P_{peak} and P_{base} respectively, and the peak and base time intervals (i.e. t_{on} and t_{off}, respectively). Peak and base frequencies are the inverse value of peak and base time intervals. Then, frequency of the pulse LASER (f_{pulse}) is obtained by the inverse of the sum of peak and base frequencies, as follows:

$$f_{pulse} = \frac{1}{t_{on} + t_{off}} \tag{3.1}$$

Duty is obtained according to the following equation:

$$D_{pulse} = \frac{t_{on}}{t_{on} + t_{off}} \tag{3.2}$$

From this value, the average power (P_{avg}) is calculated by multiplying duty times the peak power. Peak energy is obtained by multiplying peak power with pulse width:

$$W_{peak} = \frac{P_{peak}}{f_{pulse}} \tag{3.3}$$

The pulse–shape graph is used to differentiate different LASER pulses, therefore it is used to specify them. Apart of the mentioned pulse–shape graph, it is necessary to specify the following

four main parameters:

- wave length (λ_{LASER});
- minimum pulse length ($\tau_{\min,LASER}$);
- maximum pulse energy ($E_{\max,LASER}$); and
- maximum repetition rate ($F_{\max,LASER}$).

Table 3.2 shows some LASER properties used for the SSLE technique. Other LASER parameter for the SSLE technique is the photon energy (eV) which is related to the measure of the amount of photons that a LASER radiates.

Between all these LASER types, the most common used in SSLE technique is the solid state Nd:YAG LASER with a wave length of 1.06 µm. In the following paragraphs this LASER will be described in order to have some idea about its functionality.

The basic structure of the Solid State LASER (SSL) has not changed in any fundamental way since its invention in 1960 of last century (Figure 3.3). It has three principal parts:

- the energy source (usually referred to as the pump source);
- the gain medium, or LASER medium;
- two or more mirrors that form the optical resonator.

The pump source is the part that provides energy to the LASER system, and may be a high energy light which optically pumps a gain–lasing medium with significant energy to match one or more of the absorption lines of the gain medium. Then, the gain medium is excited by the pump source to produce the population inversion, and it is in the gain medium that spontaneous and stimulated emission of photons takes place, leading to the phenomenon of optical gain or amplification, after photons are reflected by the mirrors located in the optical cavity.

More than one pump sources may be used. The type of pump source used principally depends on the gain medium, and this also determines how the energy is transmitted to the medium. Pump source as also gain medium are located inside the pump chamber (Figure 3.3), which is cooled better by water.

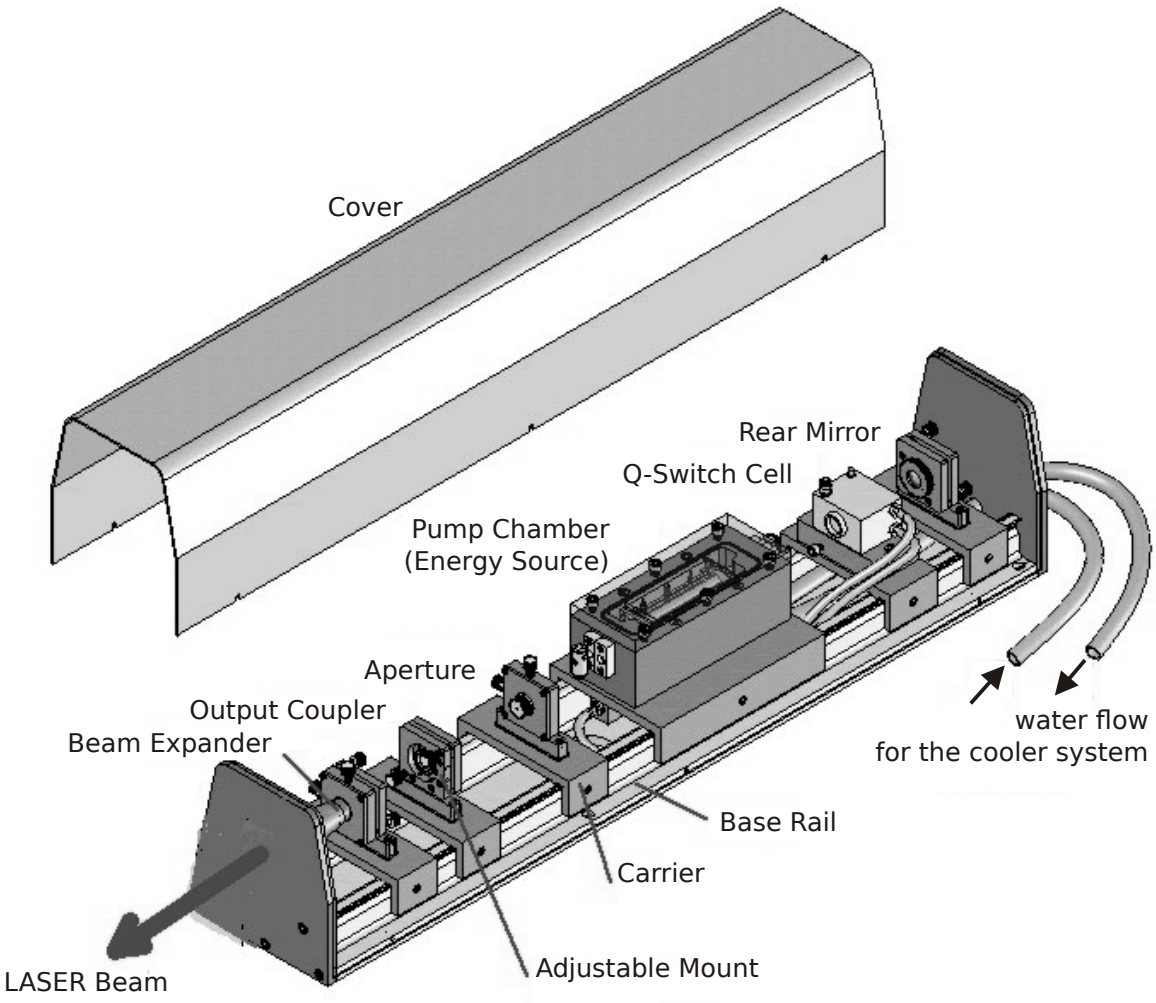

FIGURE 3.3: Main parts of a Nd:YAG LASER (adapted form: Sintec Optronics).

TABLE 3.2: Properties of some LASER used for the SSLE and Material Cutting Techniques.

LASER Type*	λ_{LASER} in nm	$\tau_{\min,LASER}$ in ns	$E_{\max,LASER}$ in J	$F_{\max,LASER}$ in kHz	Reference
s Nd:YVO4	1 064 to 532	6	2.2×10^{-3}	30	Mauersberger et al. (2008)
Nd:YAG	1 060	12	30×10^{-3}	0.012	Gorshkov et al. (2003)
Nd:YAG	532	20	150×10^{-3}	0.01	Navarrete et al. (2003)
u MXR	1 030	0.25	8×10^{-6}	25 000	Mauersberger et al. (2008)
Ti:Sapphire	800	0.04	—	10 to 250	Hnatovsky et al. (2006)

*If s or u precedes the LASER name, correspond to a Short Pulse LASER or a Ultra Short Pulse LASER, respectively.

In the so described system, the optical pump source may be a Krypton–Flashlamp or Xenon–Flashlamp, and the gain/lasing medium can be a cylindrical transparent rod doped with a small amount of impurity as the Nd:YAG crystal. For this particular gain medium, also diode LASER may be used as pump source. The gain medium is the major determining factor of the wavelength of operation, and other properties of the LASER.

Finally, the optical cavity —also called optical resonator— has an important role in the solid state LASER class. In its simplest form, it is composed by two parallel mirrors placed in front each other around the gain medium. These mirrors has the function to provide feedback of the light gained in the rod. In the majority of solid state YAG LASER systems, gold plated elliptical and close–coupled pump cavities are the preferred reflector used. Most optical pump cavities are typically produced from metals such as aluminum, stainless steel, and bronze; which after their construction–machining, the reflective surfaces are mechanically polished to mirror finish; and depending on the base metal used, a combination of under–plating is applied prior to the final gold plating process. LASER rail is provided for each optical cavity. There exist hundred of patented cavities for LASER.

The mirrors have optical coatings which determine their reflective properties. Typically, one of them is high reflective and the other is partially reflective. The latter is called the output coupler, because it allows some of the light to leave the cavity to produce the so wanted LASER output beam. Through this partial reflector mirror, the LASER travels out of the system.

The above description refers to a continuous wave LASER. In order to have a pulse LASER, a Q–switch device should be used. The Q–switch device has the objective to compress and boost the energy in the output pulse with some loss in total energy or average power at the fundamental wavelength. Q–switches heated when LASER is running, thus they are cooled with circulating air at least, and better with circulating water or other fluid.

The properly selection —of the cavity components and the driving pump source— can make all the difference in terms of output pulse energy, beam quality, and stability.

3.4 Application of OBCG–SSLE to Rock Mass Modeling

Apparently there is no precedent study in where the SSLE technique has been used in OBCG in order to create discontinuities network patters and to be used for rock mass modeling.

But, the use of the SSLE technique on rock material physical modeling has been initiated with those investigations that wanted to understand at which stress level a crack initiates to propagate, and how it propagates in a brittle material. At the beginning, researches used also plaster material in order to create their models (e.g. see Bobet and Einstein, 1998), but this technique limited them to use two dimensional cracks at two dimensional stress states. Therefore, in order to see and measure a three dimensional oriented crack under a three dimensional stress state, they appeal to use a transparent material, as PMMA.

Initially the crack were machined into blocks of PMMA. I order to have the crack at the center of the specimen, this should be cut in two equal parts, then machined in each part, and finally glued to form again the complete specimen. For example with this method, Adams and Sines (1978) introduced in PMMA a penny–shaped flaw dipping 45° inside a prismatic specimens of size 25.4 mm $\times$ 50.8 mm $\times$ 82.6 mm. Then, after using that method as standard for more than twenty years, Germanovich et al. (1994) proposed to use SSLE technique on PMMA, instead of using the old method of machining.

Since this proposal, the SSLE technique was used for the study of single penny–shaped, spherical, ellipsoidal and any shape of cracks —as also multiple cracks— under the fracture mechanics approach (e.g. Germanovich and Dyskin, 2000).

In the following two sections, it will proposed the principle and the design–process methodology for the use of the SLLE technique within OBCG, in order to introduce any discontinuity network inside that transparent material, and to create rock mass physical models.

3.4.1 Principle

The principle of the application of the OBCG–SSLE technique to rock mass modeling is to use OBCG as a representative intact rock material and to introduce inside it:

- arranged clouds of close spaced notches forming —finite or infinite planes, grouped or not, ordered or randomly ordered– with constant band with, to be representative of weakness planes inside rock material (i.e. discontinuities, discontinuities sets or a discontinuity network);
- arranged clouds of far spaced notches, to be representative of rock material mineral defects (i.e. a rock material weaker than OBCG).

Because the SSLE technique allows etching at any point inside the OBCG body, one can create any discontinuity shape, discontinuity set or discontinuity network inside it (e.g. a circular discontinuity with a determined attitude or a complete artificial 3D fracture network of varied discontinuities shapes).

3.4.2 The Design Process

In order to establish a design process, it is necessary to define constants and variables, which will be known here as etching quantities. During these quantities definition, relations (i.e. equations) among them will be established. These will be explained in the following sub–sections.

3.4.2.1 Etching Constants

In this research, the following etching constants are proposed:

- notch separation $a_{\mathrm{d}} = 200\mu\mathrm{m}$, to produce notch–coupling for the discontinuities band–width;
- minimum notch separation, to avoid notch–coupling but to produce mechanical alteration in the modeled rock material, $a_{\mathrm{mMin}} = 600\mu\mathrm{m}$.

The last constant was obtained by multiplying a_{d} by 3, because stress zone perturbation of a cavity is negligible from 2.5 or 3 times the cavity diameter, if notch volume is considered as a perfect spherical cavity.

3.4.2.2 Independent Etching Variables

The following two independent etching variables are defined, which are ratios of the number of notches per volume at rock material and at discontinuities, respectively:

- rock material notch resolution (R_{m3});
- discontinuity notch resolution (R_{d3}).

These two variables are closely related with the previous defined notch separations; but for practical purposes, these two resolutions were used here respectively as: the number of notches at rock material and at discontinuities within a solid gross volume.

Rock material and discontinuity resolutions can also be named model variables, because they may govern the mechanical behavior of the volume that is representing the rock material and the volume that is representing the discontinuities; and specially because they are closely related with the dimensional parameters of the model.

These variables represent three dimensional resolutions, i.e. the number of notches present in a cubic unit volume given in [L^{-3}] (e.g. four notches per cubic millimeter). If a regular rectangular array of notches is chosen, a one dimensional notch resolution (R_1) may be proposed as alternative, and the three dimensional notch resolution may be inferred by the following equation:

$$R_3 = R_1^3 \tag{3.4}$$

For rock material modeling, it is recommended that the one dimensional resolution be at least six per distance unit, because studies in rock material shown that in order to have an homogeneous material, one should have a minimal dimension of samples at least six times the maximum mineral size or ten times the mineral mean size.

For discontinuities, the three dimensional resolution is better to represent by a product of the roughness waviness one dimensional resolution in the amplitude direction (R_{d1}) and the corresponding discontinuity areal resolution (R_{d2}):

$$R_{d3} = R_{d1} R_{d2} \tag{3.5}$$

In order to influence the discontinuity feature of a rock mass, for this model technique, it was decided that the minimum scaled discontinuity thickness ($w_{d\,min}$) should be at least six times the roughness waviness amplitude. Thus, the one dimensional resolution of discontinuity is related to the number of notches in the direction of waviness amplitude that will represent surface roughness (n_{d1}), and R_{d1}:

$$w_{d\,min} = \frac{6 n_{d1}}{R_{d1}} \tag{3.6}$$

Here, it is recommended that n_{d1} be at least equal to 2, to minimally represent a discontinuity roughness.

3.4.2.3 Relations Between Mechanical Properties and Model Variables

In order to assess the dimensional constants in any physical mechanical model, it is necessary to know the mechanical properties of the material to be used in the model.

For example, the simplest deformational constitutive model for rock material is elastic isotropic, with its two parameters: the Young Modulus E_{i}, and the Poisson ratio ν_{i}. Also, the simplest deformational constitutive model for a discontinuity is represented by two parameters: the normal to the discontinuity stiffness k_{n}, and the shear stiffness k_{s}.

For the first two parameters, relations with R_{m} have to be obtained, whereas for the second case, only k_{n} should be related with R_{d}.

It is possible do not necessary relate the shear stiffness k_{s} with R_{d}, because the shear displacement of any discontinuity represented by an arrangement of continuous close notches in OBCG could be mainly a thermodynamic process, which is immersed in the physical response of the model when submitted to stresses. This situation was not physically verified, but could be assumed as true for this model technique if a constant discontinuity geometry and size is maintained, because the shear process including the micromechanical notch propagation will develop in the same way in OBCG.

Uniaxial compressive loading tests in samples —notched at a determined rock material resolution without any discontinuity— can be the simplest procedure to relate E_{i} and ν_{i} with R_{m}. And direct shear tests for a constant discontinuity geometry and size, can be used to relate k_{n} with R_{m}. Because this was not possible to verify in this research, it is very possible that some limitations can exist with this model technique within the deformational response of the physical specimens. Therefore, by the moment, this model technique should be applied only to simulate the influence of discontinuities to the ultimate mechanical strength, without dealing of its deformation processes and how and when the discontinuities initiates to propagate through the rock mass.

Also, it is uncertain how much a notch propagates at a determined stress (i.e. at the so called crack initiation stress threshold), this because the crack propagation modes of the notches in the material that represents rock material may be totally different from the crack propagation modes of the material that represent discontinuities.

3.4.2.4 Dependent Etching Variable

The dependent etching variable is almost the rock mass resolution (R_{rm3}) which is dependent with the all above mentioned variables and constants, because is related with the ratio of the minor sample dimension to some rock material and/or discontinuity features in the rock mass (i.e. features like the maximum block formed among total persistent discontinuities and/or the discontinuity shape, thickness and extension), and therefore related with the Rock Mass Discontinuity Network (RMDN).

For example, for the particular case of total–persistent, three–orthonormal and equal–constant spaced discontinuity sets, R_{rm3} may be inferred as it was done with rock material resolutions (i.e. Eq. 3.4), where the one dimensional rock mass resolution (R_{rm1}) is derived from the following equation:

$$R_{\mathrm{rm1}} = \frac{n_{\mathrm{b}}\, R_{\mathrm{m1}}\, s_{\mathrm{d}model} + (n_{\mathrm{d1}} - 1)\, R_{\mathrm{d1}}\, w_{\mathrm{d}model}}{n_{\mathrm{b}}\, s_{\mathrm{d}model} + (n_{\mathrm{d1}} - 1)\, w_{\mathrm{d}model}} \tag{3.7}$$

where $w_{\mathrm{d}model}$ is the scaled discontinuity thickness, $s_{\mathrm{d}model}$ is the scaled discontinuity spacing and n_{b} is the number of cubic size blocks present in the minor dimension of the volume that represent the rock mass.

In order to have a representative number of blocks in rock mass, it may be recommended to assign a value of at least six to the variable n_{b}.

3.4.2.5 Final Sample Size and Shape

To assess the final sample size, it is necessary first know the minor sample size (b) and the shape of it. This b is dependent on R_{rm3} and on the minimum minor size (b_{min}).

For the special case of rock masses with equal–constant, equal–spaced and orthonormal discontinuity sets; the minimum minor size of the sample is assessed with the following equation:

$$b_{\mathrm{min}} = n_{\mathrm{b}}\, s_{\mathrm{d}} + (n_{\mathrm{d1}} - 1)\, w_{\mathrm{d}} \tag{3.8}$$

By choosing the minor sample size ($b \geq b_{\mathrm{min}}$), it is possible to infer the other dimensions of the sample, by previously choosing the wanted sample shape.

The sample shape might be, most of the times, dependent on the shape of the real case that is analyzed, and secondary depends on the type of stresses the sample will be loaded with (i.e. the loading machine have in hand to perform the physical tests). In standard rock mechanics tests (i.e. uniaxial and triaxial axis–symmetric compression test), straight cylindrical samples shapes with a diameter to height ratio greater than 2.3 are of common use. But some tests of this kind were also performed in prismatic sample shapes, rather than in cylindrical ones. In contrast, for polyaxial rock mechanics tests (i.e. true triaxial tests), cubical sample shapes are commonly used.

3.4.2.6 Rock Mass Discontinuity Network

By knowing the size and shape of the sample, it is time to generate the Rock Mass Discontinuity Network (RMDN) that will form the final rock mass physical model. Previously, all the knowledge about the RMDN was used indirectly to determine the dependent etching variables, now this is necessary to generate each of the discontinuities present inside the model.

This RMDN finally can be ultimately represented by a group of discontinuities oriented in space. A discontinuity is completely defined by its gravity center coordinates, plane attitude, shape, size, thickness, and surface roughness; which in conjunction will define a solid discontinuity.

After the RMDN is represented by a group of discontinuities, one needs to transform them into equivalent cloud points, which are the same discontinuities but represented by points separated at a certain distance according to a specific arrangement accomplishing the previously defined resolutions.

3.4.2.7 Cloud Points Data Set

From the equivalent cloud points of discontinuities and with the material cloud points (this also accomplishing the rock material resolution previously defined), the final cloud point data set is obtained, which is the x, y, z coordinated information of each point in where the LASER beam should be focused, in order to create one notch by time inside the OBCG sample.

Generally, the cloud points data set is presented in a text file (e.g. an ASCII file), where the number of rows is the number of notches the complete model will have, and in each row, three

columns of numbers are separated by tabular space or a determined number of spaces. The first, second and the third columns correspond respectively to the x, y, z coordinates.

In order to model a rock mass with one up to *n* total–persistent discontinuity sets, a MATLAB® program was developed for this research (i.e. the `createmodel01` function), in order to generate this cloud point file which can be used for the etching process (see the complementary electronic material of this research).

The program delays from several seconds to some minutes in order to generate the cloud point file, depending on the complexity of the RMDN, and it is also limited by the memory of the computer hardware when using a 32–bits architecture. If a 64–bits architecture computer hardware is used, no limitations exist. According to the calculations performed for this research, the average calculation process velocity was estimated to be around 0.60×10^{-3} notch s^{-1} using a dual core 2.71 GHz processor and 3.25 Mbytes of RAM memory at a 32 bits with an Linux based Operating System (i.e. Debian 4.4.5-8).

3.5 Final Comments

In this chapter it was explained the SSLE technique with sufficient detail to be understood for engineers. Some machines for SSLE technique were described, and the operation of the pulse–shot LASER was explained, which are the most common LASER used for this technique.

Then, a complete explanation of the design process used within this technique for rock mass modeling was proposed, with the added contribution of a software to deal with this.

During the design proposal formulation (Section 3.4.2), it was observed that the largest drawback of this technique to be used for rock mass models, is the unverified assumption that the shear displacement of any discontinuity represented by an arrangement of continuous close notches in OBCG is mainly a thermodynamic process. Because, this situation was not physically verified and no clues were obtained in this research to do so, this technique is not by the moment useful for deformational estimations, and only can give a non–dimensional idea of rock mass failure behavior.

Also, it is believed that a lower limit and an upper limit for model variables in OBCG may exist in order to attain reasonable results (Section 3.4.2.4). This also, should be a topic to be solved in future research.

But, among these drawbacks for this technique, this research will prove the good performance of this model approach to rock mass ultimate strength modeling, as will be shown in the following chapters of this document.

The resulting physical specimens are preferred to model discontinuous rock masses with brittle rock material and rigid discontinuities, because of the mechanical behavior similitude of OBCG with brittle rock materials and the negligible deformability normal to each discontinuity. If a ductile rock material is to be modeled, probably exposing the sample to high temperatures during testing can provide that desired behavior.

With the sampling constructing technique here proposed, the scientific community may have the basis for a new kind of physical modeling material. It allows to have small specimens capable to be tested in standard rock material equipments, avoiding additional investment in creating sophisticated and big equipments. Also, this material does not require some many days and room spaces for curing, can permit any wanted arrangement of discontinuities network, allows other techniques of measuring during tests by using strain gauges, acoustic emission sensors, bender elements, or special measuring methods as electronic speckle pattern interferometry and three dimensional photo–elasticity, and the use of other commercial transducers (e.g. force cells, displacement transducers).

Chapter 4

Materials Characterization

Practically any transparent material (e.g. transparent inorganic or organic materials) is potential to be etched with the SSLE technique as described in the previous chapter. But most common used materials for this purpose are glasses, specially because their LASER Damage Thresholds (LDT) are high.

Organic materials as for example PMMA can also be engraved, but particular experience reported that this material changes in color during this process (Yeeya Art Work Corp., 2009). Even though, this material was extensive used by the research group of Professor Dyskin and co–workers (e.g. Germanovich et al., 1994).

Because Optical Borosilicate Crown Glass (OBCG) was used in this research, in the following paragraphs their glass material properties description will be empathized. OBCG was chosen in this research with the hope to allow observe the discontinuities propagation formation during the tests, as been made by some authors in transparent organic materials as PMMA; but, specially because this material is being used in the art industry, and the price and availability were favorable for this research.

Apart of the last mentioned upwards, OBCG has high strength to uniaxial compression (i.e. around 150 MPa), which can be categorized equivalent as a high strength rock–like material —under the classification of the International Society of Rock Mechanics (ISRM, 1981)—; and it has also low porosity, which is similar to brittle rock materials. Because OBCG is obtained by an industrial process, a high quality and homogeneous material may also be possible, which permits repeatability of the tested material for future research.

The advantages of using the SSLE technique to create the discontinuities has been explained in Chapter 3, but here it will be shown a micro–metric description of each notch, and it will be proposed a geometric characterization of that notch.

4.1 Optical Borosilicate Crown Glass as Representing Rock Material

Glass is an inorganic amorphous (i.e. non–crystalline) and often optically transparent vitreous solid material, grouped into the ceramic materials. There are plenty types of glasses, but the most used glass in the SSLE technique is the so called high quality Optical Borosilicate Crown Glass (chemical name), referred in this research by OBCG from it abbreviation. It is also referred by its commercial names as BK7 Glass (according to the Schott AG nomenclature, used in US references), K9 Crystal Grade A (according to Chinese references) or simply Schott Glass as named in Europe. Other trademarks of the same material are: Crystan BK7, Schott BNK-7, Corning BSCB 16-64, Ohara S-BSL7, Hoya BSC7, Hikari E-BK7 or Chinese H-K9L.

4.1.1 Chemical proportions of OBCG

Optically, this material is equivalent to a 30% lead transparent glass. It is used for precision lenses and prisms for LASER and optics because it has high homogeneity (i.e. homogeneity under the optic concepts), low bubble content and low inclusions. It weighs approximately 15% less than full (24%) leaded glass and can be polished like a leaded glass. OBCG has a low coefficient of expansion, approximately three times less than the other popular consumer glasses, such as soda–lime glass, which it makes useful for heating and other thermal–environment packaging, without the risk of cracking due to thermal shock. This glass has low production cost, around 18 US$ for each dm^3 according to this research experience. Table 4.1 shows the chemical proportions of this type of glass, provided by the OBCG supplier for this research.

TABLE 4.1: Chemical Proportions of the OBCG Crystal, after SIC (2007).

Component	Name	Proportion by weight
SiO_2	Siliceous Oxide	67% to 71%
B_2O	Boric Oxide	35% to 10%
Na_2O	Sodium Oxide	8% to 12%
K_2O	Potassium Oxide	8% to 12%
BaO	Barium Oxide	2% to 5%
ZnO	Zinc Oxide	less than 1%
P_4O_{10}	Phosphorus Pentoxide	less than 1%
CaF_2	Fluorite	less than 1%

4.1.2 Optical properties of OBCG

The basic optical properties of OBCG are:

- linear refractive index (n_{Od});
- non–linear refractive index (n_{O2});
- dispersion.

General tables of OBCG crystal report n_{Od} around 1.51 for a LASER wave length of 1.06×10^{-6} m, n_{O2} around 3.45×10^{-20} m^2 W^{-1}, and dispersion between 50 to 85 expressed by the Abbe Number.

4.1.3 LASER damage properties of OBCG

Two important crystal properties used in the SSLE technique, and will concern also this research interest, are:

- the Single Shot LASER Damage Threshold ($LDT_{\mathrm{1on1},g}$), which measures the energy per area in where a determined LASER beam damages the glass only by one single shot. The measure of this value is suggested in the standard ISO 11254-1 (2000);
- the Multiple Shot LASER Damage Threshold ($LDT_{\mathrm{Son1},g}$), which measures the energy per area in where a determined LASER beam damages the glass by multiple shots. Its measurement is suggested in the standard ISO 11254-2 (2001).

These two properties depend on such variables as: the LASER wavelength, pulse duration, pulse repetition frequency, focal spot diameter and sample temperature. For that reason, these

two values should be accompanied with the information about the spot–size of the test beam as well the type of LASER used for their determination, especially the pulse duration. With this information it is possible to scale the results to compare different sets of data. In the SSLE technique, normal short–pulse duration of the LASER is used inside the bulk glass to create one notch in one point; therefore, single shot LASER damage threshold is enough required to known.

A value for $LDT_{1on1,OBCG}$ was reported by Navarrete et al. (2003), given a mean value of 545×10^{-6} J with a 500 µm spot beam diameter (i.e. $\approx 1.38 \times 10^{4}$ J cm^{-2}) determined with a Nd:YAG LASER —with properties of $\lambda_{LASER} = 532$ nm, $\tau_{min,LASER} = 20$ ns, $E_{max,LASER} = 150 \times 10^{-3}$ J, and $F_{max,LASER} = 10$ Hz)— after performing 20 tests.

Some ambiguity may exist in the definition of LASER Damage Thresholds (LDT), because variability exists when is tried to obtain a unique value. In most all the cases, a range of values for LDT is obtained. Thus, in the moment to refer to a possible LDT value, one can use some statistics. The most common statistic for those values is the value at which there is zero probability of LASER damage, concept used in ISO 11254-1 (2000) and ISO 11254-2 (2001). For single shot tests, another definition is often used: the arithmetic average between the lowest power where damage occurred, and the highest power where no damage occurred. This value corresponds to a 50% likelihood of LASER damage occurring, and by definition it will be higher than the first one.

Gallais et al. (2002) determined a single shot threshold curve measured in bulk BK7 crystal, using a YAG LASER (λ_{LASER}= 1 064 nm, $\tau_{min,LASER}$= 7 ns, $E_{max,LASER}$= 50 $\times 10^{-3}$ J, and $F_{max,LASER}$= 10 Hz) focusing a spot size of 12 µm (Figure 4.1). From this graphic, one can determine that the lowest power —where damage occurred— is near 60 J cm^{-2} and the highest power —where no damage occurred— is near 170 J cm^{-2}, doing $LDT_{1on1,g}$ equal to 115 J cm^{-2}. According to the concept of reporting —that value at which there is zero probability of LASER damage— this is around to 60 J cm^{-2}. The same authors also presented multiple shot threshold curves for the same material.

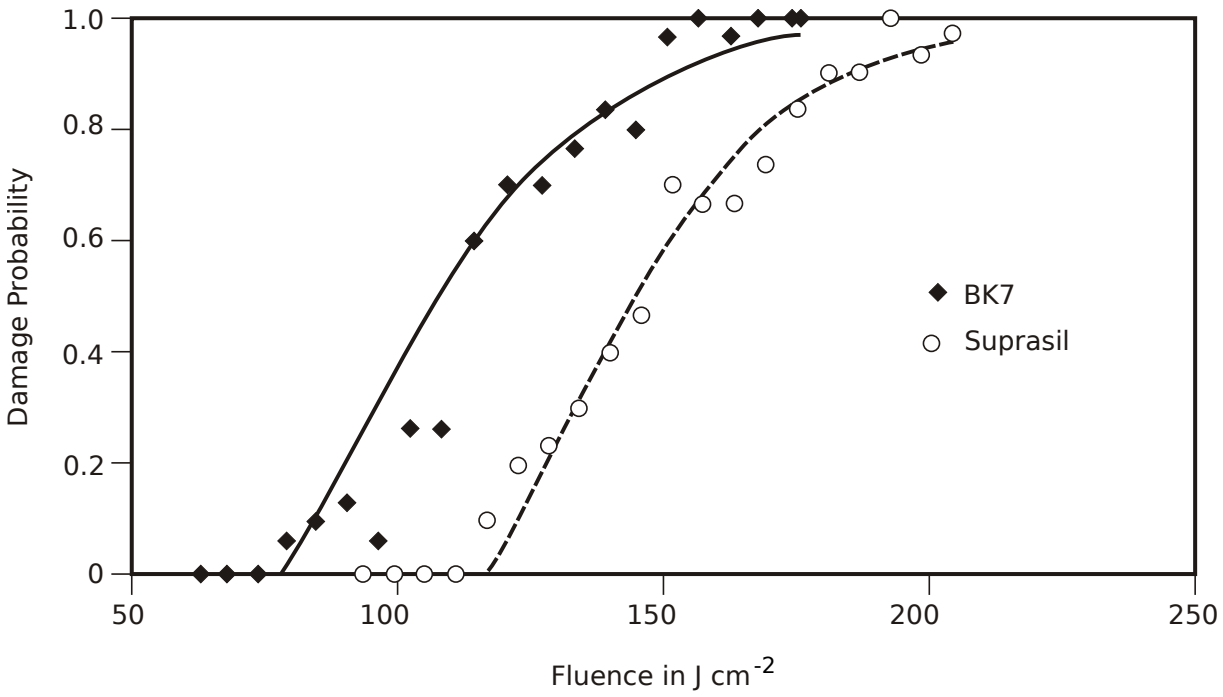

FIGURE 4.1: Single Shot Damage Threshold Curve in Bulk BK7 Crystal, after Gallais et al. (2002).

Often the LASER used for determining the LDT values are not of the exactly the same as used for the SSLE technique (i.e. they do not have the same pulse width or the same repetition rate). For the case in where only the pulse duration varies, and in order to translate the values to the required LASER, a escalation operation should be done, according to the following equation suggested in Kessler (2004):

$$LDT_{1\text{on}1,mat} = LDT^{*}_{1\text{on}1,mat} \sqrt[2]{\frac{\tau_{\text{min},LASER}}{\tau^{*}_{\text{min},LASER}}} \tag{4.1}$$

where the * sign indicates the known values.

For example, if a LDT of a material, determined with a LASER at a pulse duration of 10 ns, was 6.0 J cm^{-2}, the LDT for the same material with a same LASER but at a pulse duration of 1 ns is equal to 18.9 J cm^{-2}. The expression of Equation 4.1 is only valid for pulse durations between 0.5 ns to 50 ns. It is recommended to use this equation only as a rule of thumb.

4.1.4 Mechanical properties of OBCG

Mechanical properties of OBCG, rather than Elastic Modulus and Poisson Ratio, are not common to find in literature, this because of the low industrial applicability of this optical material as strength material apart of that used for opto–mechanics. The largest existing resource database of glass properties includes over 1 000 000 experimental values for 286 000 glasses compiled from over 22 000 references (Institute of Theoretical Chemistry, 2010), but the properties this database provides are only for density and elastic deformational parameters (i.e. elastic and shear modulus, and Poisson ratio). Unfortunately this database does not report strength properties of glasses.

Table 4.2 shows some mechanical properties encountered in literature for the special case of OBCG. As shown in this table, strength basic properties as uniaxial compressive strength and traction strength are not reported. In Jain et al. (2005), cylindrical compression tests in OBCG–BK7 crystal were reported, but performed under a temperature higher than its transformation temperature (T_g) (i.e. between 600°C to 800°C).

TABLE 4.2: Some Mechanical Properties for OBCG as Found in Literature.

Name and Reference	BK7 Liu et al. (2009)	N–BK7 Crystran (2010)
Young's Modulus, E_g in GPa	81	82
Poisson Ratio, ν_g	0.21	0.206
Mass Density, ρ_g in g cm^{-3}	2.51	2.51
Specific Gravity, $G_{s,g}$	–	2.39
Coefficient of Thermal Expansion, α_g in °K^{-1}	7.1×10^{-6}	–
Fracture Toughness, $K_{Ic,g}$ in MPa m$^{\frac{1}{2}}$	0.85 ± 0.05	
Vickers Hardness at 1.96 N, HV_g in GPa	6.8 ± 0.3	–
Knoop Hardness at 1.96 N, HK_g in GPa	5.2	–
Elastic Limit, $\sigma_{E,g}$ in MPa	–	63.5

In Pyrex glass —which is a Borosilicate glass close to be an OBCG— Handin et al. (1967) performed important mechanical tests in order to study peak strength and ductility of brittle materials. They performed uniaxial compressive, triaxial compression and triaxial traction strength tests, under triaxial axis–symmetric stress field; and also performed torsional compressive and torsional tractional test in solid and hollow cylinder samples, obtaining the strengths under polyaxial stress fields, all these using a special cell built for those purposes. All these tests in the Pyrex glass was performed at normal room temperature and with a an axial strain rate of

$10^{-7}\,s^{-1}$. A mean value of the uniaxial compressive strength of 1 100 MPa was encountered. Also, in triaxial compression stress, this glass was brittle at all confining pressures (i.e. from 0 MPa to 400 MPa) and becomes enormously strong. For example, an ultimate deviator strength of 2 600 MPa for a confining stress of 400 MPa was reported. In triaxial extension this glass was also brittle, for example a traction strength of -320 MPa for a confining compressive stress of 400 MPa was reported.

From the data results of the tests performed in the Pyrex glass by Handin et al. (1967), under a triaxial axis–symmetric stress field, here was fitted three common–in–use failure criteria (i.e. Coulomb–Navier, Hoek–Brown and Drucker–Prager) in order to have parameters for comparison with rock materials. Table 4.3 shows the resume of these calculations. Here, the parameters of the Drucker–Prager envelope are put as the equivalents of the Coulomb–Navier envelope, this last circumscribed by the former one in their major vertexes, when represented in the Haigh–Westergard space.

TABLE 4.3: Failure Criteria Parameters for Pyrex®Glass.

Criterion	Parameter 1	Parameter 2	σ_{ci} in MPa	σ_{ti} in MPa	R^2
Coulomb–Navier	ϕ= 46°	c= 141 MPa	704	-114	0.856
Drucker–Prager	ϕ= 49°	c= 119 MPa	631	-90	0.976
Hoek–Brown	m_i= 15.7	a= 0.5	979	-62	0.913

Note. ϕ is the internal friction angle; c is the shear strength of the corresponding failure criterion; m_i and a are similar parameters of the Hoek–Brown criterion.

Finally, as a reference —when no mechanical data of glass are available— could be possible assume as a complementary information a density around 2.5 g cm^{-3}, Mohs hardness between 5 to 6, elastic modulus around 70 GPa, shear modulus around 30 GPa, Poisson ratio around 0.2 , tensile strength less than 100 MPa, and compressive strength less than 1 000 MPa.

4.1.5 This research tests on OBCG

For this research, some index and mechanical properties at blank OBCG cubic specimens where obtained by testing. Here blank is referred to those specimens that did not suffered any LASER etching process (i.e. it has null notches in their body).

4.1.5.1 Blank OBCG used for this research

Blank OBCG cubical crystals used in this research came from Yeeya Art Work Corporation, a recognized and specialized factory located in the Shen Zhen province at China. They were packed in boxes of cardboard and transported by sea and terrestrial freight to the commercial representative in Brazil, located in São Paulo.

Because they are samples for art purposes, these samples were not exactly cubic as cab be observed in Table 4.5, and they have at their borders small chamfers of 1 mm length, as can be appreciated in Figure 4.2.

The following optical properties of the OBCG were provided by the supplier of the material for this research (Table 4.4), where laboratory tests were performed by the Shanghai Institute of Ceramics of the Chinese Academy of Sciences (SIC, 2007). Also, the supplier reported a density of 2.52 g cm^{-3} for this material. The supplier did not ordered mechanical tests on their material, because this material is used for art applications.

TABLE 4.4: Optical Properties of OBCG used in this Research, after SIC (2007).

Property	Values
Classification	First Class Glass
Linear Refractive Index, n_{Od}	1.51607
Bubble Diameter	≥ 0.05 mm
Bubble Area	> 0.03 m^2 cm^{-3} to 0.01 m^2 cm^{-3}
Stripes	Without Signs
Strength Refraction	Band 2 (Glass Wave Front Error < 6 mm cm^{-1})
Calorific Nature	76×10^{-7} per °C, from 20 °C to 120 °C
Transformation Temperature, T_g	567 °C

4.1.5.2 Index properties

Before any test, the three geometrical dimensions of each cubic sample (i.e. length at the North, East and Nadir directions [see Section 5.2]) were carefully measured with a micrometer, five times for each dimension; in order to obtain an average value of them (Table 4.5). Also, these samples were weighted in order to know their respective mass (w_{d}), and finally the time that a sound wave travels through the nadir direction of each cube (t_{s}).

TABLE 4.5: Basic Average Measurements on OBCG Samples.

Sample* \ Direction	Average Length in mm			t_s	w_d
	North	East	Nadir	in ms	in g
SGA	68.60	69.15	66.48	12.5	791.76
SGB	68.06	67.77	67.71	12.5	785.26
SGC	67.32	68.12	68.62	12.5	792.61
SGD	68.37	68.66	68.54	12.5	805.80

*See footnotes of Table 4.7.

All the mentioned measurements were useful to finally calculate some of the index properties of the OBCG being used (i.e. dry unit weight [$\gamma_{d,OBCG}$] and sound wave propagation velocity [$v_{sd,OBCG}$]), see Table 4.6.

TABLE 4.6: Geometrical and Index Properties of Blank OBCG Samples.

Sample*	V in m^3	A_{ne} in m^2	$\gamma_{d,OBCG}$ in kN m^{-3}	$v_{sd,OBCG}$ in m s^{-1}
SGA	0.00032	0.0047	24.6	5318
SGB	0.00031	0.0046	24.7	5418
SGC	0.00031	0.0046	24.7	5490
SGD	0.00032	0.0047	24.6	5483

Note. V is volume; A_{ne} is the transverse section parallel to the North–East plane; γ_d is the dry unit weight; and v_{sd} is the uniaxial sound propagation velocity.
*See footnotes of Table 4.7.

One can calculate that the mean sound propagation velocity $\widehat{v}_{sd,OBCG}$ is equal to 5408.7 m s^{-1} with a standard deviation ($s_{v_{sd,OBCG}}$) of 86.4 m s^{-1}, giving a coefficient of variation ($CV_{v_{sd,OBCG}}$) of 0.016 . While, unit weight can be assumed between 24.6 kN m^{-3} and 24.7 kN m^{-3}.

4.1.5.3 Ultimate Axial Strength

In this research, four blank OBCG samples were tested under uniaxial compressive stress (i.e. samples SGA to SGC), in order to obtain the strength and the deformation parameters of the material. The specimen preparation as also its arrangement and the equipment arrangement of this experimental campaign was equal to that used in the main experimental campaign of the physical models testing described in detail in Section 5.5 and Section 5.6. Please refer to this sections in order to see the details of this testing campaign. Figure 4.2 shows the UCS test performed for one of these mentioned blank samples.

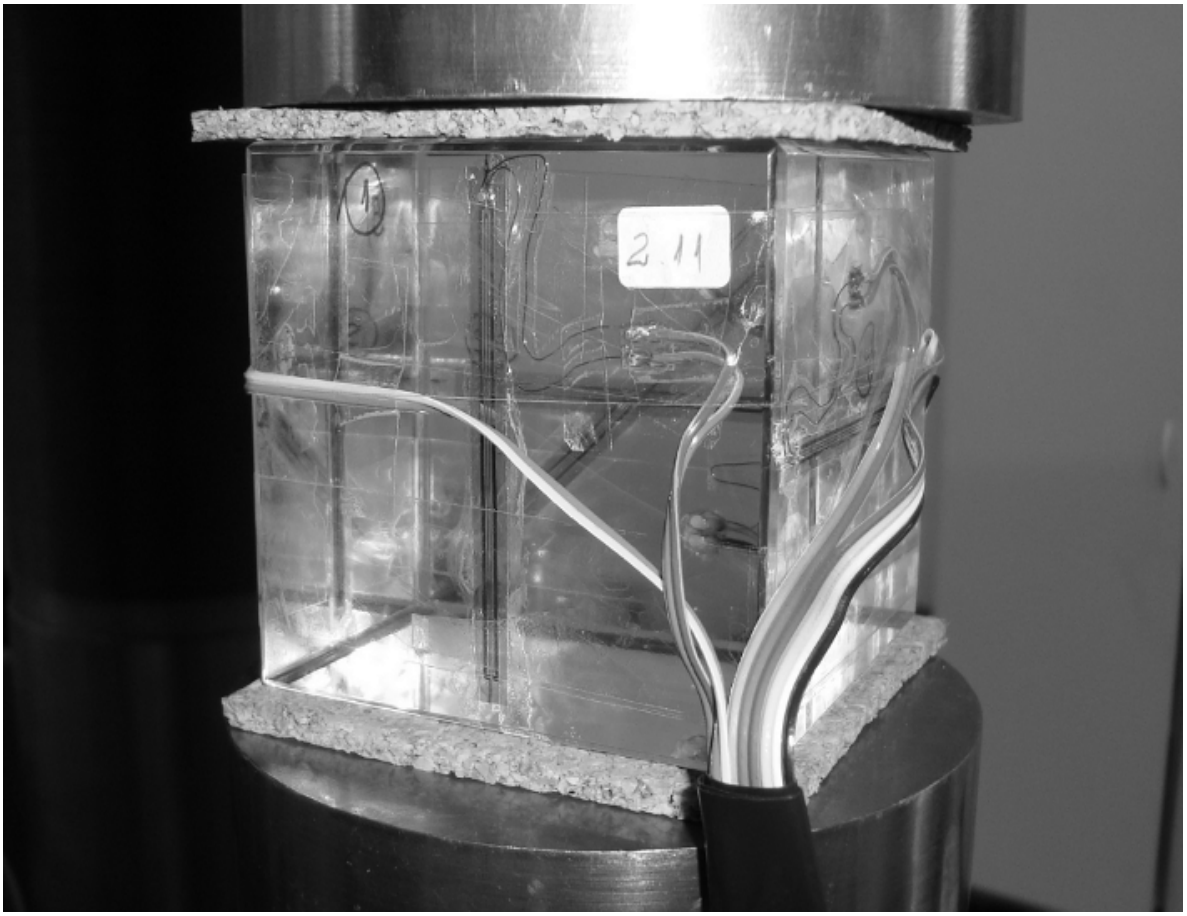

FIGURE 4.2: Uniaxial Compressive Strength Test on a Blank Sample (SGA Sample).

Therefore, the axial force —in line with to the nadir–axis— was registered, and with a graphic of the axial strain *vs.* axial strength, the ultimate strength of the OBCG was assessed. In all samples, a fragile rupture was observed. The following table shows the ultimate strength of the tested material (Table 4.7). Univariate statistics of the uniaxial compressive strength of these four tests (i.e. $n = 4$) resulted in a median value of 121.7 MPa, a mean of 144.9 MPa with a standard deviation of 91.22 MPa, and a coefficient of variation of $CV_{\sigma_{\mathrm{ci},OBCG}}$=0.630.

As can be seen in this last table, the ultimate strengths of the tested OBCG samples are very disperse, with a proportion of 4.2 times between the maximum and minimum values.

It was decided to inspect if the test rates has some influence on these values, because it is known in literature that uniaxial compressive strength of rocks are dependent with the test rates: faster is the test rate, lesser is the uniaxial compressive strength. In Table 4.8 one can observe that the test rates of each test are also variable, with a median value of 0.62 MPa s^{-1}. For example, SGA has the highest uniaxial compressive strength and the fastest test rate, while SGB has the

TABLE 4.7: Ultimate Strength of OBCG Samples.

Sample	Ultimate Axial Force f in MN	$\sigma_{ci,OBCG}$ in MPa	Proportion to Minor Value
SGA*	1.28	271.6	4.2
SGB	0.30	64.4	1
SGC†	0.68	147.8	2.3
SGD‡	0.45	95.7	1.5

*SGA was the unique sample that was tested in a different frame in respect to the others, it was tested in a SBEL rigid four column frame.

†SGC was used as compensator material during the deformation measurements. This sample was tested after all samples were tested, but unfortunately a chip in one of their faces was created just after the test beginning. Even tough, the test was concluded.

‡SGD came from a sample that should be engraved with a discontinuity set β_{sd} angle of 45° (i.e. sample 045DA), but it wasn't. Therefore, it turned to a blank material renamed as SGD. This was tested also by using SGC as a compensator material for strain gages.

lowest uniaxial compressive strength but a lower test rate. But, SGC has the slowest test rate and has the second higher uniaxial compressive strength after SGA.

TABLE 4.8: Average Axial Stress Rates During the Ultimate Strength Tests.

Sample*	$\sigma_{ci,OBCG}$ in MPa	t_σ in MPa s^{-1}
SGB	64.4	0.68
SGD	95.7	0.57
SGC	147.8	0.34
SGA	271.6	0.80

Note. t_σ is Stress application rate.

*See footnotes of Table 4.7.

When plotting the values of stress rates in the abscissas and the uniaxial compressive strength in ordinates (Figure 4.3), one can see that among all the values, if one discard the values of test SGA and perform a linear regression fit, one can obtain a very acceptable negative coefficient of correlation (R^2) equal to -0.9502. Therefore, it appears to have an existence of a relation between axial stress rates within the ultimate strength, where the inverse proportion between uniaxial compressive strength and test stress rate do accomplish.

Because no other sample was programmed to test, and no more arguments exist to invalidate or validate any of the above test results for the uniaxial compressive strength of OBCG, but because the data are very disperse, it was decided to ignore the maximum and minimum values

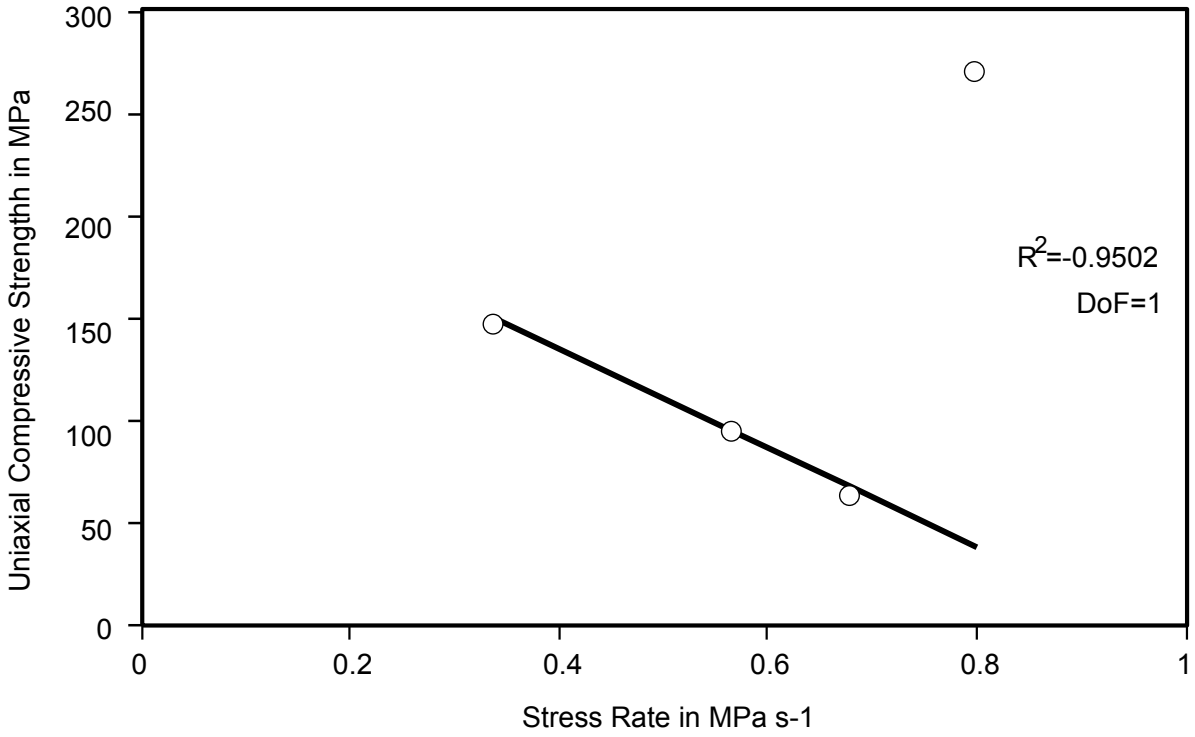

FIGURE 4.3: Stress Rate *vs.* Uniaxial Compressive Strength Correspondence

(i.e. corresponding to the sample SGA and SGB samples, respectively), which is a common method in statistics to reduce un–explainable dispersions, but better applicable for large number of statistical samples. The univariate statistics adopted finally for the uniaxial compressive strength of OBCG are therefore $\widehat{\sigma}_{\mathrm{ci},OBCG} = 121.75\,\mathrm{MPa}$ for mean, and $s_{\sigma_{\mathrm{ci},OBCG}} = 36.84\,\mathrm{MPa}$ for standard deviation, obtained for samples SGC and SGD (for $n = 2$). The media value within this last consideration remains un–altered, and the median range resulted in [95 MPa, 150 MPa].

But, if one remember the mean value of this variable —with all the four tests (i.e. the value of 144.87 MPa)— one can observe that this value is inside the media range defined above; therefore, one can conclude that the decision to ignore the maximum and minimum values was useful.

The following figure shows the axial strain *vs.* axial strength plot for one blank OBCG tested sample (Figure 4.4). The same plots for the other samples here tested are shown in Appendix A.

With the plots of the vertical strain *vs.* vertical stress and horizontal strain *vs.* vertical stress, for each sample, it was also possible to calculate the vertical deformation modulus and the Poisson ratio of them. Each modulus was calculated tangential to that curve (i.e. vertical strain

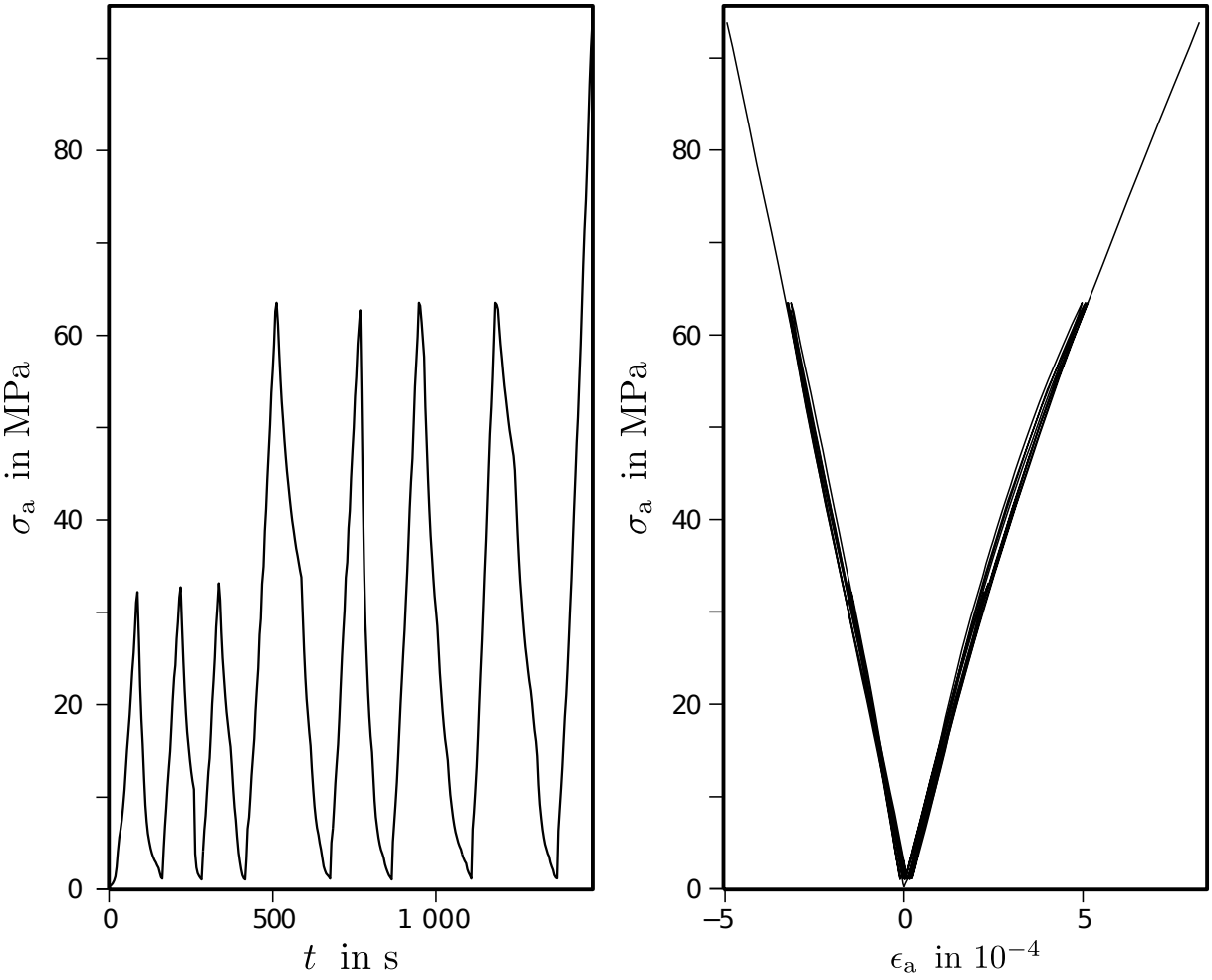

FIGURE 4.4: Plots of an OBCG Blank Sample Test (i.e. sample SGD). **a** Time *vs.* Axial Stress; **b** Axial Strain *vs.* Axial Stress.

vs. vertical stress) at the 50% of the maximum stress (i.e. 50% the ultimate strength, $E_{t,50\%}$), and Possion ratio (ν) resulted by the division of $E_{t,50\%}$ with the ratio of horizontal strain and vertical stress at the same stress level of 50% the UCS. Table 4.9 shows the resume of the values obtained for all these blank samples.

TABLE 4.9: Tangential Vertical Deformation Modulus of Blank Samples.

Sample*	t_σ in MPa s^{-1}	$E_{t,50\%,OBCG}$ in GPa	ν_{OBCG}
SGA	0.80	92	0.27
SGB	0.68	57	0.20
SGD	0.57	112	0.43
SGC	0.34	104	—†

Note. t_σ is Stress application rate.

*See footnotes of Table 4.7.

†Horizontal strains for SGC were not continuous, therefore ν_{OBCG} was not possible to calculate.

One can observe that the tangential axial vertical deformation modulus and Poisson ratio of the tested blank samples are also disperse, and that there are not a direct and clear relation between these values and the stress application rate. In order to have a reference value for $E_{t,50\%}$, it was again adopted the rule to ignore the smallest and the highest values, and apply the mean equation for the remaining two values. Therefore, the reference value for the Tangential Vertical Deformation Modulus of Blank OBCG is 98 GPa, which also represent the median value of it. Finally, adopting the same method as described above, the reference value for ν_{OBCG} adopted here is equal to 0.27.

4.2 LASER etched OBCG as Representing Discontinuities

A group of ordered notches —arranged in rectangular mat with any number of layers— produced by an etching process may represent a plane of weakness in OBCG (i.e. a weak discontinuity plane in a rock mass model).

In order to validate the above affirmation, one must at lest validate if each notch in OBCG etched by the SSLE technique produces a real damage in the material. To verify —in this research— bi–dimensional optical observations were done at different magnification scales and at two observation planes.

In the following section, one will found the results these observations gave, in order to finally propose a simplistic geometrical model of an etched notch.

4.2.1 Etching process

For this particular characterization, a small blank OBCG parallelepiped with size 20 mm × 20 mm × 40 mm—coming from the same provider at China (i.e. from Yeeya Art Work Co.)—was used.

Then, this sample was engraved at the Casa do Cristal offices —a commercial business dealing with artistic engraved crystals with the SSLE technique, located at São Paulo city (Brazil)—with a specialized–for–art SSLE machine. The machine general specifications —maximum number of points, velocity, and cooling system, as also the LASER properties— unfortunately were not provided for this research, because of a commercial protection policy of the office and also a patent protection of the machine manufacturer. Also, photographs of the machines were not allowed to take for the present research.

The etched figure consisted on an artistic three dimensional shape (i.e. a couple of persons) available at the enterprise. This figure contains surfaces that can be oriented at any direction, but a small proportion of the figure was parallel to the major size of the parallelepiped (i.e. the 20 mm × 40 mm face) (see Figure 4.5) which was the region where observations were concentrated.

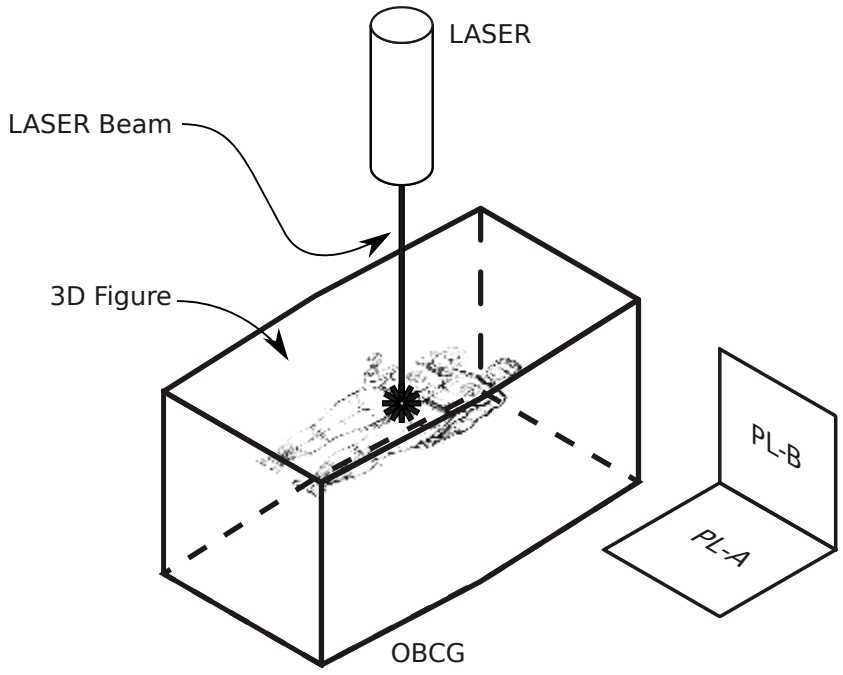

FIGURE 4.5: Observation Planes defined for Notch Observation.

4.2.2 Bi–dimensional Observations

Since a three dimensional observation of LASER notches in OBCG was not possible because on the absence of a stereo–microscope, only bi–dimensional descriptions where possible trough magnifying glasses, a petrographic microscope, and an electronic microscope.

Observations of notches in OBCG had the following objectives:

- characterize geometrically the notches (e.g. how the flaws look like, how many flaws the notch has, how they are arranged in the space);
- determine if the notches are:
  - regular in shape across the space;
  - regular in size across the space;
  - spatially equal oriented, knowing that the LASER beam is shot from a unique place; and
  - spaced regularly.

For the two initial observation techniques (i.e. magnifying glasses and petrographic microscope), two observation planes were for special attention. The first plane perpendicular to the laser beam direction (PL–A) and the second one (PL–B) parallel to the laser beam direction (Figure 4.5).

4.2.2.1 Simple Eye and Magnifying Glass Observations

Initial eye observations of the notches showed that there are very small dots. With a hand–held $10\times$ magnifying glass, some kind of three dimensional stars with regular tips can be observed. Through a desk professional magnifying glass, it can be observed that the notches were also like three dimensional stars, having more than five non–regular tips and in general around 13 tips. But, all of them presented a preferential orientation and larger tip extension, forming a kind of bird foot, parallel to the LASER beam direction.

The mentioned three dimensional stars present some times tips oriented to one preferential direction (i.e. like a bird feet). Figure 4.6 show some notches as they look like when they are observed through two magnifying glasses, with a magnifying value of $6.4\times$ and $16\times$ respectively.

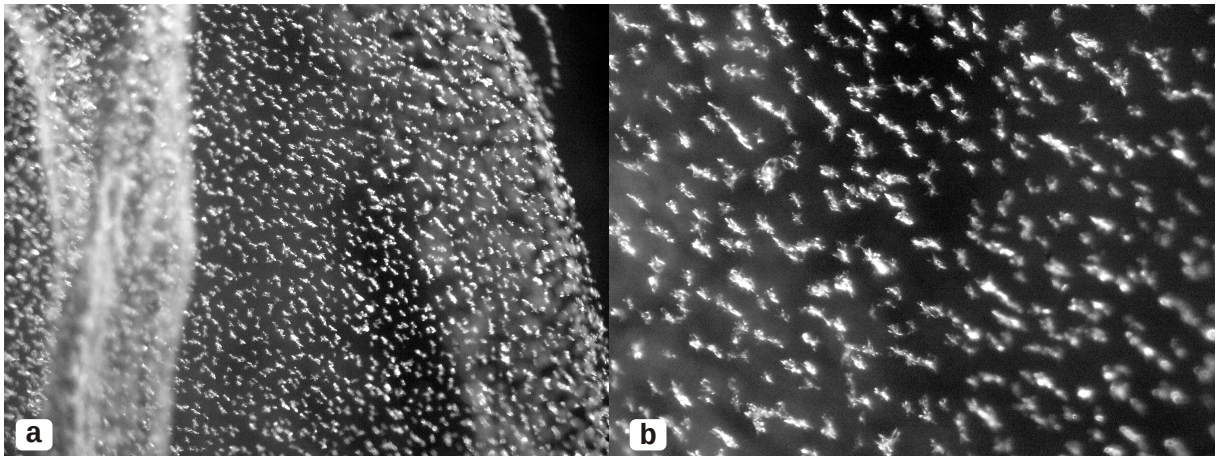

FIGURE 4.6: Notches observed through Magnifying Glasses. **a** Magnifying value of 6.4×; **b** magnifying Value of 16×.

From these observations, it was observed that notches in the OBCG are distinct in size and shape, are oriented spatially randomly, and are spaced between each other according to a determined resolution. Also, when looking them as a set, the optical observations with the magnifying glass shown that notch forming sets that are trying to represent a discontinuity plane have among them bridges of OBCG material; therefore, they will not represent essentially a full developed continuous discontinuity.

4.2.2.2 Optic Microscope Observations

By using an optical petrographical microscope, the two defined planes were observed: one perpendicular to the LASER beam direction (PL–A) and the second one (PL–B) parallel to the LASER beam direction. The objectives of observing through two perpendicular planes were:

- to find out the three dimensional irregular shape notches;
- to have a microscopically view of the notches; and
- to observe if the borders of the notches does have microscopically fissures planes that are tending to propagate into the sane OBCG.

Following the petrographic method for rocks description, a thin section should be prepared in order to observe it through a petrographic microscope. But because OBCG allows the light to pass cleanly, a thin section preparation was not necessary. Just by adjusting the focus thread of the microscope one could observe the notches at the desired depth plane.

With the optical petrographic microscope magnifying values of 10×, 25×, and 50× were possible to observe those notches. Within this technique, parallel and perpendicular polarized light observations were also available; and scaled photographs were obtained. Figure 4.7 shows a group of notches with a magnifying of 10× with parallel and perpendicular polarized light observed to the plane PL–A (i.e. perpendicular to the LASER beam direction).

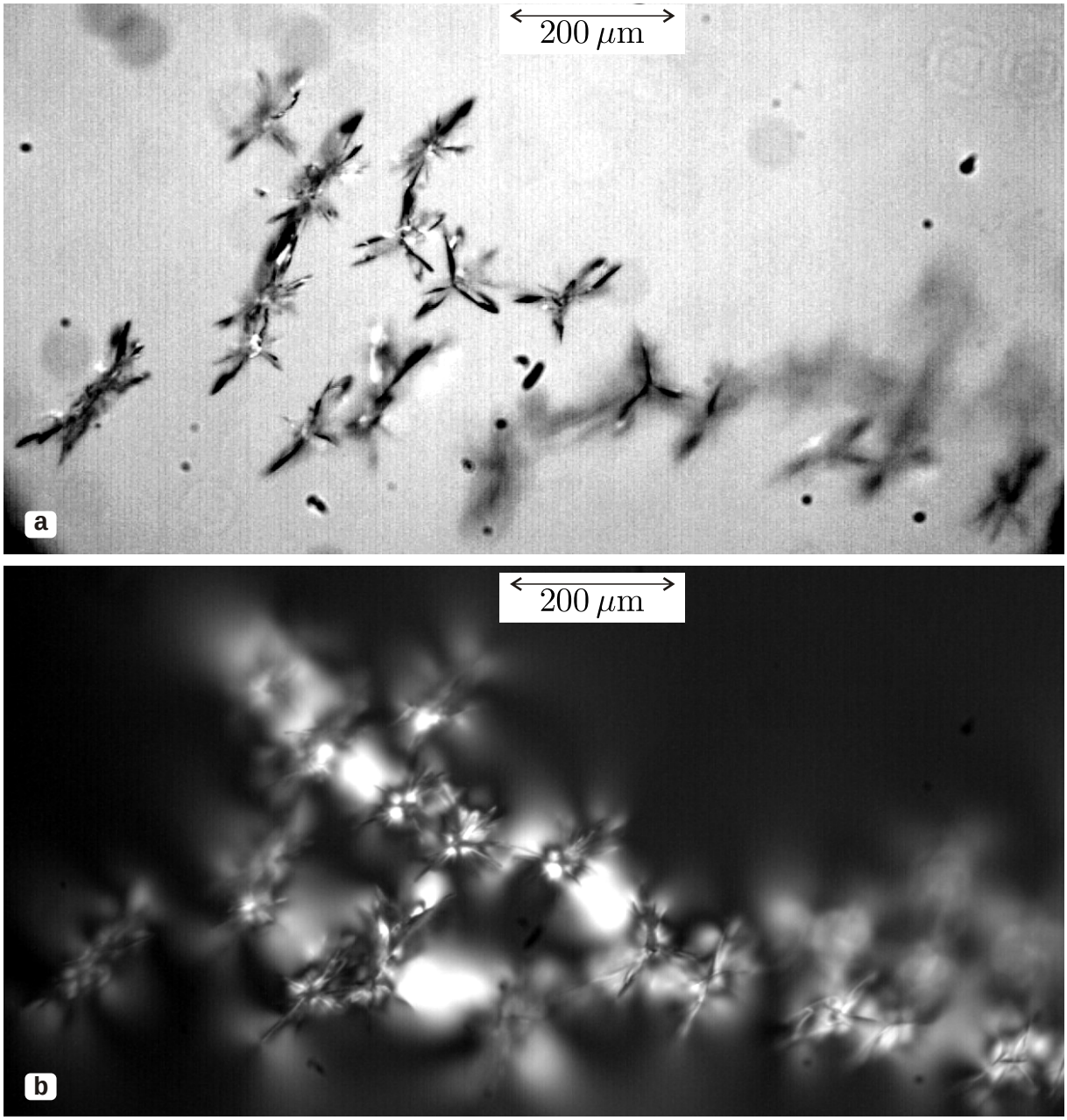

FIGURE 4.7: Notches observed through a Petrographic Microscope in the Plane PL–A. **a** Normal light; **b** polarized light.

Figure 4.8 show another group of notches observed in a plane perpendicular to PL–A (i.e. plane PL–B parallel to the LASER beam direction), also with a magnifying of 10× with parallel and perpendicular polarized light.

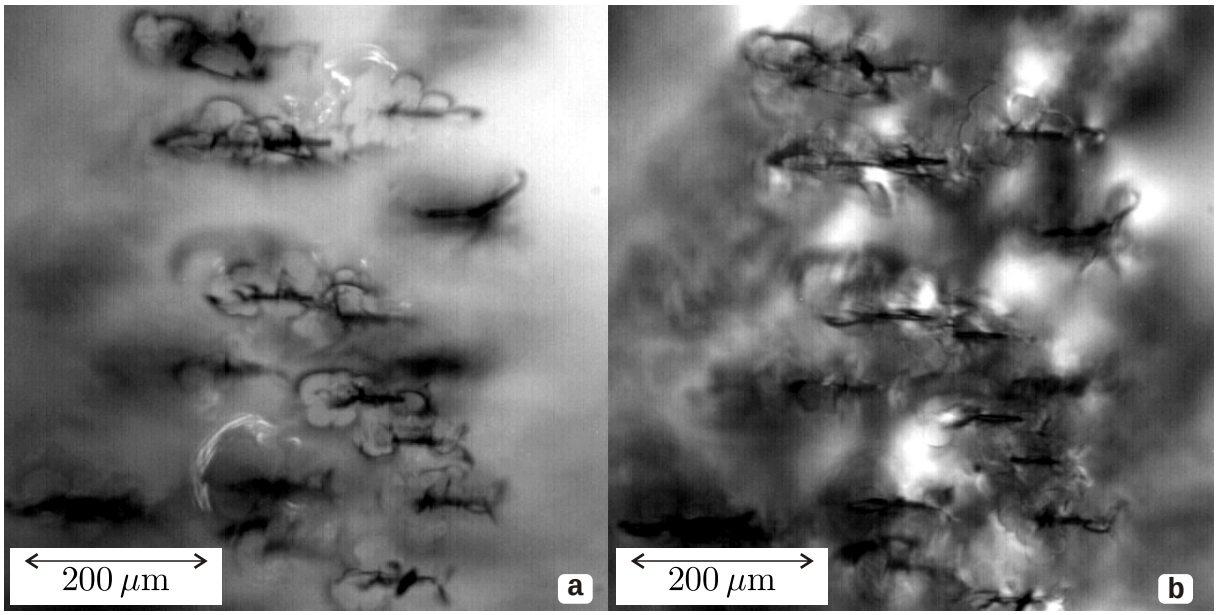

FIGURE 4.8: Notches observed through a Petrographic Microscope in the Plane PL–B. **a** Normal light; **b** polarized light.

Figure 4.9 shows a single and scaled notch composition with a magnifying of 10× with parallel polarized light observed in the plane PL–A and in the plane PL–B.

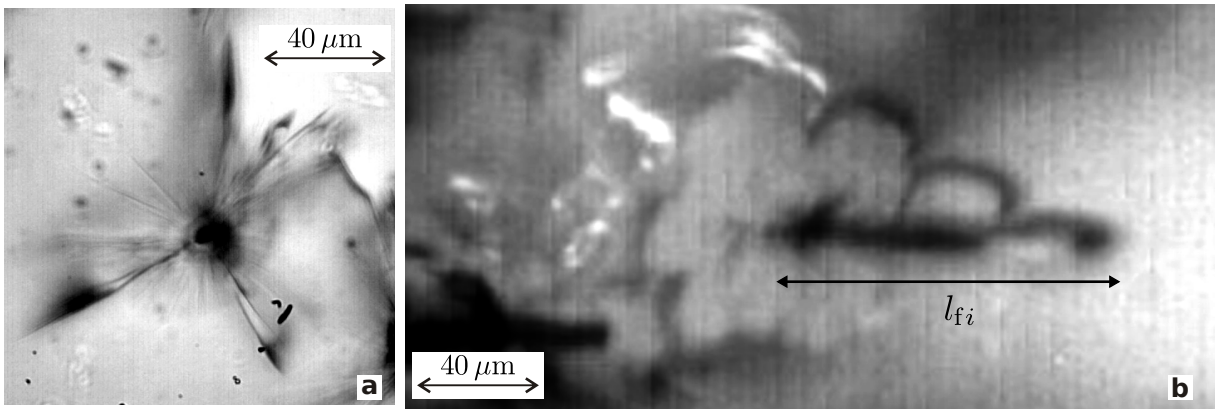

FIGURE 4.9: Notches observed through a Petrographic Microscope with Parallel Polarized Light. **a** In plane PL–A; **b** in plane PL–B.

It is observed that the star shape referred in the previous initial observations is only valid when observed parallel to the direction of the etching LASER beam direction, otherwise is possible to observe the some kind of bird foot with the multiple fingers converging in the foot.

Measurements were performed in the two observed planes, with the aim to determine mean dimensions of some linear features, as defined as follows:

- longitude of the foot parallel to its axis ($l_{\mathrm{f}i}$) [Figure 4.9b];
- diameter of the cross section of the foot ($d_{\mathrm{f}i}$) [Figure 4.10b];
- length of each finger ($l_{\mathrm{g}i}$) [Figure 4.10b];
- relative angle between two adjacent fingers projected in a plane perpendicular to the foot axis ($\beta_{\mathrm{g}i}$) [Figure 4.10b].

Figure 4.10 shows one typical frontal view of the notch–bird foot. For these particular notches, a mean value of 90 µm was obtained for $l_{\mathrm{f}i}$ measurements (l_{f}), 5 µm for $d_{\mathrm{f}i}$ measurements (d_{f}), 40 µm for $l_{\mathrm{g}i}$ measurements (l_{g}), and 28 ° for $\beta_{\mathrm{g}i}$ measurements (β_{g}) (see also Figure 4.13).

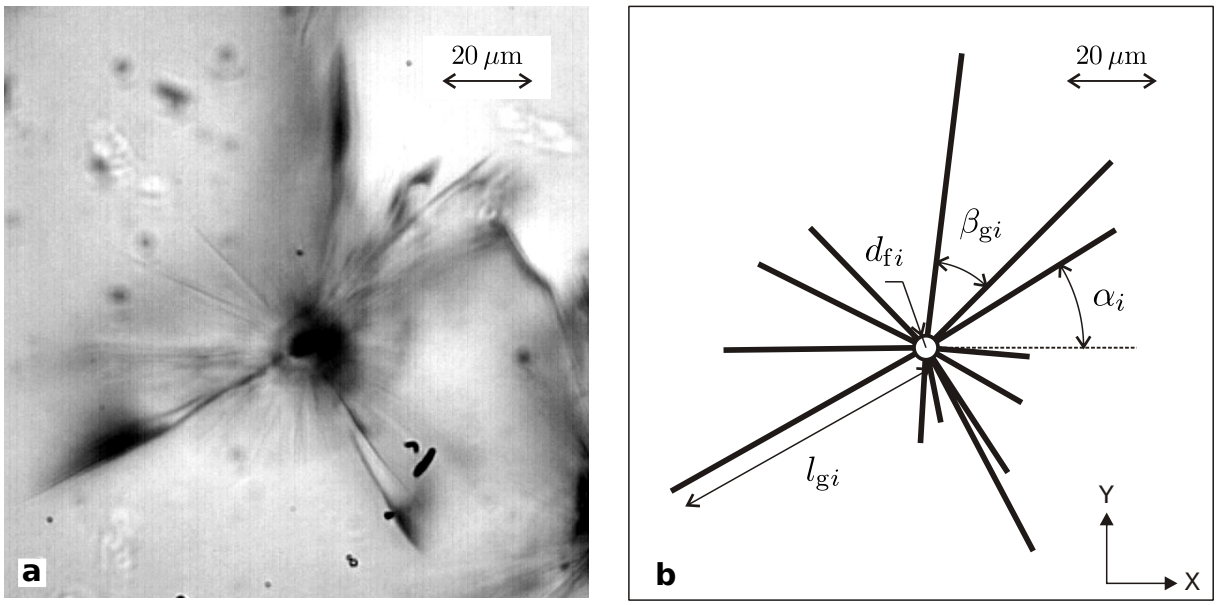

FIGURE 4.10: Front Aspect of One Typical Notch–Bird Foot. **a** Photograph; **b** scheme with measured linear features.

4.2.2.3 Comparisons of Optic Microscope Observations with other studies

Shimomura et al. (1987) made measurements of the Breakdown Channel Diameter (d_{c}) and the Maximum Radial Crack (r_{max}) when they observed the notches in the plane PL–A for a single Potassium Dihydrogen Phosphate (KDP) crystal. They found that the size of the notches depend on the Energy Density applied to the crystal. Sizes of d_{c} varied from 10 µm to 32 µm and for r_{max} from 30 µm to 40 µm were found, for a LASER beam projected perpendicular to

the crystal surface. The LASER that they used was one with a wave length of 1.053 µm with a pulse–width of 1 ns.

Morozov et al. (2006) took photographs of the appearance of the notch in the same two analyzed planes (i.e. planes PL–A and PL–B). These photographs are very similar to those observed in this research, as can be shown in Figure 4.11.

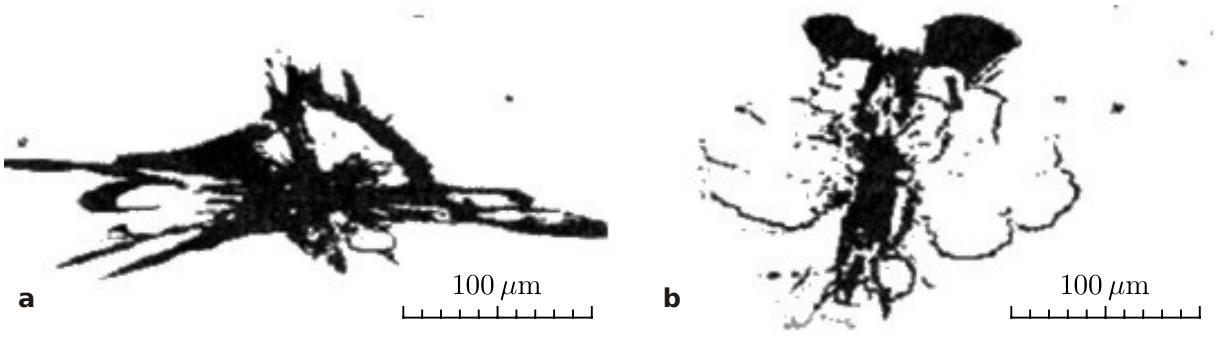

FIGURE 4.11: Notch Appearance as Photographed by Morozov et al. (2006). **a** Frontal view; **b** lateral view.

4.2.2.4 Electronic Microscope observations

A final optical observation on the notches was performed with the Scanning Electron Microscope (SEM) technique. In order to generate the observation plane for this technique, a 2 mm depth groove in the OBCG was done with a saw blade used for thin–samples preparation. Upon this groove and with a screwdriver, a shear plane was obtained after hitting it with a hammer.

Using this technique, the fractographic[1] identification was performed (Figure 4.12).

In this figure one can recognize a critical cavity where all fractures are initiated. Then, a propagation zone composed by the mirror zone is observed. Inside the mirror zone, radial scars and concentric ripples are recognized (i.e. Wallner lines). Finally, it is observed that an at–rest line defines the limiting zone of propagation, where in some places a further zone is observable called the fringe marginal zone.

The common cracking observed are conchoidal fractures planes, that develop around the critical cavity (i.e. the axis of the foot and the axis of the fingers). This type of fracture describes a

[1] Fractography is used to develop and evaluate theoretical models of crack growth behavior. One of the aims of this discipline is to determine the cause of failure by studying the characteristics features of a fracture surface.

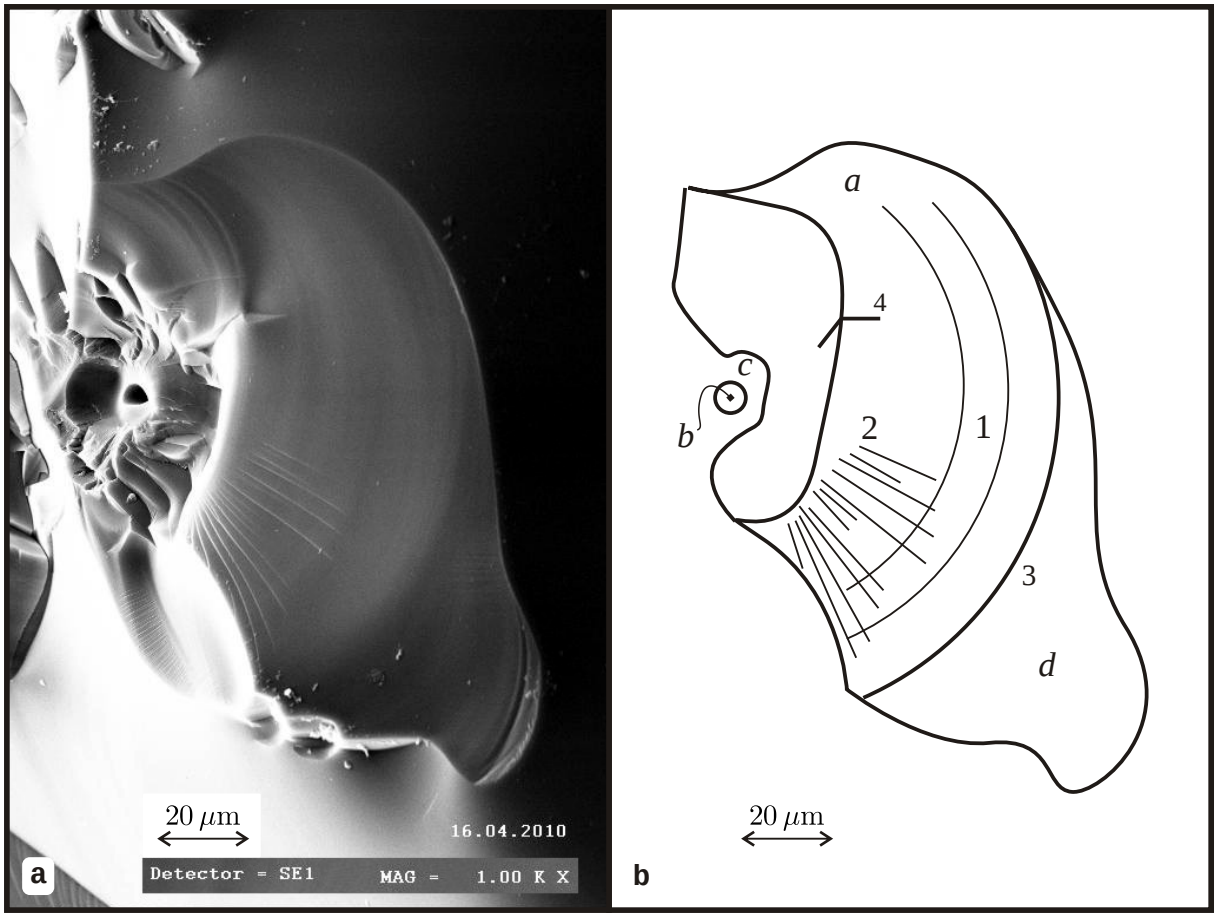

FIGURE 4.12: SEM Photograph showing the Conchoidal Fracture. **a** Photograph; **b** sketch. Areal zones: *a* mirror zone, *b* critical cavity, *c* undefined feature, and *d* fringe marginal zone. Linear features: *1* radial scars (hackle marks), *2* concentric ripple marks (rip marks or Wallner lines), *3* at–rest line, and *4* undefined feature.

typical way that brittle and amorphous materials break because they do not follow any natural definite crystallographic structural plane. Then, those fracture planes that develop from the critical cavity extend beyond the so called foot. For that reason, a surface envelope around the foot and the fracture planes was defined in order to have the total damage notch volume–geometrical model, this which will be useful to define the minor possible notch separation in order to avoid notch coupling (e.g. this permitted define the notch densities of the test campaign of Section 6.5).

4.2.3 Total damage notch volume–geometrical model

Through the bi–dimensional observations performed and explained above, the total damage notch volume–geometrical model was possible to define. This geometrical model was defined with the union of two regular solids: a half sphere and a half ellipsoid, which are welded through each of their flat ends resulted by dividing them by their respective minor symmetry planes.

The previous two–dimensional measured features were used to assess the variables that define the damage volume: the sphere radius (r_{v}) and the minor ellipsoid half–side (a_{v}), both equal to 50 µm; and the mayor ellipsoid half side (b_{v}) equal to 100 µm.

This model was useful to have an idea of the minimum separation each notch should have in regards to others adjacent to it; and in order to permit or avoid notch coupling when necessary, as required in the Design Process of the OBCG–SSLE technique and as described in Section 3.4.2. Figure 4.13 shows the proposed notch shape model.

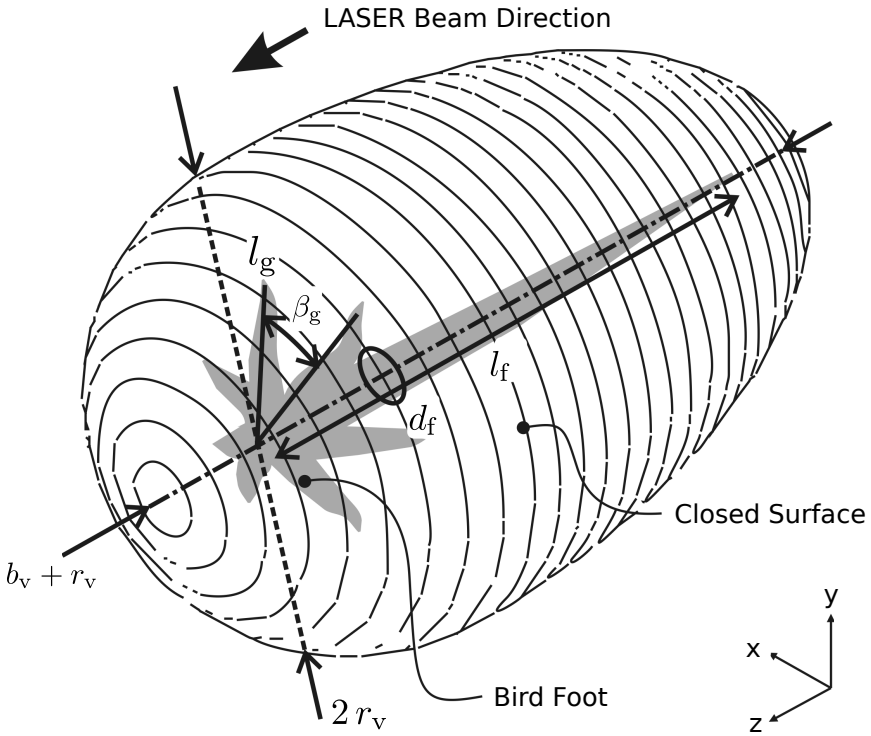

FIGURE 4.13: Proposed Total Damage Notch Volume–Geometrical Model.

From this shape model, the notch volume (V_{e}) was possible to be calculated, being equal to $7.8 \times 10^{-13}\,\mathrm{m}^3$. This value can be used to assess the notch density in the material (R_{dm}), and the notch density in the discontinuity (R_{dd}); both which are variables that can be related

in future researches with the mechanical parameters of the same material, as was explained in Section 3.4.2.

The volume value here encountered (V_e) is less than similar values encountered in literature. For example, Morozov et al. (2006) made measures of the Breakdown Channel Volume (V_{ch}) and the Total Damage Volume (V_f) of the encountered notches in two types of glasses. For the case of the single–phase glass mentioned in that research —which is similar to the OBCG— they encountered a range of volumes for V_{ch} from $5\times10^{-12}\,m^3$ to $5.5\times10^{-11}\,m^3$; and for V_f from $1\times10^{-11}\,m^3$ to $5\times10^{-10}\,m^3$. The used LASER was a YAG nano–pulsed ($\lambda_{LASER} = 1.06\,\mu m$; $\tau_{min,LASER,0.5} = 12\,ns$; $E_{max,LASER} \leq 120\times10^{-3}\,J$).

Notch density is defined here as the relation of the total notch volume (V_{et}) to the corresponding gross volume of the OBCG (V_t):

$$R_d = \frac{V_{et}}{V_t} = \frac{n_t V_e}{V_t} \tag{4.2}$$

where n_t is the total number of notches in V_t.

Here it is important to discuss the possible influence of the notch geometry. An ideally notch geometry for modeling will be a sphere. With a sphere, no possible notch–orientation influence on the deformation response may exists. But because the observed notch geometry (as idealized by the geometric model of Figure 4.13) is not a sphere, it is possible that notch orientation may influence on the deformation response of the entire physical model.

This situation (i.e. the influence of the notch orientation) may be negligible for the case of the ultimate strength value of the physical model —the situation it is dealt in this research— because propagation planes are more related to the stress regime rather than fracture shape. Even though, in future researches, could be an important task to demonstrate if the notch orientation influences in the ultimate strength of the physical model.

4.3 Final Comments

In order to have in hand a possible model material and technique, this chapter concentrated the attention to characterize the OBCG and the possible set of notches that will form a plane of weakness representing the discontinuities of a modeled rock mass.

An exhaustive description of OBCG was performed by consulting references, but also some useful–for–this–research physical and mechanical properties of this material were found by laboratory testing.

The material used to represent rock material —described here as the Optical Borosilicate Crown Glass— has properties similar to brittle rock materials.[2] For the goals of this research, the most important mechanical property studied here to validate the physical models of this research was the uniaxial compressive strength of blank OBCG. Results revealed a median range of this value between 95 MPa and 150 MPa, showing a very disperse range of values; even though OBCG came from a same production set and being the construction process a very controlled and invariable process. The reason of these disperse values could be mainly because a non unique stress rate were used for the tests, as shown in Figure 4.3, showing also that UCS of OBCG is very sensitive to stress rate application.

Also elastic parameters were obtained. The mean tangential vertical deformation modulus was defined to be near 98 GPa, and the mean Poisson ratio around 0.27.

In general it can be concluded that, even though OBCG is an optical homogeneous material, it is not necessary true that it is mechanically also an homogeneous material, because they constitute an amorphous solid. Perhaps glasses are the most studied material among other, and it was observed that they are mechanically very sensitive to their superficial conditions (Personal Conversation with Dr. J.L. Armelin).

In respect to the notches that will represent —in a set of them— the discontinuities a rock mass can have, the present research made a two dimensional notch characterization through optical instruments, from a magnification of $10\times$ —as is a hand magnification glass— up to around $10^6\times$ —as is an electron microscope.

It is concluded that notch forming sets that are trying to represent a discontinuity plane have among them bridges of OBCG material; therefore, they will not represent essentially a full developed continuous discontinuity.

Also, the optical observations revealed and confirmed that the etching process with the OBCG–SSLE technique is a real damage process; and that each microscopic damage volume itself, or separated a determined distance among others adjacent to it in an array, can influence the mesoscopic behavior of the OBCG; and that many damage volumes can be superposed also

[2] If OBCG is heated, the brittle character of this material can drop down.

in an array (i.e. if notch coupling is attained), in order to form a mesoscopic damage plane, which are the main interest for the modeling purpose of this initial research, i.e. simulate the discontinuities. And, if notch un–coupling is preserved, it could be likely possible that these un–coupled notches can modify OBCG strength and deformation properties of the rock–material–like phase, as also creating a preferential anisotropy or decreasing rigidity, because the notch shape is not as spherical as is theoretically wanted to be.

An important outcome of this optical characterization of notches, is that it was possible to offer a notch volume geometrical model, as presented in Figure 4.13. This geometrical model is useful to define notch resolutions for the materials that will represent the discontinuities as also the rock–material in the physical model.

In future research could be of great interest to measure acoustic emissions on OBCG when stressing it, in order to study how each notch couples together to form the discontinuities propagation planes. Using OBCG as rock–mass–like material, reduced models of rock masses may be possible tested in conventional frames, cells and employing their conventional active and passive monitoring systems. Also, it can be useful to achieve the construction of straight cylindrical samples.

In this research it was not possible to use straight cylindrical samples, because the engraving machine used in this research initially does not admit curved surfaces for allowing the LASER beam to pass trough, and because in the common market, cylindrical crystals are not easy available. Even though, one can create cylindrical samples after engraving by cutting prismatic samples by also LASER techniques. But when doing so, the transparency of the crystal is lost and a certain roughness at the cut surface is created —of around 18 µm, as reported by Mauersberger et al. (2008). The transparency of the cut glass surface is lost because of the roughness of the cuter surface, but it can be recovered if a very fine polisher abrasive mill is available, but this certain do not recover the initial transparency totally. Therefore, some new technique should be developed in this respect.

Chapter 5

Physical Models Testing

In this chapter it is presented the methodology, the experimental design and arrangement, the experimental execution, and the primary results of this research physical testing campaign. This will provide all the details necessary for another scientist to duplicate this work and go further with the research. The SSLE technique, the materials representing rock–like material (i.e. OBCG) and discontinuities (i.e. LASER notch arranges), were discussed in the last two chapters (Chapter 3 and Chapter 4). This chapter will concentrate the attention on the physical models testing, and the direct and primary results obtained from them (i.e. gross interpretation). A fine results interpretation, its discussion, and validation will be presented in the following chapter (Chapter 6) .

5.1 Methodology

The methodology adopted in this research has been divided in the following three Work Packages (WP):

- construction of samples;
- samples preparation and equipment arrangement;
- samples testing;

These WPs are represented by the three consecutive processes of the right side of the flow chart (i.e. the three rectangles after the bifurcation circle) shown in Figure 5.1. With this WPs one should have as a result a graphic of the influence of discontinuities orientation on the

uniaxial compressive strength of rock mass, called as model graphic —similar to that presented in Figure 2.10— which should be compared with the corresponding graphic obtained by using the Jaeger model (i.e. analytical graphic), whose theoretical basis was exposed in Section 2.1.1 of Chapter 2.

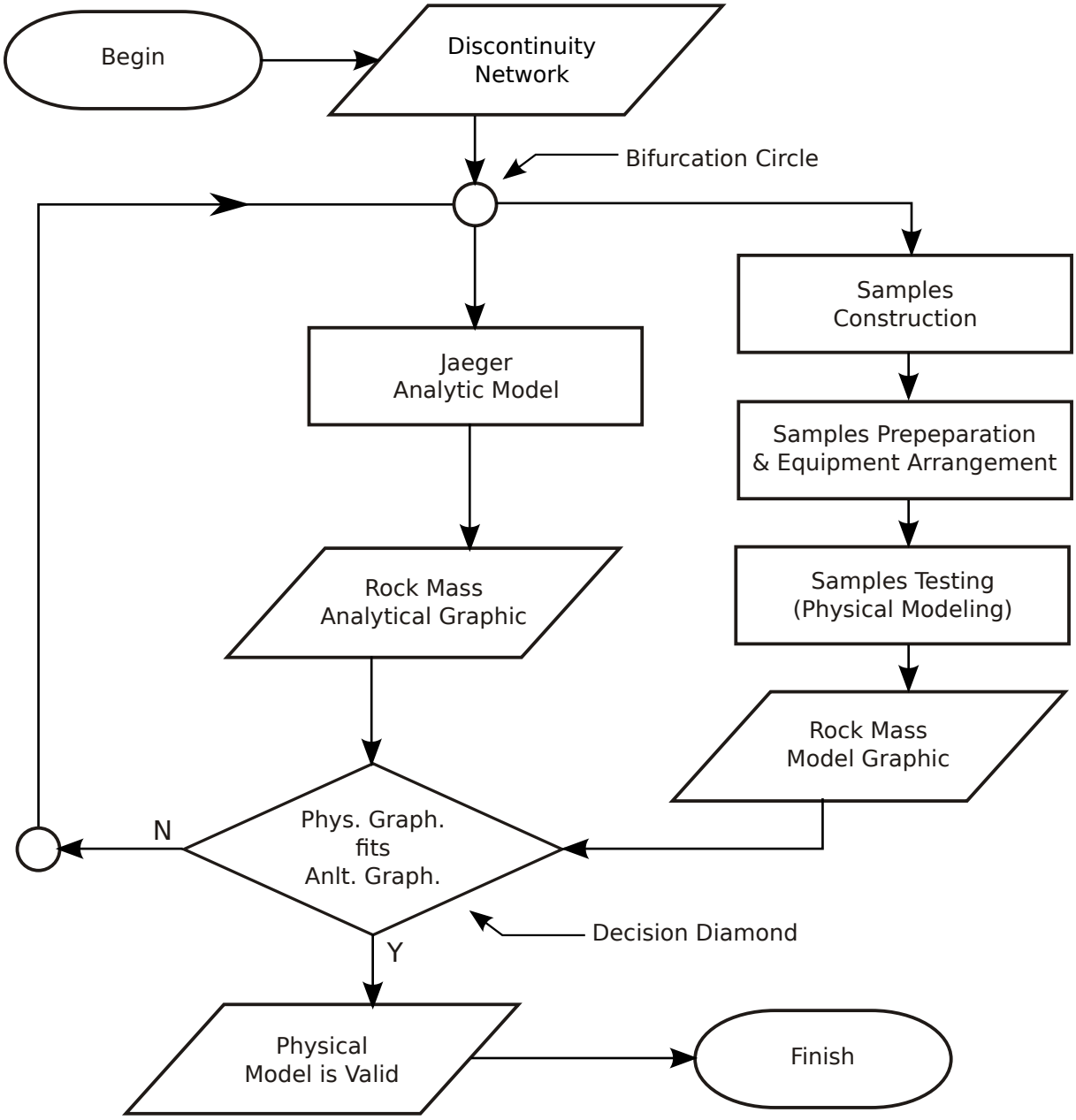

FIGURE 5.1: Flow Chart of this Research Process.

In the flow chart, the decision diamond evaluates a graphical similitude, but more accurate is to say that it is a numerical similitude, because those graphics are obtained from data resulted form the physical testing and the Jaeger equation as expressed in Equation 2.10.

As can be seen in Figure 5.1, if those two graphics are not similar —or better to say, if the measured data from physical models tests do not fit well acceptable to the Jaeger equation (Equation 2.10)— one should again initiate all the methodology exposed above until obtaining a reasonable fit. A reasonable fit can be concluded if —for example— a coefficient of determination (R^2) —the proportion of variability in a data set that is accounted for by the model— is greater than 0.7, which is a reasonable value for geotechnical variability.

Here it is assumed that the analytical model is the correct one, because it came from a simple but consistent theory. In the case of an unacceptable behavior is repeatedly found (i.e. no fit exist between the two mentioned graphics) —ideally— the process should be repeated until some reasonable behavior is encountered; but, normally the research process finishes until its logistic supplies are exhausted. According to the actual research schedule, the research would sustain up to three cycles.

5.2 Reference Coordinate System

In order to be consequent with rock mass modeling practice, the reference coordinate system adopted to all this modeling campaign was the North–East–Nadir (NEN) coordinate system, where the x–axis is oriented to the geographic North, the y–axis to the geographic East, and the z–axis to the Nadir, conforming a dextrorotatory coordinate system, which is accordingly to the right–hand rule and where depth is positive.

Even though, geographical orientation of the samples here tested are not necessary, this coordinate system was adopted in order to facilitate language expressions, when oriented lines and planes are wanted to explain.

5.3 Studied Rock Mass

The target object to be studied in this research is a rock mass having only one set of total–persistent discontinuities with constant geometrical properties. The discontinuities present in the set: do not have infilling and presence of fluids through it; and have constant spacing, persistence and width. Rock material is non–porous, and is brittle and dry.

The stress field to be studied is an uniaxial compressive stress applied vertically and parallel to the Nadir–axis, on the North–East faces of cubic samples. Discontinuities are oriented all with a dip–direction ($dipDir_{\mathrm{d}}$) of 90° from North to the East, and dip varying from 0° to 90°. The plane East–Nadir constitutes therefore the transversely isotropy plane.

The stress field is incremented from a zero stressed state until sample failure, or bursting, by following a monotonic incremental and constant rate stress path, and under biosphere ambient temperature conditions.

It was defined five specimen types, those where dip angle (dip_{d}) has 0° (i.e. β_{sd} angle equal to 90°), those with dip angle of 30° (i.e. β_{sd} angle equal to 60°), with 45° (i.e. $\beta_{\mathrm{sd}} = 45°$), 60° ($\beta_{\mathrm{sd}} = 30°$), and 90° ($\beta_{\mathrm{sd}} = 0°$). For each type, three samples were tested, having therefore in total 15 samples. Reasons for testing only three samples per type, was only an economical decision; and as it was concluded in this chapter, it would be ideally test at least 5 to 7 samples per type.

Figure 5.2 shows the five groups of specimens to be tested in this research. It can be also shown that the β_{sd} angle is here also the angle that forms the axial axis of the loading force (i.e. translated into stress) with the discontinuities planes. This β_{sd} angle is the same as described in the analytical expression of Section 2.1.1.

It is important to say that between sample types a and b and between sample types d and e —of Figure 5.2— a greater β_{sd} angle gap exist (i.e. angle difference of 30°) rather than between sample types b and c, and c and d (i.e. angle difference of 15°). This was so defined because it was not possible to create more sample sets of intermediary β_{sd} angles, and because in experimental results —on real rock materials or rock masses— most differences about the β_{sd} angle inclination on uniaxial compressive strength values were present in the range near 45°(e.g. Nasseri et al., 2003; McLamore, 1966; Hakala et al., 2007; Hudson and Harrison, 1997). Even though, it is recommended in future researches to propose small and homogeneous intervals among β_{sd} angle sets, for example an angle difference of 5°. Also, it is recommended to use more samples for each angle set; here was used three samples per set, but in the future it could be used seven samples per set, in order to study better the disperse character of the experimental values.

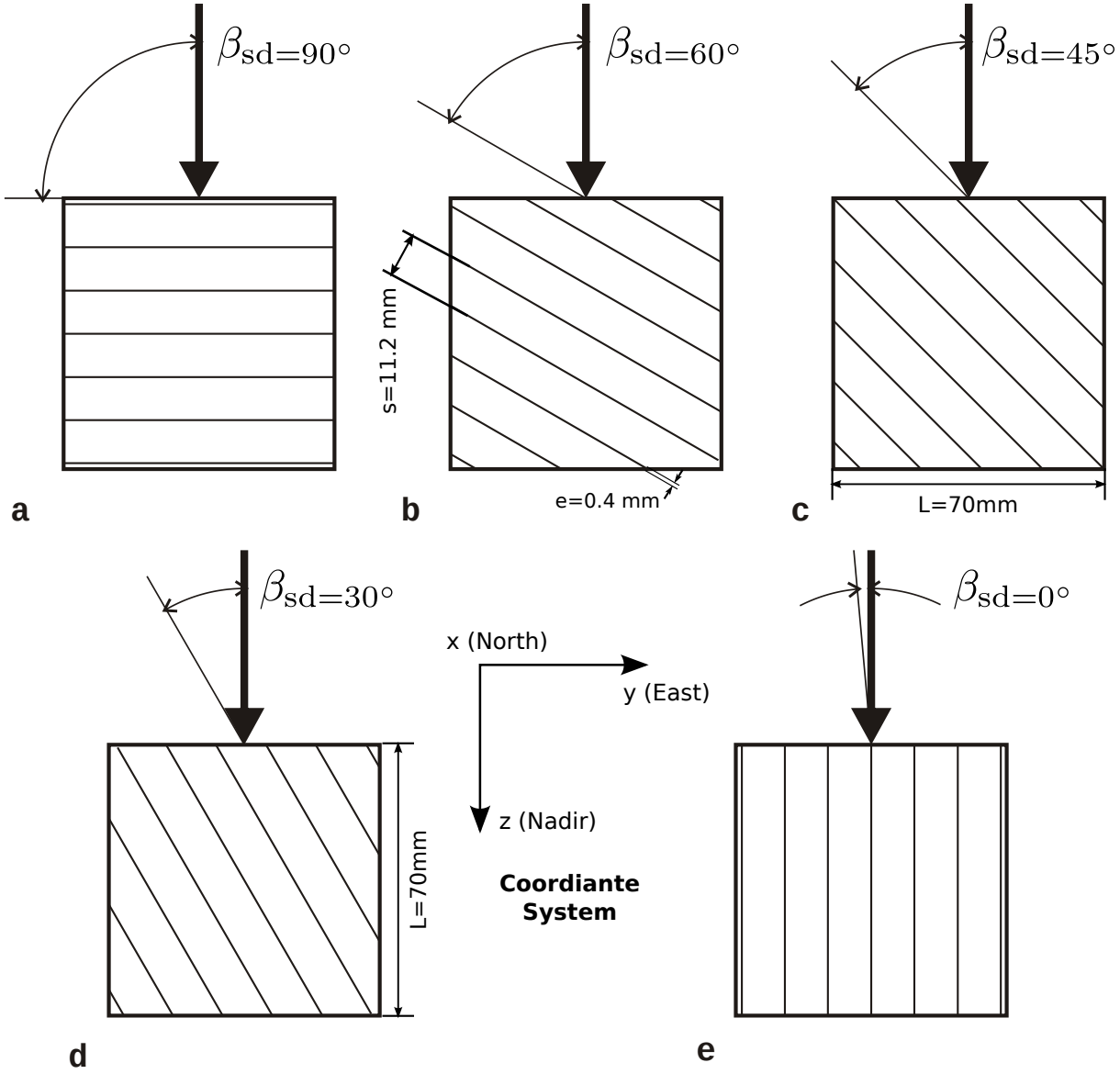

FIGURE 5.2: Sample Types Tested in this Research. **a** Discontinuities with $\beta_{sd} = 90°$; **b** with $\beta_{sd} = 60°$; **c** with $\beta_{sd} = 45°$; **d** with $\beta_{sd} = 30°$; **e** with $\beta_{sd} = 0°$.

5.4 Construction of Samples

In order to construct the samples (i.e. in order to built the pattern of notches in the blank OBCG, described as an etching process), was first: defined the discontinuity network of the rock mass, expressed it as a three dimensional solid object; transformed the solid object to a cloud object; and passed the information to the SSLE machine.

5.4.1 Discontinuity Network Creation

In common literature, the process to generate the discontinuity network is named Artificial 3D Fracture Network (A3DFN) modeling, but here it was not used it, because one have only a single discontinuity set. In this–research simple case, the discontinuity network is composed of discontinuities with constant dip–direction (i.e. N090) but variable dip (i.e. from 0° to 90°); while waviness (i.e. that given by 4 planes of notches), roughness (i.e. that given by 4 planes of notches), width (i.e. 0.4 mm), spacing (i.e. 11.2 mm), and persistence (i.e. total–persistent) remained constants. Therefore, the creation of the discontinuity network does not needed stochastic models, and it was easy to develop with a three dimensional vector graphics software (as is the Open Source FreeCAD program) and a good three dimensional viewer (as is the Open Soruce Meshlab program). Figure 5.3 shows the solid and the cloud geometrical models for the specimens type 060D (i.e. sample with a discontinuities–set plane–inclination angle of 60° respect to the load direction). To understand the cloud geometrical model see Section 3.4.2.7 of the present document.

In order to establish the position of each notch inside the model (i.e. in order to create the cloud model) a computational algorithm named 3D–CDNG program was developed for this research, using the MATLAB® program as explained shortly in Section 3.4.2.7 (see also the complementary electronic material of this research). Results of these calculations are materialized in one file for each specimen type, which contains the space coordinates of all points that in conjunction form the discontinuities. The cloud–points files are included in the accompanied DVD of this document.

5.4.2 Samples Etching Process

As mentioned in the etching process of OBCG for the optical characterization in Section 4.2; for this research, the blank OBCG samples came from the same provider at China, through the local provider located at São Paulo. Therefore, properties described in Section 4.1.5 are also applicable for these samples. Also, as their similar of blank OBCG samples, this samples had at their borders small chamfers of 1 mm length, as can be appreciated in Figure 5.8.

All samples were engraved also at the Casa do Cristal offices located at São Paulo, with that specialized SSLE machine used to produce art crystals. It is here again mentioned, that unfortunately the machine general specifications (e.g. maximum number of notch points, etching

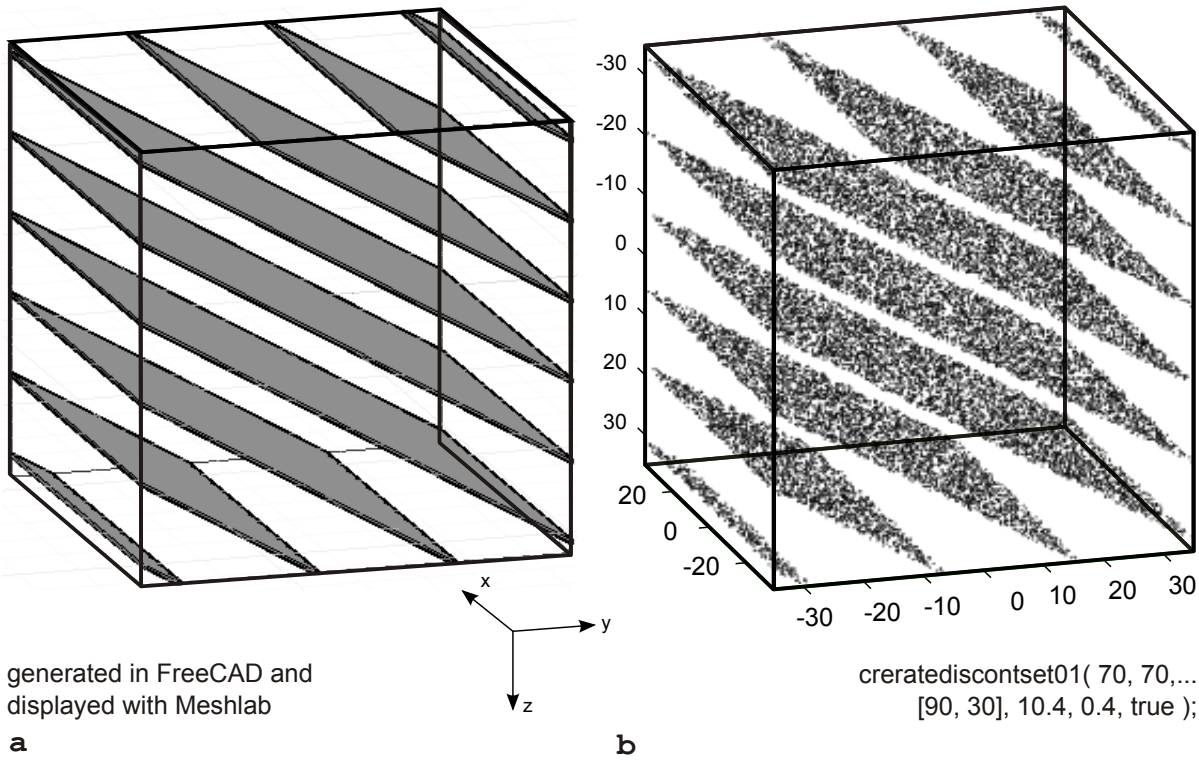

FIGURE 5.3: Discontinuity Geometrical Models (Sample 060DA). **a** Solid model; **b** cloud model.

velocity) as also the LASER properties (e.g. type, wave length, pulse length, pulse energy), were not provided for this research, because of a commercial protection policy of the office and also a patent protection of the machine manufacturer. The unique feature that can be observed during the visit to the office was that the machines were water–cooled, and that the LASER beam reaches the objective point by modifying the lens position, permitting to change the LASER focus and orientation, rather than moving the plate below the sample.

The discontinuities were etched inside blank OBCG by the SSLE technique, described in Section 3.1 and schematized in Figure 5.4. Notch density, that ratio of the number of notches per volume, for the discontinuities etching process was programmed to be 4215×10^6 notch m^{-3}. The input files used in this process were those cloud–point files created for this particular research.

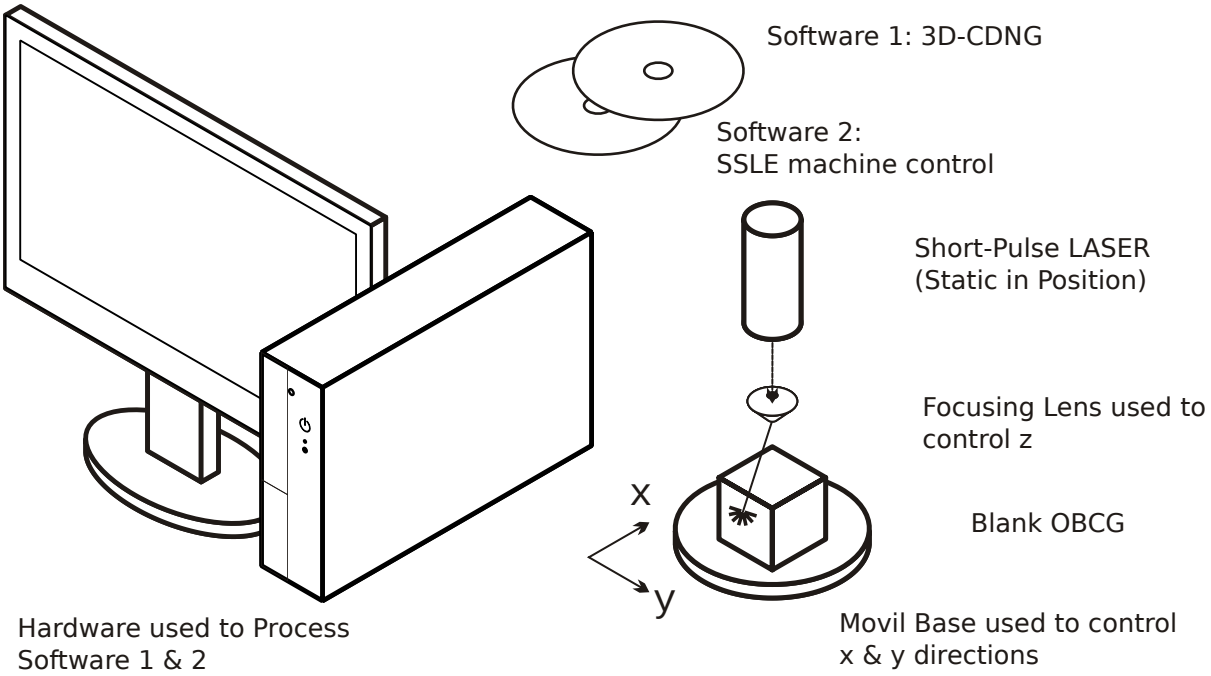

FIGURE 5.4: Scheme of the Construction Process of the Specimens Samples.

During this procedure, the total etching process time for each sample type was measured. Then, by knowing the number of notches each sample has in total, one could found out the mean etching velocity of 1 906 notch s^{-1} with a standard deviation of 45.5 notch s^{-1}. The following table resumes the data obtained (Table 5.1).

TABLE 5.1: Velocities of the Engraving Process.

Sample Type*	β_{sd} in °	n_{notch}	$t_{etching}$ in minutes	$\widehat{v}_{etching}$ in notch s^{-1}
000D†	0	2 370 816	19.7	2 002
030D	30	1 784 685	15.3	1 948
045D	45	1 433 241	12.5	1 919
060D	60	1 807 176	15.5	1 943
090D	90	2 370 816	20.9	1 895

Note. n_{notch} is the total number of notches; $t_{etching}$ in the total etching time; and $\widehat{v}_{etching}$ is the mean etching velocity.
*Sample type is divided in five: those samples whose discontinuities sets have a β_{sd} angle from 90° to 0° (i.e. 90°, 60°, 45°, 30° and 0°).
†The letter D corresponds to discontinuity.

After the engraving process was concluded, the samples where inspected if possible cracks existed, and then packed each one in their respective single blue cardboard package, and finally all the group in one bigger package containing the 15 samples. All samples finally were transported

terrestrially first from São Paulo to Brasília, and then from Brasília to the Electrobrás–Furnas Laboratory, located near the city of Goiânia. At the laboratory headquarters, each of the samples were verified for any crack or pattern defect occurred during their transportation. Only the sample 045DA was rejected by accusing absence of any engraving pattern (this sample was turned to the SGD sample, whose test results were presented in Section 4.1.5); but none of the other samples shown any defect by fabrication or transportation. Figure 5.5 shows all the samples as they arrived to the final place in where were prepared for testing. Individual photographs for each sample are present in Appendix A.

FIGURE 5.5: This Research Test Samples.

5.5 Samples Preparation

All samples were prepared in order to register only deformational information during the testing. Therefore the monitoring instrumentation allocated in each sample consisted on five uniaxial

strain gages, located as following, when looking the sample perpendicular to the negative East–Nadir plane:

- one strain gage glued in a horizontal position at the lateral right–hand face that stores data in the variable reported as strain number 1 (ε_1);
- two strain gages glued at the back face, one in a horizontal position that stores data in the variable reported as strain number 2 (ε_2); and other in an inclined 45° position that stores data in the variable reported as strain number 3 (ε_3);
- one strain gage glued at the frontal face in a vertical position that stores data in the variable reported as strain number 4 (ε_4);
- one strain gage at the lateral left–hand face in a vertical position that stores data in the variable reported as strain number 5 (ε_5).

Same position description will be easier when using the oriented planes and the adopted NEN coordinate system:

- one strain gage oriented 000\00 and glued at the negative North–Nadir plane;
- two strain gages glued at the positive East–Nadir plane, one oriented 090\00 and the other 090\45;
- one strain gage at the negative East–Nadir plane oriented 180\90;
- one strain gage at the positive North–Nadir plane oriented 270\90.

The following Figure 5.6 shows the allocation of these strain gages. Data stored in the data base therefore resulted in two vertical strains (i.e. strain gages 4 and 5), two horizontal strains (i.e. strain gages 1 and 2), and one inclined (i.e. strain gage 3).

From these measurements, strain gage 5 always gave the deformation perpendicular to the discontinuities planes but parallel to the applied load, and strain gage 1 always gave the deformation parallel to discontinuities planes but perpendicular to the applied load, independent to the discontinuities planes set inclination. While strain gages 2, 3, and 4 were affected by the inclination of the discontinuities planes set.

Strain gage 5 lectures were used to calculate the axial stress to the strain–5 ratio (σ_a/ε_5) at the 50% the uniaxial compressive strength tangential to the curve, named here as a kind of rock mass tangential vertical deformation modulus ($E_{t,50\%,mat.,5}$); and with strain gage 1 lectures, also was calculated the —here called— rock mass vertical to the horizontal strain ratio ($\nu_{mat.,5-1}$), which is the strain–5 to the strain–2 ratio ($\varepsilon_5/\varepsilon_1$) at the 50% the uniaxial compressive strength.

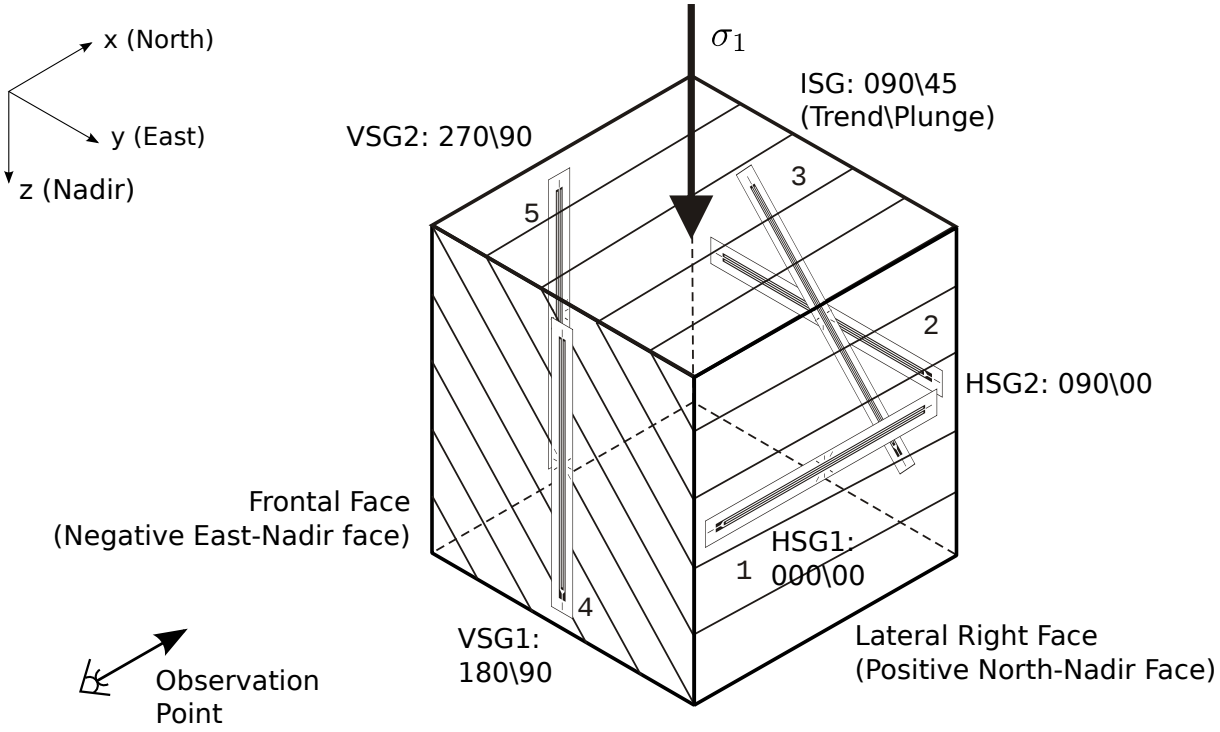

FIGURE 5.6: Strain Gages Disposals at Etched OBCG Samples: *HSG1* refers to Horizontal Strain Gage 1 at channel 1, *HSG2* for Horizontal Strain Gage 2 at channel 2, *ISG* Inclined Strain Gage at channel 3, *VSG1* for Vertical Strain Gage 1 at channel 4, and *VSG2* for Vertical Strain Gage 2 at channel 5.

The data acquisition system used in this research (see: Section 5.6.2.2) retrieves the lectures of the strains in 10^6 times the real strain values (i.e. $\mu m/m$); that means, that in order to have values in strains (dimensional of zero) one should multiply that data by 10^{-6}. The crude data (i.e. without any convertion) are stored in the data base created for this research, see: Section 5.8 and Section B.8.2.

The strain–gages–type used in all these campaigns was a standard–in–shape, simple–unidirectional, and electric–resistance strain gage; coded with the alpha numeric chain PA–06–201BA–120–L, which are distributed and commercialized by the Excel–Sensores company located in São Paulo (Brazil).

Most of the strain gages had a Strain–Factor of 2.15 which belonged to a same set, but there were also strain gages boxes with Strain–Factors of 2.11 and 2.12 that belonged to other sets. This difference was registered carefully in order to take into account during the strain values calculations. Table 5.2 shows the technical specifications of the strain gages used in this experimental campaign, and Table 5.3 shows the details of the quantity of strain gages used from each

set. During the preparation of all samples, 18 strain gages were lost and replaced (i.e. approximately less than 10% of total strain gages needed to instrument all samples). Lost causes were for bad glued or bad oriented strain gages.

TABLE 5.2: Technical Specifications of the Strain Gage PA–06–201BA–120–L used in this Research.

Property	Unit	Value
Resistance	Ω	120
Active Length	mm	51.1
Active Width	mm	2.03
Total Length	mm	53.8
Total Width	mm	2.05

TABLE 5.3: Particular Specifications of the Strain Gages used in this Research.

Set	Strain Factor	Quantity Used*
110603	2.15	125
110516	2.11	77
101125	2.12	25
110325	2.12	6

*Total quantity of strain gages used in this research.

The above mentioned strain–gages–type was designed to be auto–compensated for concrete material and not for crystals. But in the market of strain gages, it is not common to find such types of auto–compensated to any crystal.

The election of the strain–gages–type was mainly governed by its size (i.e. its active length). For the cubic samples trying to represent rock mass behavior, it was necessary to have a strain gage length that covers at least 70% the side of the cubic sample, in order to register the rock mass deformation (i.e. the rock material phases and the discontinuities planes deformations) at the strain gage axial direction. In the case of small strain gages supposed be used, probably only the rock material phase deformation of the rock mass would be registered, and the influence of all discontinuities deformations would be lost.

The strain gages were glued in each sample using a Cyanoacrylate Based Fast–Acting Adhesive, named Super Bonder® of Loctite®, which has been used for at least fifteen years at the Furnas–Electrobrás Laboratory, with very good results when gluing strain gages in rock materials.

The procedure of gluing the strain gages did not go out from the standard one (i.e. surface wiping with Isopropyl alcohol, glue application, pressure application, and resting), and a senior worker of the laboratory was in charge of the supervision of the present researcher work, where he also took part in the process of gluing the majority of the strain gages (i.e. 75% of all of them).

In order to improve the time and repeatability of all the strain gages positions, templates were constructed from an acrylic sheet of 1 mm of thickness. Figure 5.7 shows all the templates used here, but the most used was the template **e**, because it allowed to install the strain gage in any of three possible positions used here.

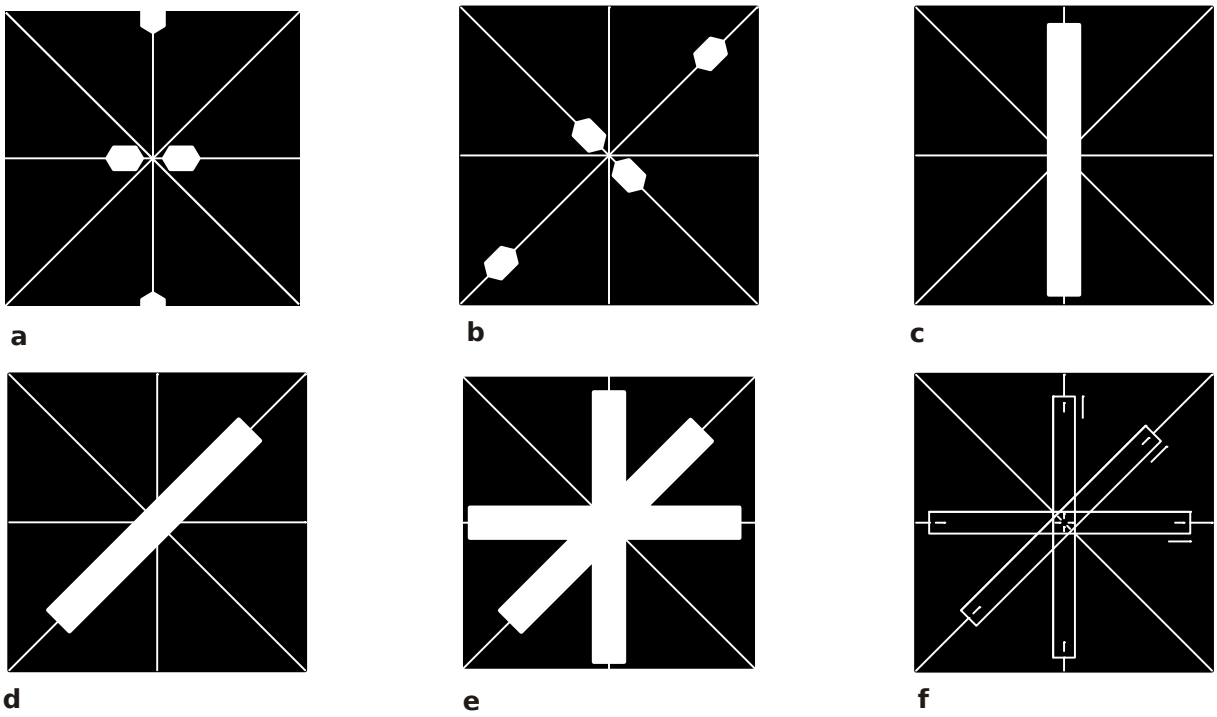

FIGURE 5.7: Strain Gages Templates. Used to: **a** drawing lines for strain gages at 0° and 90°; **b** drawing lines for strain gages at 45°; **c** gluing strain gages at 0° and 90°; **d** gluing strain gages at 45°; **e** gluing strain gages at 0°, 45°, and 90°; **f** for verification after gluing.

A blank OBCG specimen was also prepared in order to serve as a sample with dummy strain gages, which will act as temperature and material compensator. Quantity and positions of the strain gages of this sample were the same as the active strain gages of the testing samples, in order to have for each active strain gage their respective dummy one.

After strain gages were glued in each sample, the wires were connected. For this, 12–pieces Dupont wire color cables (34 AWG) were used, which were welded at terminals with hot tin by an electric soldering iron. It was defined to have one color–pair wires for each strain gage connection, and to maintain constant this pattern for all the samples, in order to permit repeatability with a minor probability of error occurrence. Table 5.4 shows the color pattern used for each strain gage.

TABLE 5.4: Color Pattern for Strain Gages Wires.

Channel	Strain Gage			Wire Color	
	Designation	Position	Location	Wire 1	Wire 2
1	HSG1	Horizontal	Right Face	Green	Blue
2	HSG2	Horizontal	Back Face	White	Black
3	ISG	Inclined 45°	Back Face	Gray	Purple
4	VSG1	Vertical	Frontal Face	Red	Brown
5	VSG2	Vertical	Left Face	Yellow	Orange

Finally, at the end of the two wires each strain gage had, a L–60 male terminal type was installed. Figure 5.8 shows how one sample finally looks like, with all the strain gages, wiring and terminals.

5.6 Sample and Equipment Arrangement

Here will be described shortly how samples and equipments were arranged just before initiate the tests. Also the equipments technical characteristics will be described.

5.6.1 Sample Arrangement

Before any sample testing, the strain gages were tested for the last time for conductivity; this performed with a multimeter. Then, talc powder was put at the two opposite surfaces of the physical models (i.e. crystal etched samples) that will receive the loads (i.e. at the two North–East planes), in order to reduce friction, and do not produce high shear stresses among the loaded and contact surfaces. Immediately after that and adjacent to those two mentioned surfaces, sheet of cork —of 5.5 ± 0.3 mm— were put, and the whole system —composed by sample and cork sheets— were maintained into position with elastic bands.

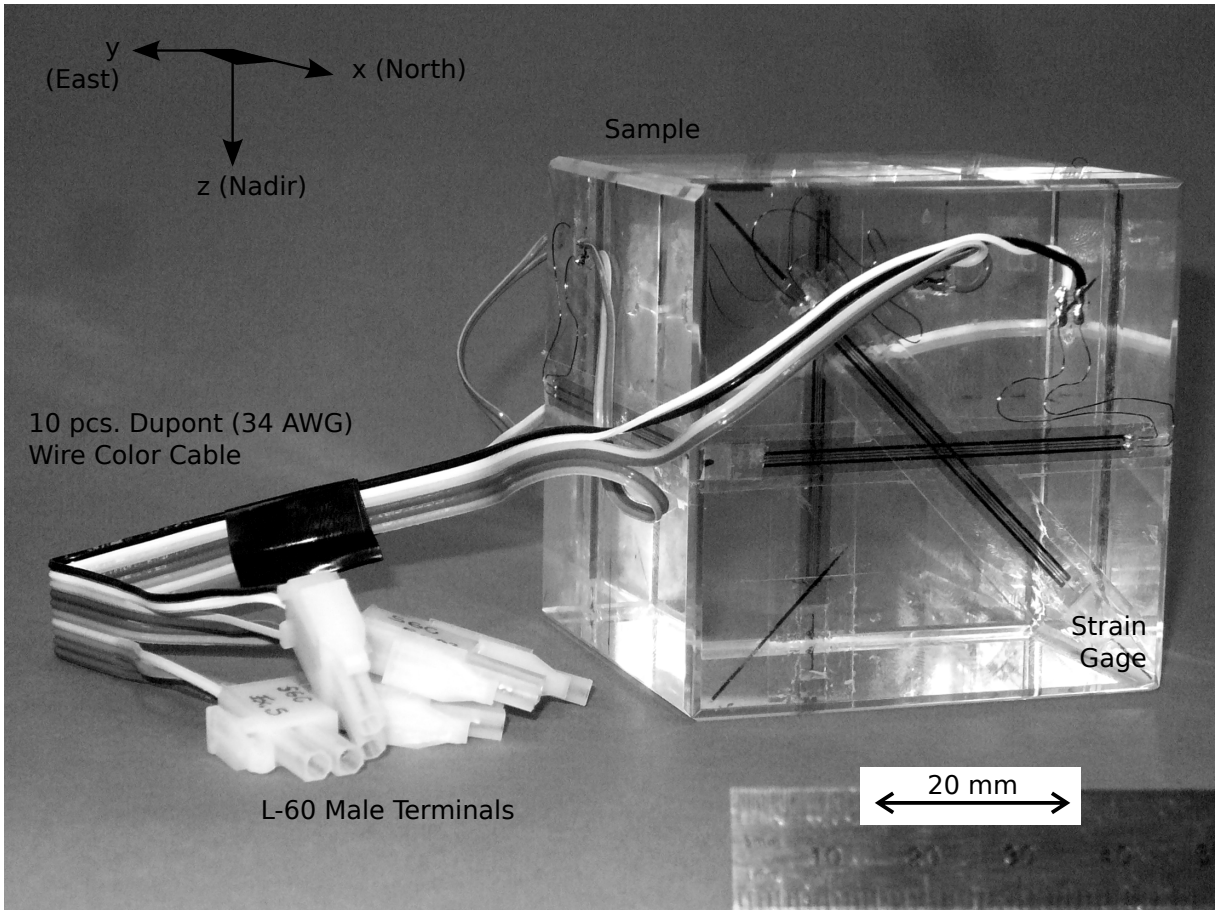

FIGURE 5.8: Typical Etched OBCG Sample Configuration with Strain Gages, Wiring, and Terminals.

After preparing all the equipment arrangement, as will be explained in the following section of this document, the elastic bands that hold the sample–system were cut. The inferior surface of the cork that covered the inferior sample surface was put over a rigid cylindrical steel platen of 156 mm diameter and 50 mm of height; and also over the superior cork, another similar rigid platen was put (Figure 5.9). Then, this new sample–system was installed inside the test system (i.e. the system used to tests under the equipment arrangement described here further), making coincidence of their vertical axis with the corresponding axial axis of the load cell and the axial hydraulic jack.

Finally, this axial hydraulic jack —located at the superior beam of the press frame— was activated manually in order to made possible the establishment of a small contact between the superior steel platen and a hinged rigid loading platen installed over this. In the case of some misaligned between both surfaces could be present, this last platen facilitated a good contact between the closest–to–the–sample–system loading platen, and therefore with the specimen.

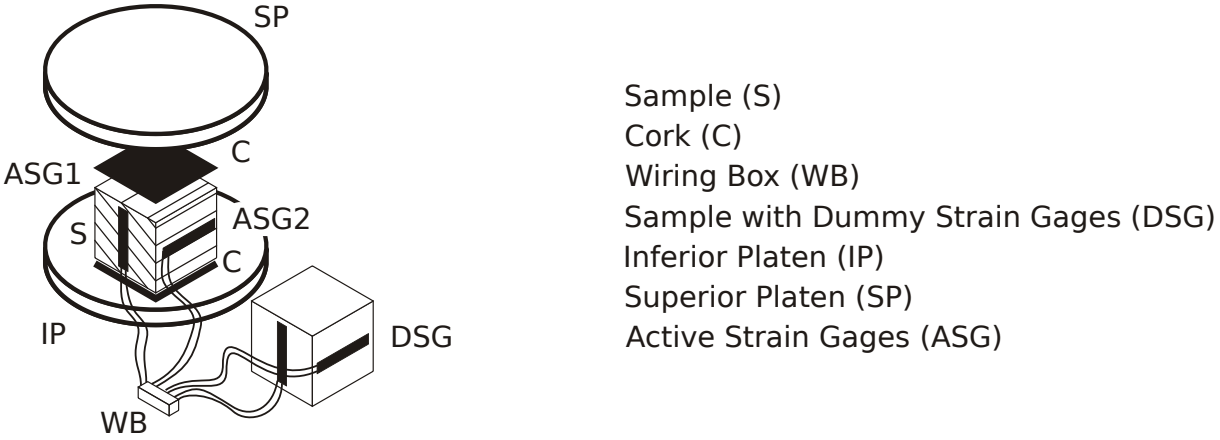

FIGURE 5.9: Sample–System Arrangement.

Above the hinged rigid loading platen, a load cell was installed. This cell had an extension steel solid cylinder that was in contact with the reaction beam of the frame. This arrangement maintained the sample–system ready to test.

5.6.2 Equipment Arrangement

As described in the above section, the samples so described were ready for testing, but before going further with this, here it will be described the equipments involved to: apply the axial force; read that axial force and the strain measurements; and the equipment to centralize all these mentioned readings.

5.6.2.1 Equipment used to apply and read axial force

The frame used here was a rectangular frame composed by I type steel sections (the I section had approximately 0.37 m height and also 0.37 m width). The global approximate dimensions of this frame are 3 m length and 2.3 m height. The rigidity of the frame was not possible to establish.

The loading device was composed by an axial cylindrical hydraulic jack located at the inferior side of the frame roof, capable to apply a maximum nominal compressive axial vertical force of 13.3 kN (Furnas Serial Number: 354 4 15912). The last calibration of the loading device was on August 20, 2011 and it is being calibrated every year.

The loading device was powered by one hydraulic manual pump (Furnas Serial Number: 354 4 15917).

The load measurements were attained with a load cell of also 13.3 kN of nominal capacity (Furnas Serial Number: 355 0 16370), which was calibrated on January, 12 2012 and is calibrated every two years.

The loading device was controlled manually by the operator in order to attain the desired force rates. This was possible by looking to the computer monitor which shown in real–time the force values the loading device had in each force increment.

All of the above mentioned equipments for applying the force, reading the axial force, as also to control the loading velocity conform the testing system apparatus. The whole system occupies a total area of 1.5 m^2 and was located outside the main building of the laboratory, in a space covered with a zinc alloy roof with no walls; and can be operated by a single but experienced technician. In order to protect the technician during the tests —on an eventual situation a spalling phenomenon of a sample will present— temporally walls of a thick plastic were installed by hinging them from the mentioned zinc alloy roof. Figure 5.10 shows the test system used here.

5.6.2.2 Equipment used to read strains

A data logger was used for reading the measured strains. This was built by the Vishay–Measurement Group, located at North Carolina (USA). The model was a 6000 Scanner of 20 channels, with a strain–gages–card Model 6010.

The lectures for the five strain gages and the axial force where registered simultaneously and time synchronized, from the beginning up to the final of each test. The data logger unit was connected to a desk computer trough a data acquisition card installed in, and readings were obtained every 1 s. Active and dummy strain gages were installed at the system ports, whose circuit are described in Figure 5.11.

The program used to re–direct the data from the system to the computer was the Strain Smart® data systems software, Version 4.31 (Built 993, Year 2008) of Vishay Micro–Measurements. After all data of all tests were stored in the computer, the data for each test were exported to an Excel–file (XLS) and later to the POSTGRESQL® data base manager used in this research.

FIGURE 5.10: General View of Test System, i.e. frame, load cell, hydraulic jack, extensions.

5.6.3 Whole Experimental Arrangement

The above mentioned equipment and samples–system were arranged as follows:

- the sample–system arrangement was put inside the frame;
- all L–60 active and dummy strain gages terminals where connected to a wiring box, and from them to the independent Vishay data logger unit;
- the load cell was connected also to the independent Vishay data logger unit;
- the Vishay data logger unit was connected to the personal computer;

Load incremental rate was controlled visually by observing the load readings in the computer display, and strains and load readings were obtained with the Vishay data logger unit. This arrangement are shown in Figure 5.12.

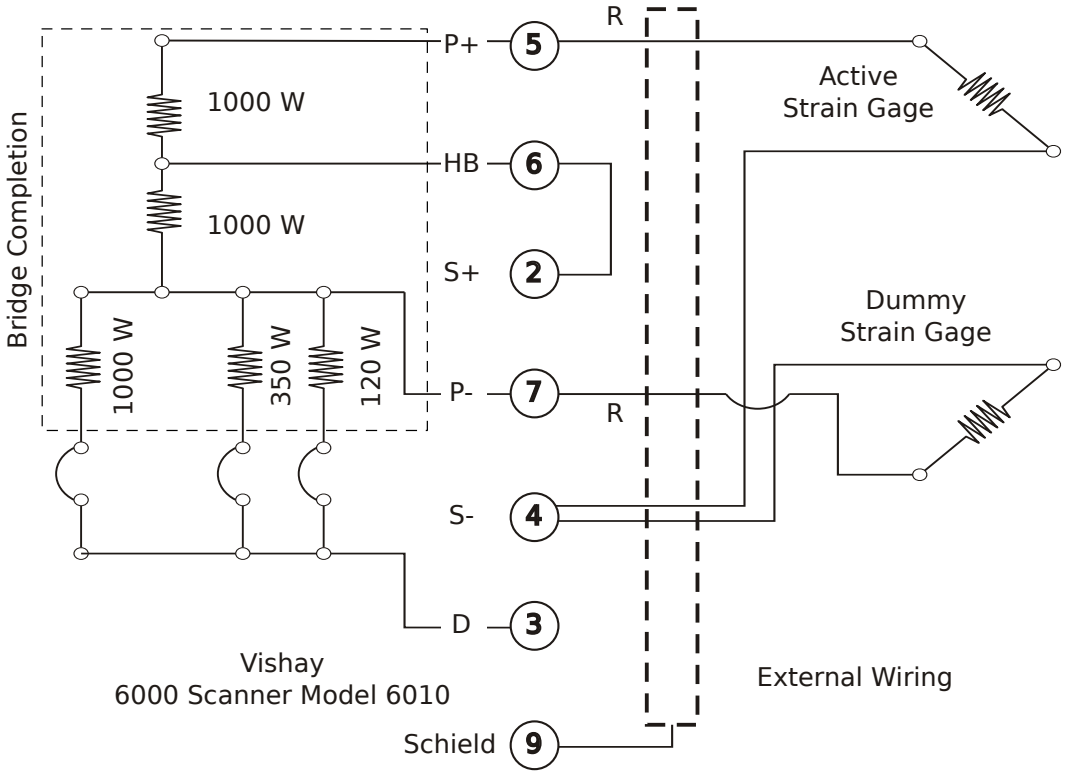

FIGURE 5.11: Half Bridge for Separate Strain Gages Circuit Scheme, Vishay (2008).

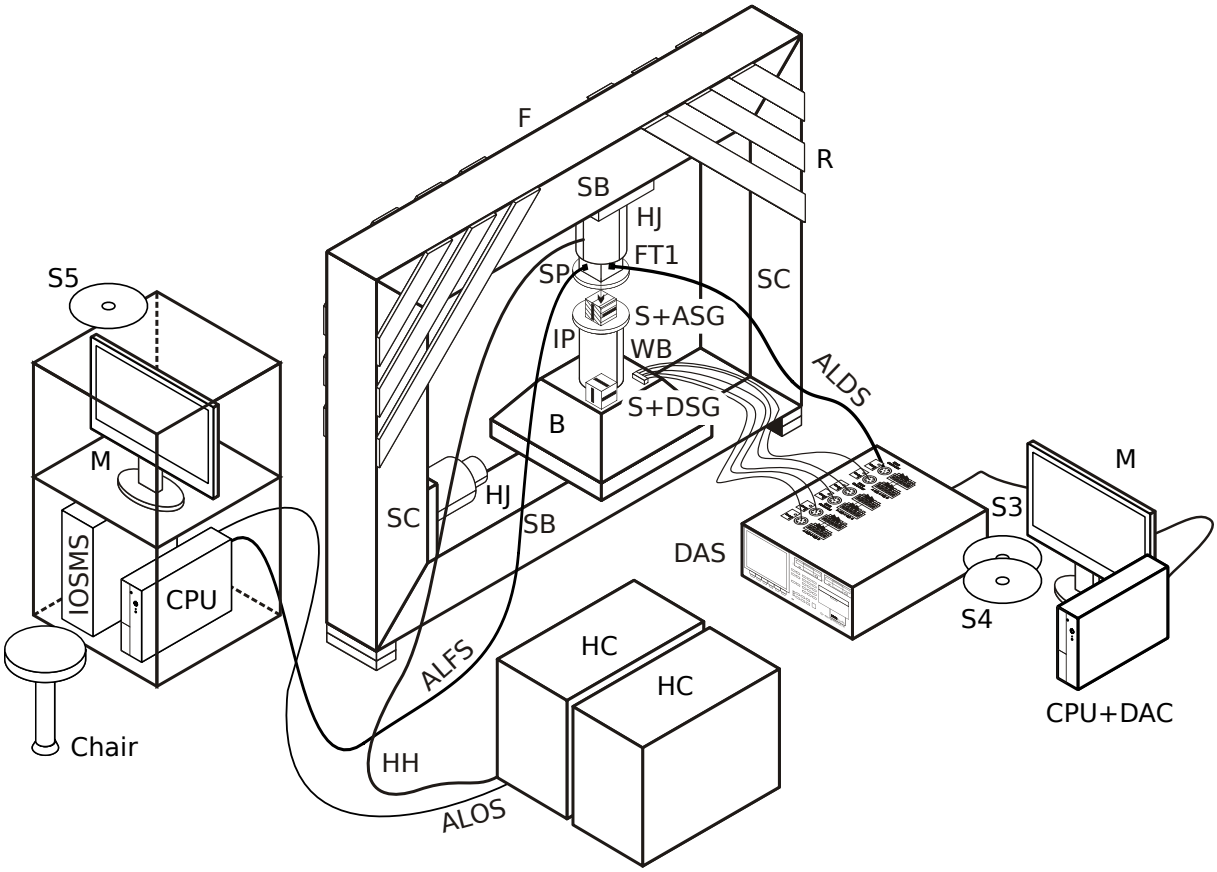

FIGURE 5.12: Scheme of the Experiment Arrangement. *ALDS* Axial Load Data Signal; *ALFS* Axial Load Feedback Signal; *ALOS* Axial Load Output Signal; *ASG* Active Strain Gage(s); *B* Steel Base; *CPU* Central Processing Unit; *DAC* Data Acquisition Card; *DAS* Data Acquisition System (input channels: channel 1 for Horizontal Strain Gage 1 *HSG1*, channel 2 for Horizontal Strain Gage 2 *HSG2*, channel 3 for Inclined Strain Gage *ISG*, channel 4 for Vertical Strain Gage 1 *VSG1*, channel 5 for Vertical Strain Gage 2 *VSG2*, and channel 6 for Force # 1 Transducer *FT1*); *DSG* Dummy Strain Gage(s); *F* Frame; *FT* Force Transducer; *FT1* Force Transducer #1 Signal; *HC* Hydraulic Compressors, Servo Controls, and Intensifiers; *HH* Hydraulic Hose; *HJ* Servo–Controlled Hydraulic jack for Axial Vertical Force; *HSG* Horizontal Strain Gage; *IOSMS* Input & Output Data Management System; *IP* Inferior Platen; *ISG* Inclined Strain Gage; *M* Monitor; *R* Steel Reinforcement plates (thickness 3/4", width 5"); *S* Sample; *S3* Software 3 about Data Retrieving; *S4* Software 4 about 3D–OSPM; *S5* Software 5 about Servo Controlled System; *SB* Steel Beam (section H type of 14"); *SC* Steel Column (section H type of 14"); *SP* Superior Platen; *VSG* Vertical Strain Gage; *WB* Wiring Box.

5.7 Etched Discontinuities Samples Testing

Physical models of rock mass with discontinuities —the etched discontinuities samples (ED), (i.e. samples with arranged notches) — were tested at the Rock Mechanics Laboratory Ludgero Pimenta Ávila of the Electrobrás–Furnas S.A. enterprise at the DCT.T located in Aparecida de Goiânia, state of Goiás in Brazil. Because this laboratory follows ISO standards, tests were performed by the qualified personnel of the same laboratory. Therefore, the researcher of this thesis do not participate directly in the tests execution.

The material properties maintained constant in all the physical models were:

- shape of the sample (i.e. cubic of gross side of 70 mm, mean 68.6 mm);
- type of material (i.e. engraved OBCG);
- porosity of material (i.e. non–porous);
- shape and extension of discontinuities (i.e total persistent);
- discontinuities spacing, width and roughness.

Detailed dimensions of the tested ED samples are shown in Table 5.5.

TABLE 5.5: Measured Dimensions of ED Samples.

Sample	Direction / β_{sd} in °	Average Length in mm			t_s	w_d
		North	East	Nadir	in ms	in g
000DA	0	68.84	69.14	68.66	12.5	818.33
000DB		68.82	68.67	68.41	12.5	810.48
000DC		68.67	68.60	69.03	12.5	814.78
030DA	30	68.71	69.01	69.10	12.5	820.02
030DB		68.49	68.57	68.02	12.5	797.02
030DC		67.82	67.77	68.21	12.5	792.01
045DB	45	68.35	68.51	68.58	12.5	806.69
045DC		68.01	68.89	68.99	12.5	809.00
060DA	60	68.34	68.25	68.24	12.5	799.71
060DB		68.13	68.96	68.33	12.5	806.75
060DC		69.32	68.72	68.72	12.5	820.31
090DA	90	68.30	68.62	69.60	12.5	818.16
090DB		69.32	68.79	68.97	12.5	825.21
090DC		68.23	68.04	68.28	12.5	793.78

The mayor appreciation observed in the geometrical shape of samples was the external surface irregularities they had. It was observed that the load surfaces of samples had irregularities major than 20 µm. For that reason, it was decided to use the thick cork between the two sample surfaces and the two load platens (i.e. inferior and superior load steel platens), as explained in Section 5.6.

Constant environment conditions during tests were:

- humidity (i.e. dry state);
- temperature (i.e. ambient temperature from 15 °C to 25 °C);
- pore–pressure conditions (i.e null pore–pressure);
- compliance of the test frame (the exception of this was sample SGA).

The variable parameter on the samples was the discontinuity inclination in relation with the axial load (i.e. β_{sd} angle). For each configuration —among the five defined in Section 5.3 and shown in Figure 5.2— three uniaxial compressive strength tests were performed. Therefore, a total of fifteen specimen tests were waited to have, but one of those was rejected before testing (i.e. sample 045DA) due to bad etching process, as mentioned in the last section of Section 5.4.2. So, a total of fourteen engraved OBCG cubes samples were finally tested under uniaxial stress until its rupture, in order to simulate the influence of the discontinuities in the strength of the material.

All tests have been carried out in axial force control, whose rate was controlled visually. Therefore, an exact stress rate value for all samples was not possible to obtain, and certain differences in this velocity were reported. The following table (Table 5.6) shows the stress rate each sample was submitted during testing. The median value of stress rate for all samples was therefore of 0.62 MPa s^{-1}, while mean rate was of 0.64 MPa s^{-1}, and standard deviation of 0.27 MPa s^{-1}. Strain measurements were read every 1 s.

Figure 5.13 shows the condition of the frontal face of sample 030DB immediately previous and posterior to its testing. One can also observe the sample arrangement as described in Section 5.6.1.

TABLE 5.6: Stress Application Rates during ED Samples Testing.

Sample Group	β_{sd} in °	t_σ in MPa s^{-1}		
		A	B	C
000D	0	0.34	0.62	1.05
030D	30	0.23	0.78	0.36
045D	45	—*	0.51	1.00
060D	60	0.50	0.62	0.68
090D	90	0.43	0.82	1.07

Note. t_σ is stress application rate.

*The sample 045DA was not etched, even it had the corresponding label, which should be correspond to a sample with discontinuities engraved with a dip angle of 45°. Because this sample had been not etched, it was converted to a new blank sample named SGD as shown in Table 4.7.

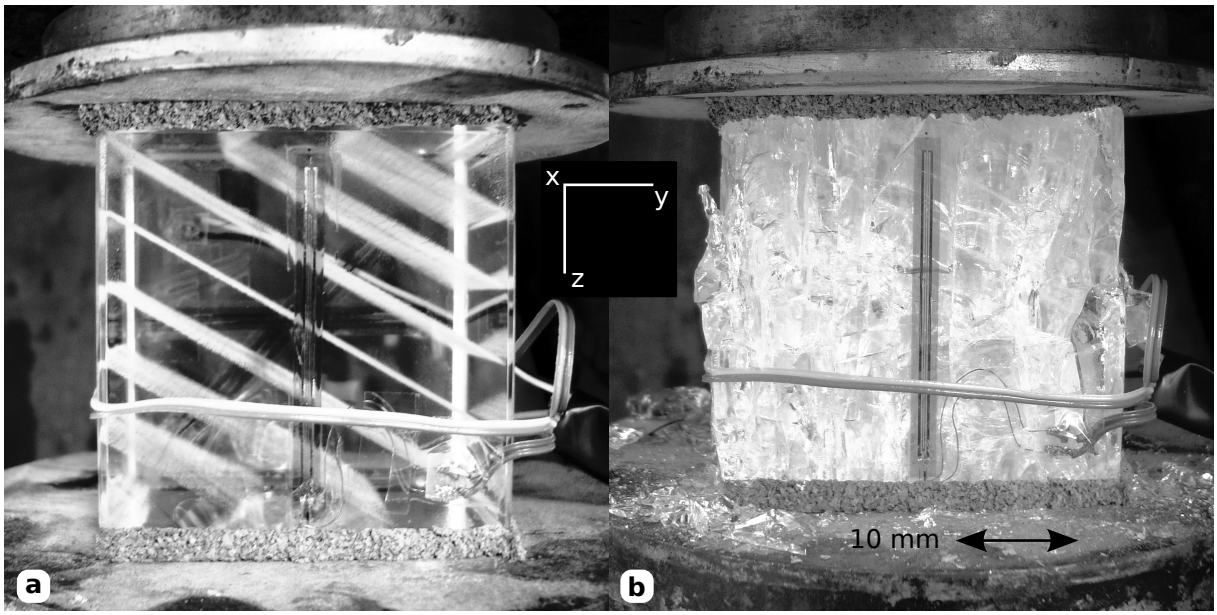

FIGURE 5.13: Condition of the Frontal Face of 030DB Sample. **a** Before testing; **b** after testing.

Some common experiences where encountered during these samples testing. First, most of the samples exposes an intense bursting sound when fail. For example the sound was so high, that when the first sample failed, all the personnel of the building went afraid to the testing room asking if all things were going well. After this experience, when each sample was near to fail, the personnel should be informed about the coming burst sound. The second thing important to say is that most of the samples destroyed completely (Figure 5.14a), without given the possibility to analyze some rupture or failure characteristic. In the first test —because the bursting of the sample— all the resulting small particles thrown away in the room, making a dirt

in it. In order to avoid this, the frame was covered with plastic, in order to retain —in a small place— all the small glass particles each sample thrown away after they reach their maximum strength.

In some samples, cracking audible sounds were possible to hear when they were loaded. These crack sounds were short but strong.

After failure, in some samples were observed that some glass particles encrusted the cork sheets put between the sample and the two steel platens (Figure 5.14a); while in other samples the disintegration was present (Figure 5.14b).

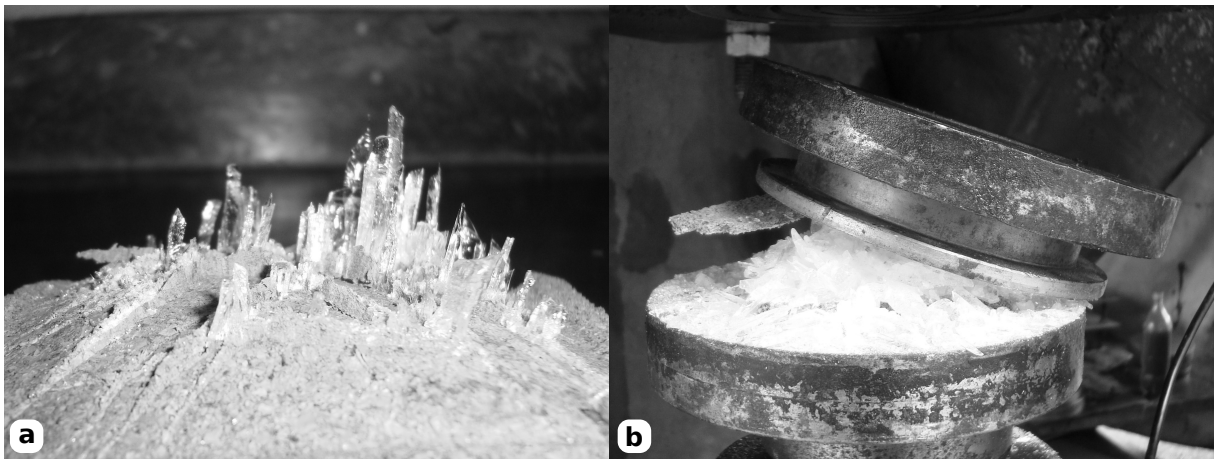

FIGURE 5.14: Special Sample Conditions after Testing. **a** Glass particles encrusted the cork sheet; **b** total sample disintegration.

5.8 Gross Data Processing and Results

Interpretation for these tests suggested use an interesting data management approach by using software, even though this research did not generate huge quantities of data. Here, this approach is described shortly, but one can consult a more detailed explanation in Appendix B and in Appendix C of this document.

The general approach suggests the use of specialized software for data storage and consulting (i.e. POSTGRESQL® 8.4.9 open source software) and another software for data calculations (i.e. MATLAB® 7.10.0.499 commercial software), both connected by hosts via Ethernet. This made possible store all input and output data in a same environment, and avoided same data to be duplicated and incurring in errors when manipulating them.

Most of the data exposed in tables were queried using Structured Query Language (SQL) in POSTGRESQL® . Also, calculations were programmed in MATLAB® by using a Procedural Programming (PP) approach or an Object Oriented Programming (OOP) approach, this last which possibilities controllable data calculations. In the complementary electronic material of this research, one will find two programs performed under the PP approach; while in Section C.3, one may find —as an example— the code of how index–properties of the actual tested samples were calculated with the OOP approach.

Table 5.7 shows the final results of index properties obtained for the tested samples. One can observe that unit weight of these sample can be mainly around 24.6 kN m^{-3}, and that the mean sound propagation velocity ($\widehat{v}_{sd,ED}$) and its standard deviation ($s_{v_{sd,ED}}$) are 5 492.2 m s^{-1} and 35.3 m s^{-1}, respectively.

TABLE 5.7: Geometrical and Index Properties of ED Samples.

Sample	β_{sd} in °	V in m^3	A_{ne} in m^2	$\gamma_{d,ED}$ in kN m^{-3}	$v_{sd,ED}$ in m s^{-1}
000DA		0.00033	0.0048	24.6	5493
000DB	0	0.00032	0.0047	24.6	5473
000DC		0.00033	0.0047	24.6	5522
030DA		0.00033	0.0047	24.6	5528
030DB	30	0.00032	0.0047	24.5	5442
030DC		0.00031	0.0046	24.8	5457
045DB	45	0.00032	0.0047	24.6	5486
045DC		0.00032	0.0047	24.6	5519
060DA		0.00032	0.0047	24.6	5459
060DB	60	0.00032	0.0047	24.7	5466
060DC		0.00033	0.0048	24.6	5498
090DA		0.00033	0.0047	24.6	5568
090DB	90	0.00033	0.0048	24.6	5518
090DC		0.00032	0.0046	24.6	5462

ED samples might be different in properties than samples without any notch (i.e. blank samples). Therefore, with the calculated sound velocity propagation through the nadir–dimension, a variance analysis was performed —also called significance analysis or randomness analysis.

During this analysis, it was wanted to investigate if the presence of notches in OBCG modify the sound propagation velocity —by decrementing or incrementing— when comparing with the corresponding sound propagation velocity of the same OBCG without any notch. That

meant, that the null hypothesis (H_o) was: "there is no change in sound propagation velocity even though notches are present". The alternative hypothesis (H_1) said: "there is a change in sound propagation velocity when notches are present".

Using the mean and the standard deviation of the measured sound propagation velocity of blank samples tested in Section 4.1.5.2, assuming they were representative of the population (i.e. $\mu_o \approx \widehat{v}_{\mathrm{sd},OBCG}$ and $\sigma \approx s_{v_{\mathrm{sd},OBCG}}$), and adopting the t–student bilateral distribution, it was possible to reject H_o with a confidence (C) of 97.3%.

That means, that it is very probable that the presence of notches within OBCG varies the sound propagation velocity. And, because this index property in certain manner is related directly with the uniaxial compressive strength, it could be possible also that the presence of notches within OBCG varies also this value; even more, because $\widehat{v}_{\mathrm{sd},ED}$ is greater than $\widehat{v}_{\mathrm{sd},OBCG}$, it appears to be that uniaxial compressive strength of ED is greater than blank OBCG samples, situation that is contrary to the expected behavior (i.e. ED presence drop global resistance in the rock mass). With this first finding, one questions: Does the notches–set create a weak discontinuity plane? —This will tried to be answered in the following sections and chapters.

In respect to the uniaxial compressive strength results, initially one attempted to use all the data readings, but during this gross data interpretation, it was observed that by plotting the large data set of each test (around hundreds of reading instances), the axial stress *vs.* axial strain relation —for example— was obscured by their own existing pattern.

For this reason, a data cutting procedure was applied, which consisted in using only a subset of all the collected data. There are at least three data cutting methods, in all of them it is important to define an integer value m less than the number of the total data obtained n, or a cutting factor defined as m/n. The three known cutting methods are the following:

- method by a random selection;
- method by considering those data that falls in a defined index interval;
- method by considering those data that falls in a defined variable interval.

For this research tests, data was cut by the variable interval method with a Data Cutting Factor (f_r) of 0.3. After this data cutting procedure, a data smoothing procedure was performed by the use of the Locally Weigthed Scatterplot Smoothing (LOWESS) method (with a span value of 0.25), which finally permitted obtain the searched uniaxial compressive strength values for each tested specimens, and the plots of axial stress (σ_a) *vs.* strains (ε). The chosen value of UCS

was the maximum mathematical value of stresses obtained from the cut–smooth axial stress *vs.* strain–5 curve. Table 5.8 shows the final calculated and adopted data.

TABLE 5.8: Ultimate Uniaxial Compressive Strength of ED Samples.

Sample Group	β_{sd} in °	$\sigma_{cm,ED}$ in MPa		
		A	B	C
000D	0	121.0	177.8	159.8
030D	30	146.3	172.1	147.3
045D	45	—*	221.6	175.0
060D	60	158.6	172.2	170.5
090D	90	100.4	215.2	107.0

*See footnote of Table 5.6.

In order to compare the uniaxial compressive strength data with the tested blank samples shown in Table 4.7, a variance analysis was also performed, similar to that analysis performed above for the case of sound propagation velocities. This analysis was used to determine whether or not the averages of uniaxial compressive strength of ED samples differs from blank samples significantly.

Being rigorous with this test method, the samples sizes (samples as being statistical samples, and sizes as being number of values) must be equal, as must variance; but there are other t–tests available for the case for unequal sample sizes: one with assumed equal variance in the two sample groups, and other with assumed unequal variance for both. In this analysis, unequal samples sizes but equal sample variances were assumed.

Therefore, if null hypothesis (H_o) is true, then the two samples are not significant different in relation to their uniaxial compressive strength. It was assumed that $\widehat{\sigma}_{c,OBCG}$ is equal to 121.7 MPa and $s_{\sigma_{c,OBCG}}$ equal to 36.84 MPa, for $n = 2$ (see Section 4.1.5.3).

If all results of uniaxial compressive strength at samples with ED are assumed to be the same statistical sample set, one found that the mean uniaxial compressive strength of that samples is equal to 160.3 MPa, the standard deviation equal to 35.10 MPa, and median value of 165.1 MPa. By doing the variance analysis, it was encountered —with a 83.1% of confidence— that notches affects uniaxial compressive strength. Even more, that uniaxial compressive strength of ED samples is greater than the corresponding for blank samples (i.e. OBCG samples); which verifies the anticipated conclusion obtained from the sound propagation velocities variance analysis in the above paragraphs. Again here, one questions if notches–set creates a plane of weakness or a stronger plane.

Now, if all results of uniaxial compressive strength at samples of only the same β_{sd} angle is considered, the maximum possible confidence value to reject null hypothesis varies within the sample sets, as shown in Table 5.9.

TABLE 5.9: Particular Variance Analysis for UCS of ED Samples.

Sample Set	β_{sd} in °	C_{max} in %
000D	0	63.7
030D	30	77.0
045D	45	84.0
060D	60	89.0
090D	90	26.3

Note. C_{max} is the maximum confidence value to reject null hypothesis.

Here it is observed that —for samples sets 000D and 090D— the confidence values are low. This might reflect that for these inclinations, the uniaxial compressive strength of ED samples do not differ significantly with the corresponding value of blank samples. But this situation is favorable to the analytical model —assumed for this tests validation (i.e. the Jaeger model)— because in this model it is assumed that these two values for discontinuities with β_{sd} angles of 0° and 90° should be equal to the corresponding samples without discontinuities (see Section 2.1.6).

Now ignoring the samples set 000D and 090D, it was performed another variance analysis within the UCS values; and it was found —with a 70.9% of confidence— that these samples are significant different —and significant greater— than the corresponding values of blank samples.

Here was also calculated the tangential vertical deformation modulus of the strain gage number five in respect the axial force ($E_{t,50\%,ED,5}$), and the strain ratio of strain gage five in respect to strain gage one ($\nu_{ED,5-1}$) (i.e. a vertical to horizontal strains ratio); see Table 5.10] and Table 5.11). These two ratios does not explain anything, because —in the case deformations are possible to observe within this physical models— they are a case of transverse–isotropic material rather than an isotropic material; but here was exposed in order to observe some similarity or not with the same variables obtained at the blank samples (i.e. $E_{t,50\%,OBCG}$ and ν_{OBCG}, of Table 4.9), this last being an isotropic material.

Data for those two variables exposed in Table 5.10 and Table 5.11 reveals a high disperse in values. Median value of $E_{t,50\%,ED,5}$ is 91.8 GPa, and median value of $\nu_{ED,5-1}$ is 0.38.

Variance analysis shows that samples does not differ significantly in respect to the values of

TABLE 5.10: Vertical Deformation Modulus of ED Samples.

Sample Group	β_{sd} in °	$E_{t,50\%,ED,5}$ in GPa		
		A	B	C
000D	0	75.3	82.7	107.5
030D	30	117.6	96.0	109.8
045D	45	—*	78.6	101.2
060D	60	87.6	71.9	110.8
090D	90	60.5	77.1	96.3

*See footnote of Table 5.6.

TABLE 5.11: Strain Ratio of ED Samples.

Sample Group	β_{sd} in °	$\nu_{ED,5-1}$		
		A	B	C
000D	0	0.27	0.33	0.48
030D	30	0.67	0.40	0.57
045D	45	—*	0.30	0.48
060D	60	0.38	0.24	0.56
090D	90	0.19	0.28	0.39

*See footnote of Table 5.6.

$E_{t,50\%,ED,5}$ and $E_{t,50\%,OBCG}$, which allows conclude that notches etched on OBCG do not modify deformation properties. Same is concluded by doing the same variance analysis of same samples in respect the values of $\nu_{ED,5-1}$ and ν_{OBCG}.

5.9 Final Comments

The general methodology of this experimental campaign consisted essentially on the three WPs described in Section 5.1, which consisted in construction, preparation, and testing of the physical models (i.e. samples).

The novelties of this process could be resumed in:

- the computational program creation in order to define the discontinuity network;
- the ability to create physical model samples with the SLLE technique, as anticipated in the precedent chapters;
- the samples instrumentation for deformations and axial force;

- the data processing technique by using a powerful Data Base Manager, as is POSTGRESQL® with the program language MATLAB® .

Results that were found in the initial gross data processing and that are of interest for this research are resumed as follows:

- the presence of notches in the OBCG modify the sound propagation velocity of material;
- the presence of notches in the OBCG modify the uniaxial compressive strength;
- the presence of notches in the OBCG increment sound propagation velocity and uniaxial compressive strength of material;
- the presence of notches in the OBCG do not modify the deformation properties of material.

The influence of the inclination of ED in uniaxial compressive strength will be validated and discussed in the following chapter (i.e. Chapter 6).

Chapter 6

Model Validation

In order to accept or reject the main hypothesis, it is necessary to validate the results obtained in the previous physical modeling campaign, presented in detail in the last chapter of this document. This validation will be made in the light of an analytical model, because any analytical models is robust and reliable for their particular case and condition for what it was proposed.

6.1 Comparison of Tests Results with an Analytical Model

As was announced above and in the previous chapter: the test results of samples with etched–discontinuities (ED samples) will be compared with the analytical model of Jaeger. Please refer to Section 2.1.1 of this document, or to the original reference Jaeger (1969) for more details about this model.

In order to attain the calculations, again MATLAB® functions —this time under a procedural approach— were developed, which in conjunction was named: OBCG SSLE Physical Model program (i.e. 3D–OSPM program). The source codes of these functions are included in the complementary electronic material DVD that is enclosed in this research document.

This group of codes allow the user to introduce the data results of the tests as a text array having two columns and n rows (i.e. a $n \times 2$ array), in which the first column describes the β_{sd} angle in sexagesimal grades, and the second column describes the tested uniaxial compressive strengths in mega pascals.

In principle, it is assumed that all results are well to fit the Jaeger model, therefore all the fourteen uniaxial compressive strengths of Table 5.8 are used in the program as inputs in order to fit into the Jaeger expression, and to obtain the correlation coefficient (R^2) and the degree–of–freedom values (DoF) as outputs, among other useful information.

But later, the program supposes that perhaps at least one of the tested values is bad for any reason (e.g. bad tested, errors during lectures, un–common behavior of samples etc.). Therefore, the program in their second attempt to fit the tested values, avoids consider one input value. In their third attempt, the program restores the previous avoided value, but avoids another different, and so on until all possible combinations will be considered.

After all combinations of missing one value was finished, the program assumes that perhaps not only one data could be wrong, instead two. Therefore, it makes all the combinations of data avoiding an unrepeatable pair of values. And so, the program makes a similar calculation of fitting values to the Jaeger model, by finding all the combinations of data by avoiding not only one or two values at a time, but also a group of three, four, five, ..., and eleven values.

As said above, parallel to the calculation of the R^2 value of each iteration, the program calculated also the DoF each combination had. Therefore, the chosen combination of data assumed to be best representative should be the closest–to–one R^2 of the greatest DoF value.

Under this procedure, and for the fourteen tested data of this research, the 3D–OSPM program made 7 203 different fitting calculations (by combining all possible data), and after that he ordered in descendent form the R^2 output value from the most near–to–one value, but for each degree–of–freedom set. In a good behavior, the major value of R^2 should be present for the greatest degree–of–freedom value, and converge of this value should be observed as DoF increments.

In the data set here analyzed, for the greatest degree–of–freedom (i.e. $DoF = 6$, means that all data are assumed in the calculation), the resulting R^2 value gave a value of 0.181 5. This means a bad fit. Figure 6.1 shows the resulting analytical plot and with circles the tested data.

By plotting with white circles all DoF–R^2 pairs in abscissas and ordinates, respectively; and with a continuous line the greatest positive values of R^2 and with segmented line the greatest negative values for each degree–of–freedom —for this test data set— it was observed that the major positive R^2 value was of 0.546 7 for a $DoF = 4$, and the major negative R^2 value was for a $DoF = 2$. The plot in Figure 6.2 shows this situation.

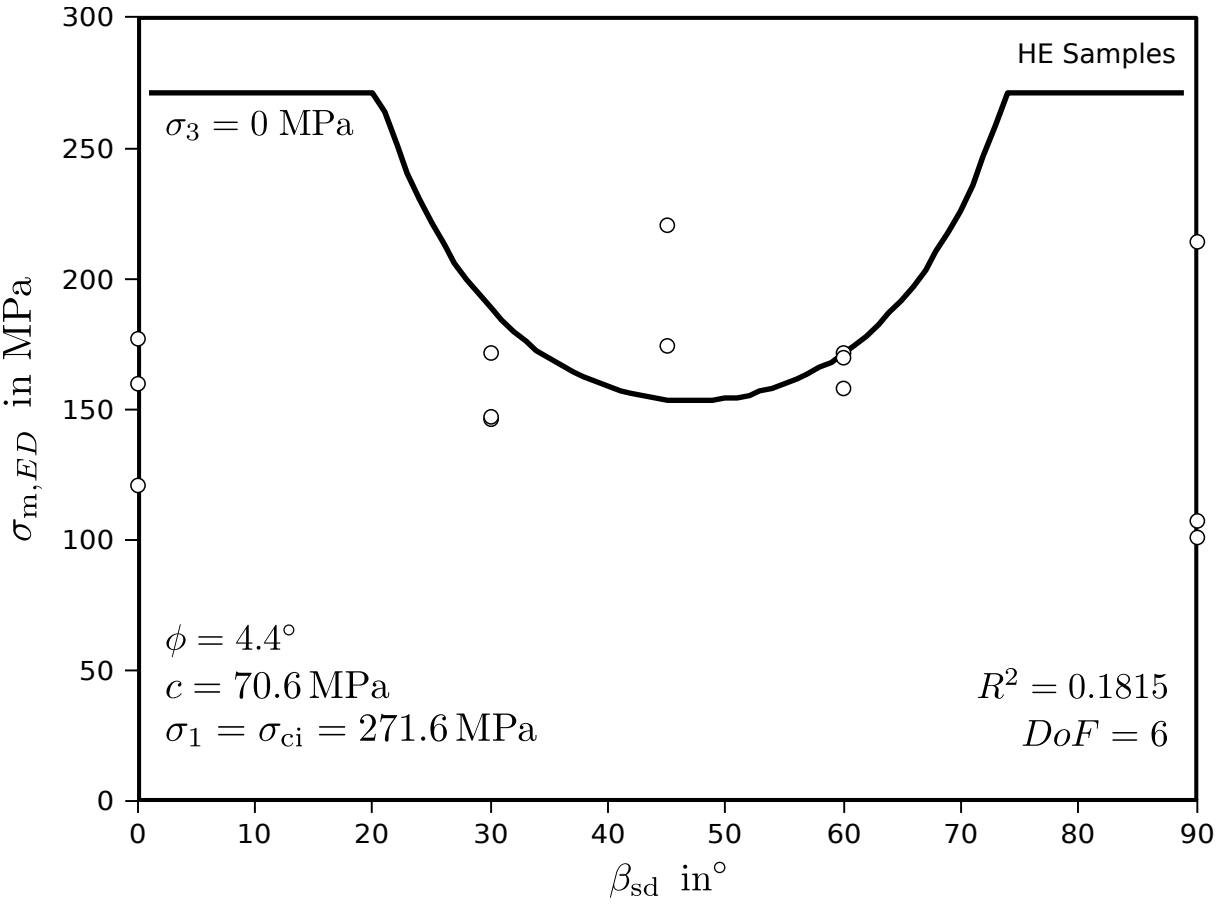

FIGURE 6.1: Jaeger Model Plot of the Tested ED samples, $DoF = 6$.

In order to discern a possible cause of the low value of the positive R^2 value, the data combination that gives this major value was analyzed (i.e. combination # 249). Therefore, the program reported that the data combination do not include the values of the following three samples: 030DA, 030DC, and 045DB among the data shown in Table 5.8.

By rejecting these three values a new R^2 was obtained, with a value of 0.5467. Even tough the R^2 value was improved by rejecting those three sample results in the fit calculation, the resulting found value is being still low. Figure 6.3 shows the new scenario of the Jaeger model plot of ED samples, when it is avoided the results of samples: 030DA, 030DC and 045DB.

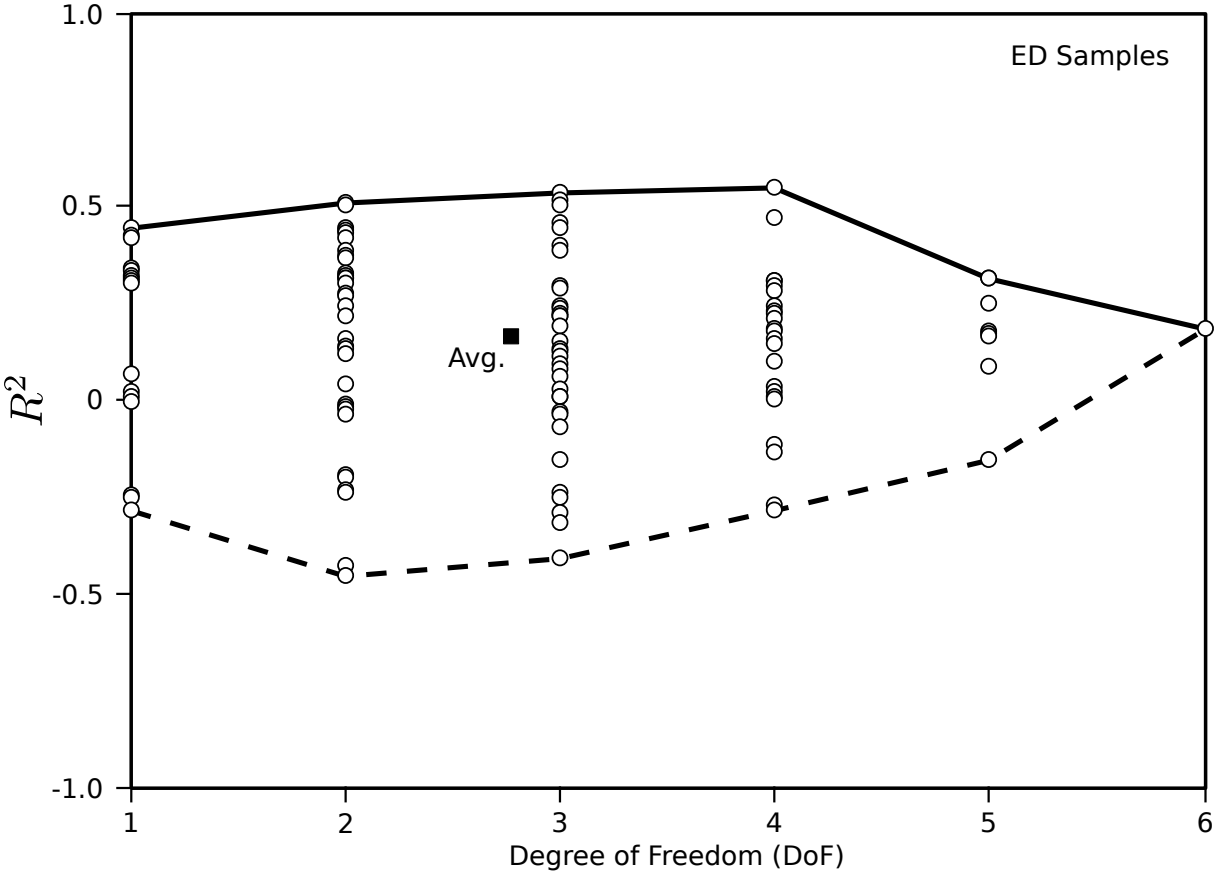

FIGURE 6.2: *DoF vs.* R^2 Plot of the Physical Modeling Results Fit–Procedure on ED Samples.

6.2 Discussion

As could be observed in Figure 6.1, physical model results are not near to a good fit. This is evident by the low value of the R^2 coefficient for *DoF* equal to six (i.e. 0.1815). Inspection on results of samples 030DA, 030DC and 045DB was performed after knowing the possible source of error. Even though the program routine suggests to avoid data values of samples 030DA, 030DC and 045DB to increment R^2 from 0.1815 to 0.5467; there was not found any reason to discard those values.

The first idea it comes to mind, is to repeat the tests with more groups of specimens for different β_{sd} angles and at a shorter interval (e.g. β_{sd} angles from 0° to 90° in a 5° interval), and to test more specimens for each group (e.g. five or seven specimens per group); in order to find a convergence in the plot *DoF vs.* R^2 and a prevailing positive correlation.

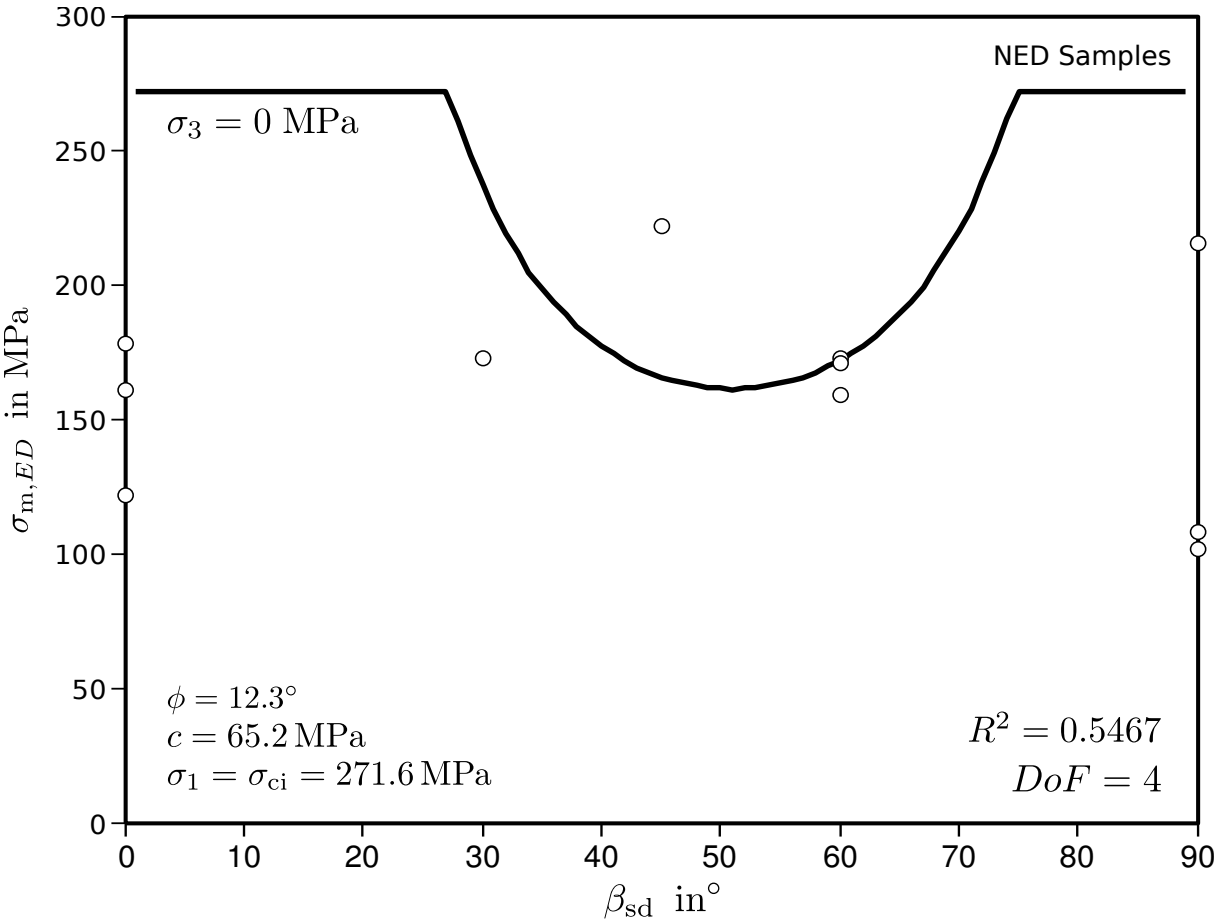

FIGURE 6.3: Jaeger Model Plot of Chosen Tested ED Samples, $DoF = 4$.

Figure 6.2 shows that there are many combinations of data: with different *DoF* from 1 to 6, and with different positive and negative R^2 values. The best situation for a positive correlation was commented in Figure 6.3, while the best situation for a negative correlation exists when $Dof = 2$ with a value of $R^2 = -0.458\,8$.

In general all data combinations reflect a positive correlation. If one makes a pondered average calculation by giving more weight to greater *DoF*; one can observe that among all values, a positive —but weak— correlation prevails over the negative ones (see the blank filled square point in Figure 6.2 that is at an ordinate of $R^2 = 0.161\,6$ and at an abscissa of $Dof \approx 3$). This could mean that even though all shortcomings, ED samples test results are trying to correlate with the Jaeger Analytical model; but also the obtained values were very disperse, not enough to affirm with solvency a reliable correlation.

The positive correlation tendency can also be supported with the best R^2 values for positive

and negative correlations, as commented above, because $|0.5467| > |-0.4588|$. Inclusive —by doing more calculations— when one runs the Jaeger model for the two best situations and found out the friction angle and the cohesion of the discontinuity set, one observe reasonable–coherent values of these variables for the the positive correlation (i.e. $\phi_{\mathrm{d},ED} = 12.3^{\circ}$ and $c_{\mathrm{d},ED}$=65.2 MPa), and un–reasonable values for the negative correlation (i.e. $\phi_{\mathrm{d},ED} = -9.4^{\circ}$ and $c_{\mathrm{d},ED}$=86.8 MPa).

If one wanted to consider the opposite situation against the situation expressed in the preceded paragraph, one can also observe that the expected curve formed when plotting the β_{sd} angle *vs.* the UCS is apparently inverted (i.e. instead to form a $\cup$ shape as it was shown in Figure 2.10, it forms an inverse U shaped [$\cap$]) (Figure 6.4). If this is so inverted, because could also be possible that the etched discontinuities formed with the SSLE technique on OBCG are stronger than the OBCG material, by adding a shear resistance due to roughed planes. This last hypothesis could be also a new evidence to this apparent stronger UCS values found on ED samples, as shown in Section 5.8, and also resumed in Section 5.9.

Until this part of the present research document, because it was found contradictions on results, it was not possible to accept or reject the main hypothesis as expressed in Section 1.2, but the last above two statements opens a possible alternative to solve it, if additional testing are performed.

By deciding to the second alternative which says that notches increment UCS, it was proceeded to construct OBCG samples with Negative Etched Discontinuities (NED). What does it means? —It means: to etch with the SSLE technique all the three dimensional regions that represent the rock material, and to leave blank all the three dimensional regions that represent the discontinuities.

In the following section, it will described this new testing campaign performed with these new samples. Also, it will show the results obtained and the proper validation made with the Jaeger model, in order to see if tests results will verify the last mentioned quote about the inverse U shape.

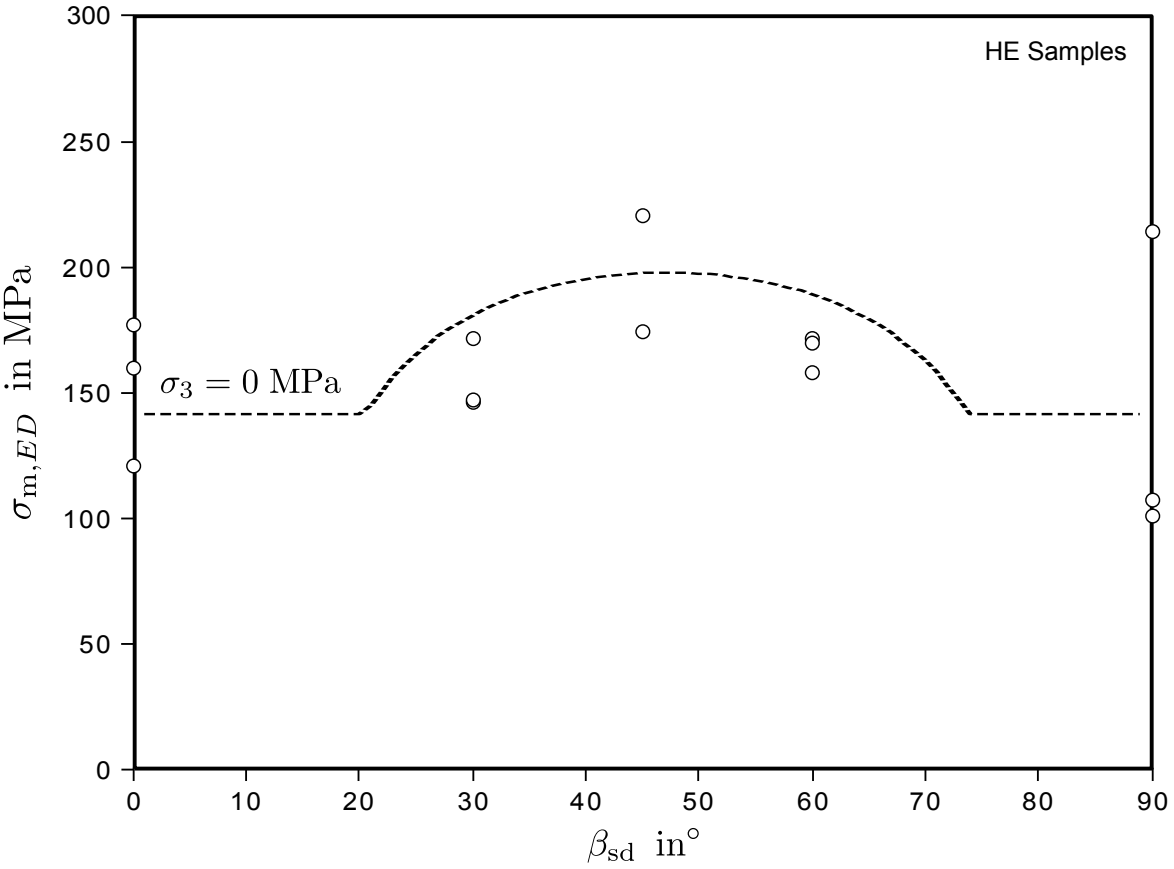

FIGURE 6.4: Jaeger Model Plot in the Hypothetical Case the Notches–Set Create a Strong Plane.

6.3 New Tests on OBCG with Negative Etched Discontinuities

Basically all the methodology described in Chapter 5 was maintained for this new test campaign. The studied rock mass is the same, with the same discontinuity network (i.e. one total–persistent, unfilled, and dry discontinuities set) but it the inverse form, therefore the notch density of the etched phase was of 4215×10^6 notch m^{-3}. Figure 6.5 shows the scheme of those NED samples.

The construction methodology was followed the same guidelines as described for the first testing campaign, with the exception to invert the notches pattern after creating the discontinuity network. The notches density on the etched volume of these samples was of 156×10^6 notch m^{-3}.

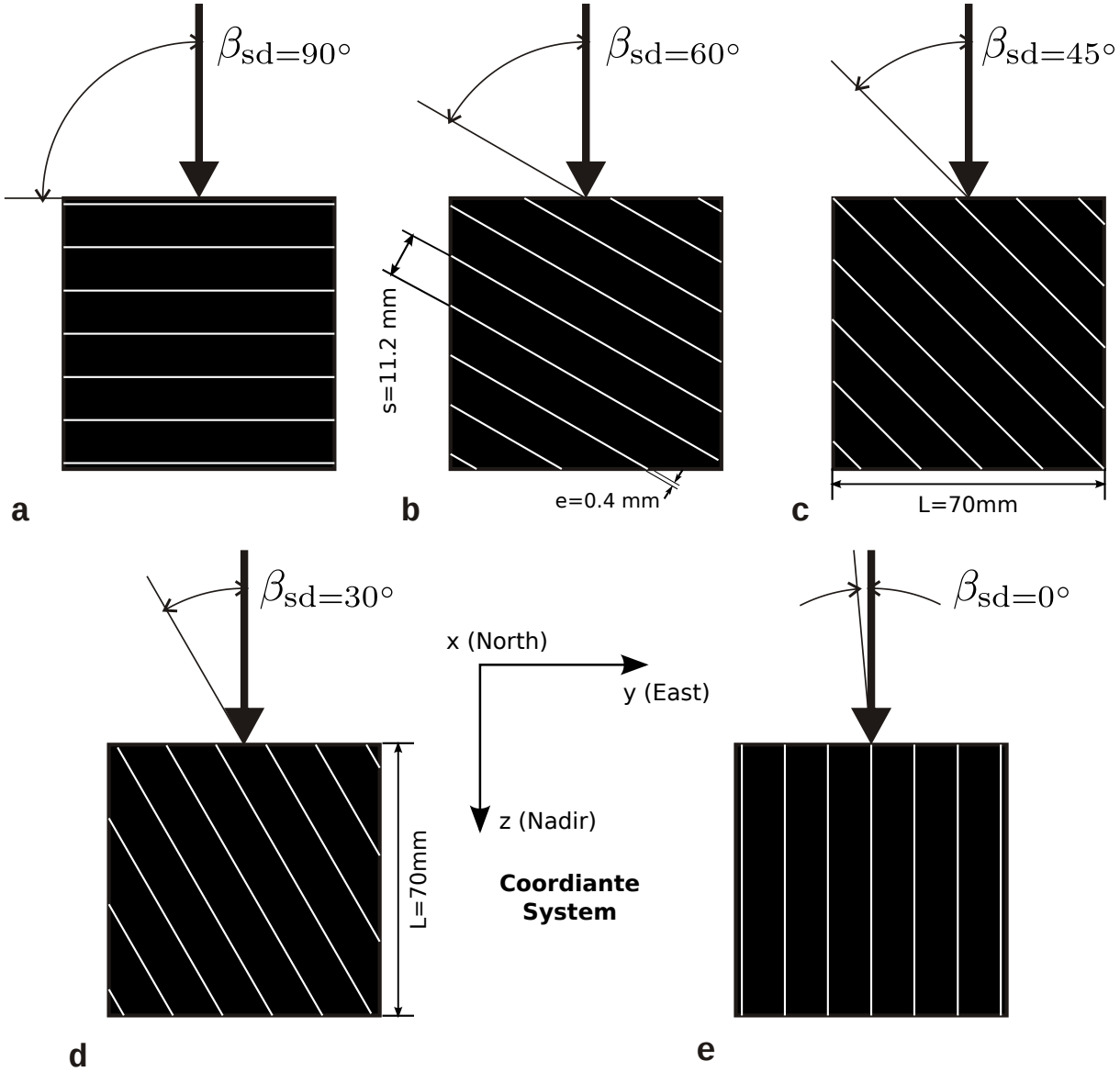

FIGURE 6.5: NED Samples Types Tested in the New Campaign, black areas represent etched areas. **a** Discontinuities with $\beta_{sd} = 90°$; **b** with $\beta_{sd} = 60°$; **c** with $\beta_{sd} = 45°$; **d** with $\beta_{sd} = 30°$; **e** with $\beta_{sd} = 0°$.

Also, the samples etching process with the SSLE technique remained the same. For this campaign, also the etching time was registered as shown in the following table (Table 6.1).

All the samples were instrumented with the strain gages and at the same positions as shown in Figure 5.6. The same strain–gages–type was used, and the same gluing method was followed. The samples and equipment arrangement for their testing were the same as that shown in Figure 5.9 and Figure 5.12.

TABLE 6.1: Velocities of the Engraving Process for NED Samples.

Sample Type*	β_{sd} in °	n_{notch}	$t_{etching}$ in minutes	$\widehat{v}_{etching}$ in notch s^{-1}
000V†	0	1 389 674	12.6	1 875
030V	30	1 325 716	11.8	1 872
045V	45	1 331 592	11.8	1 878
060V	60	1 341 762	11.9	1 879
090V	90	1 353 514	12.0	1 875

Note. n_{notch} is the total number of notches; $t_{etching}$ is the total etching time; and $\widehat{v}_{etching}$ the mean etching velocity.
*Samples are divided in five types: those samples whose discontinuities sets have a β_{sd} angle from 90° to 0° (i.e. 90°, 60°, 45°, 30°, and 0°).
†The letter V corresponds to Negative Discontinuity (initially called Vein);

Before the individual testing of each sample, their three sides length dimensions, the weight, and the sound propagation time were also measured, as shown in Table 6.2.

TABLE 6.2: Measured Dimensions of NED Samples.

Sample	Direction / β_{sd} in °	Average Length in mm			t_s	w_d
		North	East	Nadir	in ms	in g
000VA		70.03	69.17	67.08	12.5	816.49
000VB	0	69.16	67.39	69.58	12.5	813.43
000VC		68.01	67.31	68.74	12.5	789.13
030VA		69.26	69.45	69.82	12.5	825.75
030VB	30	68.05	68.05	68.40	12.5	793.30
030VC		68.94	67.89	68.63	12.5	813.59
045VA		70.00	67.41	69.20	12.5	819.48
045VB	45	68.66	68.48	67.63	12.5	795.97
045VC		68.04	69.15	69.02	12.5	817.16
060VA		68.57	68.50	68.09	12.5	801.18
060VB	60	69.33	70.13	68.06	12.5	828.81
060VC		68.60	68.01	67.93	12.5	794.47
090VA		68.54	69.19	68.35	12.5	811.45
090VB	90	68.06	67.67	68.23	12.5	789.36
090VC		67.57	68.08	67.94	12.5	782.28

With the above mentioned measurements, the geometrical and index properties of the NED samples were obtained; which are shown in Table 6.3.

TABLE 6.3: Geometrical and Index Properties of NED Samples.

Sample	β_{sd} in °	V in m^3	A_{ne} in m^2	$\gamma_{d,NED}$ in kN m^{-3}	$v_{sd,NED}$ in m s^{-1}
000VA		0.00032	0.0048	24.7	5366
000VB	0	0.00032	0.0047	24.6	5566
000VC		0.00031	0.0046	24.6	5499
030VA		0.00034	0.0048	24.1	5586
030VB	30	0.00032	0.0046	24.6	5472
030VC		0.00032	0.0047	24.8	5490
045VA		0.00033	0.0047	24.6	5536
045VB	45	0.00032	0.0047	24.6	5410
045VC		0.00032	0.0047	24.7	5522
060VA		0.00032	0.0047	24.6	5447
060VB	60	0.00033	0.0049	24.6	5445
060VC		0.00032	0.0047	24.6	5434
090VA		0.00032	0.0047	24.6	5468
090VB	90	0.00031	0.0046	24.6	5458
090VC		0.00031	0.0046	24.6	5435

Here is of great interest to inspect again the sound propagation velocities results. The median value of this variable for these new samples was of 5468 m s^{-1}, the mean ($\widehat{v}_{sd,NED}$) equal to 5475.6 m s^{-1}, and the standard deviation ($s_{v_{sd,NED}}$) of 59.00 m s^{-1}. Doing the same variance analysis as performed in Section 5.8, by comparing within the same values of blank samples, one obtain for a confidence of 67.8% that both blank and NED samples are significant different, and that sound propagation velocity of NED samples is greater than the corresponding of blank samples.

In the same manner as the previous test campaign —by using the same gross data processing as described in Section 5.8— the uniaxial compressive strength values were obtained, as resumed in Table 6.4. The stress application rate of each sample is described in Table 6.5. The median rate of this test campaign was of 0.82 MPa s^{-1}, and its mean and standard deviation of 0.74 MPa s^{-1} and 0.25 MPa s^{-1}, respectively.

Same analysis of significance for uniaxial compressive strength was performed for this new sample test campaign. Therefore, if all results of uniaxial compressive strength of NED samples are assumed to be the same sample set, it was encountered with a confidence of 66.0% that NED samples are other samples —in the statistical sense— among blank samples.

TABLE 6.4: Ultimate Strength of NED Samples.

Sample	β_{sd} in °	$\sigma_{cm,NED}$ in MPa		
		A	B	C
VN00	0	220.4	133.2	64.9
VN30	30	225.0	33.1	235.3
VN45	45	144.7	180.2	194.4
VN60	60	176.8	100.5	241.7
VN90	90	230.5	169.4	164.5

TABLE 6.5: Stress Application Rates during Physical Modeling Testing of NED Samples.

Sample	β_{sd} in °	t_σ in MPa s^{-1}		
		A	B	C
VN00	0	0.63	0.82	0.90
VN30	30	0.84	0.53	0.89
VN45	45	0.36	0.77	0.97
VN60	60	0.35	0.80	0.99
VN90	90	0.29	0.90	1.11

Note. t_σ is stress application rate.

By considering separately the influence of β_{sd} angle, the following Table 6.6 resulted. In this table, it was more difficult to extract any special behavior, specially when analyzing the samples sets 000V and 090V, because in this case both have the extreme confidence values. The unique simple thing one can conclude within this table is that sample sets 045V, 060V and 090V are significantly different to the uniaxial compressive strength of blank samples.

TABLE 6.6: Particular Variance Analysis for UCS of NED Samples.

Sample Set	β_{sd} in °	C_{max} in %
000V	0	20.9
030V	30	34.3
045V	45	84.4
060V	60	57.1
090V	90	85.7

Note. C_{max} is the maximum confidence value to reject null hypothesis.

Here was also calculated the tangential vertical deformation modulus of the strain gage number five in respect the axial force ($E_{t,50\%,NED,5}$), and the strain ratio of strain gage five in respect

to strain gage one ($\nu_{NED,5-1}$); see Table 6.7 and Table 6.8, respectively. As was explained previously, these two ratios does not explain anything, because —in the case deformations are possible to observe within this physical models— they are a case of transverse–isotropic material. But here was exposed again in order to observe some similarity or not with the same values obtained at the blank samples (i.e. $E_{t,50\%,OBCG}$ and ν_{OBCG}, of Table 4.9).

TABLE 6.7: Vertical Deformation Moduli of NED Samples.

Sample	β_{sd} in °	$E_{t,50\%,NED,5}$ in GPa		
		A	B	C
VN00	0	74.6	59.0	—
VN30	30	99.0	73.1	92.4
VN45	45	91.9	61.4	104.5
VN60	60	84.4	47.9	93.1
VN90	90	85.7	58.5	104.5

TABLE 6.8: Strain Ratio of NED Samples.

Sample	β_{sd} in °	$E_{t,50\%,NED,5}$ in GPa		
		A	B	C
VN00	0	0.21	0.13	—
VN30	30	0.50	0.31	0.41
VN45	45	0.43	0.14	0.46
VN60	60	0.33	0.08	0.41
VN90	90	0.34	0.15	0.77

Data for those two variables exposed in Table 6.7 and Table 6.8 reveals again a high dispersion in values. The median value of $E_{t,50\%,NED,5}$ is 85.0 GPa, and the median value of $\nu_{NED,5-1}$ is equal to 0.33; while mean and standard deviation are 83.6 GPa and 24.5 GPa, respectively for $E_{t,50\%,NED,5}$; and 0.33 and 0.18, respectively for $\nu_{NED,5-1}$.

Variance analysis of both variables reveals that both sample sets corresponds to the same event, that means that deformation is not influenced by the notches pattern in the samples, same result as encountered in the first test campaign with ED samples (see: Section 5.8).

Further conclusions will be discussed in the next sections, when one will analyze samples that were etched homogeneously in all the OBCG volume, without any pattern of discontinuities. But, by the moment, let see now, if the new test results of these NED samples are more reliable with the Jaeger model. This will be discussed in the following section.

6.4 Comparison of New Tests Results with Analytical Model

The data processing —in order to compare the NED samples tests results with the same Jaeger analytical model— was performed with the same software tool as described in Section 6.1 (i.e. the 3D–OSPM program). Here was also calculated the all possible combinations the total number of input data can offer.

Performing the above mentioned calculations, it was observed that the resulting highest R^2 value for the highest DoF —for this new test campaign data— was better than the last test campaign; and therefore to this research expectation. With a value of R^2 equal to 0.690 4, for the combination number 1 corresponding to the maximum possible degree–of–freedom (i.e. none sample was discarded, $Dof = 6$), it is possible to assume a good fitting between the physical and the analytical models. Figure 6.6 shows how is related the physical modeling data to the analytical model curve.

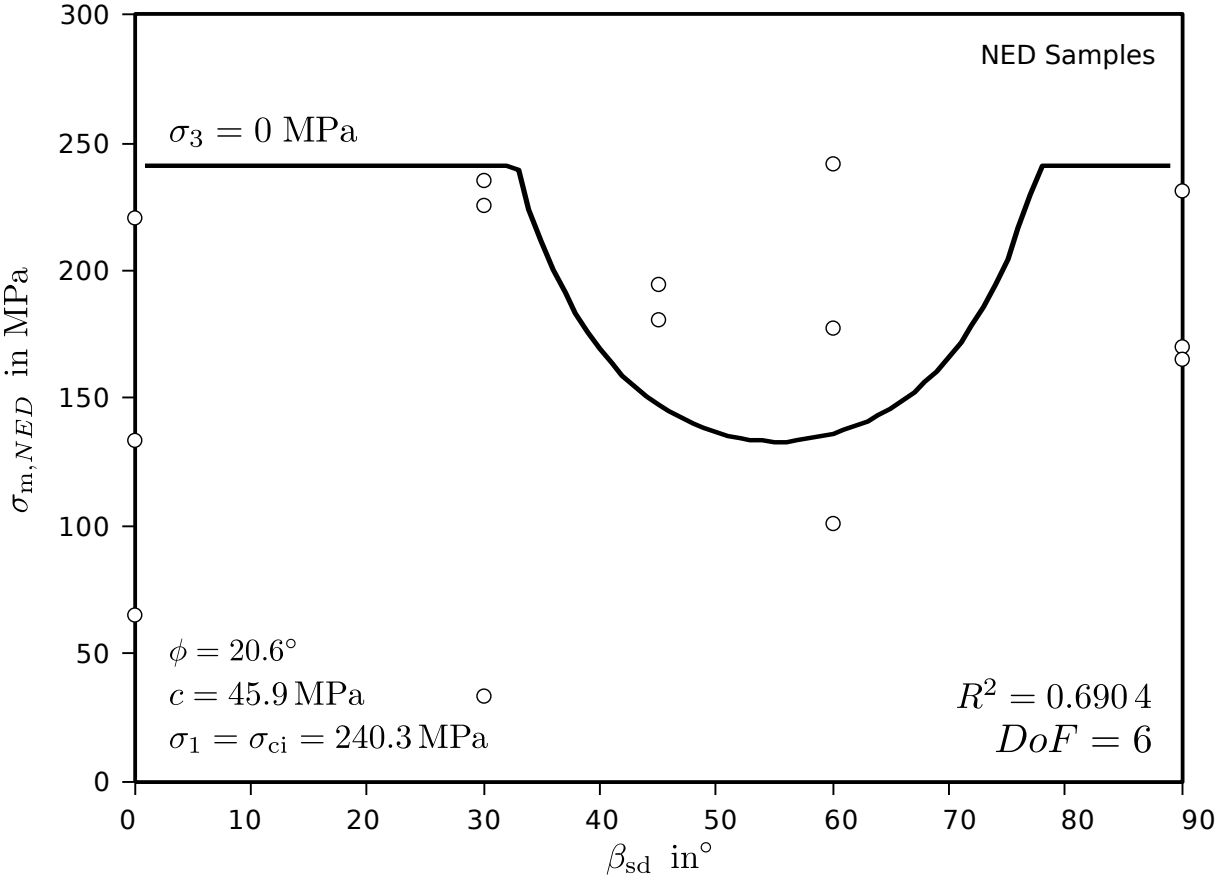

FIGURE 6.6: Jaeger Model Plot of Tested NED samples, $DoF = 6$.

A special issue that was not present in the previous test campaign (i.e. campaign with ED

samples), but was present in this test campaign analysis, is that one obtained better R^2 values for smaller than 6 *DoF* (see Figure 6.7). For example, for a *DoF* of 3, one obtained a high and near–to–one value of R^2 (i.e. 0.899 6). Also this figure shows that in general, positive correlation prevails. For example, the pondered average value gives a R^2 of 0.694 4 at a $Dof \approx 3$ (see the square black filled point of Figure 6.7).

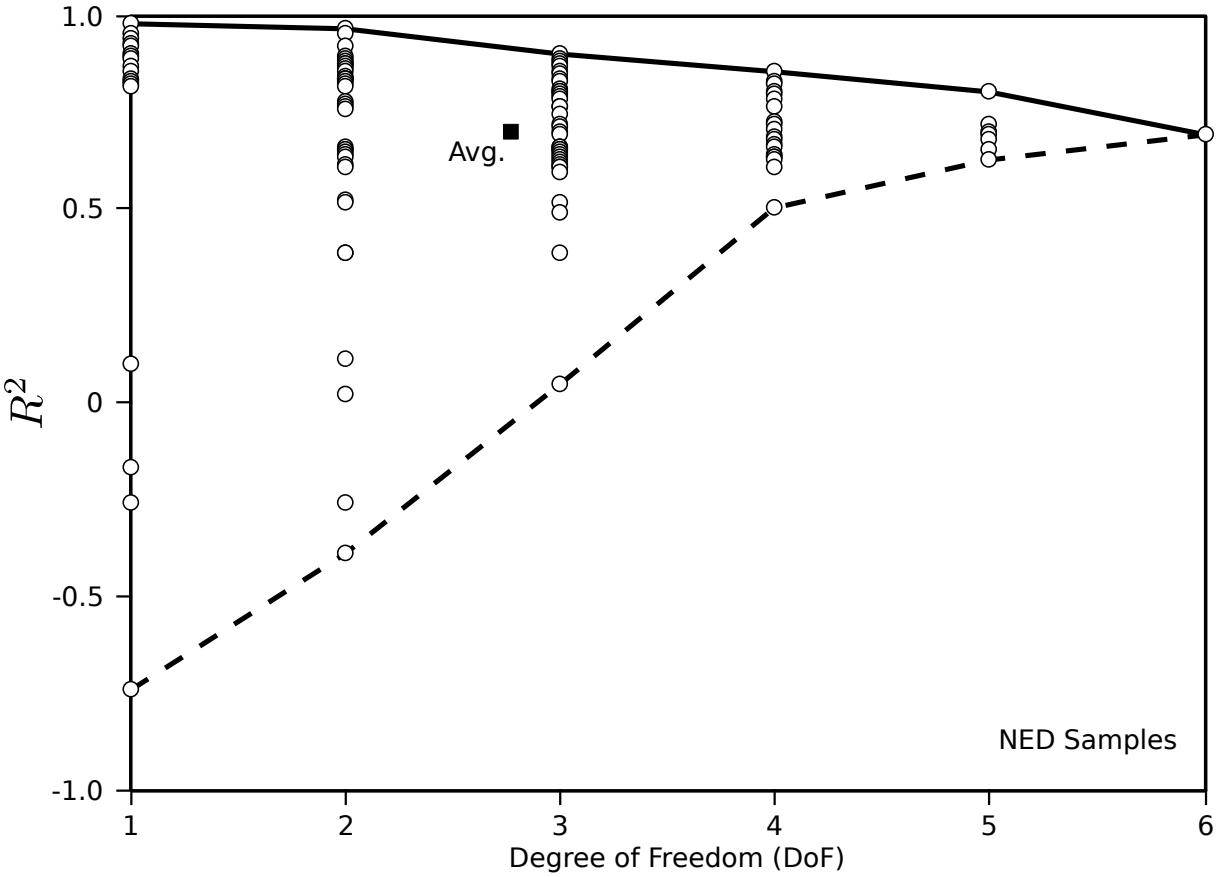

FIGURE 6.7: *DoF vs.* R^2 Plot of Physical Modeling Results Fit–Procedure on NED Samples.

Extreme situations can be commented: the highest positive R^2 was obtained for a $Dof = 1$ with a value of 0.977 0; while the highest absolute negative R^2 had a value of $-0.742\,7$, also for a $Dof = 1$. But again, when running the Jaeger model in order to calculate the $\phi_{\mathrm{d},NED}$ and the $c_{\mathrm{d},NED}$ of these two extreme values of R^2, the corresponding to the positive correlation gives reasonable numbers (i.e. $\phi_{\mathrm{d},NED}$ =10.4 ^{circ} and $c_{\mathrm{d},NED}$ =70.4 MPa) while the corresponding to the negative correlation gives un–reasonable numbers (i.e. $\phi_{\mathrm{d},NED}$ =-3.3 ^{circ} and $c_{\mathrm{d},NED}$ =106.0 MPa).

With the R^2 value of 0.6904 for $DoF = 6$, and with the plot shown in Figure 6.7, one can conclude that the physical modeling results are trying to respond good to the analytical model and with positive correlation coefficients. Unfortunately, a convergence of R^2 when incrementing DoF was not possible to attain, but this is too much to expect with small quantities of tests. The reason of this and the R^2 not to be near the unity for the largest DoF, could be because finally the notch sets forming each of the discontinuity planes are essentially not a full developed continuous discontinuity, because among notches will ever exist a bridge of OBCG material.

By assuming that the fit of the $DoF = 6$ is the more–appropriate to generalize the results, one can calculate the discontinuity–set friction angle ($\phi_{\mathrm{d},NED}$) and the discontinuity–set cohesion ($c_{\mathrm{d},NED}$) to represent the NED samples campaign, which are equal to 20.6° and 45.9 MPa, respectively. Also, the uniaxial compressive strength of rock material ($\sigma_{\mathrm{ci},NED}$) was calculated with a value equal to 240.3 MPa, where it is observed that this value is greater than its homologue obtained by testing in Section 4.1.5.3 in a proportion of 1.9 times. The three values are reasonable valid, because they are positive. Comparisons of these values with those in literature was not possible, because it appears to have non–existence of shear strength values under the Coulomb–Navier model of etched surfaces at OBCG.

It is pertinent to mention that even though one have in hand the discontinuities failure envelope within this model (i.e Jaeger model, that includes the Coulomb–Navier model for discontinuities), the campaign design will not allow find out the rock material envelope and the rock mass failure envelope (i.e. the graphic obtained as final result in Figure 6.6 is not a failure envelope), because for those to have, it should be tested a similar set of samples under at least three different triaxial axis–symmetric stress fields. Only standard triaxial axis–symmetric tests can obtain all the model parameters, in order to show the failure envelope of rock masses with a single discontinuity set.

But even though that limitation, this second testing campaign on physical models was considered to be acceptable, but another question arises from this result: Why the tests on NED samples reflected better fit to the Jaeger model? — It might be possible that:

- etched–discontinuities increment the shear strength and create surface of stiffness instead to create surface of weakness; or
- a negative–etched–discontinuities configuration represent a rock mass with wide discontinuities, and etched–discontinuities still decrement shear strength.

In order to accept or reject the first possible answer of the last emerged question, a third small test campaign was designed, as shown as follows.

6.5 Tests on Homogeneously Etched Samples

Still with the wish to find out answers about the mechanical influence of notches in OBCG material and to find out an answer to a good fitting of NED samples to the Jaeger model, another test campaign was design (a short test campaign). This time, cubic samples —of the same dimensions of those upon here tested— were constructed, where OBCG were etched homogeneously in all the sample volume without forcing any discontinuous plane (i.e. becoming the name of Homogeneously Etched [HE] samples). The goal of this campaign is to see if the presence of notches on OBCG increment or not the strength of the entire OBCG material.

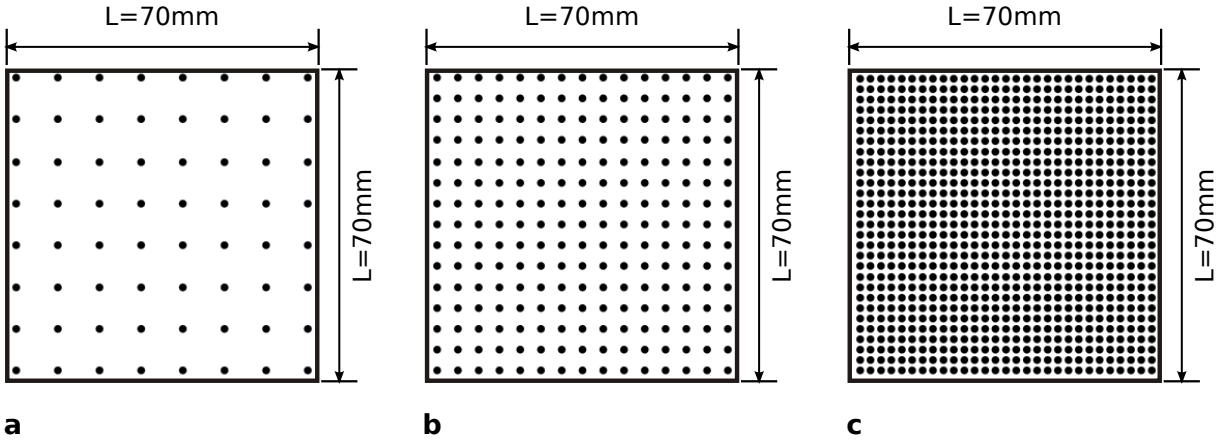

FIGURE 6.8: HE Samples Types Tested in the New Campaign. **a** With wide spaced notches, $\rho_{\text{notch}} = 20 \times 10^6$ notch m^{-3}; **b** with middle spaced notches, $\rho_{\text{notch}} = 156 \times 10^6$ notch m^{-3}; and **c** with close spaced notches, $\rho_{\text{notch}} = 4215 \times 10^6$ notch m^{-3}.

It was defined —as a proposal— three sample categories according to their notch density, this last which is defined here as the ratio of the total notches quantity present in a determined volume. The notch density was grouped conceptually in three groups:

- wide spaced notches giving low notch density;
- middle spaced notches giving intermediate notch density;
- close spaced notches giving high notch density.

The following table shows the values of notch density of these three proposed categories (Table 6.9).

TABLE 6.9: Notch Densities on HE Samples.

Category	Sample Group	n_{notch}	ρ_{notch}* in notch m^{-3}
Wide Spaced	00M	6346	20×10^6
Middle Spaced	18M	49931	156×10^6
Close Spaced	06M	1349094	4215×10^6

*ρ_{notch} which is the Notch Density, was calculated for a mean sample volume of 0.00032 m^3.

For each category, three samples were tested under uniaxial compressive strength, and under the same procedure until now maintained in all the research test campaigns of this research (i.e. same specimens preparation and instrumentation, same specimen arrangement, same equipment arrangement etc.). Table 6.10 shows the uniaxial compressive strength results obtained from this new test campaign, and Table 6.11 shows the simple statistics of the uniaxial compressive strength value. Values found for the test campaign of samples group 06M can be also representative of the uniaxial compressive strength of a called negative blank material (BNED) for the test campaign at NED samples (see: Section 6.3); which have values of $\widehat{\sigma}_{c,BNED}$=74.02 MPa, $s_{\sigma_{c,BNED}}$= 38.96 MPa, and $CV_{\sigma_{c,BNED}}$=0.526.

TABLE 6.10: Uniaxial Compressive Strength of HE Samples.

Sample Group	ρ_{notch} in notch m^{-3}	Uniaxial Compressive Strength $\sigma_{cm,HE}$ in MPa		
		A	B	C
00M	20×10^6	54.58	64.05	—*
18M	156×10^6	99.07	94.77	125.23
06M	4215×10^6	105.43	30.43	86.21

*00MC was rejected because a small piece dislodged from a lateral sample face just after the beginning of the test.

TABLE 6.11: Uniaxial Compressive Strength Statistics of HE Samples.

Sample Group	Category	$\widehat{\sigma}_{c,HE}$ in MPa	$s_{\sigma_{c,HE}}$ in MPa	$CV_{\sigma_{c,HE}}$	n
00M	Wide Spaced	59.31	6.70	0.113	2
18M	Middle Spaced	106.39	16.54	0.155	3
06M	Close Spaced	74.02	38.96	0.526	3

Note. $\widehat{\sigma}_c$ is the mean value, s_{σ_c} the variance, and CV_{σ_c} the coefficient of variation of uniaxial compressive strength; and n is the number of tests for each group.

By doing the variance analysis and compared with the blank samples results, it is observed that two sample series (i.e. sample categories 00M and 06M) have smaller uniaxial compressive

strengths than blank samples: the 00M sample series with a confidence of 85.8%, and the 06M sample series with a confidence of 73.5%. While, the 18M sample series might be unaltered within the corresponding values of blank samples.

Also, a regression procedure was performed, in order to relate the etch densities with the uniaxial compressive strength values. But this time a lognormal fit function was proposed, being the etch densities under the logarithm of base 10 ,and the uniaxial compressive strength maintained as is. Making a similar analysis as done for the other test campaigns, by considering different combination of values (i.e. this time 147 combinations) and the degrees of freedom; the following plot resulted (Figure 6.9).

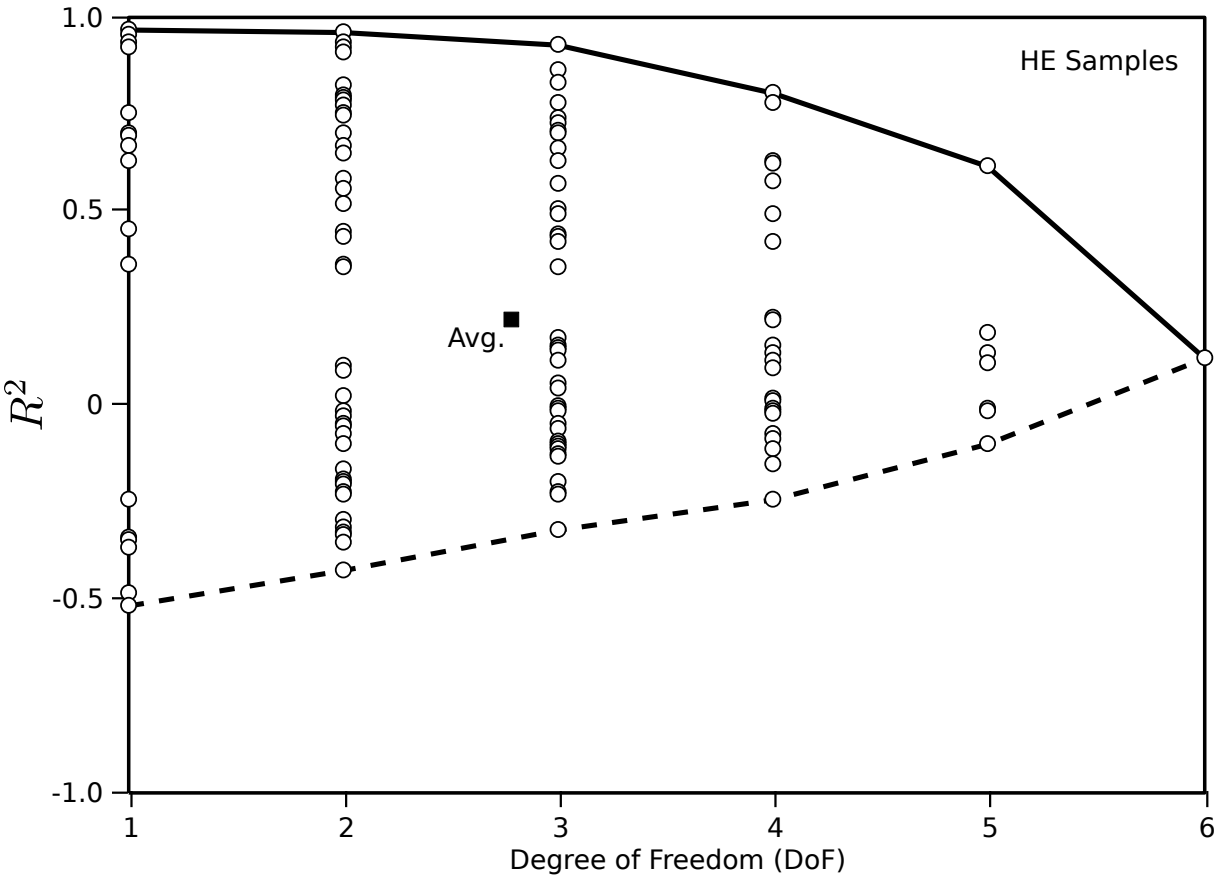

FIGURE 6.9: *DoF vs.* R^2 Plot of Physical Modeling Results Fit–Procedure on HE Samples.

With these results, it is not clear a prevailing–distinct positive or negative correlation; *id est* if notch density takes an incremental or a decremental role on the uniaxial compressive strength on HE samples. But it appears that exist a low tendency to have a positive correlation between the two values (i.e. ρ_{notch} and $\sigma_{\text{cm},HE}$), because most of the correlation coefficients are positive

and closer to one when comparing with the remaining negative correlation coefficients. This can be shown numerically when doing the weighted average calculation of all the correlation coefficient of the combinations, taking the *DoF* as the weights; which gives a value of $\widehat{R}^2 = 0.2146$ for a *DoF* near to 3 (see also the black square on Figure 6.9).

If one takes the data whose correlation coefficients were nearest to 1 and -1 (i.e. the highest positive and the highest negative R^2), one can observe that both tendencies —a positive or a negative line slopes– can be assumed (Figure 6.10). Therefore, a clear conclusion if a positive or negative correlation prevails, is to yet possible.

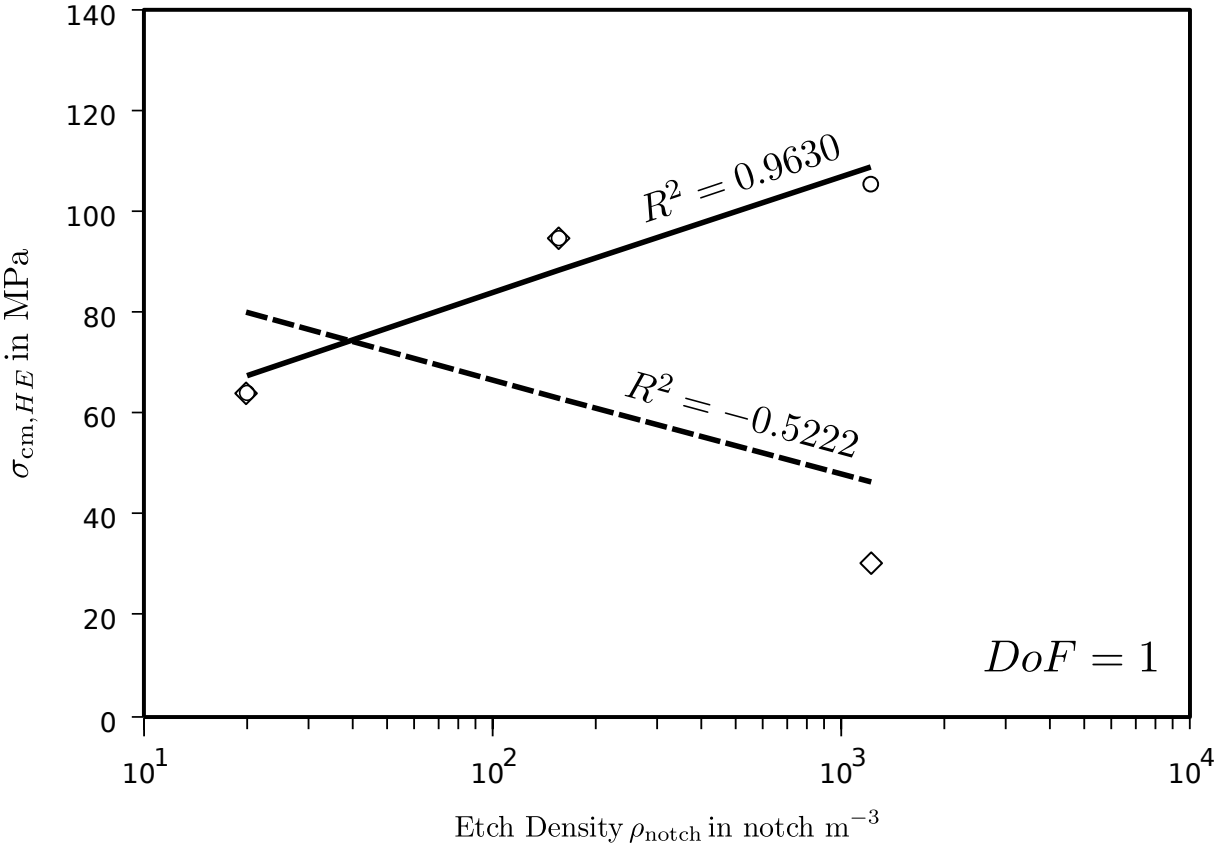

FIGURE 6.10: Lognormal Curve Fits on Two Extreme Optimistic Cases of HE Samples.

If the possible weak positive correlation is assumed to be true, one can conclude that there can be a possible tendency of samples in increment their uniaxial compressive strength when notch density also increments. But particularly, it is difficult to assume that, when it was observed in this research that the etching process with the OBCG–SSLE technique is a real damage process (see Section 4.3).

With this testing campaign and their analysis, the ultimate attempt to dazzle a reasonable explanation of the mechanical influence of notches on OBCG was lost, because the results did not give sufficient evidence to the determine if there is a positive or negative correlation.

6.6 Final Comments

There are two possible explanations about the reasons the second campaign brought a better fit to the Jaeger model than the first campaign:

- etched–discontinuities increment the shear strength instead to create a weakness surface;
- a negative–etched–discontinuities configuration represent a rock mass with wide discontinuities, and etched–discontinuities still decrement shear strength.

External references were not found about the evidence for the first possible explanation, but in all the variance analysis of the sound propagation velocities, the uniaxial strength values, and finally the adjustment of data to the Jaeger model performed in this research, seems to show that etched discontinuities incremented the shear strength, and that the possible manner to model weak discontinuities is to create negative–etched–discontinuities. But unfortunately, the last tests campaign on HE samples could not demonstrate this quote.

Therefore, the second possibility might be more reasonable, inclusive because under the light of the notch characterization by optical methods performed in this research (refer to Section 4.2), which revealed a true damage process that necessary should low the strength of OBCG, or at least promote a faster strength deterioration on the OBCG.

The last tests campaign on HE samples could not demonstrate strongly one of the two possible explanations. Even tough this last situation, one is more comfortable to assume that a wider band of etched discontinuities could allow to model qualitatively the phenomenological response of weak discontinuities of rock masses at ultimate uniaxial strength.

It might be possible that it is arising only a scale effect problem of etched discontinuities: when discontinuities are thin as the case of ED samples, they increment the material shear strength or its influence to the OBCG is weak; but when discontinuities are wide (thick) as the case of NED samples they decrement their shear strength.

More research should be performed in order to confirm with more evidence this new hypothesis for this physical modeling approach. Also, the methodology exposed in Chapter 5 could be the start point in order to perform more research.

Accepting the Main Hypothesis It is observed with this work that the main hypothesis of this research —presented in Section 1.2 at Page 9— has a good probability to be accepted as true, because tests on NED samples presented an acceptable positive correlation with the analytical model of Jaeger, and strength parameters of discontinuities were accordingly with common material properties (Section 6.4).

In order to improve the probability of acceptance of the main hypothesis of this research, it is important to perform other tests according to what will be recommended in the following chapter (Chapter 7).

Chapter 7

Conclusions

In this final chapter, one will present the general conclusions found with this research, the usefulness of the model approach, the limitations it has, and possible future research one can follow.

7.1 General Conclusions

In this research it was shown that the mechanical behavior at the ultimate strength under uniaxial compressive stress of brittle rock masses —with a totally persistent unfilled secondary discontinuities single–set— has a good probability and the potential to be modeled with reduced physical models of some transparent optical homogeneous material (may be OBCG, or another with better properties accordingly to the proposed usefulness) prepared with the Sub–Surface Laser Engraving technique.

In order to conclude that, the model materials (i.e. the material that represent the discontinuities, and the material that represent the rock material itself) were characterized (Chapter 4).

The characterization of the OBCG representing the rock material revealed that mechanically this optical material is very disperse, as revealed the uniaxial compressive tests (i.e. $CV_{\sigma_{\mathrm{ci},OBCG}} = 0.630$) and the elastic parameters measurements (Section 4.1.5.3 and 5.9); even though, the sound propagation velocities revealed contradictory un–disperse results (i.e. a $CV_{v_{\mathrm{sd},OBCG}} =$

0.016) (Section 4.1.5.2). The tests results dispersion of these blank OBCG samples was identified to be primarily due to the different stress rates used during the tests; the imperfect lubricated surfaces contact between sample and load platens; the nonexistence of an accurate parallelism and planarity between the two loaded sample–surfaces; and the mechanical in–homogeneity of amorphous material.

In respect to the performed visual microscopical inspections of notches, it was revealed that a true damage process exist when the LASER etches into the blank material (Section 4.3). But essentially, notches forming sets are not representing essentially a full developed continuous discontinuity, because they have among them bridges of OBCG material.

Also, experimental campaigns on cubical specimens were performed in order to support the main conclusion (Chapter 5 and Section 6.3). The first experimental campaign —consisted in creating a discontinuity–like network with thin discontinuities with the SLLE technique— gave a poor fit and a low positive correlation with the analytical model used to validate it (Section 6.2); but the second one —consisted in making a negative etched sample (i.e. remain blank —without notches— those phases that represented the discontinuities, and etching with the SLLE technique the phases that initially represented the rock material)— gives a better positive correlation fit (Section 6.4).

Explanation about this better result have two tails:

- etched–discontinuities increment the shear strength instead to create a weakness surface;
- a negative–etched–discontinuities configuration makes to represent a rock mass with wider discontinuities than the rock material, and etched–discontinuities still decrement shear strength.

The first explanation has some evidences when some variance analysis were performed during this research; where it was observed that etched samples appear to have higher uniaxial compressive strengths than blank samples (Section 5.8 on Pages 136 and 137; Section 5.9). But in contradiction to it, etched samples appear to have lower uniaxial compressive strengths than blank samples, as found in Section 6.3 on Page 149. In both cases, low confidence values were found (around 50%). This contradiction was also influenced by the disperse results one obtained, that was identified to be caused by also by: the different stress rates used during the tests; the imperfect lubricated surfaces contact between sample and load platen; the non–existence of an accurate parallelism and planarity between the two loaded sample–surfaces; the insufficient discontinuities thickness, and the mechanical in–homogeneity of amorphous material.

The main reason to disregard with this first explanation (i.e. etches incrementing mechanical properties) is that in the case of this may be true, one should expected a strong negative correlation between the tests results of NED samples with the analytical model; and one observed that this was contrary: one found a good positive correlation (see Figure 6.7 and their comments about it in Section 6.4), which possibilities to assume that etched samples on discontinuities are producing a weaker effect on material.

A further but a short experimental campaign was here performed in order to validate more these two explanation (Section 6.5), but unfortunately it did not give a clear and definitive position. Even tough this last shortcoming, the second explanation (i.e. about the wider etched discontinuity) seems to be more comfortable, because it has more sense when the visual microscopical inspection of notches revealed a true damage process made by the LASER in the blank material (Section 4.3).

It could be probably that the process of creating thick etched discontinuities networks on OBCG with the SSLE technique, possibilities the phenomenological physical modeling of weak discontinuities on rock masses at ultimate mechanical strength if bigger samples are tested (say for example: cubical samples greater than four times a 70 mm side with discontinuities thicker than 8 mm). It might be possible that the optimum sample size and discontinuity thickness was not reached with this research.

Because the first explanation (i.e. etches incrementing mechanical properties) was not rejected at all, one can also make other hypothesis about that situation; therefore, it might also possible that for smaller samples scales and thin discontinuities here tested: etched discontinuities networks on OBCG with the SSLE technique possibilities model a rock mass with discontinuities of stronger mechanical characteristics than the rock material.

By the other way, it was concluded that this physical modeling approach with OBCG does not possibilities model deformational responses at the scale here tested (Section 5.8 on Page 138, Section 5.9, and Section 6.3 on Page 152). But, it seems probable that this important behavior will be possible to be reached at all at scale levels greater than the samples here tested and with a more deformable material. If clear deformation response is attained, one could propose a dimensional analysis for deformations, turning this model proposal into an quantitative physical modeling approach of rock mass deformation. This can be possible if further research is performed in order to find relations between the material deformational properties with notch densities.

It is important to underline that with this proposed modeling approach —about only the ultimate strength— only a non–dimensional idea of rock mass behavior can be possibly observed, this because ultimate strength is a progressive coalescence process of material, and this can be only modeled quantitatively if the material used in the prototype (i.e. the rock mass) is equal to the model material (i.e. the etched OBCG). Because this modeling approach proposal needs use an optical transparent material, this last condition will never be accomplished, therefore only a qualitative modeling is possible.

7.2 Usefulness

With this research, the scientific community may have in hand a first research of a new possible kind of physical modeling approach, using OBCG and applying the SSLE technique, potentially useful to generate any desired discontinuous rock mass physical model.

This physical model approach —if finally will solve all their shortcomings— will also be useful to understand complex situations or to ensure how other present models adequately represent rock mass reality by creating key verification tests, which will be the benchmarks for further model verifications.

Further research will define if this approach has the advantages it expects.

7.3 Limitations

This physical modeling approach has a main limitation: this research solved the complete modeling approach to deal with ultimate mechanical strength only. The principal shortcoming of this, is that dimensional analysis is not possible for ultimate mechanical strength under the conditions this approach uses, therefore the model will be ever qualitative for that material property.

Also, this physical modeling approach —present as it is until now— has by the moment the following temporally limitation: the deformation response of the physical models with OBCG —at the sizes here created and tested— is undetectable. But, this last limitation can be solved by performing future research, as it is commented in the following section.

7.4 Future Research

Future research about this modeling approach is very important in order to have a better and reliable modeling tool.

The first important task to be solved is to improve the probability of acceptance of the main hypothesis here proposed, by doing the following:

- still use OBCG, even though it is an optically homogeneous but amorphous solid and possible a mechanically inhomogeneous material;
- perform a broader research review about the mechanical behavior of amorphous solids and the special case of OBCG, and if necessary program special tests on OBCG;
- etch only one discontinuity, instead of a set of discontinuities in each sample;
- design a wider etched discontinuity with the here used 156×10^6 etch density, say for example twenty times the thickness here used (i.e. 8 mm)
- maintain the cube shape and dimensions as here used, but avoid the chamfer the samples base in their contours;
- guarantee a high parallelism and minimum roughness of the loaded surfaces, by machining the surfaces after etching;
- instead of using cork and talc powder, use Teflon to minimize the shear resistance between the sample surface and the load platen;
- use more samples per a β_{sd} angle discontinuity set (i.e. minimum five);
- use shorter intervals as used here, between a β_{sd} angle discontinuity set (e.g. each 5°);
- maintain a slow, a very controlled and a constant stress rate in all tests, and use a servo–controlled and stiff frame;
- validate the results by using as first option —but not the unique— the Jaeger analytical model, and consider to use other models (e.g. crack propagation numerical models);
- still investigate possible hypothesis about the incremental–in–strength of etches, therefore perform similar samples as the above mentioned with the negative version of them;
- still try to find an uniaxial compressive strength of model with the notch densities.

The second thing it is necessary to solve, is to accept or reject the two new hypotheses expressed in this chapter in Section 7.1, which are: etched–discontinuities increment the shear strength instead to create a weakness surface; and a negative–etched–discontinuities configuration makes to represent a rock mass with wider discontinuities than the rock material, and etched–discontinuities still decrement shear strength. This could also possible to be solve with the campaign expressed in the above paragraph.

The third important task to be solved is to find out the relations between model mechanical ultimate strength and notch densities, of both phases: that representing rock material, and that representing discontinuities. This can be done by making a more refined test campaigns as performed here about the Tests on Homogeneously Etched Samples (see Section 6.5), for example:

- define a wider range of notch densities;
- test more samples for each notch density (e.g. five, seven or more);
- maintain a slow, a very controlled and a constant stress rate in all tests, and use a servo–controlled and stiff frame;

After that, it is recommended to investigate and demonstrate clearly if there exist a scale effect on the mechanical behavior of the specimens; and if so, determine the proper limit sizes. Therefore, it is necessary to answer to the following question: what is the minimum possible sample size to be used under this approach without loosing the mechanical behavior equivalence? — For this, one can repeat the first of the above proposed campaign tests, but this time for four —or more— different samples size, maintaining the shape equal. A size limit of the biggest sample can be 280 mm.

Other research possibilities, after the above described, can be:

- test samples with the same discontinuity network used here, but under triaxial axis–symmetric stress fields and minimum under three different chamber pressure values;
- use other samples shapes, for example cylindrical samples, and perform the same testing campaign described here: under uniaxial and then under triaxial axis–symmetric stress fields (the advantages one will receive by performing testing with cylindrical samples is that will allow use all the standard monitoring equipments used in rock material characterization [e.g. acoustic emission sensors, lateral and axial deformations]);
- do more realistic tests under complicated stress states, which may be possible only with the development of properly tests cells and equipments (e.g. submit back again cubical specimens to poly–axial stresses and/or to non–monotonically stress paths).

Parallel to the above proposed researches, it will be interesting to look for a better material for this kind of physical modeling proposal, that accordingly to this research experience could be one that:

- be optically homogeneous, in order to properly etch with accuracy;
- be mechanically homogeneous, in order to reduce disperse values on mechanical properties;

- has a non–amorphous molecular arrange (i.e. be a crystalline material), in order to anticipate a behavior by a material theory;
- has a non–brittle mechanical behavior;
- has low uniaxial compressive strength;
- be more deformable, in order to perceive a deformational response;
- be more easy–workable (i.e. cut, milled, polished);
- has properties to perform photo–elasticity, which can be of great usefulness for this kind of modeling.

If one of these materials is found, it will increment the potentiality of this model approach, and will reduce the limitations of OBCG is giving now. Then for this, physic scientists should be find the proper short–pulse LASER for those proposed material (i.e. the multiple shot LASER damage threshold of the proper chosen material). But, if amorphous transparent materials will still considered to be used, it will be necessary to understand more their mechanical response, which is complex and well studied in the Physic science.

One would like to encourage ongoing research in order to advance the knowledge of rock masses physical modeling with the SSLE technique.

7.5 Closing the Entire Research Document

Physical model testing is not a panacea, even thought well designed experiments may yield important insights into behavior that are not available from other non–physical models. In closing this document, it is important to say that it is of great importance consider physical models —being laboratory or field tests— as a first answer alternative for complex situations, because these are the unique medium to answer the fundamental questions of rock mechanics, as it expressed Cook (1981).

References

Abou-Sayed, A. and C. Brechtel (1976, August). Experimental investigation of the effects of size on the UCS of Cedar City quartz diorite. In W. Brown, S. Green, and W. Hustrulid (Eds.), *Proceedings of the 17th U.S. Symposium on rock mechanics, site characterization*, Volume 1, Snowbirds- Utah, pp. 5D6–1–5D6–6. University of Utah.

Adams, M. and G. Sines (1978). Crack extension from flaws in a brittle material subjected to compression. *Tectonophysics 49*, 97–118.

Adey, R. and R. Pusch (1999). Scale dependency in rock strength. *Engineering Geology 53*, 254–258.

Amadei, B. (1988). Strength of a regularly jointed mass under biaxial and axisymmetric loading conditions. *International Journal of Rock Mechanics and Mining Sciences & Geomechanics Abstracts 25*, 3–13.

Arora, V. (1987). *Strength and deformation behavior of jointed rocks*. PhD thesis, Indian Institute of Technnology, Delhi. TH-1456.

ASTM D5878-08 (2008). Standard guides for using rock-mass classification systems for engineering purposes. Technical report, PA: ASTM International, Philadelphia.

Bakhtar, K. (1997). Impact of joints and discontinuities on the blast-response of responding tunnels studied under physical modeling at 1-g. *International Journal of Rock Mechanics and Mining Sciences 34*(3-4), Paper 021.

Barton, N. and V. Choubey (1977). The shear strength of rock in theory and practice. *Rock Mechanics 10*, 1–54.

Barton, N., R. Lien, and J. Lunde (1974). Engineering classification of rock masses for the design of tunnel support. *Rock Mechanics 6*, 189–236.

Behrestaghi, M. (1992). *Strength and deformational responses of schistose rocks*. PhD thesis, Indian Institute of Technology, Delhi. TH-1982.

Bieniawski, Z. (1968). The effect of the specimen size on compressive strength of coal. *International Journal of Rock Mechanics and Mining Sciences & Geomechanics Abstracts 5*, 325–335.

Bieniawski, Z. (1974, March). Estimating the strength of rock materials. *Journal of the South African Institute of Mining and Metallurgy*, 312–320.

Bieniawski, Z. (1975). Prediction of the rock mass behavior by geomechanics classification. In *Proceedings of the 2nd Australian & New Zealand Conference on Geomechanics*, Case studies, Brisbane, Autralia, pp. 36–41.

Bobet, A. and H. Einstein (1998). Numerical modeling of fracture coalescence in model rock material. *International Journal of Fracture 92*, 221–252.

Bortolucci, A. (1993). *Modelo de ruptura em compressão de materiais frágeis baseado na mecânica da fratura e aplicado ao efeito–escala*. PhD thesis, Universidade de São Paulo, São Paulo, Brazil.

Bray, J. (1967). A study of jointed and fractures rock, part I. *Rock Mechanics and Engineering Geology 5*, 117–136.

Brown, E. (1970, November). Strength of models of rock with intermittent joints. *Journal of Soil Mechanics and Foundation Division 96*(SM6), 1935–1949. Paper 7697.

Brown, E. (2008). Estimating the mechanical properties of rock masses. In Y. Potvin, J. Carter, A. Dyskin, and R. Jeffrey (Eds.), *SHIRMS 2008*, Perth, pp. 3–21. Australian Center for Geomechanics.

Brown, E. and D. Trollope (1970). Strength of a model of jointed rock. *Journal of Soil Mechanics and Foundation Division 96*(SM2), 685–704.

Cai, M. and H. Horii (1993). A constitutive model and FEM analysis of jointed rock masses. *International Journal of Rock Mechanics and Mining Sciences & Geomechanics Abstracts 30*(4), 351–359.

Cai, M., P. Kaiser, H. Uno, Y. Tasaka, and M. Minami (2004). Estimation of rock mass deformation modulus and strength of jointed hard rock masses using the GSI system. *International Journal of Rock Mechanics and Mining Sciences 41*, 3–19.

Cai, M., H. Morioka, P. Kaiser, Y. Tasaka, H. Kurose, M. Minami, and T. Maejima (2007). Back-analysis of rock mass strength parameters using AE monitoring data. *International Journal of Rock Mechanics and Mining Sciences 44*(4), 538–549.

Camacho Tauta, J., O. Reyes-Ortiz, A. Nieto Leal, S. Millán Montejo, and F. Rincón Morantes (2009, June). Resistencia al corte en discontinuidades con diferentes grados de rugosidad. *Ciencia e Ingeniería Neogranadina 19*(1), 55–70.

Chang, S.-H. and C.-I. Lee (2004, October). Estimation of cracking and damage mechanisms in rock under triaxial compression by moment tensor analysis of acoustic emission. *International Journal of Rock Mechanics and Mining Sciences 41*(7), 1069–1086.

Chen, E. (1989, March). A constitutive model for jointed rock mass with orthogonal sets of joints. *Journal of Applied Mechanics 56*, 25–32.

Chen, S. and S. Qiang (2004). Composite element model for discontinuous rock masses. *International Journal of Rock Mechanics and Mining Sciences 41*, 865–870.

Cho, N., C. Martin, and D. Sego (2007). A clumped particle model for rock. *International Journal of Rock Mechanics and Mining Sciences 44*, 997–1010.

Cook, N. (1981). Geomechanics in the laboratory. *Nature, News & Views 294*, 213–214.

Crystran (2010, January). Optical glass (N-BK7 B270 and others). http://www.crystran.co.uk.

Doty, J. (2000). Damage control, a practical guide to avoiding laser damage to optics. *Photonics Spectra Magazine unknown*(unknown), 113–116.

Drucker, D. and W. Prager (1952). Soil mechanics and plastic analysis of limit design. *Quarterly of Applied Mathematics 10*(2), 157–165.

Du, D., X. Liu, G. Korn, J. Squier, and G. Mourou (1994). Laser–induced breakdown by impact ionization in SiO_2 with pulse widths from 7 ns to 150 fs. *Applied Physics Letters 64*, 3071.

Eberhardt, E., B. Stimpson, and D. Stead (1999). Effects of grain size on the initiation and propagation thresholds of stress-induced brittle fractures. *Rock Mechanics and Rock Engineering 32*(2), 81–99.

Edelbro, C., J. Sjöberg, and E. Nordlund (2006). A quantitative comparison of strength criteria for hard rock masses. *Tunnelling and Underground Space Technology 22*, 57–68.

Einstein, H. and R. Hirschfield (1973). Model studies on mechanics of jointed rock. *Journal of Soil Mechanics and Foundation Division 99*, 229–242.

Einstein, H., R. Nelson, R. Bruhn, and R. Hirschfeld (1969, June). Model studies of jointed rock behavior. In *Proceedings of the 11^{th} Symposium on Rock Mechanics*, Berkeley, CA.

Feng, X.-T. and J. Hudson (2011). *Rock Engineering Design* (1 ed.). London: CRC Press.

Ferrero, A., A. Godio, L. Sambuelli, and I. Voyat (2007). Geophysical and geomechanical investigations applied to the rock mass characterization for distinct element modelling. *Rock Mechanics and Rock Engineering 40*(6), 603–622.

Fleury, S. (2001). Análise da distribuição de tensões em descontinuidades de rocha utilizando a técnica da fotoelasticidade. MSc thesis, Departamento de Engenharía civil e ambiental, Universidade de Brasília, Brasilia, Brazil.

Fouché, O. and J. Diebolt (2004). Describing the geometry of 3D fracture systems by correcting for linear sampling bias. *Mathematical Geology 36*(1), 33–63.

Franklin, J. (1971). Triaxial strength of rock material. *Rock Mechanics 3*, 86–98.

Gaitán-Oliva, V. (2005). Propagação de fraturas em juntas rugosas não- persistentes. MSc thesis, Escola Politécnica de São Carlos, Universidade de São Paulo, São Paulo, Brazil.

Gallais, L., J. Natoli, and C. Amra (2002). Statistical study of single and multiple pulse laser-induced damage in glasses. *Optics Empress 10*(25), 1465–1474.

Germanovich, L. and A. Dyskin (2000). Fracture mechanics and instability of openings in compression. *International Journal of Rock Mechanics and Mining Sciences 37*, 263–284.

Germanovich, L., R. Salganik, A. Dyskin, and K. Lee (1994). Mechanisms of brittle fracture of rock with pre-existing cracks in compression. *Pure and Applied Geophysics 143*(1-3), 117–149. doi: 10.1007/BF00874326.

Goldfarb, B. (1996, November). Process and apparatus for etching an image within a solid article. United States Patent Application 5557936, United States Patent and Trademark Office.

Goldstein, M., B. Goosev, N. Pyrogovsky, R. Tulinov, and A. Turovskaya (1966, September). Investigation of mechanical properties of cracked rock. In *Proceedings of the First Congress of the International Society of Rock Mechanics*, Volume 1, Lisbon, pp. 521–524. International Society of Rock Mechanics: Laboratório Nacional de Engenharia Civil.

Gorshkov, A., K. Vukolov, I. Bel'bas, M. Maslov, and V. Sannikov (2003, July). Laser damage thresholds of single crystal tungsten mirror. In ECA (Ed.), *30th EPS Conference on Controlled Fusion and Plasma Physiscs*, Volume 27A of *2.82*, St. Petersburg. Balkema Rotterdam.

Haimson, B. and C. Chang (2000). A new true triaxial cell for testing mechanical properties of rock and its use to determine rock strength and deformability of Westerly granite. *International Journal of Rock Mechanics and Mining Sciences 37*, 285–296.

Hakala, M., H. Kuula, and J. Hudson (2007). Estimating the transversely isotropic elastic intact rock properties for in situ stress measurements data reduction: A case study of the olkiluoto mica gneiss, finland. *International Journal of Rock Mechanics and Mining Sciences 44*, 14–46.

Handin, J., H. Heard, and J. Magouirk (1967, January). Effects of the intermediate principal stress on the failure of limestone, dolomite and glass at different temperature and strain rates. *Journal of Geophysical Research 72*(2), 611–640.

Hayashi, M. (1966, September). Strength and dilatancy of brittle jointed mass- the extreme value stochastic and anisotropic failure mechanism. In *Proceedings of the First Congress of the International Society of Rock Mechanics*, Volume 1, Lisbon, pp. 295–302. International Society of Rock Mechanics: Laboratório Nacional de Engenharia Civil.

Henry, E., D. Marcotte, and P. Kavanagh (2001). Classification of non-oriented fractures along boreholes to joint sets and its success degree. *Rock Mechanics and Rock Engineering 34*(4), 257–273.

Hnatovsky, C., R. Taylor, E. Simova, P. Rajeev, D. Rayner, V. Bhardwaj, and P. Corkum (2006). Fabrication of microchannels in glass using focused femtosecond laser radiation and selective chemical etching. *Applied Physics Letters A84*, 47–61.

Hoek, E. (1983). Strength of jointed rock masses. *Géotechnique 33*(3), 187–223.

Hoek, E. and E. T. Brown (1980, September). Empirical strength criterion for rock masses. *Journal of the Geotechnical Engineering Division 106*(GT9), 1013–1035. Art. 15715.

Horino, F. and M. Ellikson (1970). A method of estimating the strength of rock containing planes of weakness. Investigation Report 7449, U.S. Bureau of Mines, Washington, D.C.

Hoseinie, S., H. Aghababaei, and Y. Pourrahimian (2008). Development of a new classification system for assessing of rock mass drillability index (RDI). *International Journal of Rock Mechanics and Mining Sciences 45*, 1–10.

Hudson, J. and J. Harrison (1997). *Engineering rock mechanics: An introduction to the principles* (1 ed.), Volume 1. Pergamon.

Hustrulid, W. (1976). A review of coal pillar strength formulas. *Rock Mechanics 8*, 115–185.

Institute of Theoretical Chemistry (2010, January). Glass property information system. http://www.sciglass.info/.

ISO 11254-1 (2000). Determination of laser damage threshold of optical surfaces, part 1: 1-on-1 test. Draft standard, International Organization for Standardization, Geneva- Switzerland.

ISO 11254-2 (2001). Determination of laser damage threshold of optical surfaces, part 2: S-on-1 test. Draft standard, International Organization for Standardization, Geneva- Switzerland.

ISRM (1981). Suggested methods for determining the uniaxial compressive strength and deformability of rock material. Technical report, Commission on standardization of laboratory and field tests, International Society for Rock Mechanics, Lisbon.

Ivars, D., D. Potyondy, M. Pierce, and P. Cundall (2008, June). The smooth-joint contact model. In *Proccedings of the 8th World Congress on Computational Mechanics and 5th European Congress on Computational Methods in Applied Sciences and Engineering*, Venice, pp. 2–3. International Association for Computational Mechanics and the European Community on Computational Methods in Applied Sciences.

Jaeger, J. (1969, January). *Elasticity, fracture and flow: with engineering and geological applications* (3 ed.). Methuen's Monographs on Physical Subjects. London: Methuen & Co. Ltd.

Jaeger, J. and N. Cook (1979). *Fundamentals of rock mechanics* (Third ed.). London: Chapman & Hall.

Jaeger, J., N. Cook, and R. Zimmermann (2007). *Fundamentals of rock mechanics* (Fourth ed.). Oxford: Blackwell Publishing.

Jain, A., G. Firestone, and A. Yi (2005). Viscosity measurement by cylindrical compression for numerical modeling of precision lens molding process. *Journal of the American Ceramic Society 88*(9), 2409–2414.

Jones, R. and C. Wykes (1989). *Holographic and speckle interferometry* (2 ed.). Cambridge: Cambridge University Press.

Kemeny, J. and R. Post (2003). Estimating three-dimensional rock discontinuity orientation from digital images of fracture traces. *Computers and Geosciences 29*, 65–77.

Kessler, H. (2004). Laser damage thresholds of optical coatings, UV-NIR. Technical Report 200441108, CVI Technical Optics Ltd., Optical Components and Assemblies, Albuquerque, NM.

Kikuchi, K., K. Saito, and K. Kusunoki (1982). Geotechnically integrated evaluation on the stability of dam foundation rocks. Technical report, Commission International on Large Dams, Rio de Janeiro, Brazil.

Kostak, B. and H. Bielenstein (1971). Strength distribution in hard rock. *International Journal of Rock Mechanics and Mining Sciences 8*, 501–521.

Kramadibrata, S. and I. Jones (1993). Size effect on strength and deformability of brittle intact rock. In A. P. da Cunha (Ed.), *Proceedings of the Second International Workshop on Scale Effects in Rock Masses*, pp. 277–284. Balkema.

Krsmanovic, D., M. Tufo, and Z. Langof (1965). Some aspects of the rupture of rock masses. *Felsmechanik and Ingenieurgeologie 11*, 143–155.

Krsmanovic, D., M. Tufo, and Z. Langof (1966). Shear strength of rock masses and possibilities of its reproduction on models. In *Proceedings of the 1st Congress of the International Society Rock Mechanics*, Volume 1, Lisbon, pp. 537–542.

Kulatilake, P., B. Malana, and J. Park (2003). A new rock mass failure criterion for biaxial loading conditions. In *Proccedings of the 10^{th} Congress of the International Society of Rock Mechanics*, Gauteg, pp. 669–675.

Kulatilake, P., S. Wang, and O. Stephansson (1993, October). Effect of finite size joints on the deformability of jointed rock in three dimensions. *International Journal of Rock Mechanics and Mining Sciences & Geomechanics Abstracts 30*(5), 479–501.

Ladanyi, B. and G. Archambault (1970, June). Simulation of shear behavior of a jointed rock mass. In W. Somerton (Ed.), *Proceedings of the 11th U.S. Symposium on Rock Mechanics, Rock Mechanics: theory and practice*, Berkeley, CA, USA, pp. 105–125. University of California at Berkeley: The American Institute of Mining, Metallurgical and Petroleum Engineers.

Ladanyi, B. and G. Archambault (1972). Evaluation of shear strength of a jointed rock mass. In *Proceedings of the 24^{th} International Geological Congress*, Section 13D, Monreal, Canada, pp. 249–270.

Ladanyi, B. and G. Archambault (1977). Effect of block size on the shear behavior of jointed rock. In *Proceedings of the 23rd US Symposium on Rock Mechanics*, Berkeley CA, USA, pp. 739–760.

Lai, Y., C. Wang, and Y. Tien (1997). Micromechanical analysis of imperfectly bonded layered media. *Journal of Engineering Mechanics 123*(10), 986–995.

Lajtai, E. (1969). Strength of discontinuous rocks in direct shear. *Géotechnique 19*, 218–233.

Lama, R. D. (1974). The uniaxial compressive strength of jointed rock. In *Prof. L. Müller Festschrift*, pp. 67–77. Karlsruhe: International Center for Mechanical Sciences, University of Karlsruhe.

Laubscher, D. (1990, October). A geomechanics classification system for the rating of rock mass in mine design. *Journal of the South African Institute of Mining and Metallurgy 90*(10), 257–273.

Lenk, A. and T. Witke (1998, October). Decoration of glass by surface and sub-surface laser engraving. In C. Fotakis, T. Papazoglou, and C. Kalpouzos (Eds.), *Contributions to the 5th Conference on Optics within Life Sciences, Optics and lasers in biomedicine and culture, OWLS V*, Crete, Greece, pp. 155–158.

Lin, S.-J. and C.-Y. Ku (2006). Two-scale modeling of jointed rock masses. *International Journal of Rock Mechanics and Mining Sciences 43*, 426–436.

Lin, Y. (1998). *Advances in rock mechanics*, Chapter An introduction of the Chinese Standard for engineering classification of rock mass (GB50218-94), pp. 317–327. Singapure: World Scientific Publishing Co.

Liu, H., Y. Wu, and J. Lambropoulos (2009). Thermal shock and post-quench strength of lapped borosilicate optical glass. *Journal of Non-Crystalline Solids 355*(48–49), 2370–2374.

Lundborg, N. (1967). The strength-size relation of granite. *International Journal of Rock Mechanics and Mining Sciences 4*, 269–272.

Maghous, S., D. Bernaud, J. Fréard, and D. Garnier (2008). Elastoplastic behavior of jointed rock masses as homogenized media and finite element analysis. *International Journal of Rock Mechanics and Mining Sciences 45*, 1273–1286.

Martynyuk, P. and E. Sher (2002). Statistical model of rock failure under compression. *Journal of Mining Science 38*(6), 579–586.

Mauersberger, S., U. Löschner, H. Exner, J. Schille, R. Ebert, P. Regenfuss, and L. Hartwig (2008, October). Micromachining of glass with short Ns-pulses and highly repetitive FS-laser pulses. In *Proceedings of the 27th International Congress on Applications of Lasers & Electro-Optics (ICAELO 2008)*, Orlando, Florida USA. Paper 403.

Mauldon, M. (1998). Estimating mean fracture trace length and density from observations in convex windows. *Rock Mechanics and Rock Engineering 31*(4), 201–216.

McLamore, R. (1966). *Strength–deformation characteristics of anisotropic sedimentary rocks*. Phd thesis, University of Texas, Austin Texas.

McLamore, R. and K. Gray (1967). The mechanical behavior of anisotropic sedimentary rocks. *Transactions of the American Society of Mechanical Engineers B*, 62–76.

Menard, R. (1978, May). Method of decorating a transparent plastics material article by means of laser beam. United States Patent Application 4092518, United States Patent and Trademark Office.

Meyer, T. and H. Einstein (2002). Geologic stochastic modeling and connectivity assessment of fracture systems in the boston area. *Rock Mechanics and Rock Engineering 35*(1), 23–44.

Mogi, K. (1962). The influence of the dimensions of specimen on the fracture strength of rocks. *Bulletin of the Earthquake Research Institute 40*, 175–185.

Morozov, N., Y. Startsev, Y. Sudénkov, A. Suslikov, G. Baranov, and A. Belyaev (2006). Laser-induced breakdown threshold and fracture versus the nanostructure of two-phase glass. *Technical Physics 51*(7), 872–877.

Mughieda, O. and A. Alzo'ubi (2004). Fracture mechanisms of offset rock joints: a laboratory investigation. *Geotechnical & Geological Engineering 22*, 545–562.

Mughieda, O. and I. Karasneh (2006). Coalescence of offset rock joints under biaxial loading. *Geotechnical and Geological Engineering 24*(4), 985–999.

Nasseri, M., K. Rao, and K. Ramamurthy (2003). Anisotropic strength and deformational behaviour of himalayan schist. *International Journal of Rock Mechanics and Mining Sciences 40*(1), 3–23.

Navarrete, M., M. Villagrán-Muniz, L. Ponce, and T. Flores (2003). Photoacoustic detection of microcracks induced in BK7 glass by focused laser pulses. *Optics & Lasers in Engineering 40*, 5–11.

Palmström, A. (1996). Characterization of rock masses by the RMi for use in practical rock engineering. *Tunnelling and Underground Space Technology 11*(2), 175–186.

Pariseau, W., S. Puri, and S. Schmelter (2008). A new model for effects of unpersistent joint sets on rock slope stability. *International Journal of Rock Mechanics and Mining Sciences 45*, 122–131.

Patiño-Henao, S. (2005). Flujo a través del macizo rocoso de la margen izquierda de fundación de la presa Porce II: factores que propician el flujo. MEng. thesis, Universidad Nacional de Colombia, Medellín, Colombia.

Patton, F. (1966). Multiple models of shear failure in rock. In *Proceedings of the 1st Congress of the International Society of Rock Mechanics*, Volume 1, Lisbon, pp. 509–513.

Potyondy, D. and P. Cundall (2004). A bonded-particle model for rock. *International Journal of Rock Mechanics and Mining Sciences 41*, 1329–1364.

Prakoso, W., A. ASCE, F. Kulhawy, and F. ASCE (2004). Bearing capacity of strip footings on jointed rock masses. *Journal of Geotechnical and Geoenvironmental Engineering 130*(12), 1347–1349.

Prudencio, M. and M. Van Sint Jan (2007). Strength and failure modes of rock mass models with non–persistent joints. *International Journal of Rock Mechanics and Mining Sciences 44*, 890–902.

Prudencio-Salcedo, M. (2009, May). *Estudio de la resistencia y modos de falla de macizos rocosos con fracturas no persistentes*. PhD thesis, Escuela de Ingeniería, Pontificia Universidad Católica de Chile, Santiago.

Ramamurthy, T. (2004). A geo-engineering classification for rocks and rock masses. *International Journal of Rock Mechanics and Mining Sciences 41*, 89–101.

Rao, K. (1984). *Strength and deformation behavior of sandstones*. PhD thesis, Indian Institute of Technnology, Delhi. TH-1206.

Rao, K. and R. Tiwari (2008). A polyaxial system for testing of jointed rock mass models. *Geotechnical Testing Journal 31*(4), 1–10.

Reik, G. and M. Zacas (1978). Strength and deformation characteristics of jointed media in true triaxial compression. *International Journal of Rock Mechanics and Mining Sciences & Geomechanics Abstracts 15*(6), 295–303.

Romana, M. (2003, September). DMR (Dam Mass Ratting) an adaptation of RMR geomechanics classification for use in dams foundations. In *Proceedings of the 10^{th} Congress International Society of Rock Mechanics: Technology roadmap for rock mechanics*, Johannesburg, South Africa, pp. 977–980. South African National Institute of Rock Engineering & South African Institute of Mining and Metallurgy.

Roy, N. (1993). *Engineering behavior of rock masses through study of jointed models*. PhD thesis, Indian Institute of Technnology, Delhi. TH-2010.

Sainsbury, B., M. Pierce, and D. Mas Ivars (2008, August). Simulation of rock mass strength anisotropy and scale effects using ubiquitous joint rock mass (UJRM) model. In R. Hart, C. Detournay, and P. Cundall (Eds.), *Proceedings of the 1st International FLAC/DEM Symposium, Continuum and Distinct Element Numerical Modeling in Geo-Engineering*, Minneapolis. Itasca. Paper 06-02.

Shen, B. (1993). *Mechanics of fractures intervening bridges in hard rocks*. PhD thesis, Royal Institute of Technology, Stockholm, Sweden.

Sheorey, P., A. Biswak, and V. Choubey (1989). An empirical failure criterion for rocks and jointed rock masses. *Engineering Geology 26*, 141–159.

Shimomura, O., A. Yokotani, T. Sasaki, K. Yoshida, and C. Yamanaka (1987). Laser damage threshold of KDP single crystal at 1053μm. *Electronics and communications in Japan 70*(12), 12–20.

SIC (2007, September). Yeeya K9 crystal. Report GB903-87, Shanghai Institute of Ceramics, Chinese Academy of Sciences, Shanghai, China.

Singh, M. and K. Rao (2005). Empirical methods to estimate the strength of jointed rock masses. *Engineering Geology 77*, 127–137.

Singh, M., K. Rao, and T. Rammamurthy (2002). Strength and deformational behavior of jointed rock mass. *Rock Mechanics and Rock Engineering 35*(1), 45–64.

Singh, M. and B. Singh (2008). High lateral strain ration in jointed rock masses. *Engineering Geology 98*, 75–85.

Sinha, U. and B. Singh (2000). Testing of rock joints filled with gouge using a triaxial apparatus. *International Journal of Rock Mechanics and Mining Sciences 37*(6), 963–981.

Sitharam, T., J. Sridevi, and N. Shimizu (2001). Practical equivalent continuum characterization of jointed rock masses. *International Journal of Rock Mechanics and Mining Sciences 38*, 437–448.

Song, J. (2006). Estimation of areal frequency and mean trace length of discontinuities observed in non-planar surfaces. *Rock Mechanics and Rock Engineering 39*(2), 131–146.

Sridevi, J. and T. Sitharam (2000). Analysis of strength and moduli of jointed rocks. *Geotechnical & Geological Engineering 18*, 3–21.

Sridevi, J. and T. Sitharam (2003). Characterization of strength and deformation of jointed rock mass based on statistical analysis. *International Journal of Geomechanics 3*(1), 43–54.

Starzec, P. and J. Andersson (2002). Probabilistic predictions regarding key blocks using stochastic discrete fracture networks: example from a rock cavern in south-east Sweden. *Bulletin of Engineering Geology and the Environment 61*, 363–378.

Stuart, B., M. Feit, S. Herman, A. Rubenchik, B. Shore, and M. Perry (1996). Optical ablation by high-power short-pulse lasers. *Journal of the Optical Society of America B13*(2), 459–468.

Szirtes, T. (2007). *Applied dimensional analysis and modeling* (2 ed.). Burlington, MA: Butterworth-Heinemann.

Tanaka, H. (1964). *Introduction of geology for civil engineers*. Japan: Sankaidou.

Teja, P. (2008). An experimental study on strength behavior of jointed rock mass through modeling under uniaxial compression. Bsc. thesis, Department of Civil Engineering, National Institute of Technology, Rourkela.

Tien, Y., M. Kuo, and C. Juang (2006). An experimental investigation of the failure mechanism of simulated transversely isotropic rocks. *International Journal of Rock Mechanics and Mining Sciences 43*, 1163–1181.

Tien, Y. and P. Tsao (2000). Preparation and mechanical properties of artificial transversely isotropic rock. *International Journal of Rock Mechanics and Mining Sciences 37*, 1001–1012.

Tiwari, R. and K. Rao (2004). Physical modeling of a rock mass under a true-triaxial stress state. *International Journal of Rock Mechanics and Mining Sciences 41*(3), unknown. Paper 2A14.

Tiwari, R. and K. Rao (2007). Response of an anisotropic rock mass under polyaxial stress state. *Journal of Materials in Civil Engineering 19*(5), 393.

Vacek, J., J. Vacek, and J. Chocholousov'a (2008). Rock bursting mechanics: insight from physical and mathematical modeling. *Acta Polytechnica 48*(6), 38–44.

Vishay (2008). *System 6000 Model 6100 Scanner*. Raleigh, North Carolina: Instruments Division Measurement Group Inc.

Wang, J., Y. Ichikawa, and C. Leung (2003). A constitutive model for rock interfaces and joints. *International Journal of Rock Mechanics and Mining Sciences 40*, 41–53.

Wang, T.-T. and T.-H. Huang (2009). A constitutive model for the deformation of a rock mass containing sets of ubiquitous joints. *International Journal of Rock Mechanics and Mining Sciences 46*, 521–530.

Wang, X., Y. Zhao, and X. Lin (2011). Determination of mechanical parameters for jointed rock masses. *Journal of Rock Mechanics and Geotechnical Engineering 3*, 398—406.

Wang, Y. and F. Tonon (2009). Modeling Lac du Bonnet granite using a discrete element model. *International Journal of Rock Mechanics and Mining Sciences 46*, 1124–1135.

Weibull, W. (1939). *Generalstabens Litografiska Anstalts Forlag*, Chapter A statistical theory of the strength of material. Number 151. Stockholm: Ingeniors Vetenskaps Akademiens.

Wijerathne, M., K. Oguni, and M. Hori (2008). Stress field tomography based on 3D photoelasticity. *Journal of the mechanics and physics of solids 56*, 1065–1085.

Wu, F.-Q. and S.-J. Wang (2002). Statistical model for structure of jointed rock mass. *Géotechnique 52*(2), 137–140.

Xie, H., J.-A. Wang, and W.-H. Xie (1997). Fractal effects of surface roughness on the mechanical behavior of rock joints. *Chaos, Solitons and Fractals 8*(2), 221–252.

Yaji, R. (1984). *Shear strength and deformation response of jointed rocks*. PhD thesis, Indian Institute of Technnology, Delhi. TH-1210.

Yang, Z. and T. Huang (1995, September). Effect of joint sets on the anisotropic strength of rock masses. In T. Fuji (Ed.), *Proceedings of the 8^{th} International Congress of the ISRM*, Volume 1, Tokio Japan, pp. 364–370. International Society of Rock Mechanics: A.A. Balkema.

Yeeya Art Work Corp. (2009, November). e–mail communication.

Yudhbir, W. Lemanza, and F. Prinzl (1983). An empirical failure criterion for rock masses. In *Proceedings of the 5th International Conference on Rock Mechanics*, Volume 1, Melbourne, pp. B1–B8.

Zhang, L. and E. Einstein (1998). Estimating the mean trace length of rock discontinuities. *Rock Mechanics and Rock Engineering 31*(4), 217–235.

Zhu, W., Y. Li, S. Li, S. Wang, and Q. Zhang (2011). Quasi-three-dimensional physical model tests on a cavern complex under high in-situ stresses. *International Journal of Rock Mechanics and Mining Sciences 48*, 199–209.

Zhu, W., Q. Zhang, H. Zhu, Y. Li, J.-H. Yin, S. Li, L. Sun, and L. Zhang (2010, september). Large-scale geomechanical model testing of an underground cavern group in a true three-dimensional (3-D) stress state. *Canadian Geotechnical Journal 47*(9), 935–946. doi: 10.1139/T10-006.

Appendix A

Experimental Program Rough Results

In this appendix it is shown the photographs of the samples before and after its failure, as also the plots of time *vs.* vertical stress, and vertical and lateral deformations *vs.* the vertical stress. The tables included before the photographs and plots show the resume of availability of them in this appendix.

A.1 Blank Samples

TABLE A.1: Photographs and Plots shown of Blank Samples in this Appendix.

Sample	Photographs		Plots		
	Before Testing	After Testing	Testing Speed	Strain Modulus	Elastic Modulus
SGA	1	0	1	1	1
SGB	0	1	1	1	1
SGC	0	0	1	1	1
SGD	1	0	1	1	1

Note. 1 corresponds to yes, and 0 corresponds to no.

A.1.1 Specimen SGA

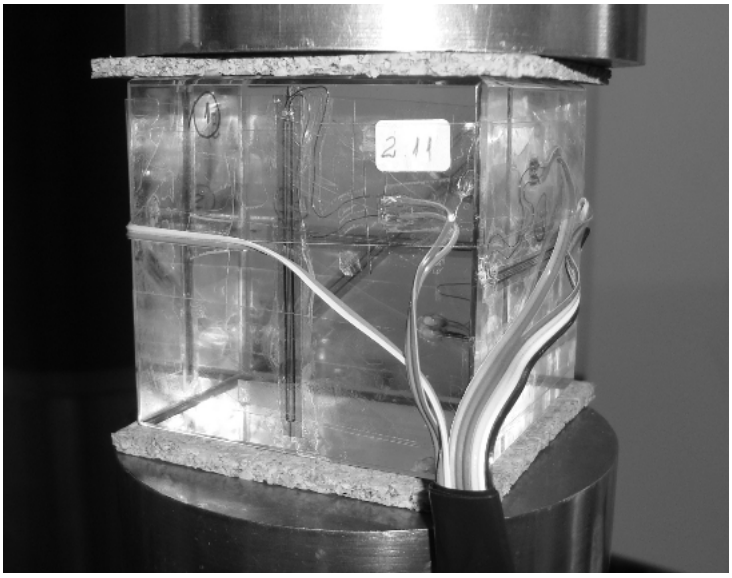

FIGURE A.1: Sample SGA before testing

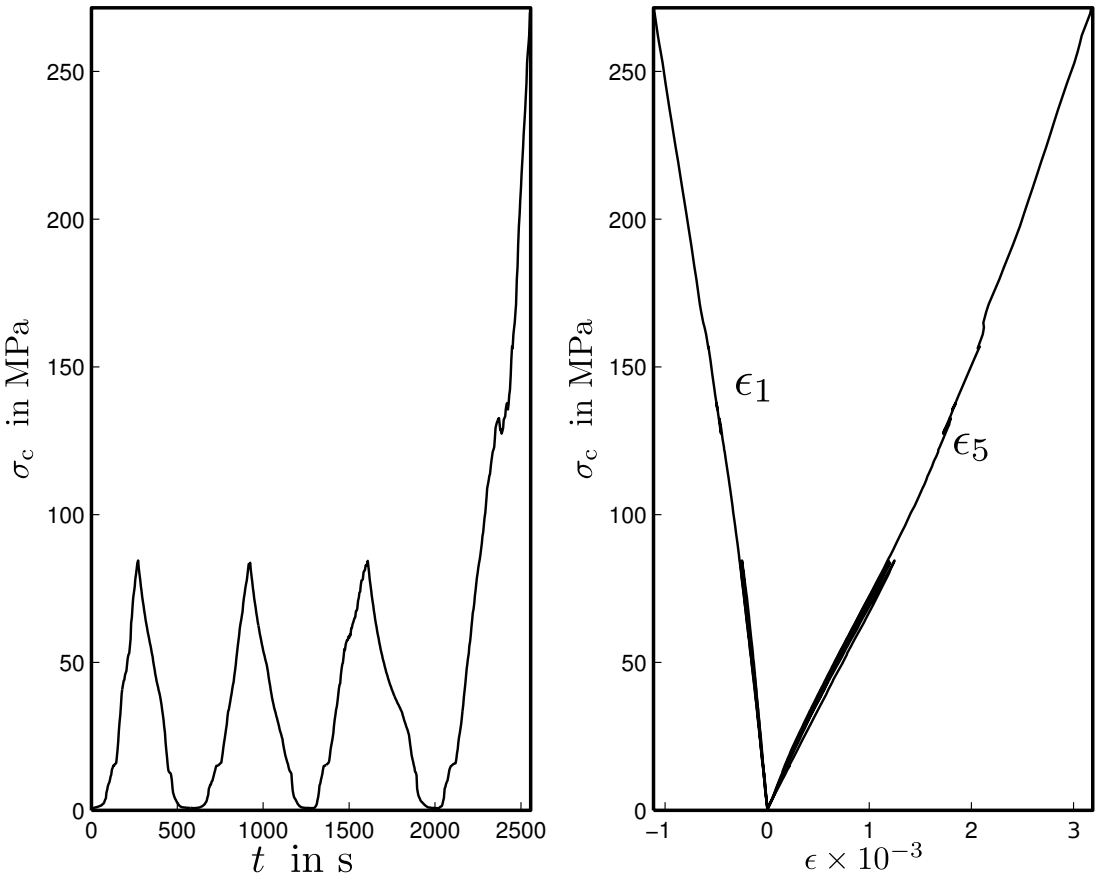

FIGURE A.2: Plots of time and deformations *vs.* vertical stress of sample SGA

A.1.2 Specimen SGB

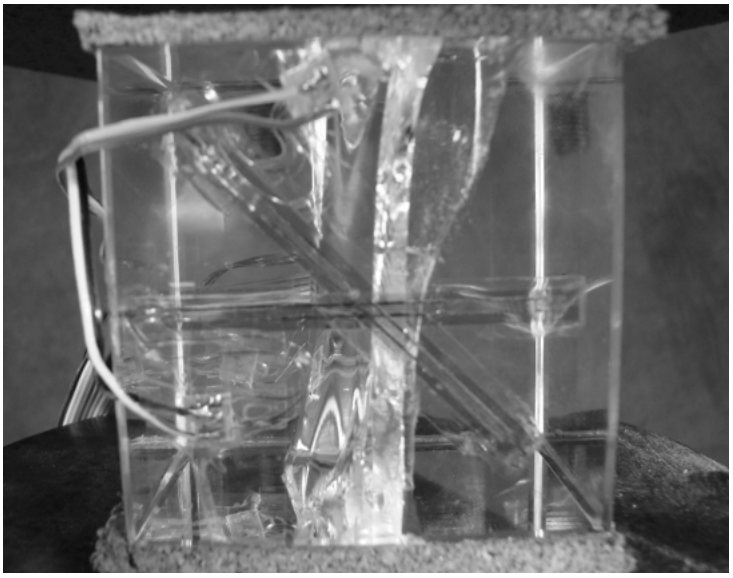

FIGURE A.3: Sample SGB after testing

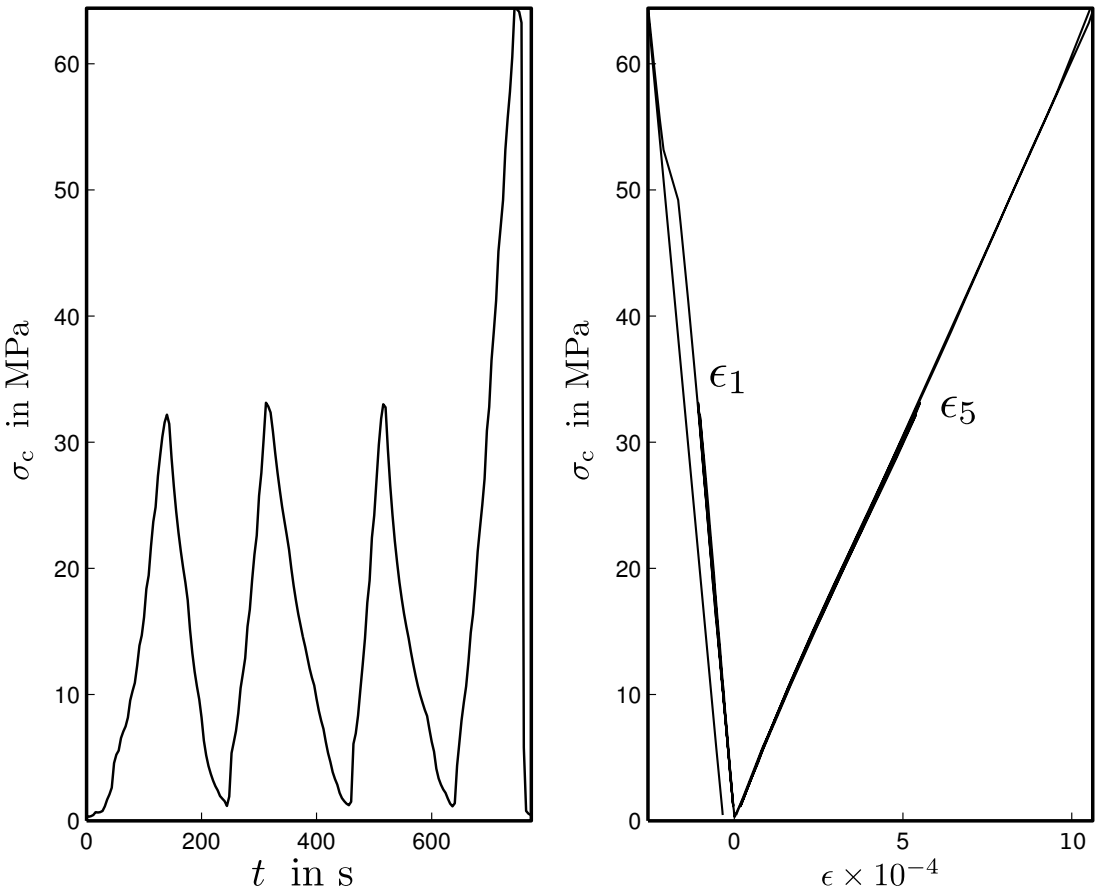

FIGURE A.4: Plots of time and deformations *vs.* vertical stress of sample SGB

A.1.3 Specimen SGC

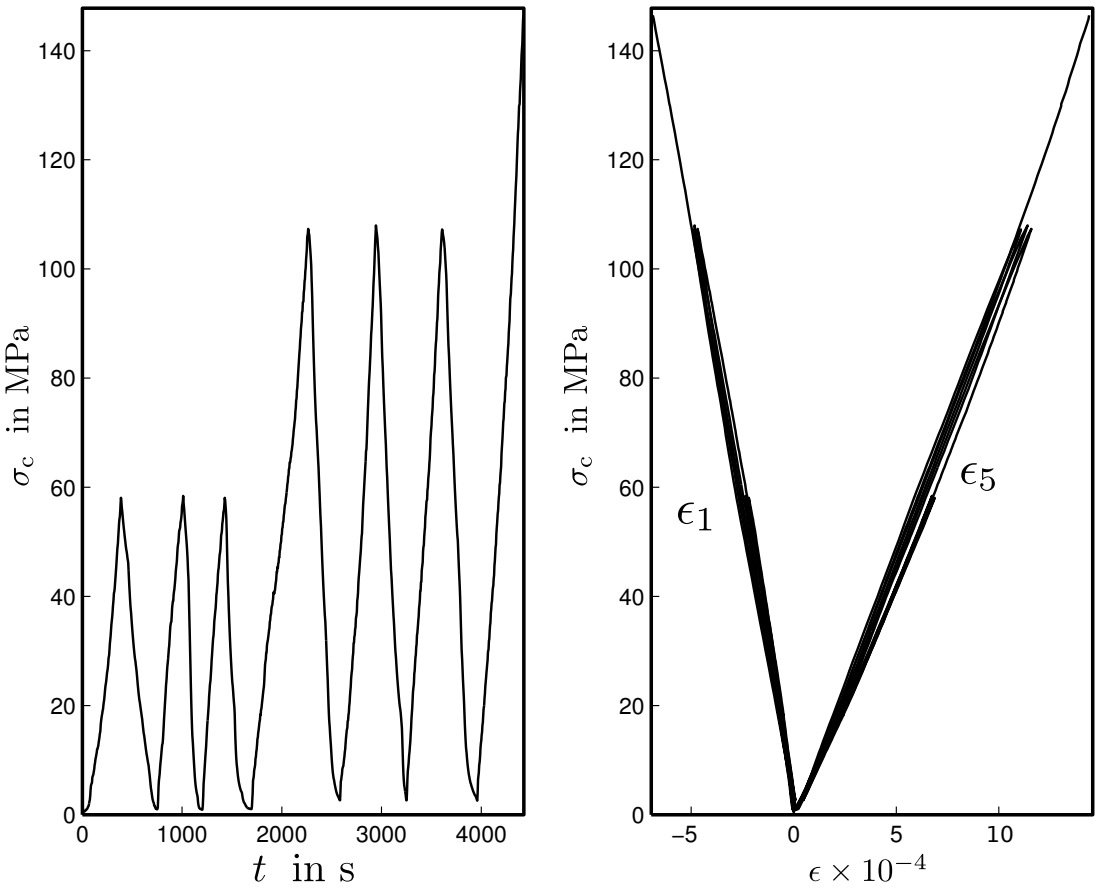

FIGURE A.5: Plots of time and deformations *vs.* vertical stress of sample SGC

A.1.4 Specimen SGD

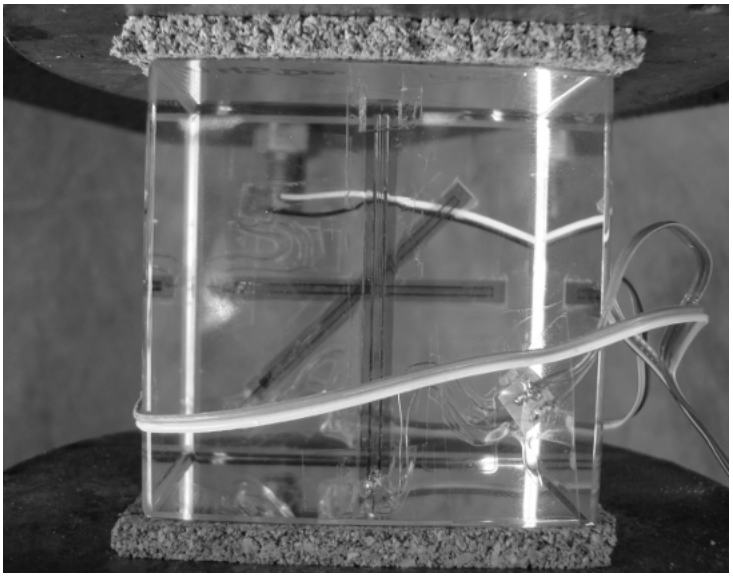

FIGURE A.6: Sample SGD before testing

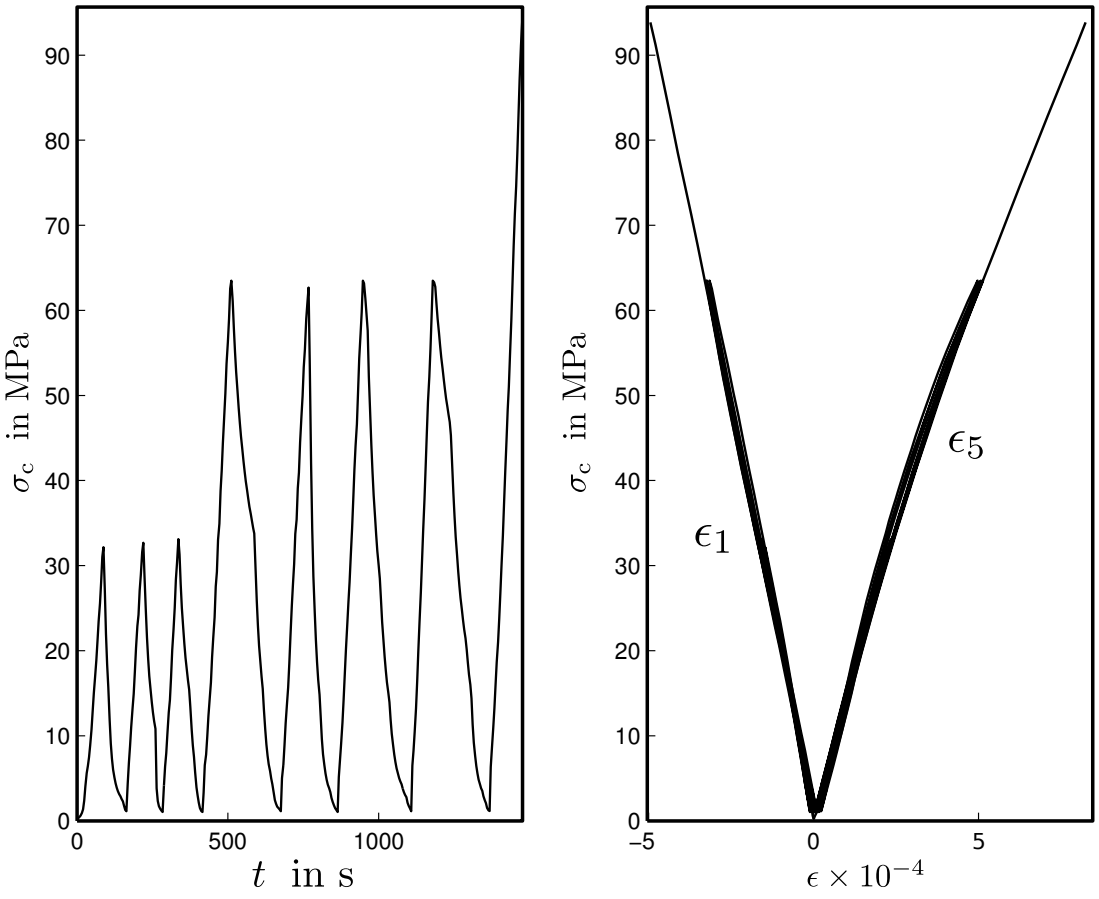

FIGURE A.7: Plots of time and deformations *vs.* vertical stress of sample SGD

A.2 NE Samples

TABLE A.2: Photographs and Plots shown of NE Samples in this Appendix.

Sample	Photographs		Plots		
	Before Testing	After Testing	Testing Speed	Strain Modulus	Elastic Modulus
000DA	1	1	1	1	1
000DB	1	1	1	1	1
000DC	1	1	1	1	1
030DA	1	1	1	1	1
030DB	1	1	1	1	1
030DC	1	1	1	1	1
045DB	1	0	1	1	1
045DC	1	1	1	1	1
060DA	1	1	1	1	1
060DB	1	0	1	1	1
060DC	1	1	1	1	1
090DA	1	1	1	1	1
090DB	1	1	1	1	1
090DC	1	1	1	1	1

Note. 1 corresponds to yes, and 0 corresponds to no.

A.2.1 Specimen 000DA

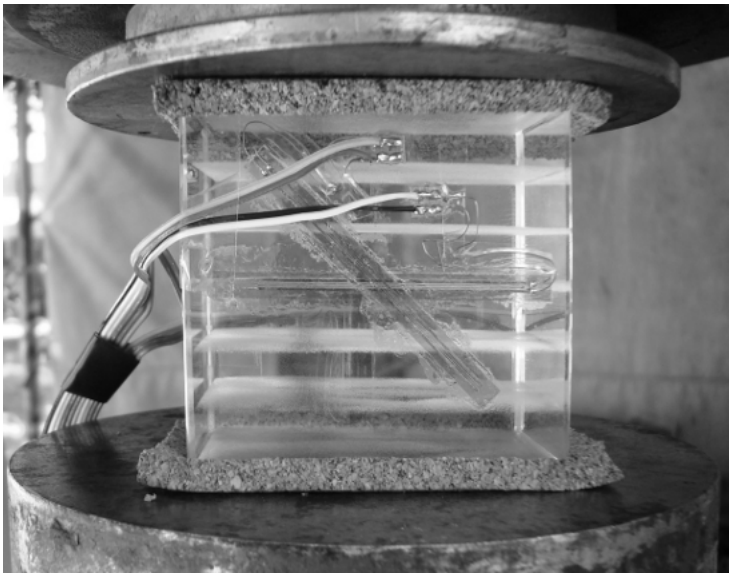

FIGURE A.8: Sample 000DA before testing

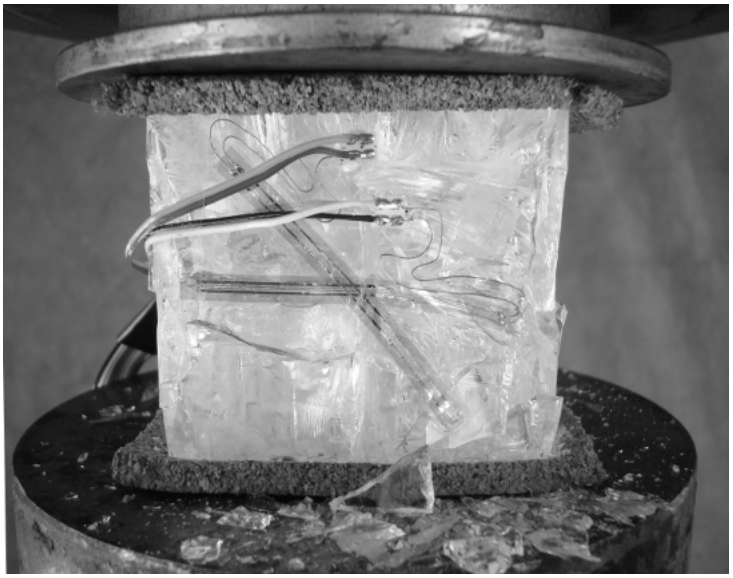

FIGURE A.9: Sample 000DA after testing

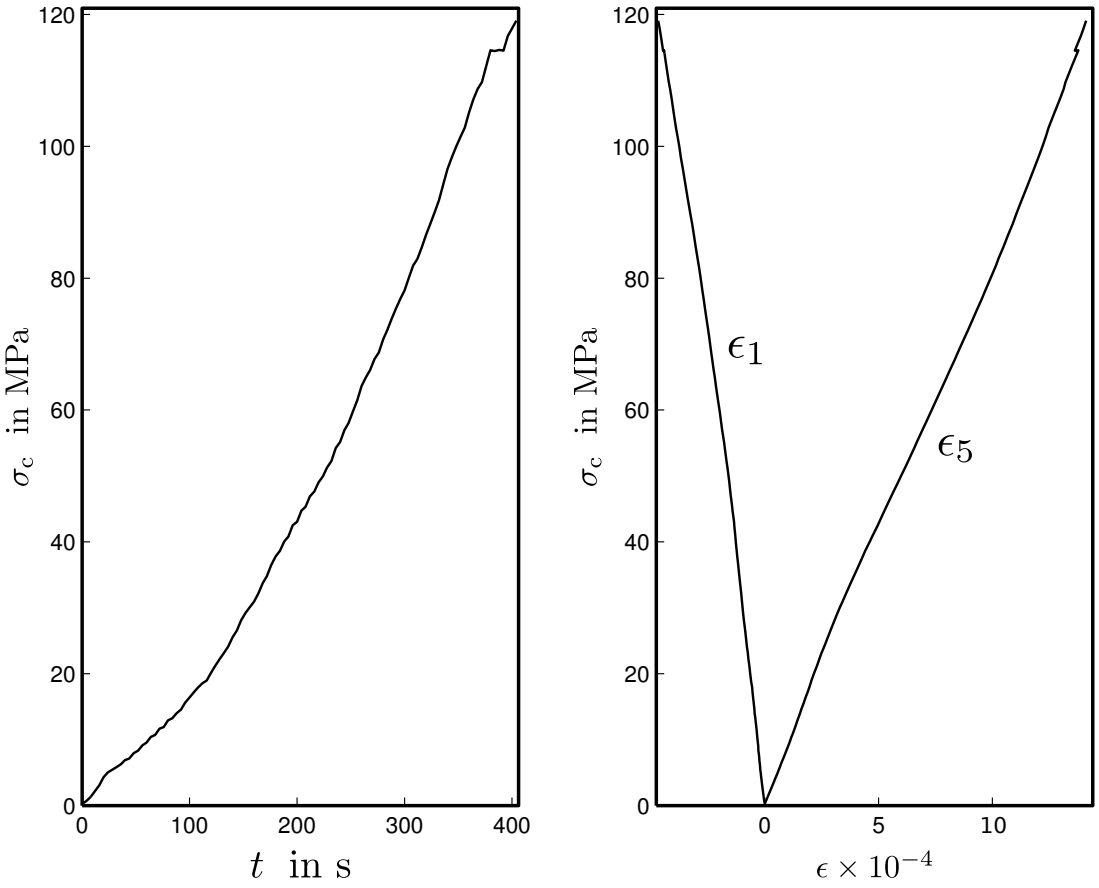

FIGURE A.10: Plots of time and deformations *vs.* vertical stress of sample 000DA

A.2.2 Specimen 000DB

FIGURE A.11: Sample 000DB before testing

FIGURE A.12: Sample 000DB after testing

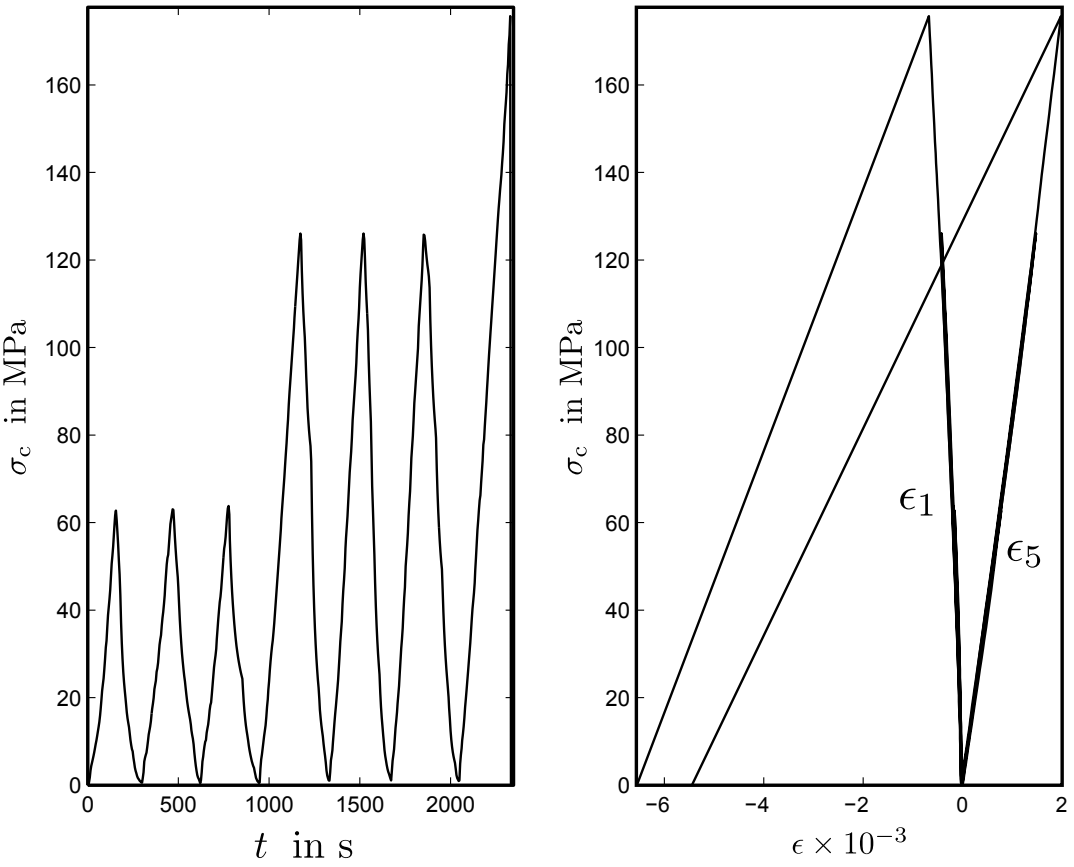

FIGURE A.13: Plots of time and deformations *vs.* vertical stress of sample 000DB

A.2.3 Specimen 000DC

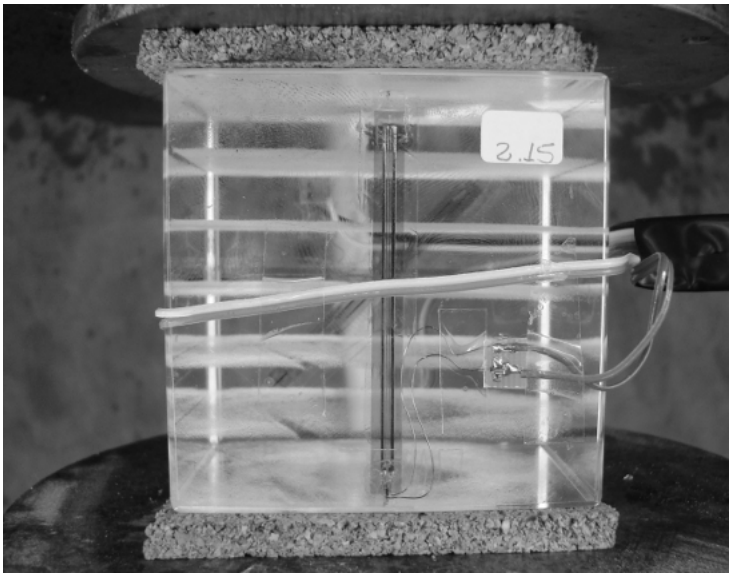

FIGURE A.14: Sample 000DC before testing

FIGURE A.15: Sample 000DC after testing

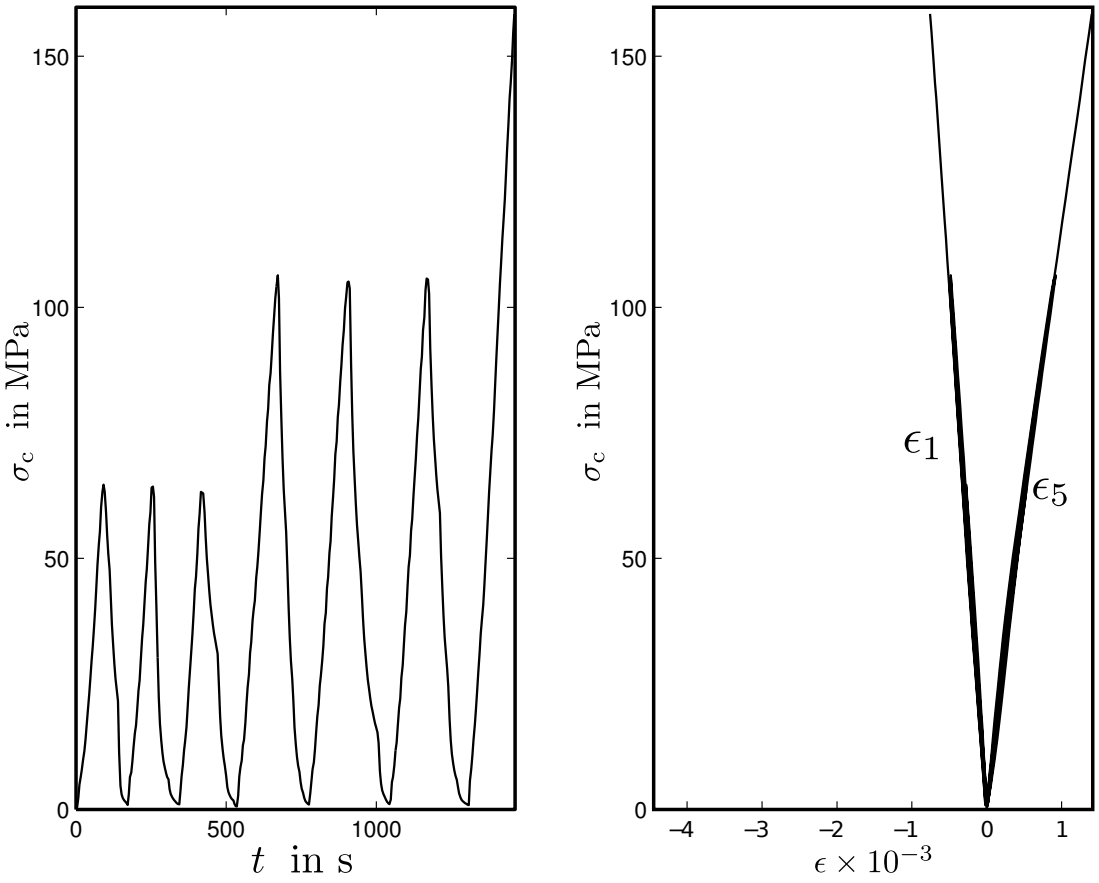

FIGURE A.16: Plots of time and deformations *vs.* vertical stress of sample 000DC

A.2.4 Specimen 030DA

FIGURE A.17: Sample 030DA before testing

FIGURE A.18: Sample 030DA after testing

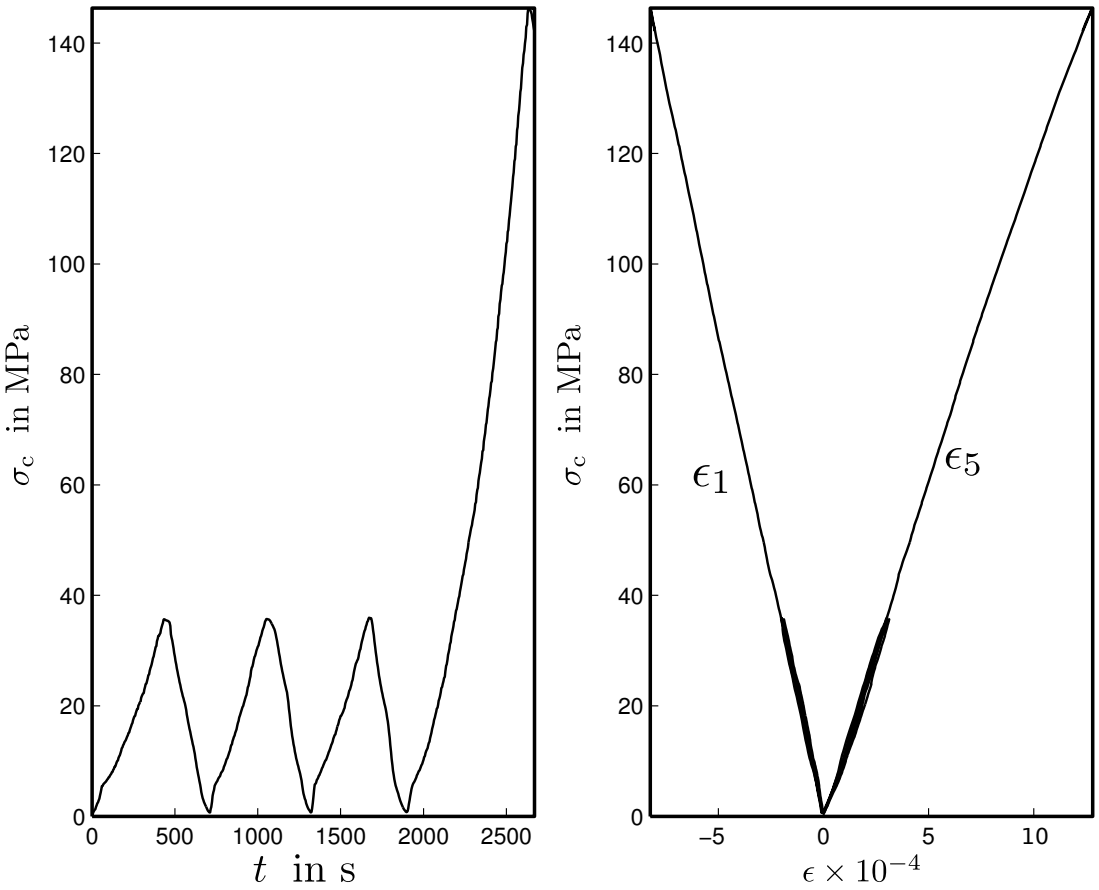

FIGURE A.19: Plots of time and deformations *vs.* vertical stress of sample 030DA

A.2.5 Specimen 030DB

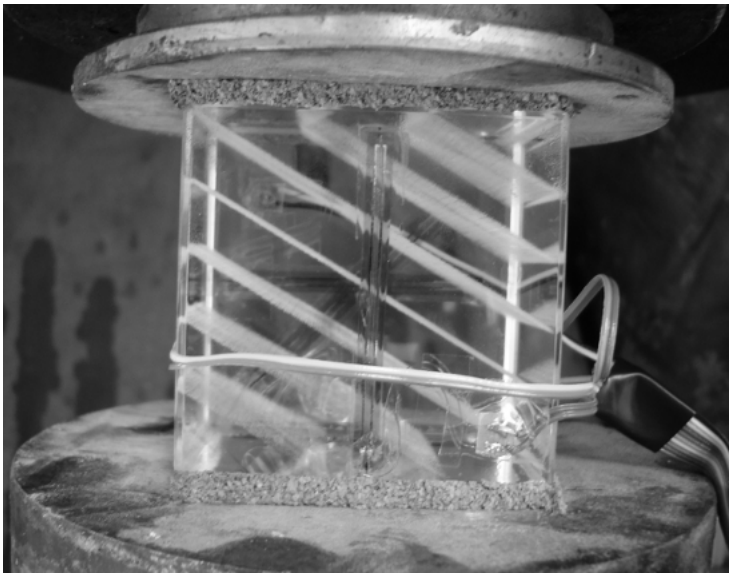

FIGURE A.20: Sample 030DB before testing

FIGURE A.21: Sample 030DB after testing

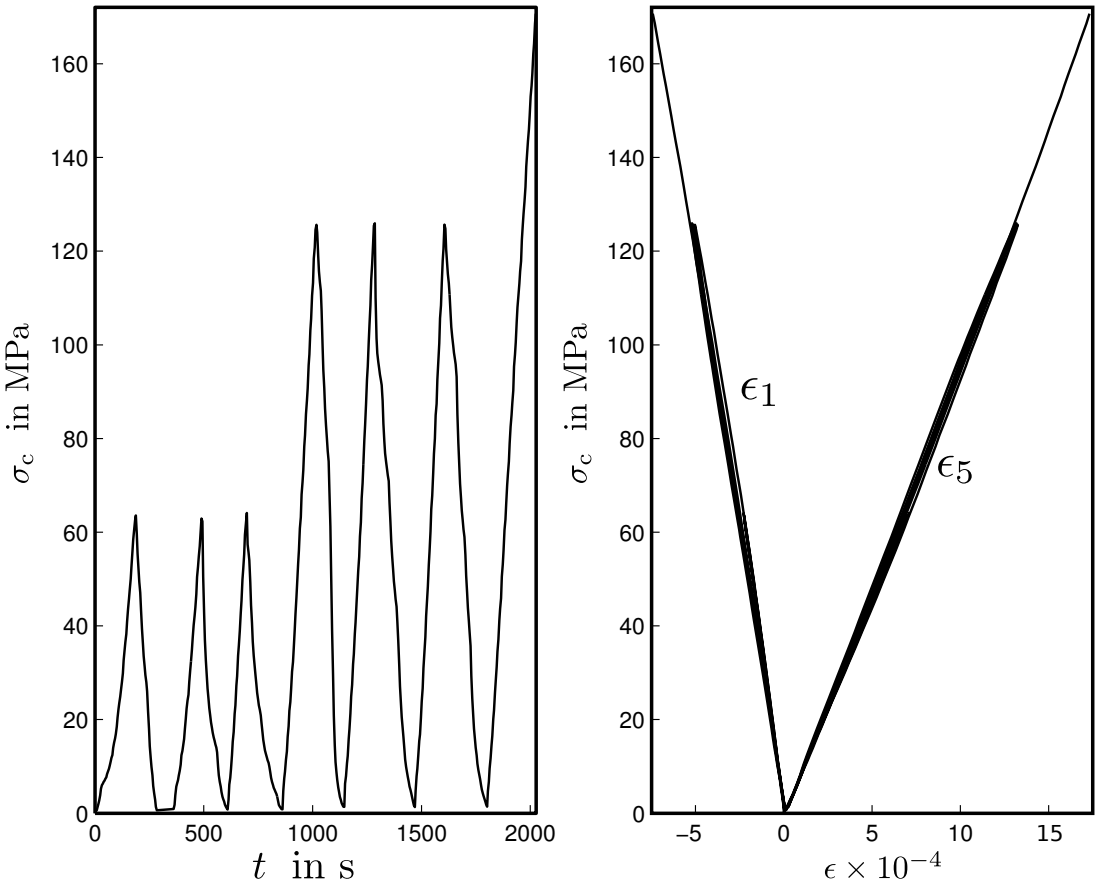

FIGURE A.22: Plots of time and deformations *vs.* vertical stress of sample 030DB

A.2.6 Specimen 030DC

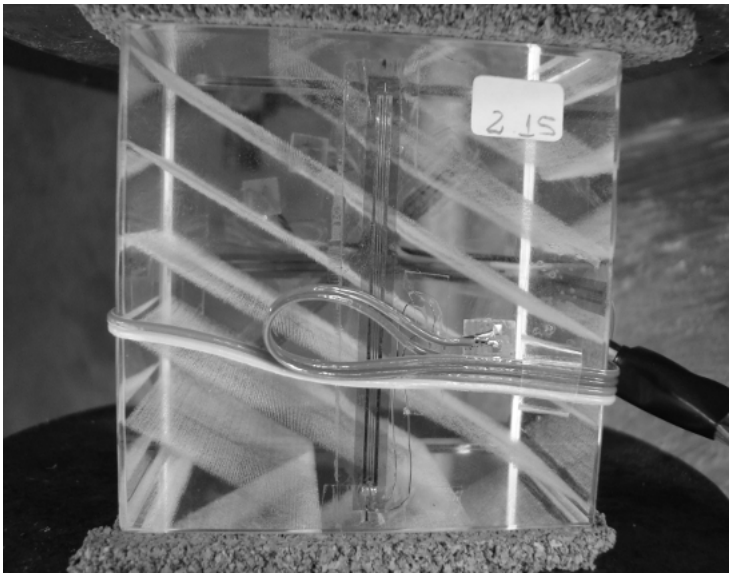

FIGURE A.23: Sample 030DC before testing

FIGURE A.24: Sample 030DC after testing

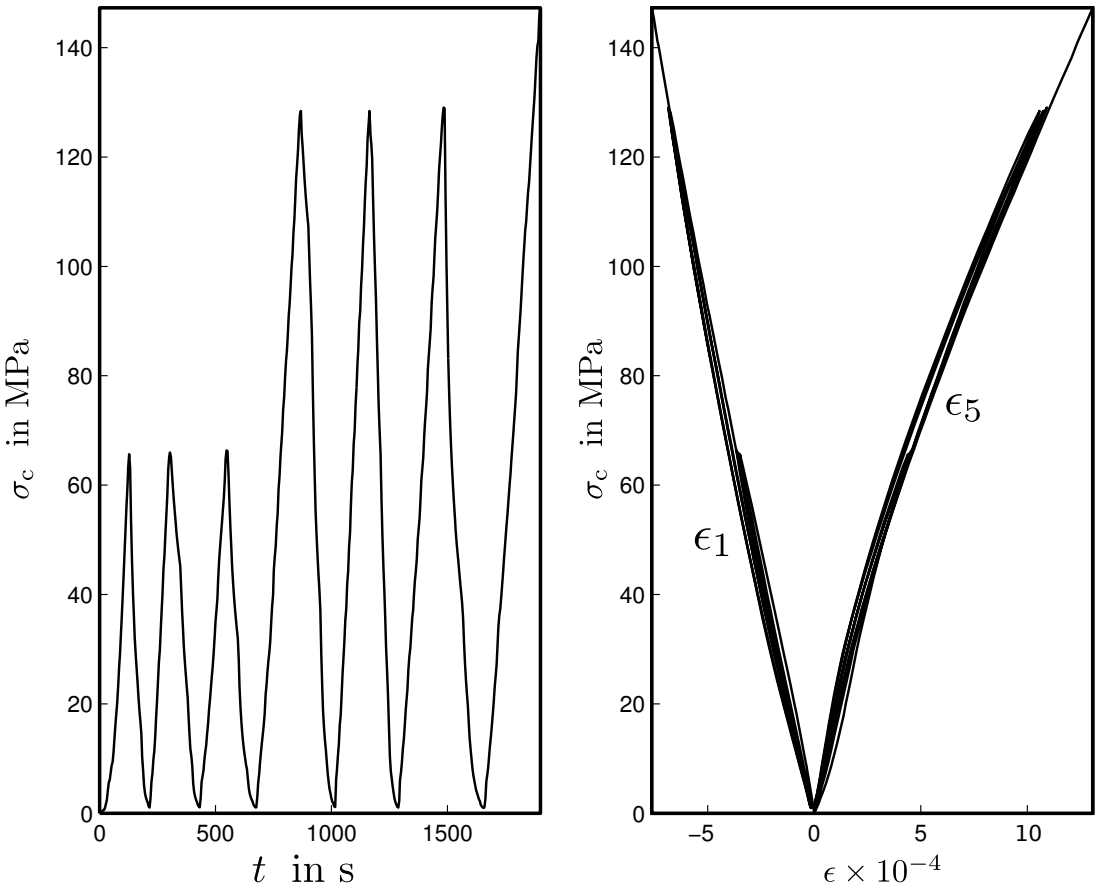

FIGURE A.25: Plots of time and deformations *vs.* vertical stress of sample 030DC

A.2.7 Specimen 045DB

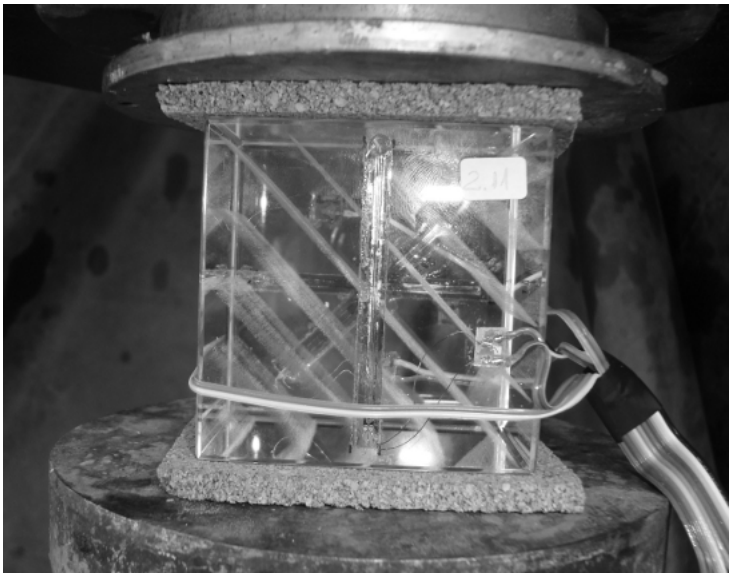

FIGURE A.26: Sample 045DB before testing

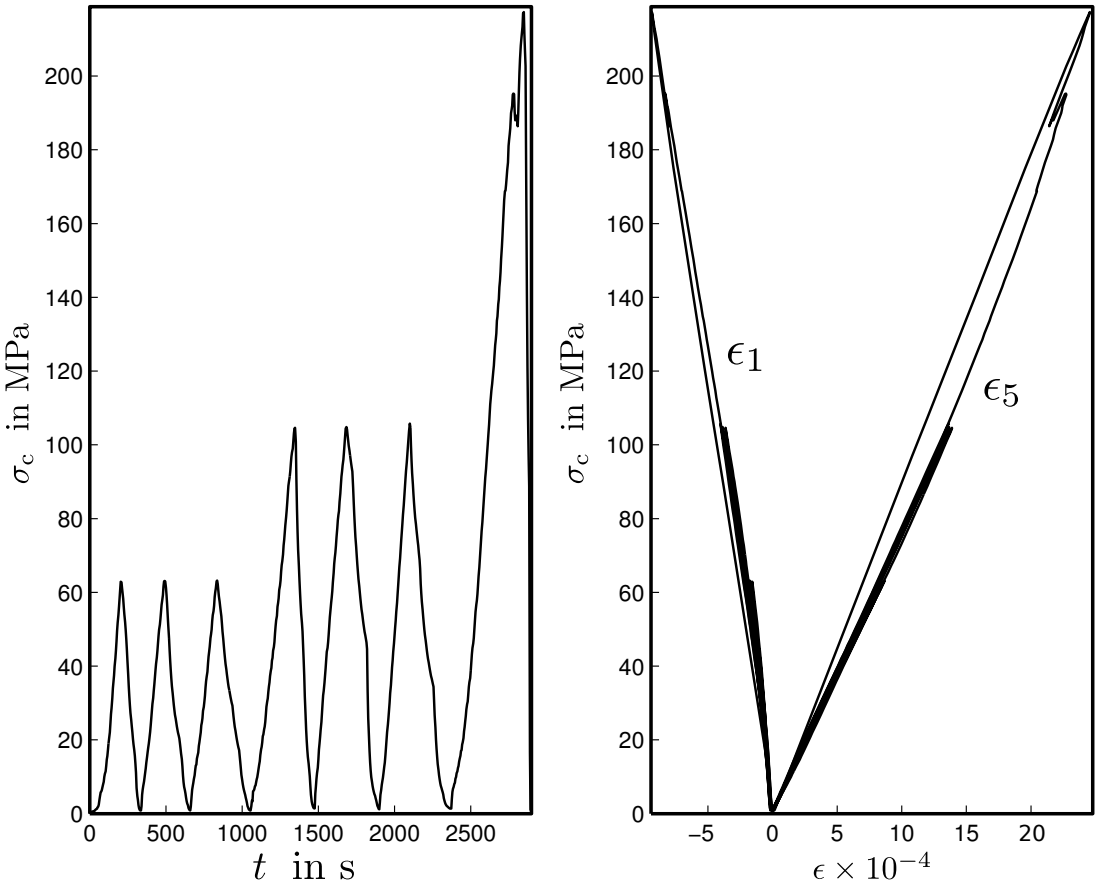

FIGURE A.27: Plots of time and deformations *vs.* vertical stress of sample 045DB

A.2.8 Specimen 045DC

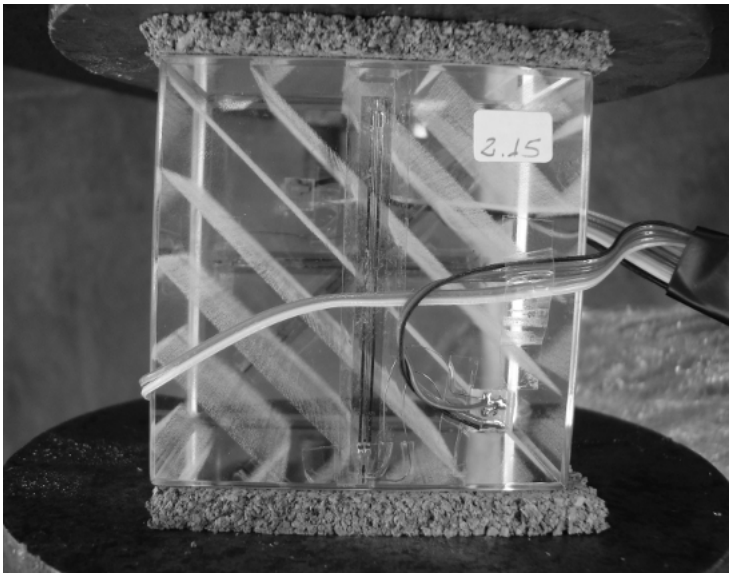

FIGURE A.28: Sample 045DC before testing

FIGURE A.29: Sample 045DC after testing

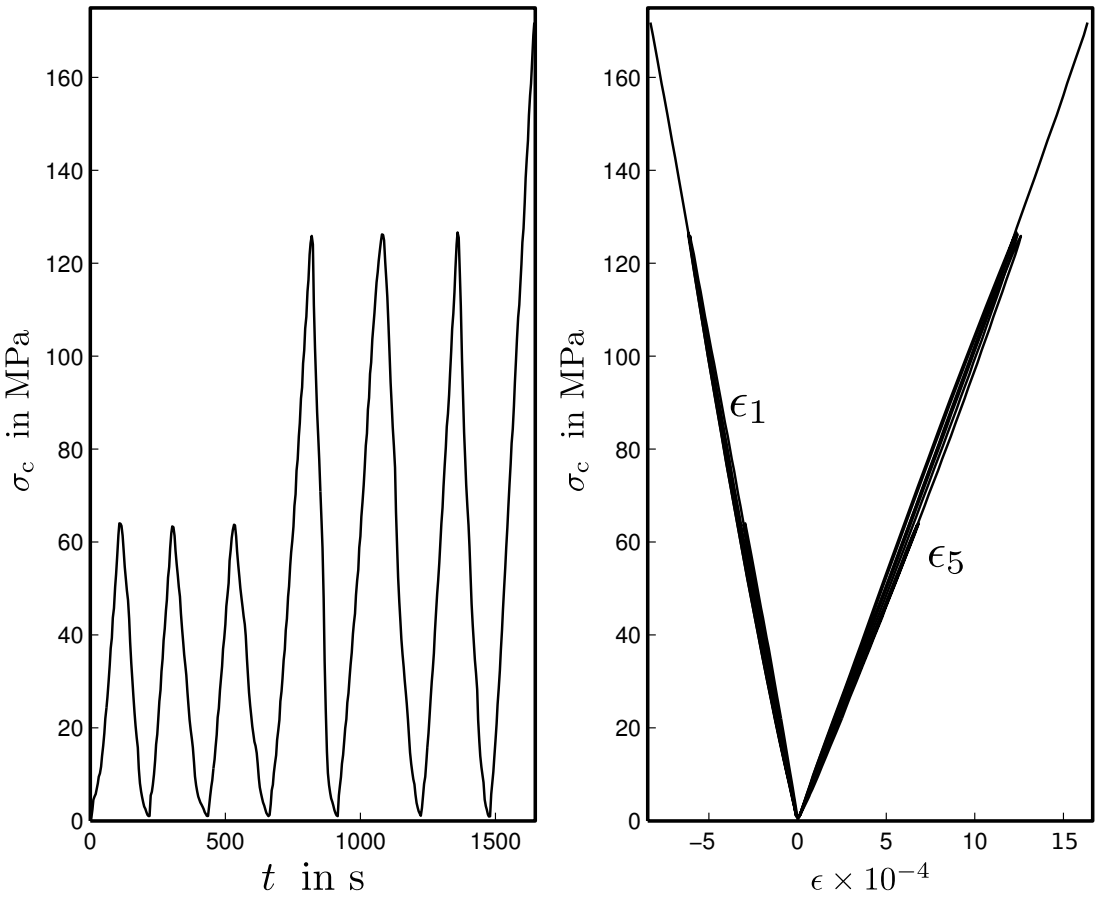

FIGURE A.30: Plots of time and deformations *vs.* vertical stress of sample 045DC

A.2.9 Specimen 060DA

FIGURE A.31: Sample 060DA before testing

FIGURE A.32: Sample 060DA after testing

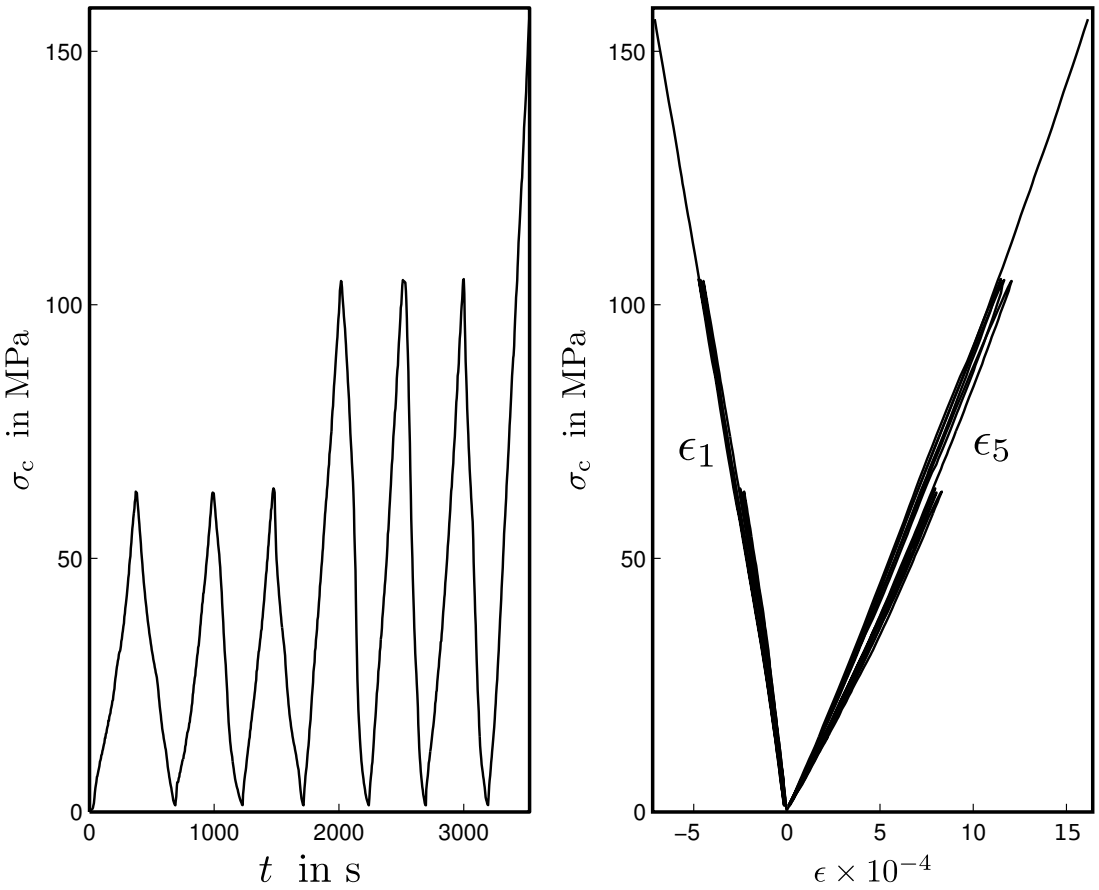

FIGURE A.33: Plots of time and deformations *vs.* vertical stress of sample 060DA

A.2.10 Specimen 060DB

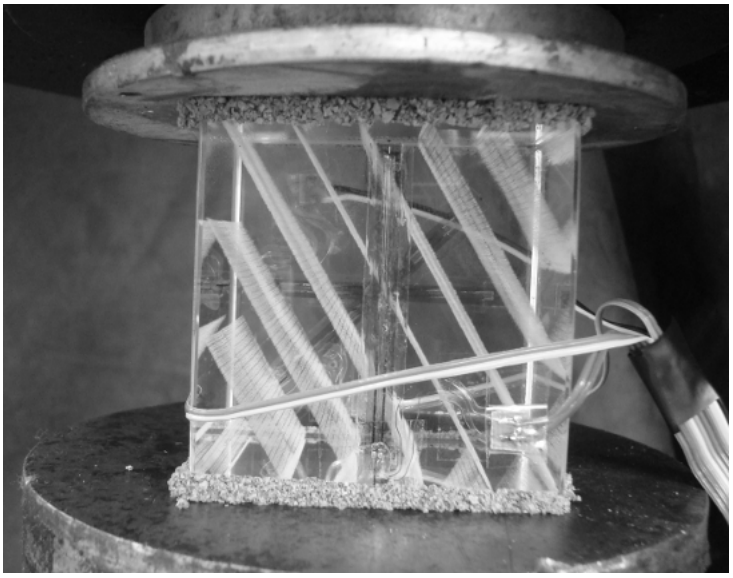

FIGURE A.34: Sample 060DB before testing

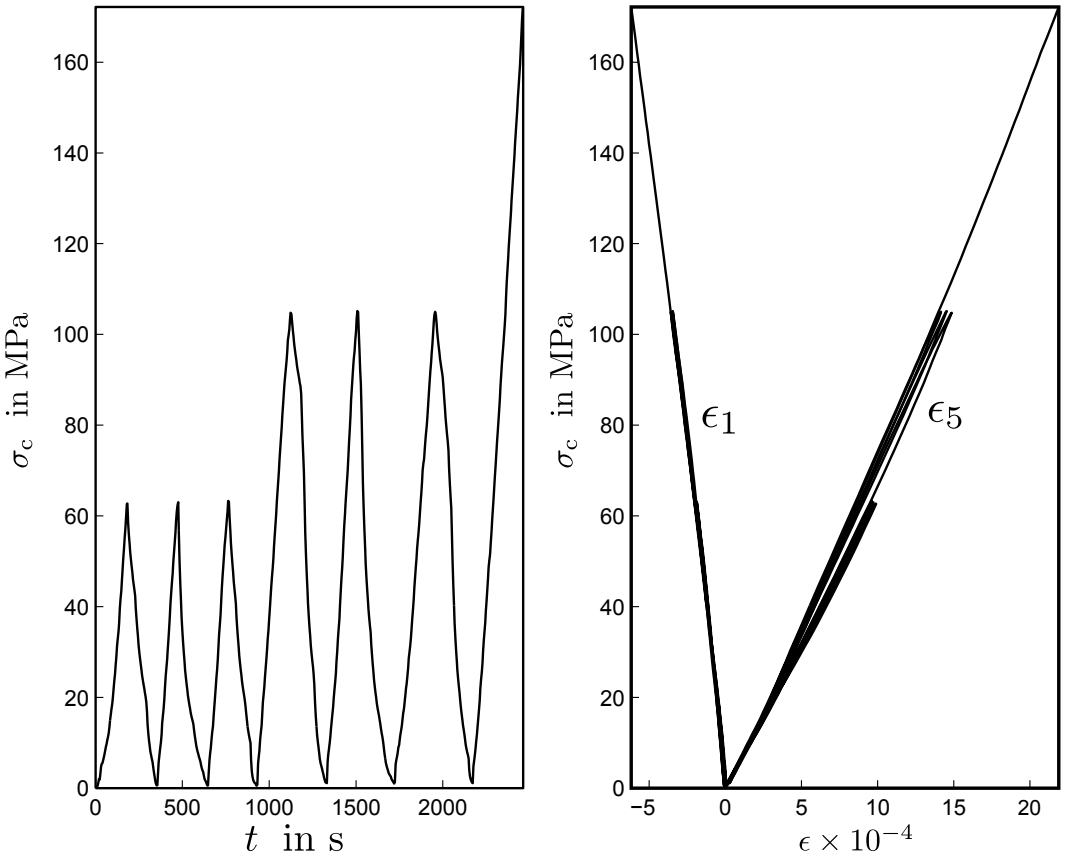

FIGURE A.35: Plots of time and deformations *vs.* vertical stress of sample 060DB

A.2.11 Specimen 060DC

FIGURE A.36: Sample 060DC before testing

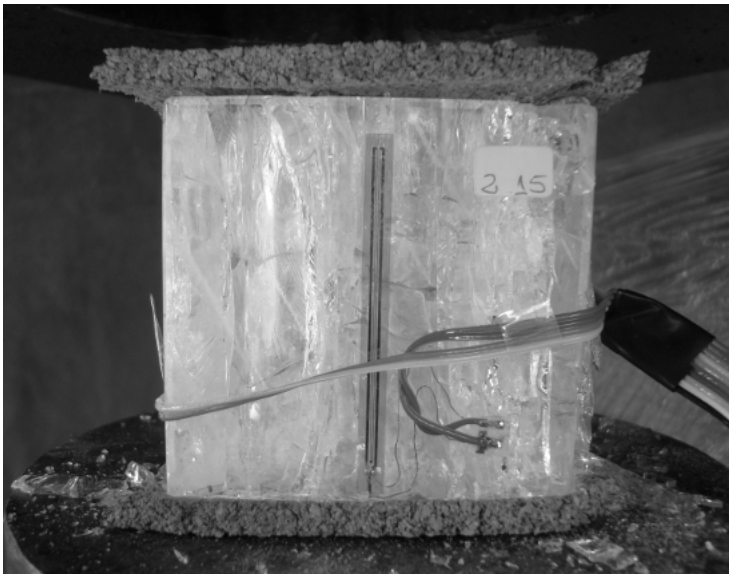

FIGURE A.37: Sample 060DC after testing

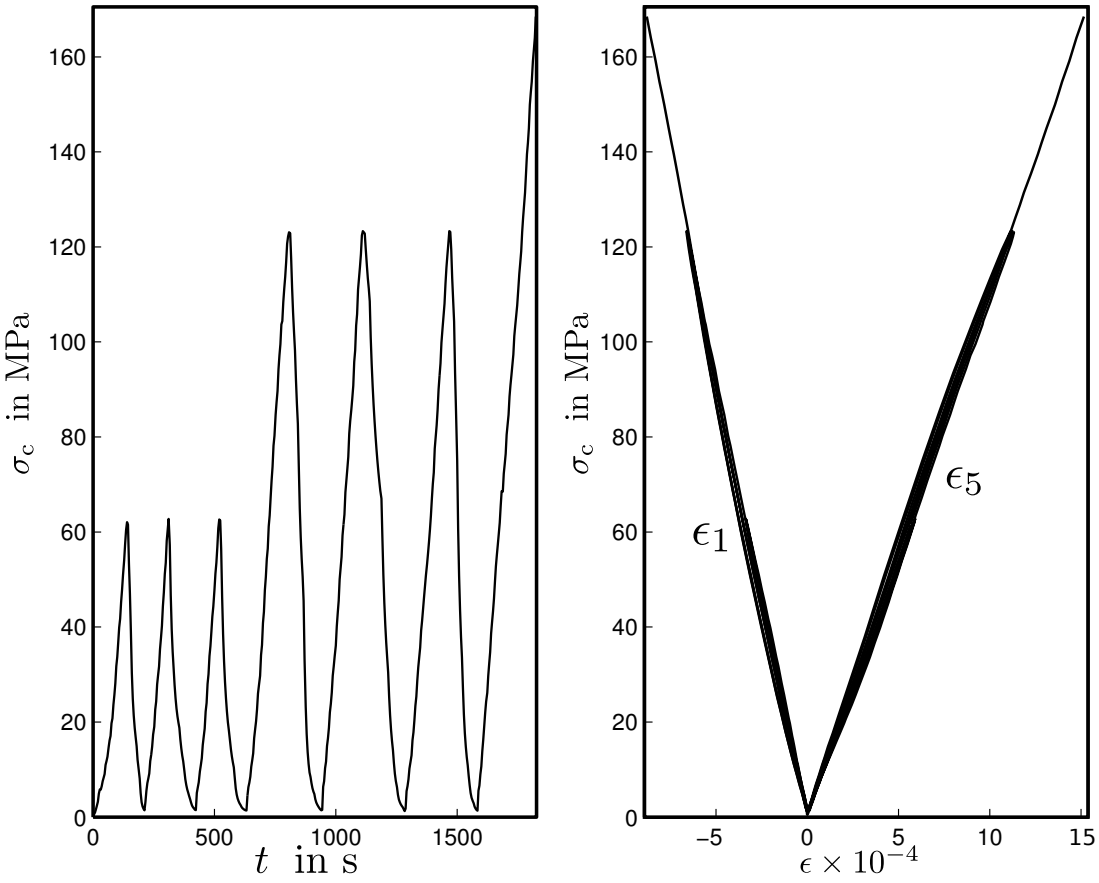

FIGURE A.38: Plots of time and deformations *vs.* vertical stress of sample 060DC

A.2.12 Specimen 090DA

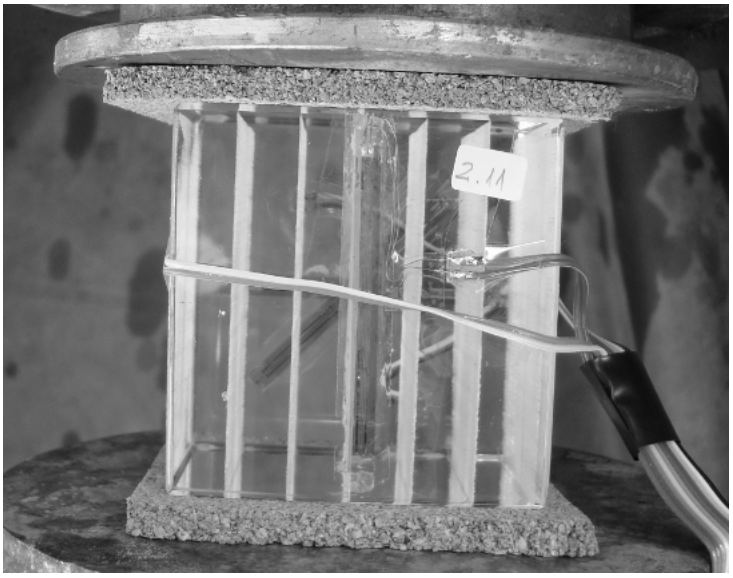

FIGURE A.39: Sample 090DA before testing

FIGURE A.40: Sample 090DA after testing

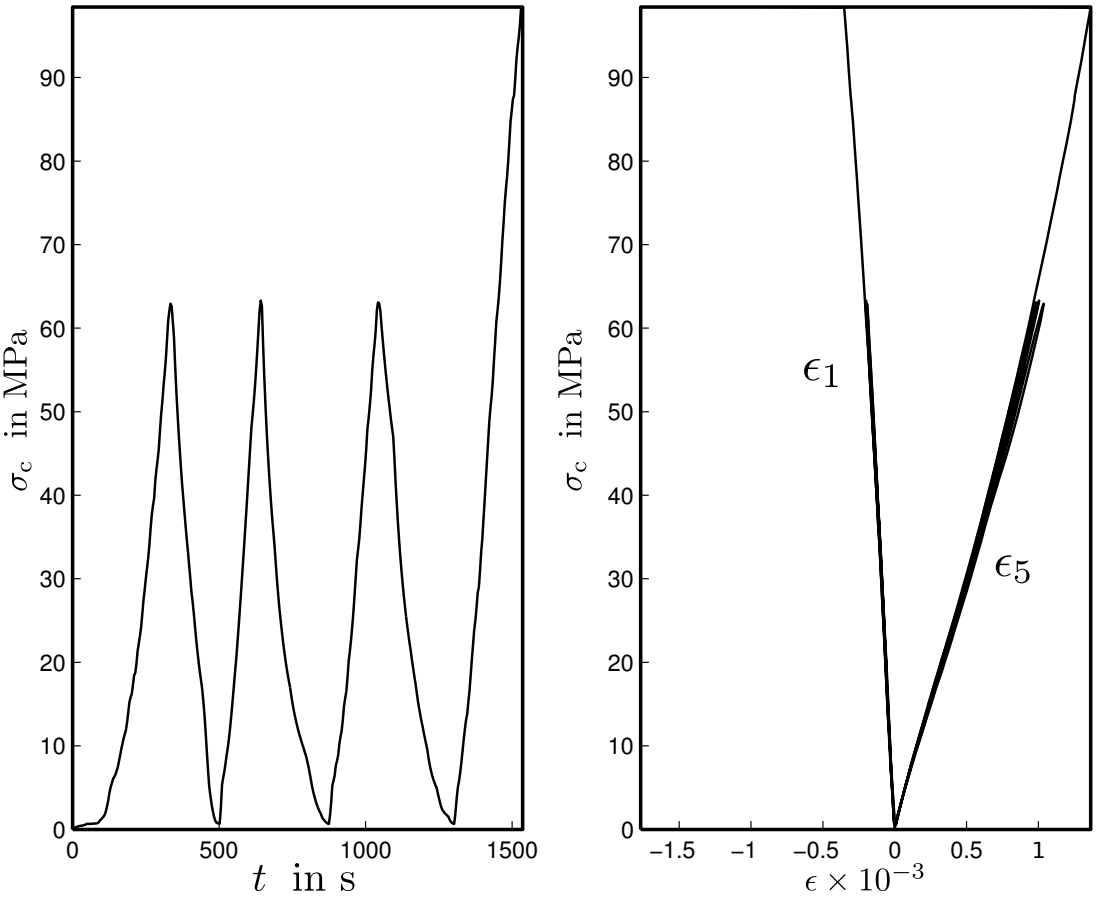

FIGURE A.41: Plots of time and deformations *vs.* vertical stress of sample 090DA

A.2.13 Specimen 090DB

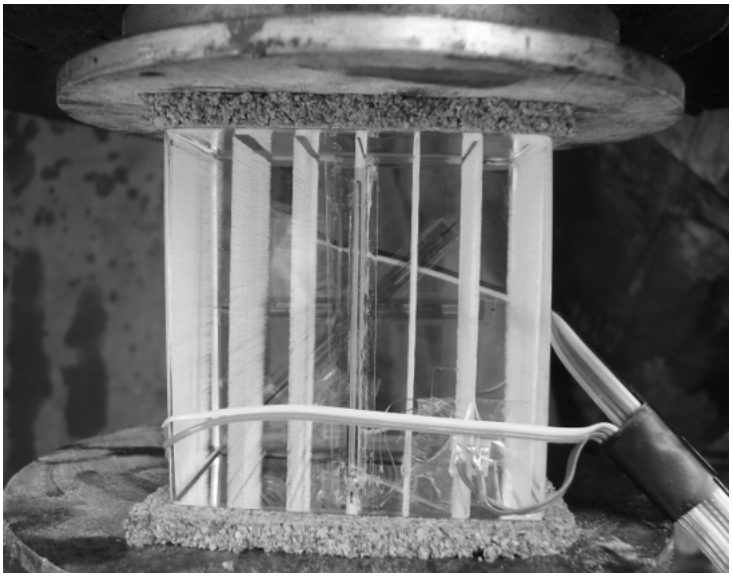

FIGURE A.42: Sample 090DB before testing

FIGURE A.43: Sample 090DB after testing

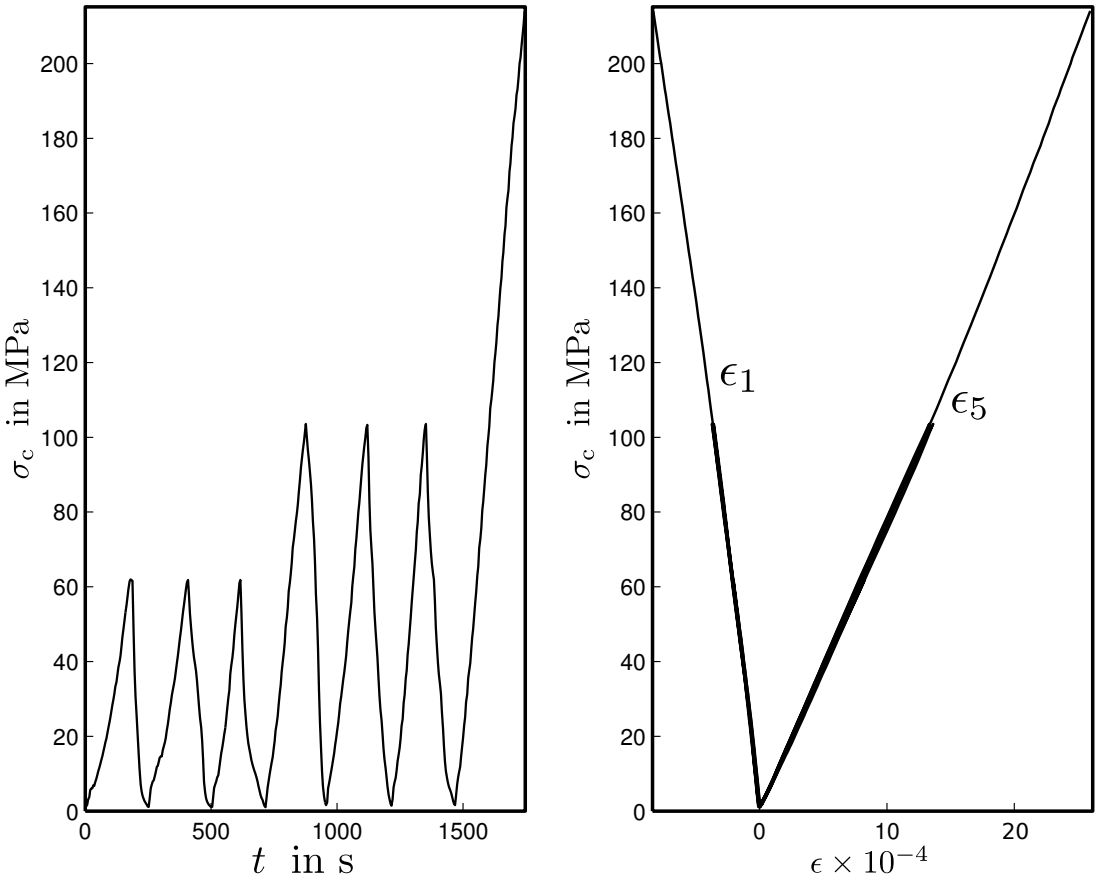

FIGURE A.44: Plots of time and deformations *vs.* vertical stress of sample 090DB

A.2.14 Specimen 090DC

FIGURE A.45: Sample 090DC before testing

FIGURE A.46: Sample 090DC after testing

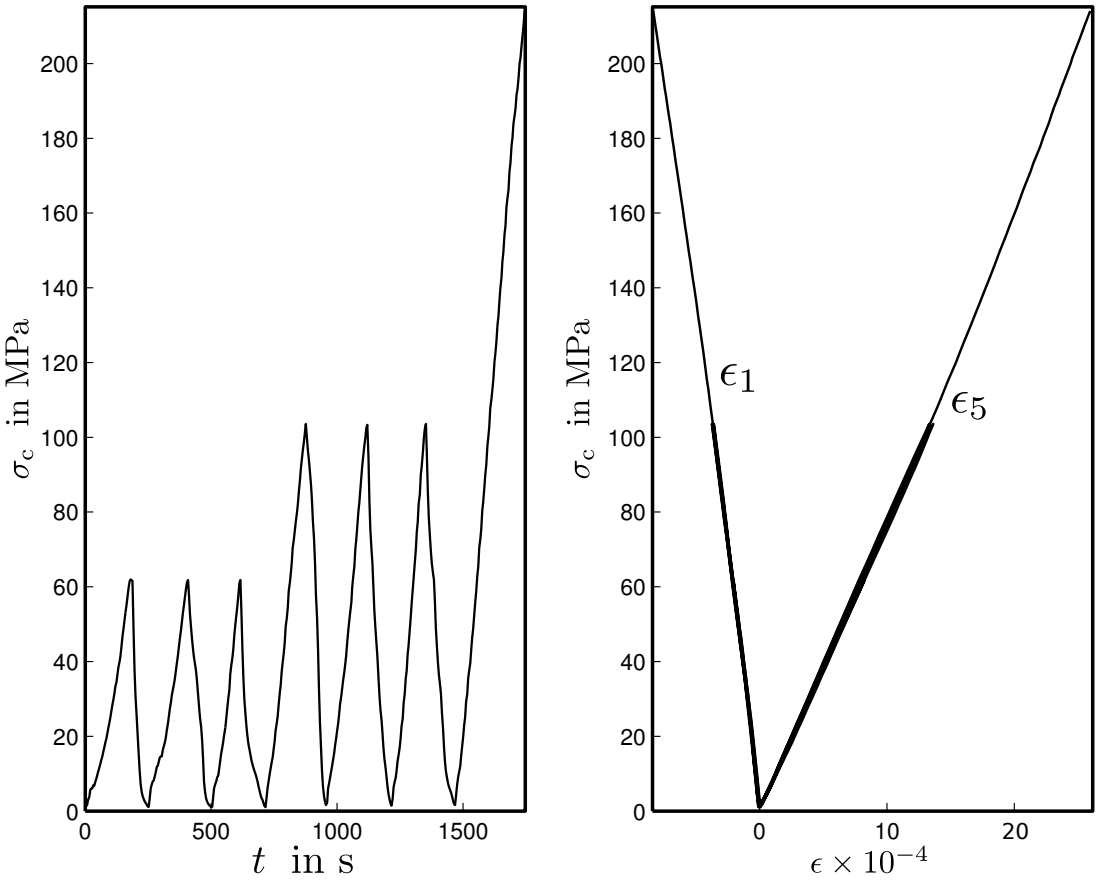

FIGURE A.47: Plots of time and deformations *vs.* vertical stress of sample 090DC

A.3 NED Samples

TABLE A.3: Photographs and Plots shown of NED Samples in this Appendix.

Sample	Photographs		Plots		
	Before Testing	After Testing	Testing Speed	Strain Modulus	Elastic Modulus
000VA	1	0	1	1	1
000VB	1	1	1	1	1
000VC	1	1	1	1	1
030VA	1	1	1	1	1
030VB	1	1	1	1	1
030VC	1	1	1	1	1
045VA	1	0	1	1	1
045VB	1	1	1	1	1
045VC	1	1	1	1	1
060VA	1	1	1	1	1
060VB	1	1	1	1	1
060VC	1	0	1	1	1
090VA	1	0	1	1	1
090VB	1	1	1	1	1
090VC	1	0	1	1	1

Note. 1 corresponds to yes, and 0 corresponds to no.

A.3.1 Specimen 000VA

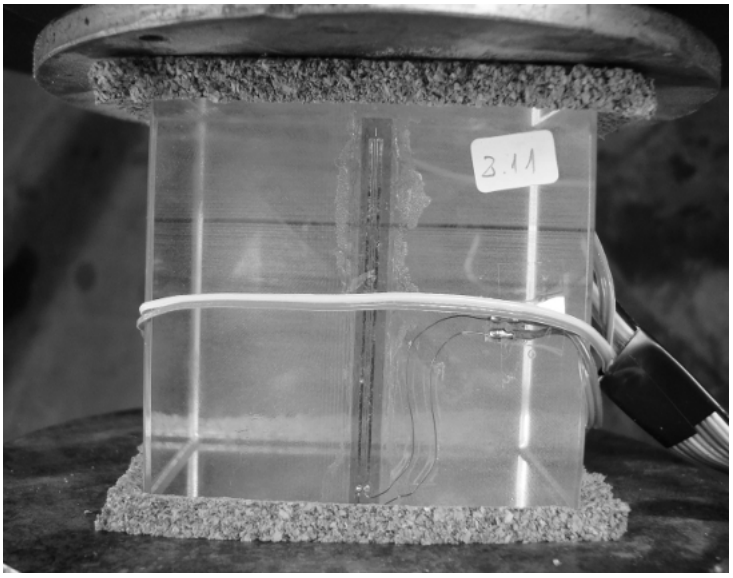

FIGURE A.48: Sample 000VA before testing

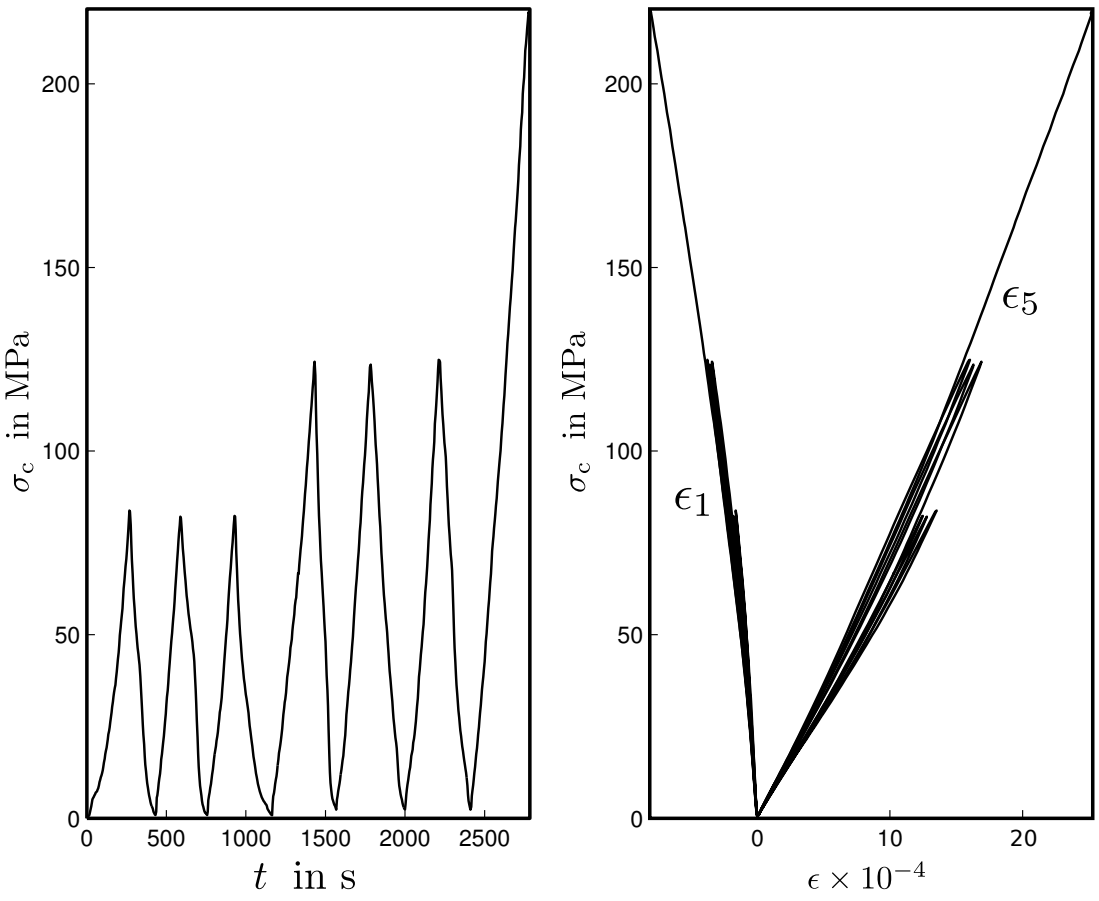

FIGURE A.49: Plots of time and deformations *vs.* vertical stress of sample 000VA

A.3.2 Specimen 000VB

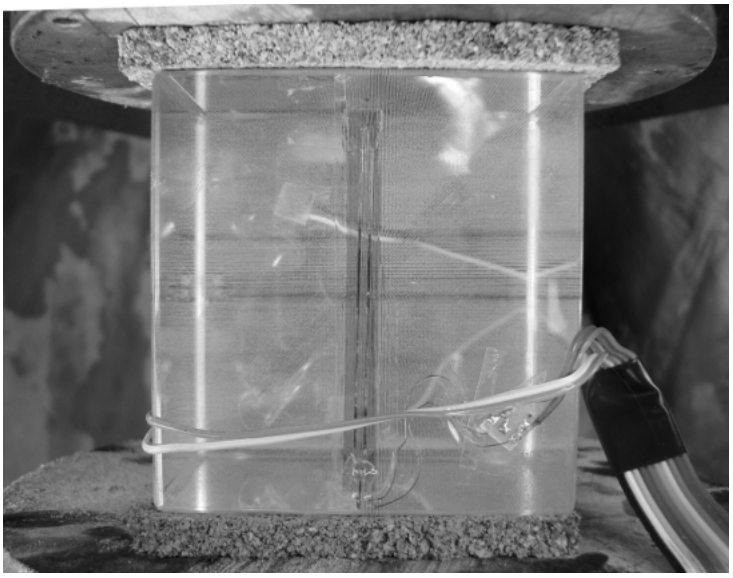

FIGURE A.50: Sample 000VB before testing

FIGURE A.51: Sample 000VB after testing

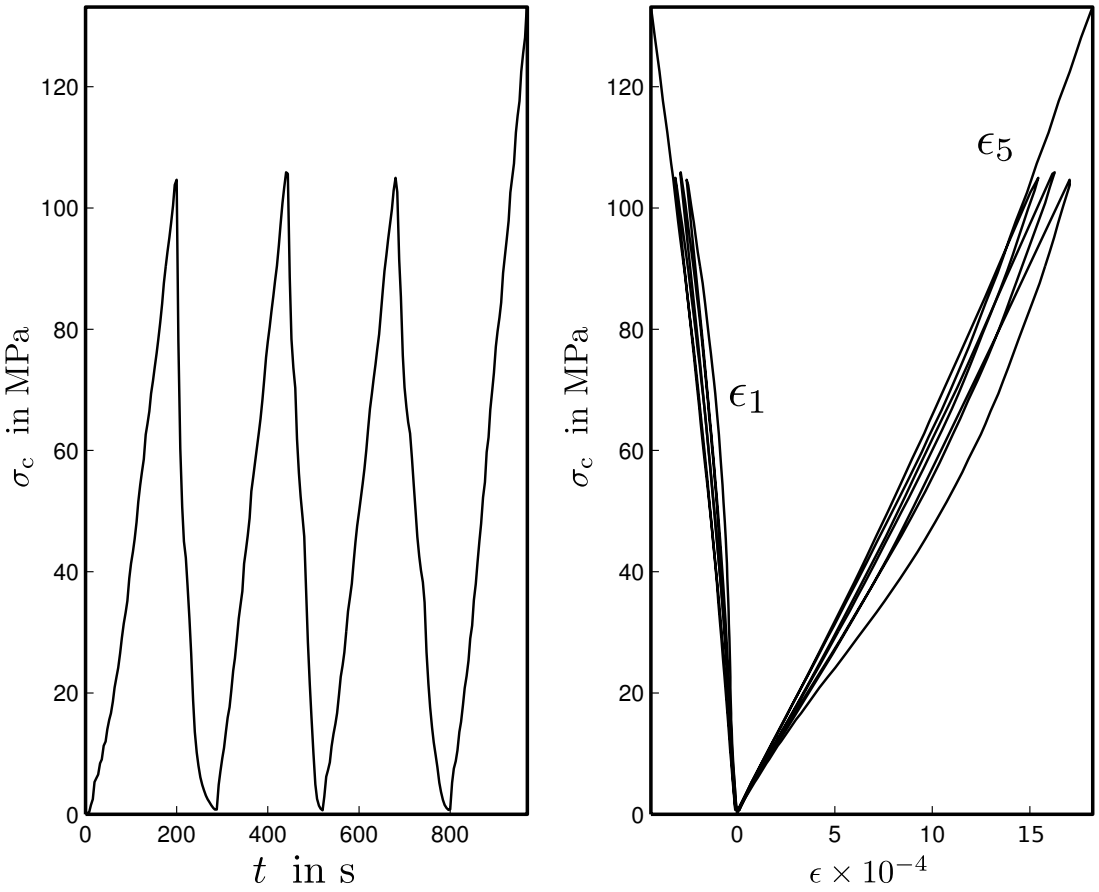

FIGURE A.52: Plots of time and deformations *vs.* vertical stress of sample 000VB

A.3.3 Specimen 000VC

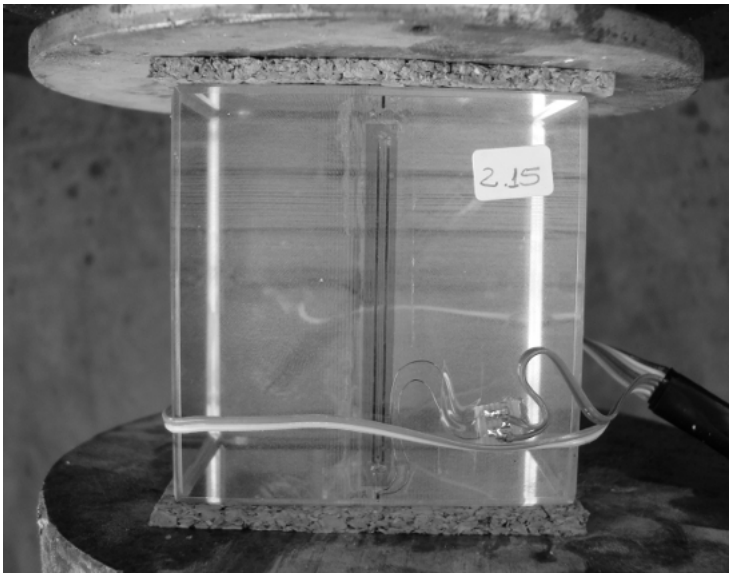

FIGURE A.53: Sample 000VC before testing

FIGURE A.54: Sample 000VC after testing

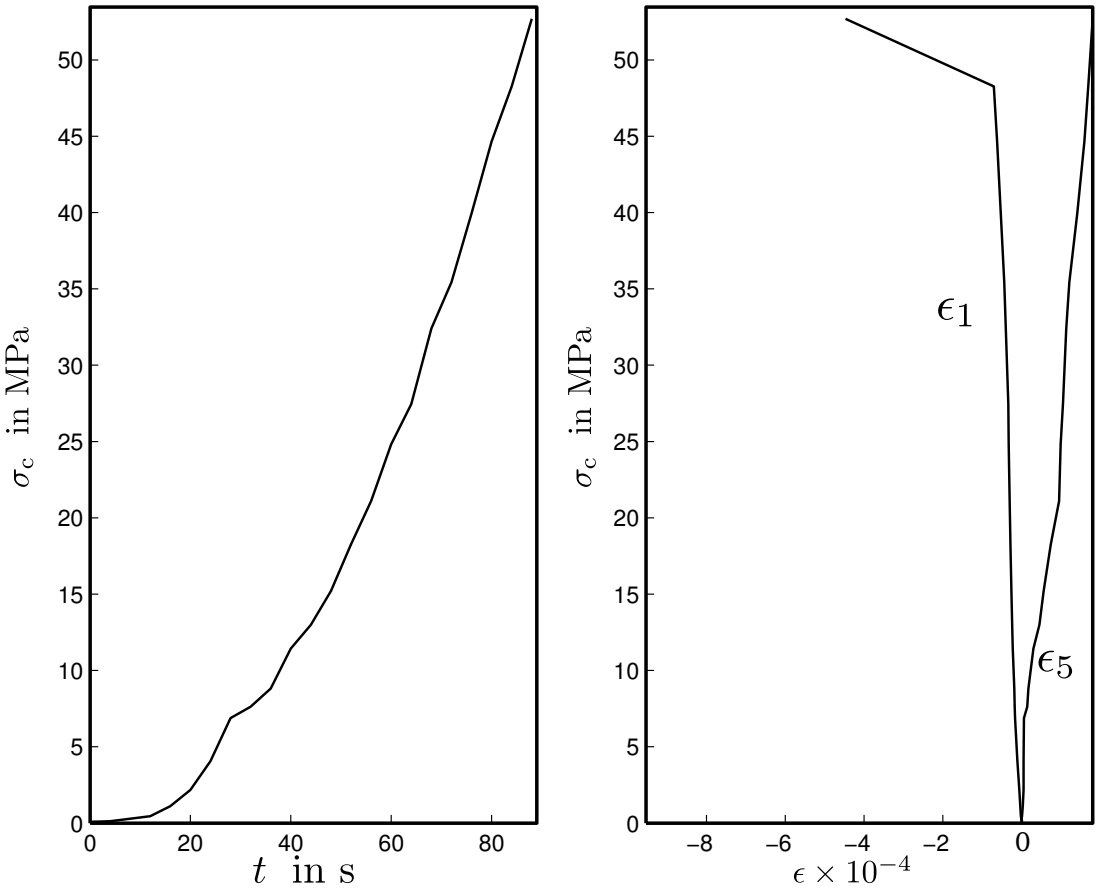

FIGURE A.55: Plots of time and deformations *vs.* vertical stress of sample 000VC

A.3.4 Specimen 030VA

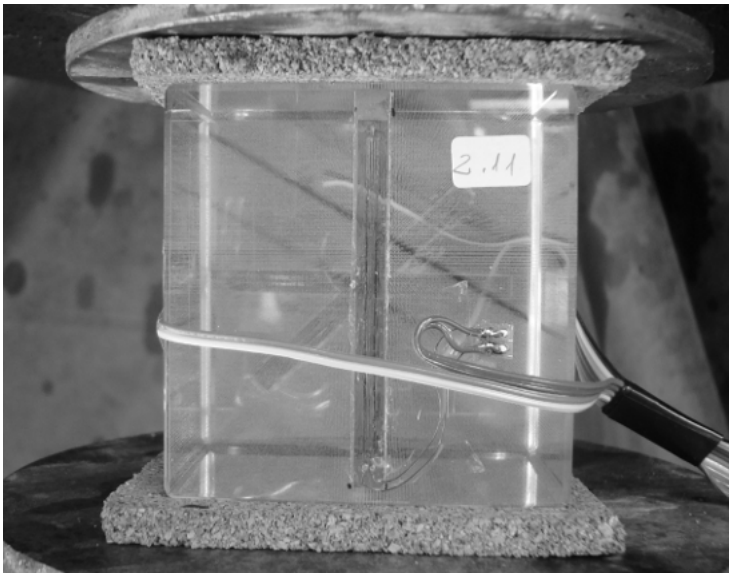

FIGURE A.56: Sample 030VA before testing

FIGURE A.57: Sample 030VA after testing

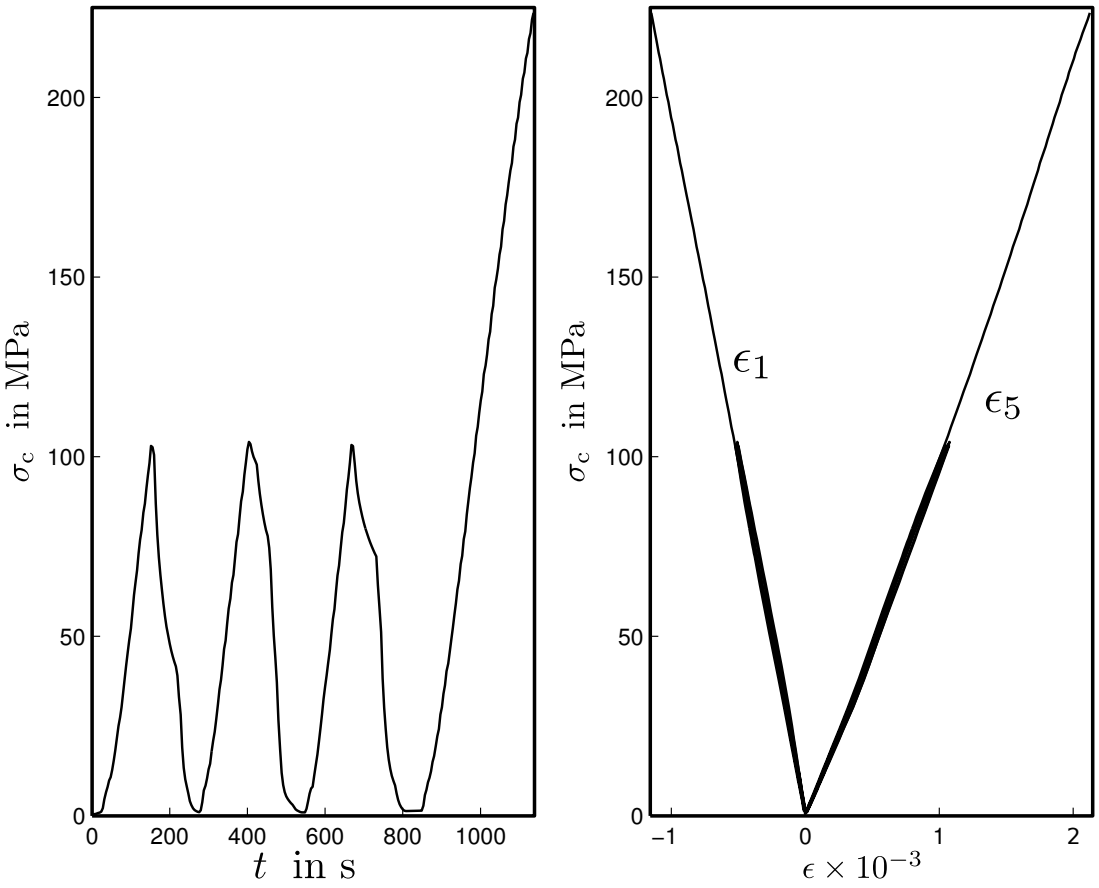

FIGURE A.58: Plots of time and deformations *vs.* vertical stress of sample 030VA

A.3.5 Specimen 030VB

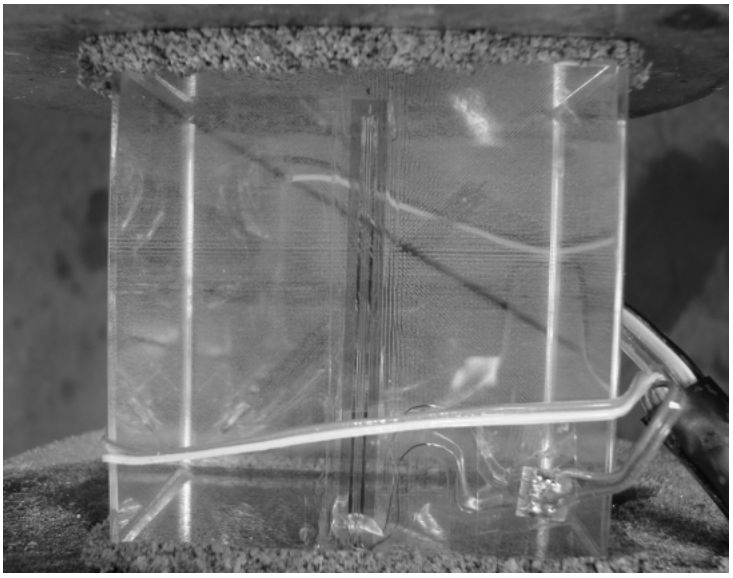

FIGURE A.59: Sample 030VB before testing

FIGURE A.60: Sample 030VB after testing

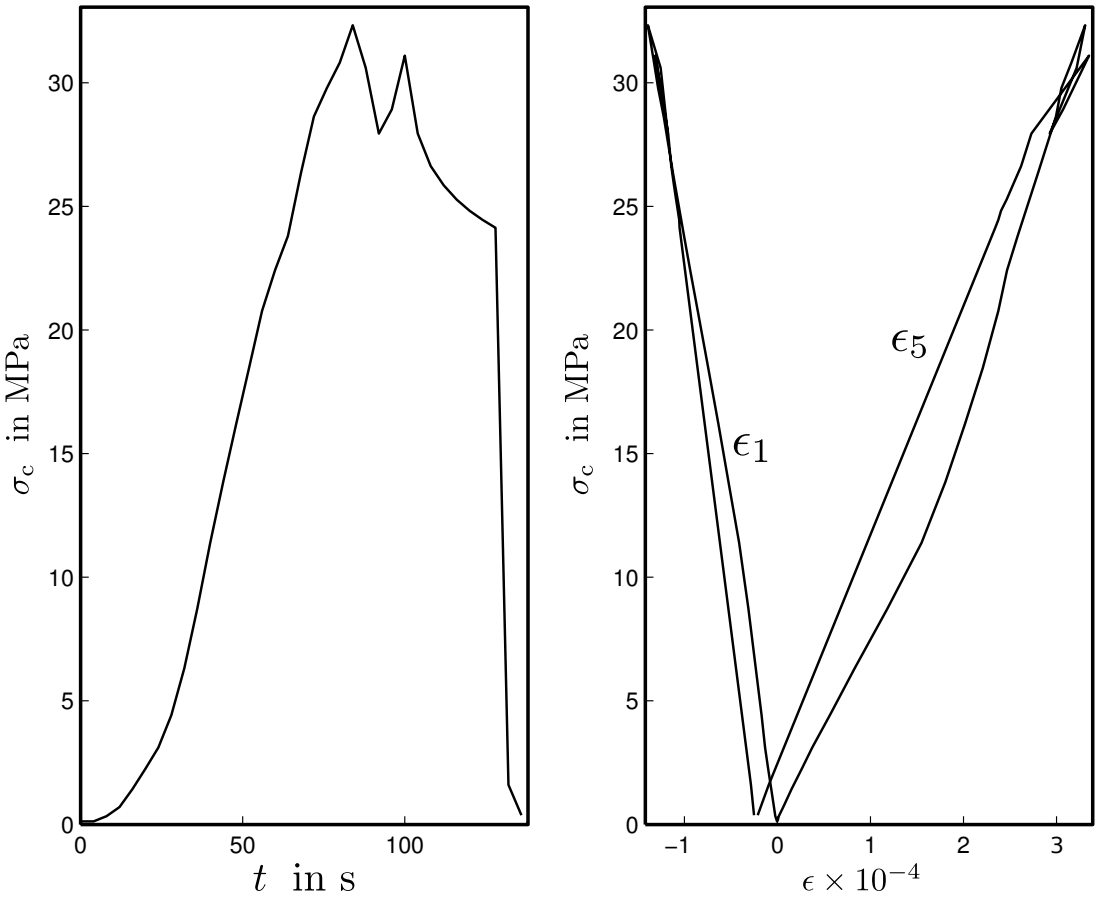

FIGURE A.61: Plots of time and deformations *vs.* vertical stress of sample 030VB

A.3.6 Specimen 030VC

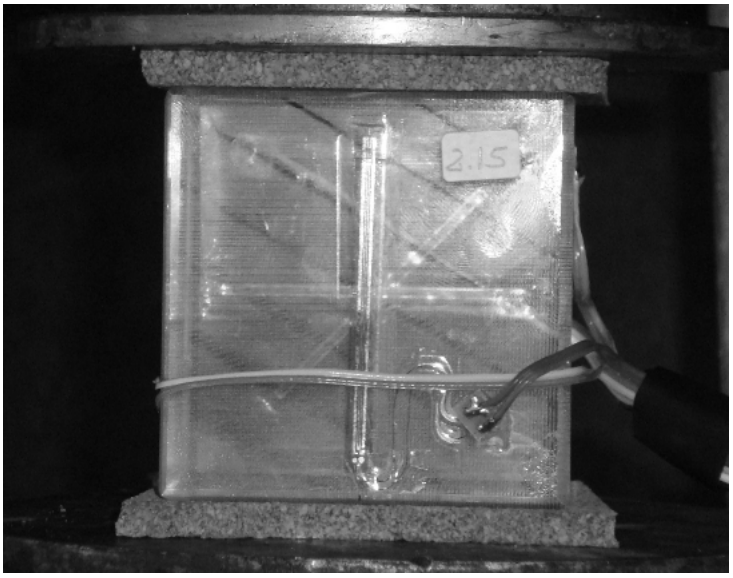

FIGURE A.62: Sample 030VC before testing

FIGURE A.63: Sample 030VC after testing

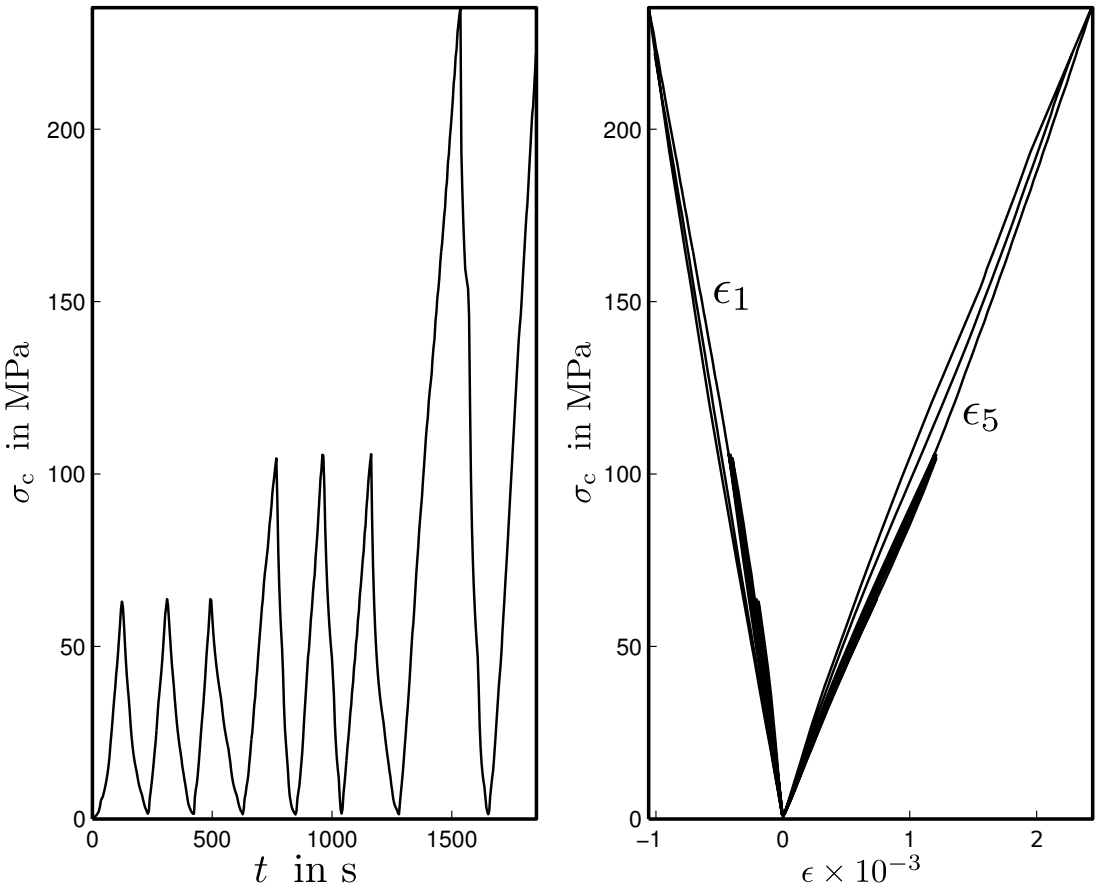

FIGURE A.64: Plots of time and deformations *vs.* vertical stress of sample 030VC

A.3.7 Specimen 045VA

FIGURE A.65: Sample 045VA after testing

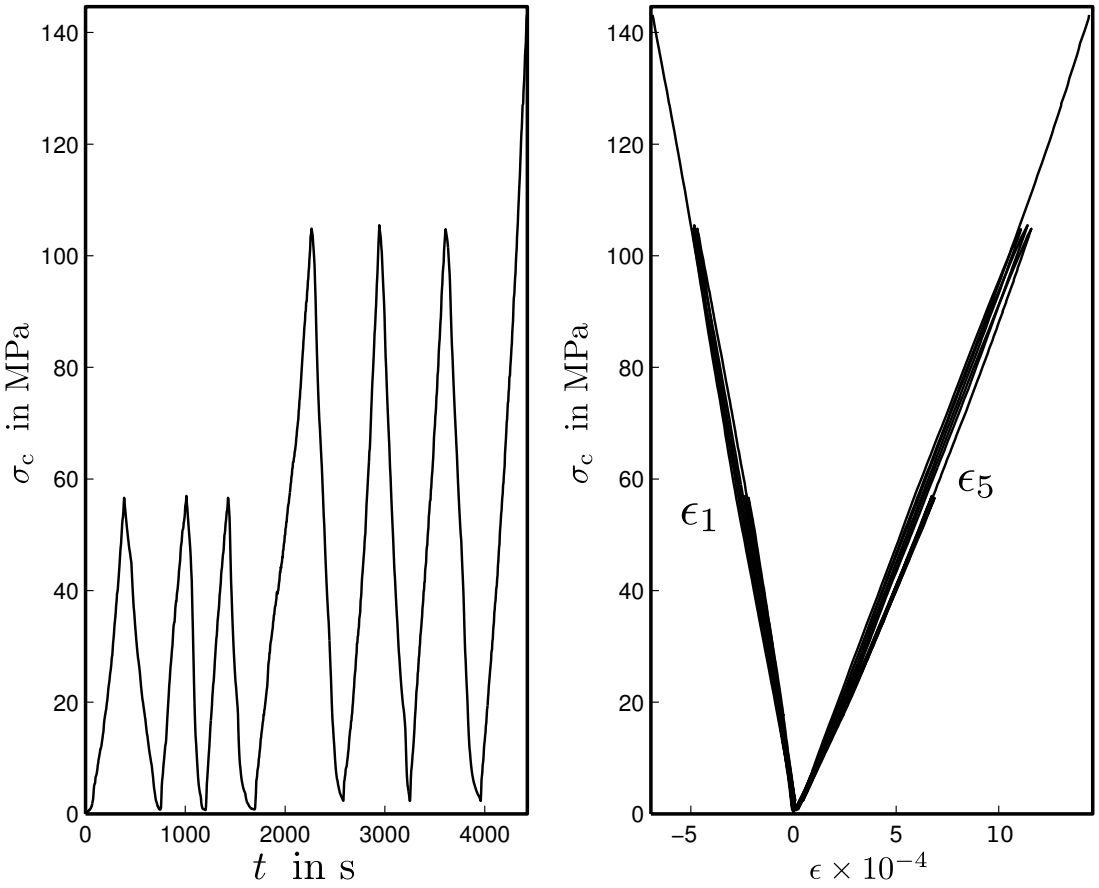

FIGURE A.66: Plots of time and deformations *vs.* vertical stress of sample 045VA

A.3.8 Specimen 045VB

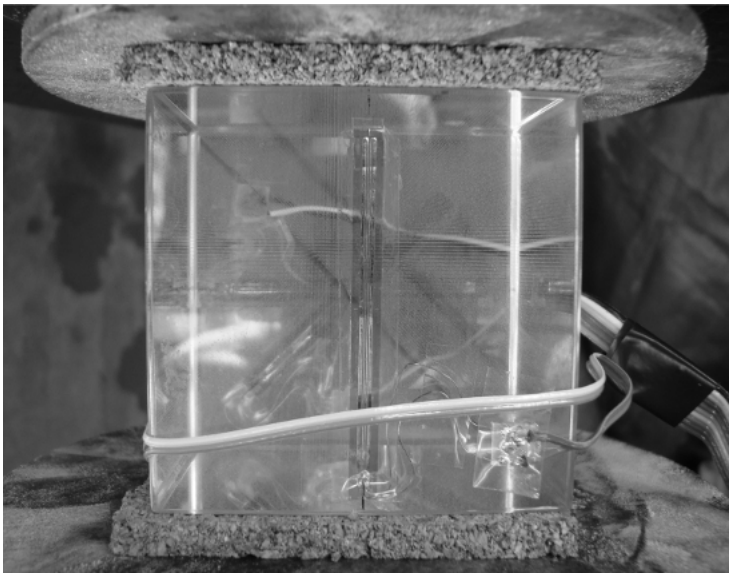

FIGURE A.67: Sample 045VB before testing

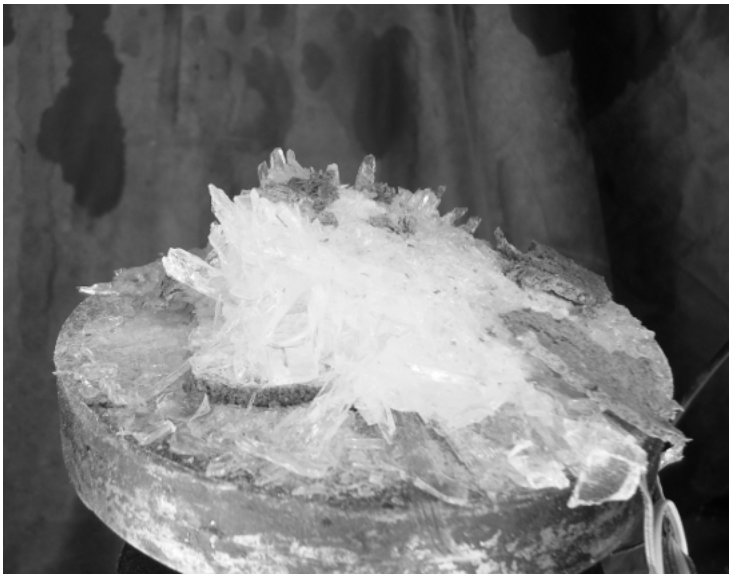

FIGURE A.68: Sample 045VB after testing

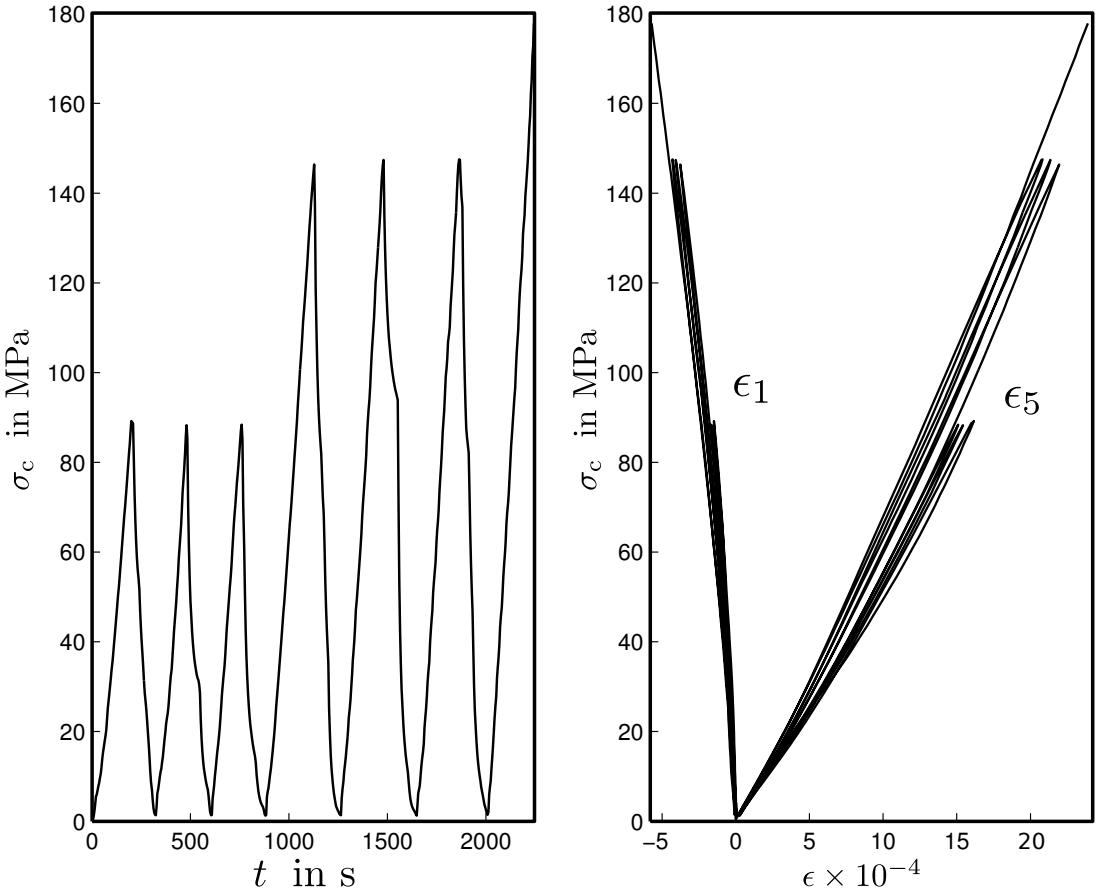

FIGURE A.69: Plots of time and deformations *vs.* vertical stress of sample 045VB

A.3.9 Specimen 045VC

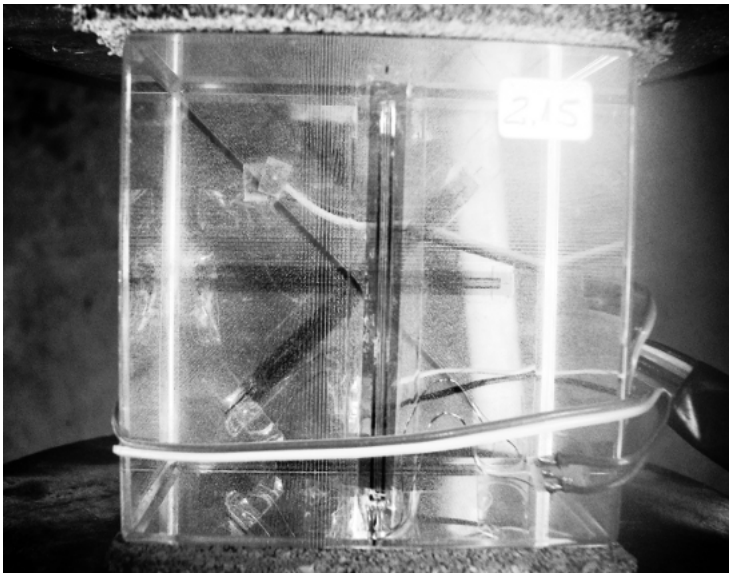

FIGURE A.70: Sample 045VC before testing

FIGURE A.71: Sample 045VC after testing

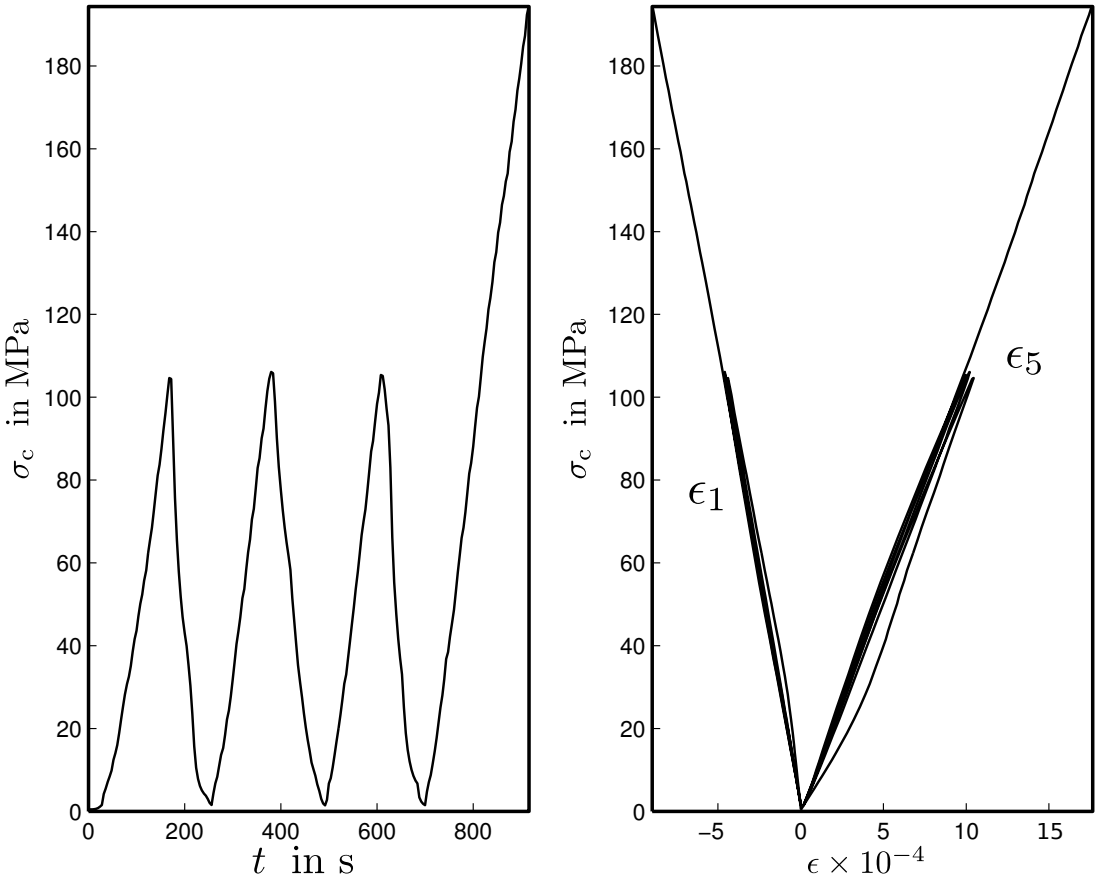

FIGURE A.72: Plots of time and deformations *vs.* vertical stress of sample 045VC

A.3.10 Specimen 060VA

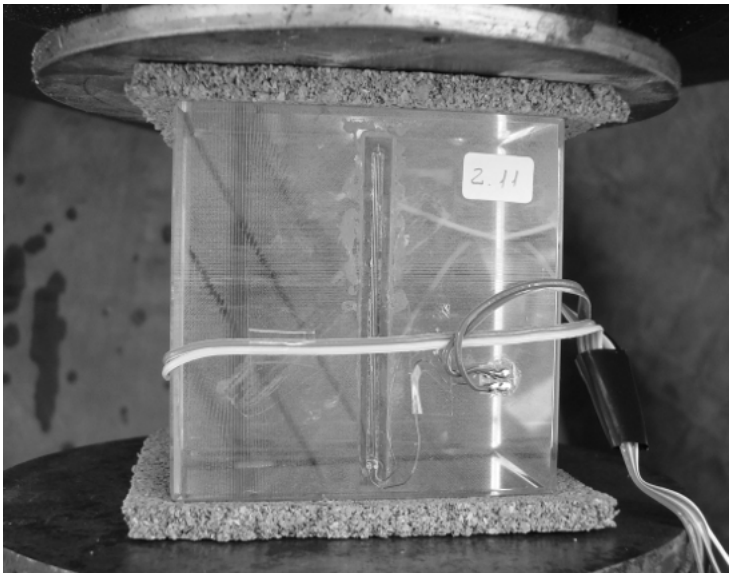

FIGURE A.73: Sample 060VA before testing

FIGURE A.74: Sample 060VA after testing

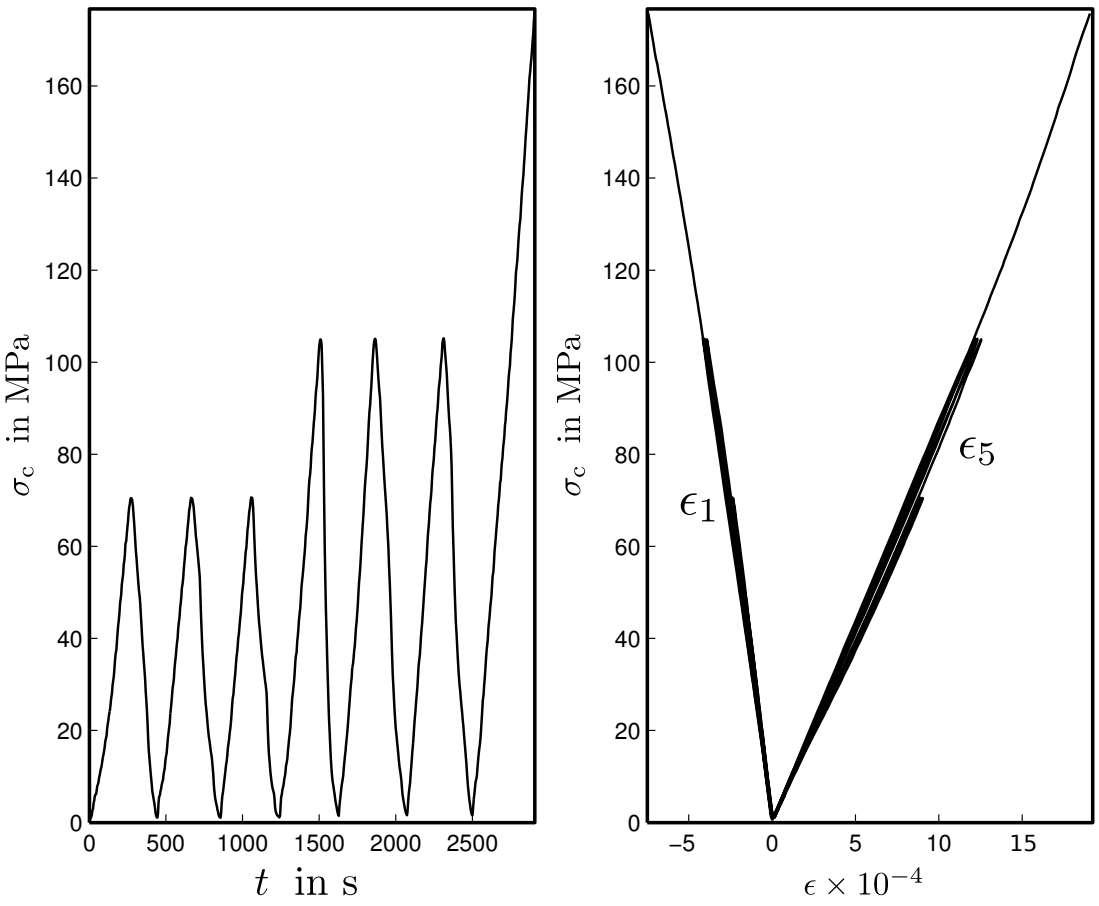

FIGURE A.75: Plots of time and deformations *vs.* vertical stress of sample 060VA

A.3.11 Specimen 060VB

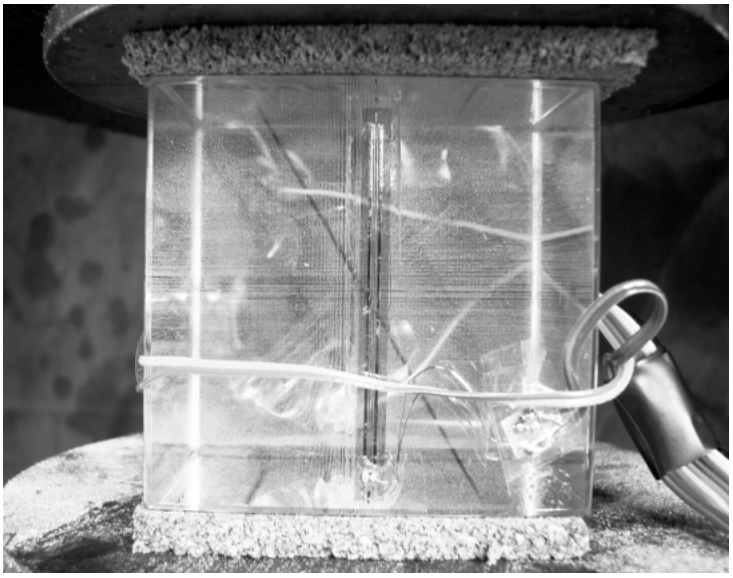

FIGURE A.76: Sample 060VB before testing

FIGURE A.77: Sample 060VB after testing

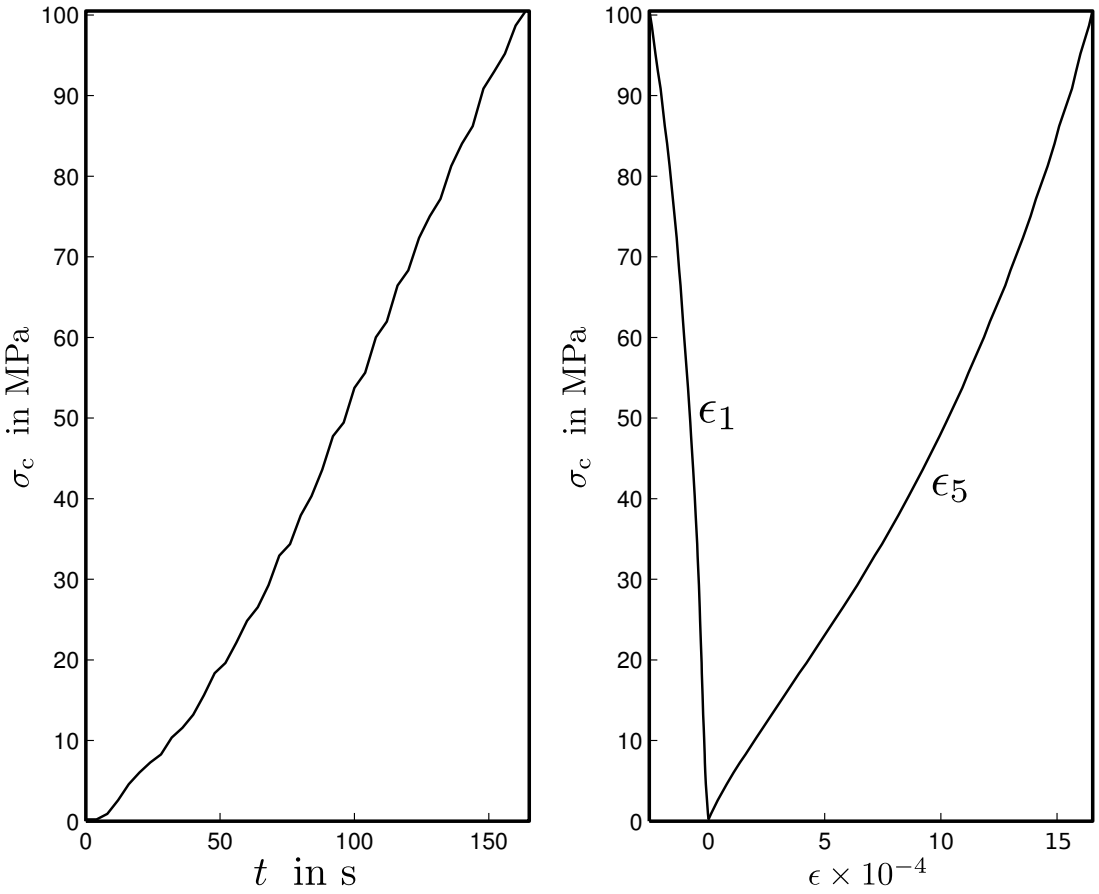

FIGURE A.78: Plots of time and deformations *vs.* vertical stress of sample 060VB

A.3.12 Specimen 060VC

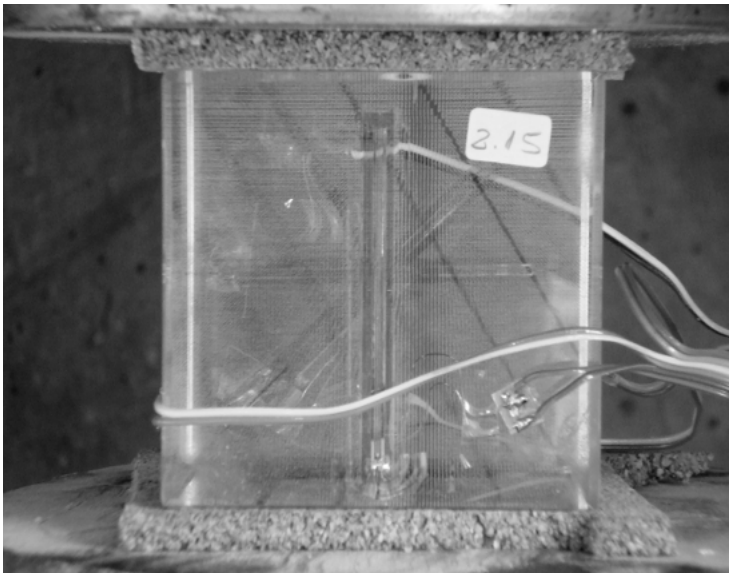

FIGURE A.79: Sample 060VC before testing

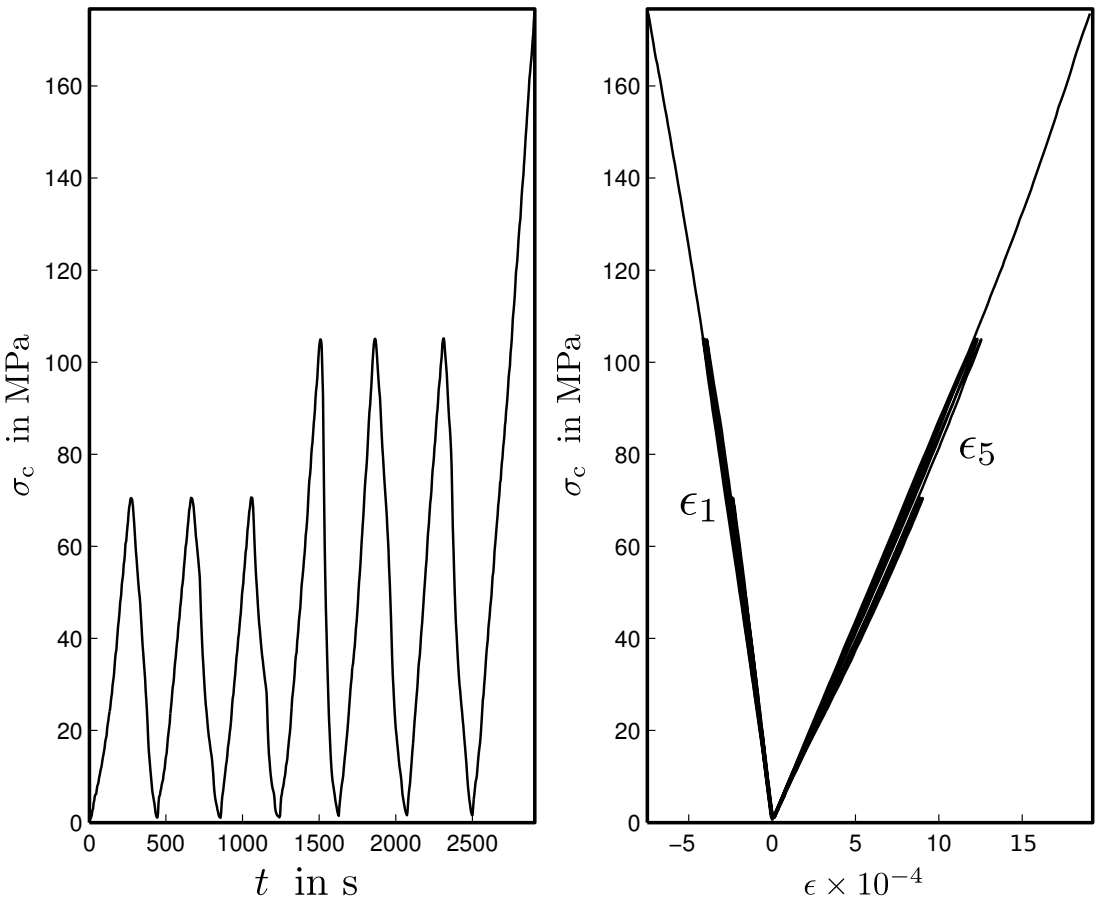

FIGURE A.80: Plots of time and deformations *vs.* vertical stress of sample 060VC

A.3.13 Specimen 090VA

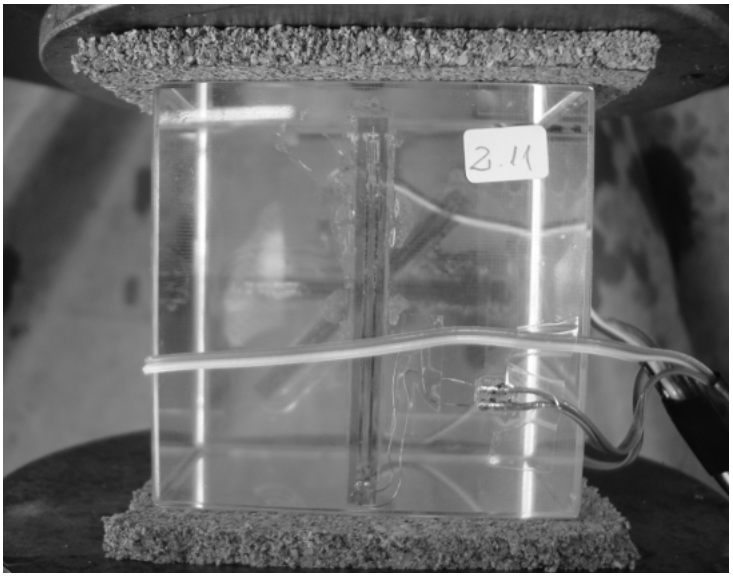

FIGURE A.81: Sample 090VA before testing

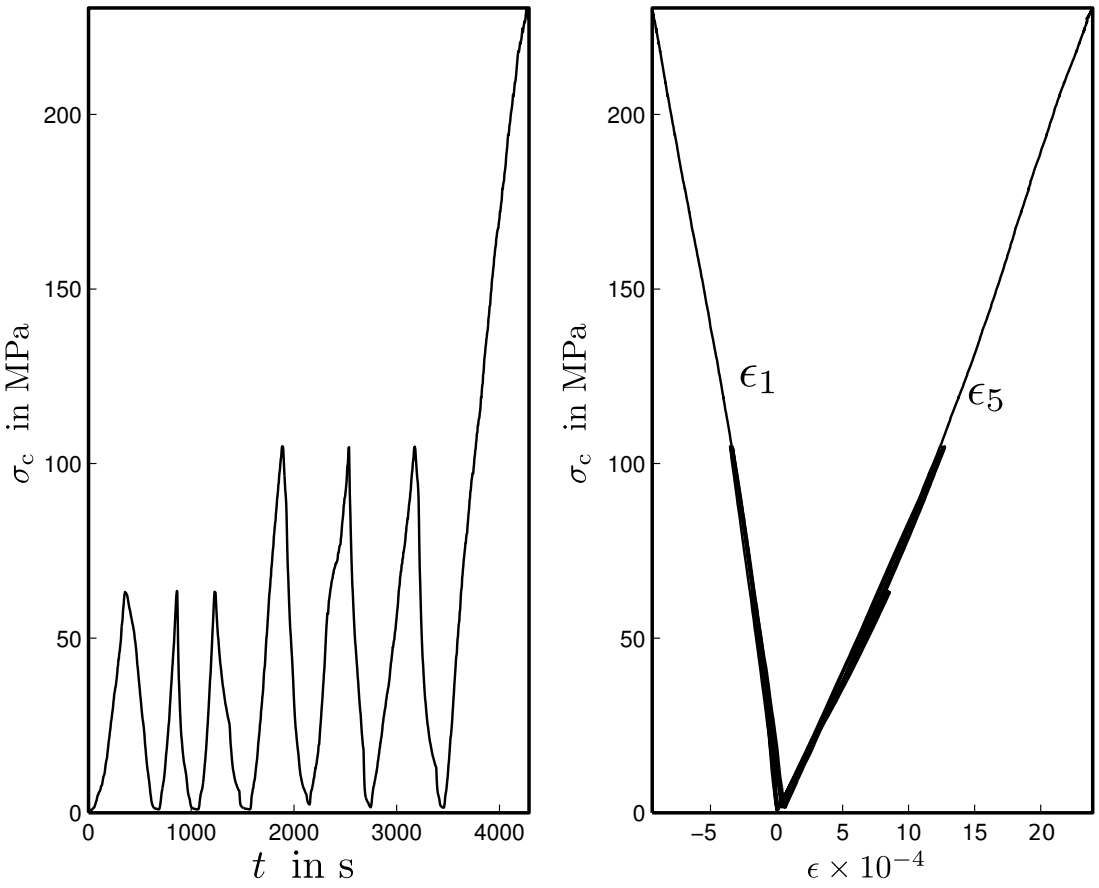

FIGURE A.82: Plots of time and deformations *vs.* vertical stress of sample 090VA

A.3.14 Specimen 090VB

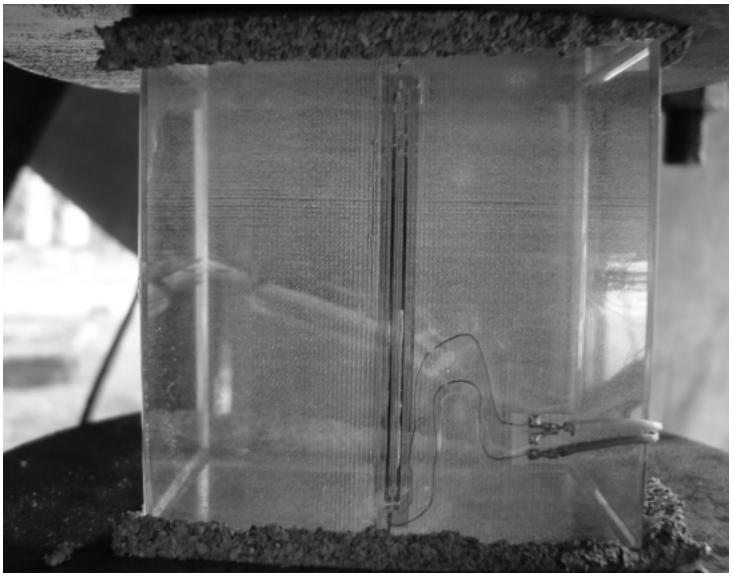

FIGURE A.83: Sample 090VB before testing

FIGURE A.84: Sample 090VB after testing

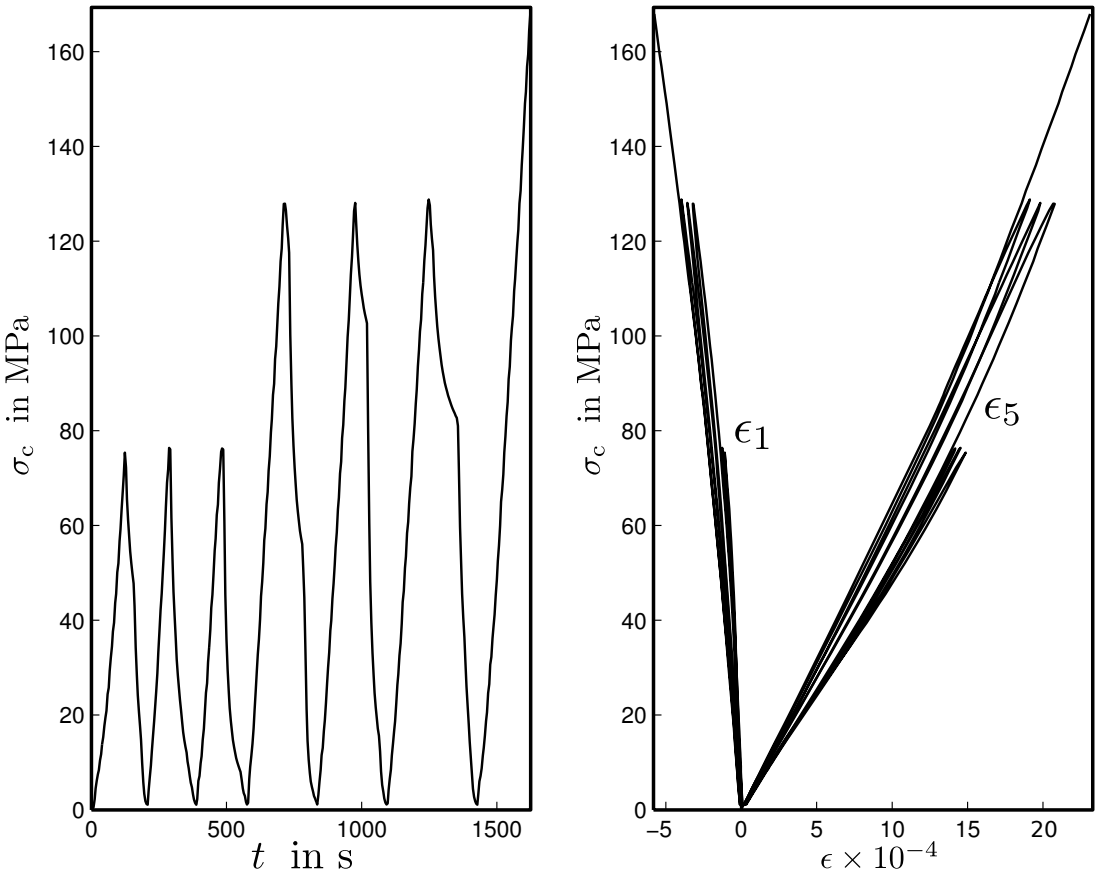

FIGURE A.85: Plots of time and deformations *vs.* vertical stress of sample 090VB

A.3.15 Specimen 090VC

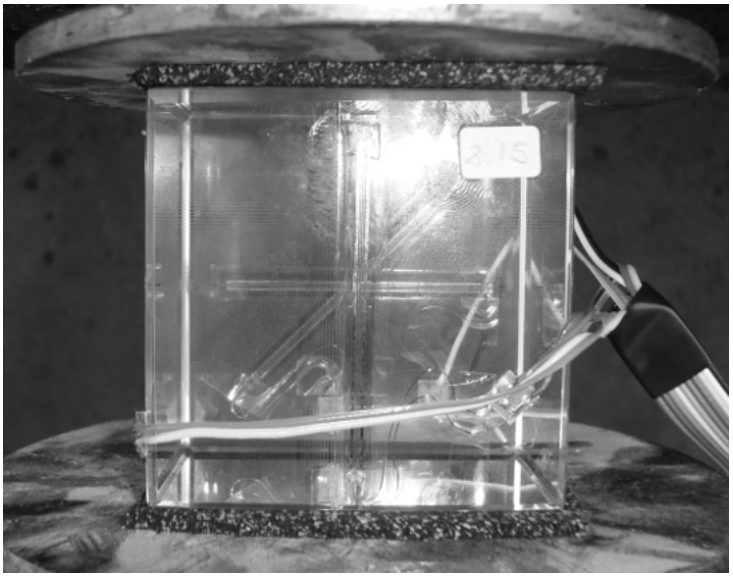

FIGURE A.86: Sample 090VC before testing

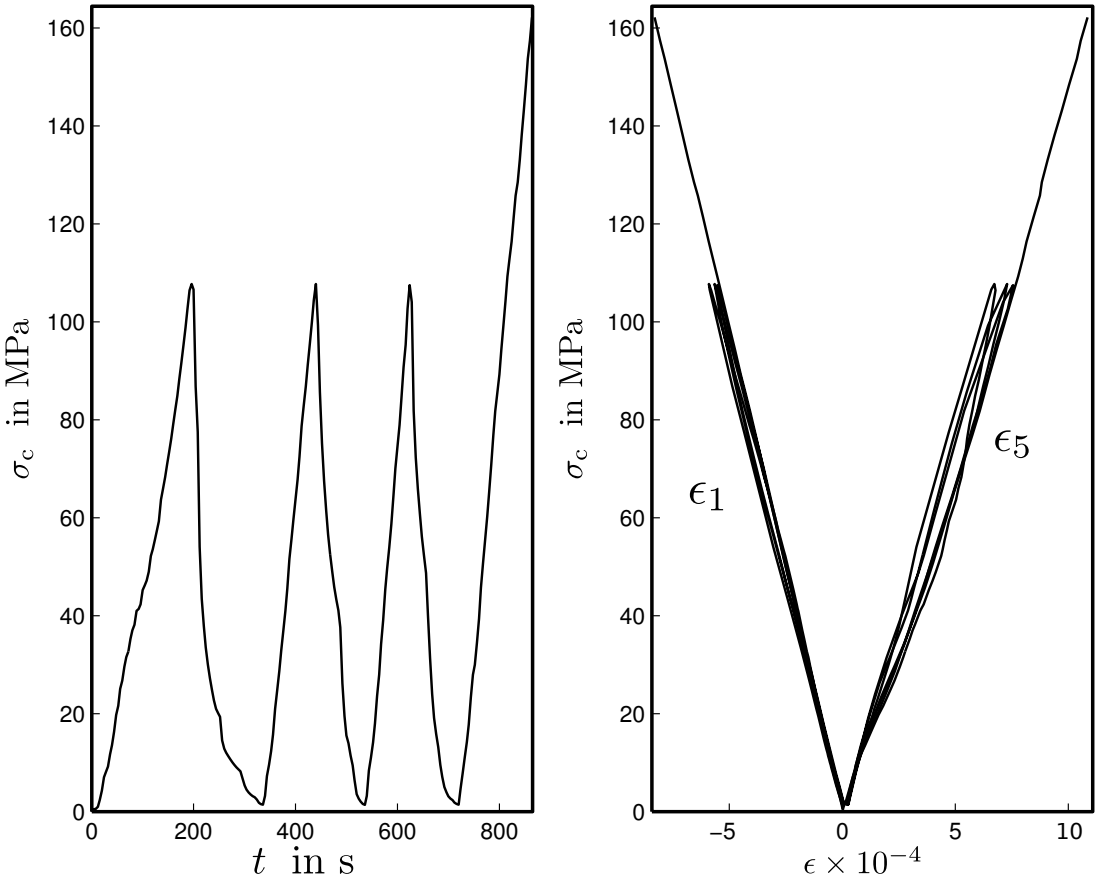

FIGURE A.87: Plots of time and deformations *vs.* vertical stress of sample 090VC

A.4 HE Samples

TABLE A.4: Photographs and Plots shown of HE Samples in this Appendix.

Sample	Photographs		Plots		
	Before Testing	After Testing	Testing Speed	Strain Modulus	Elastic Modulus
00MA	1	1	1	1	1
00MB	1	1	1	1	1
06MA	0	1	1	1	1
06MB	1	1	1	1	1
06MC*	1	1	0	0	0
18MA	1	1	1	1	1
18MB	1	1	1	1	1
18MC†	0	1	0	0	0

Note. 1 corresponds to yes, and 0 corresponds to no.

Strain gages lectures did not produced signal during testing, therefore no data was read and no plots related with strains were possible to perform: *channel 1 corresponding to the HSG1 values; and †channel 5 corresponding to the VSG2 values.

A.4.1 Specimen 00MA

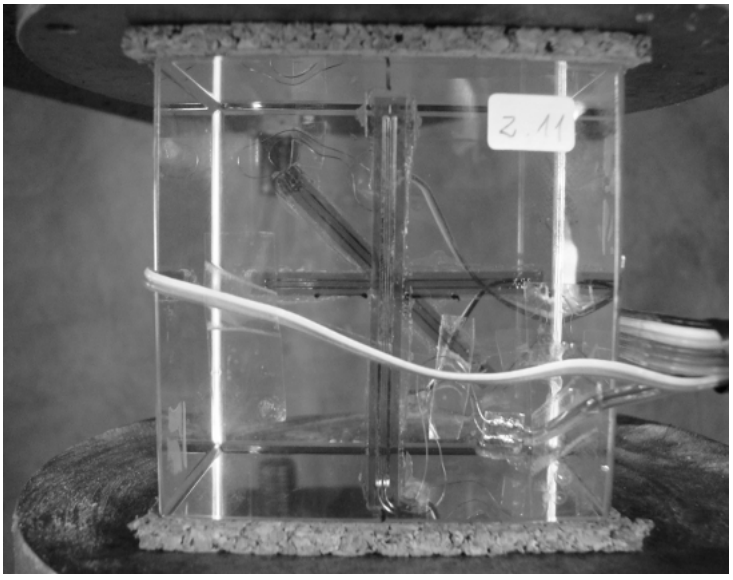

FIGURE A.88: Sample 00MA before testing

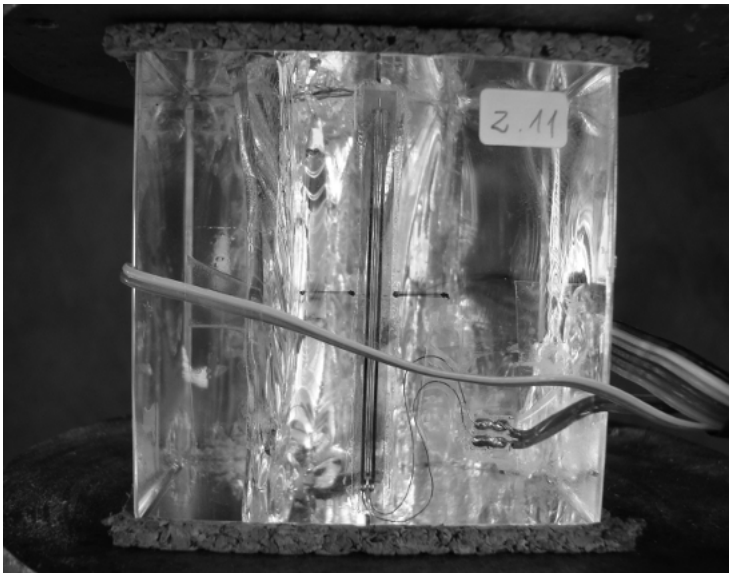

FIGURE A.89: Sample 00MA after testing

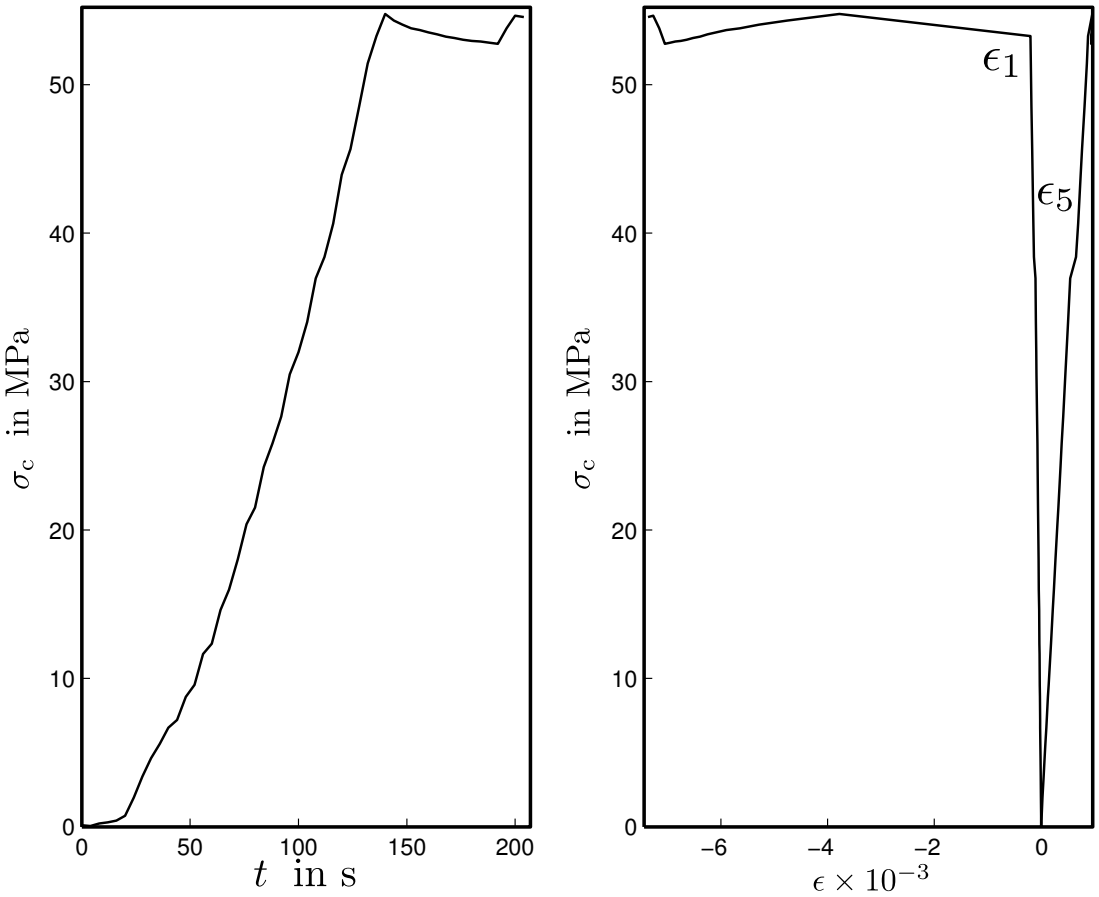

FIGURE A.90: Plots of time and deformations *vs.* vertical stress of sample 00MA

A.4.2 Specimen 00MB

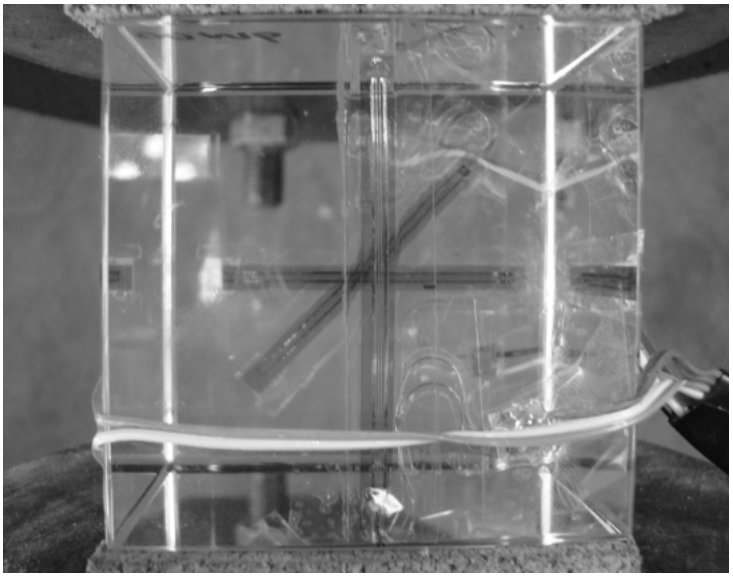

FIGURE A.91: Sample 00MB before testing

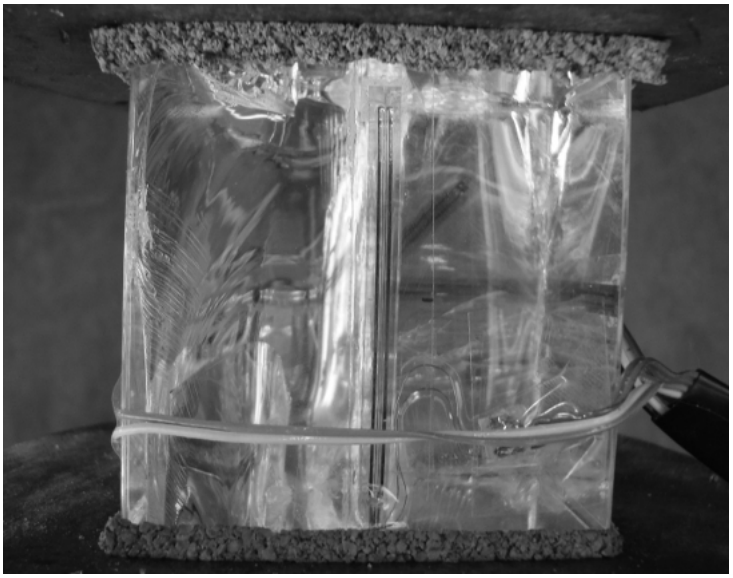

FIGURE A.92: Sample 00MB after testing

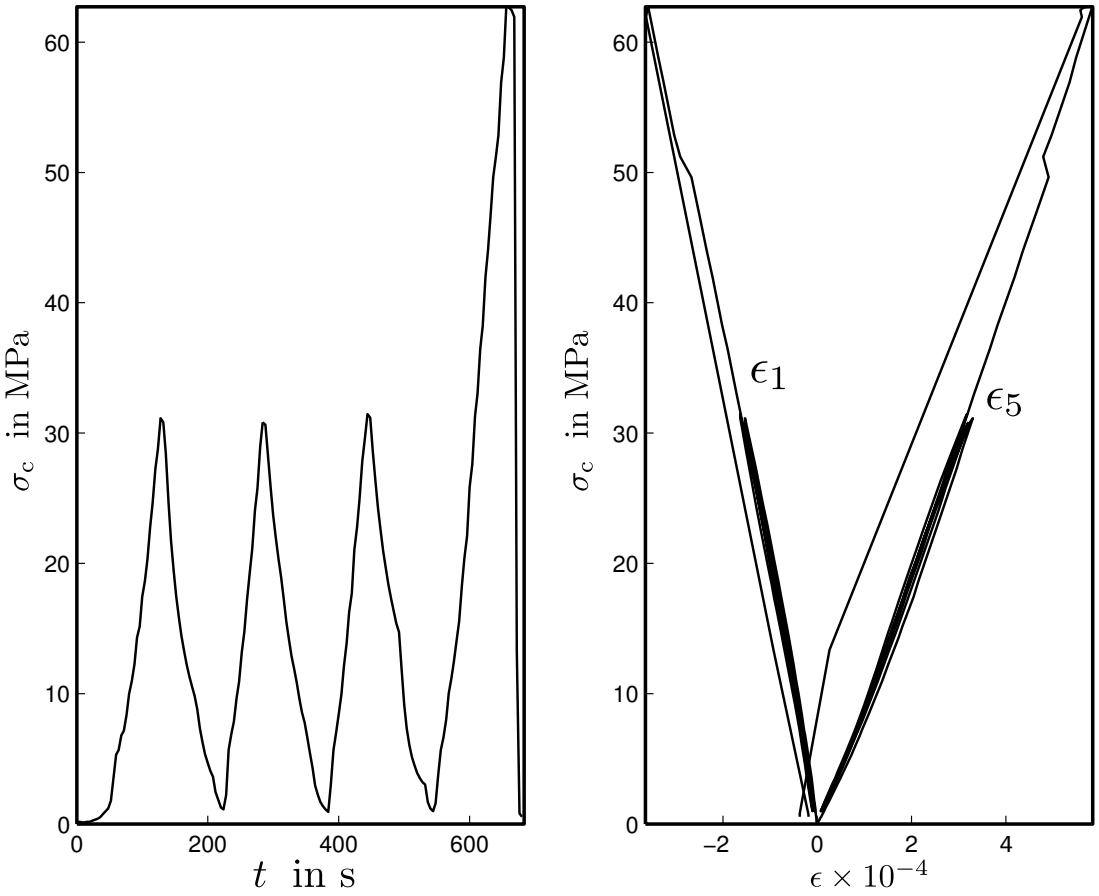

FIGURE A.93: Plots of time and deformations *vs.* vertical stress of sample 00MB

A.4.3 Specimen 06MA

FIGURE A.94: Sample 06MA after testing

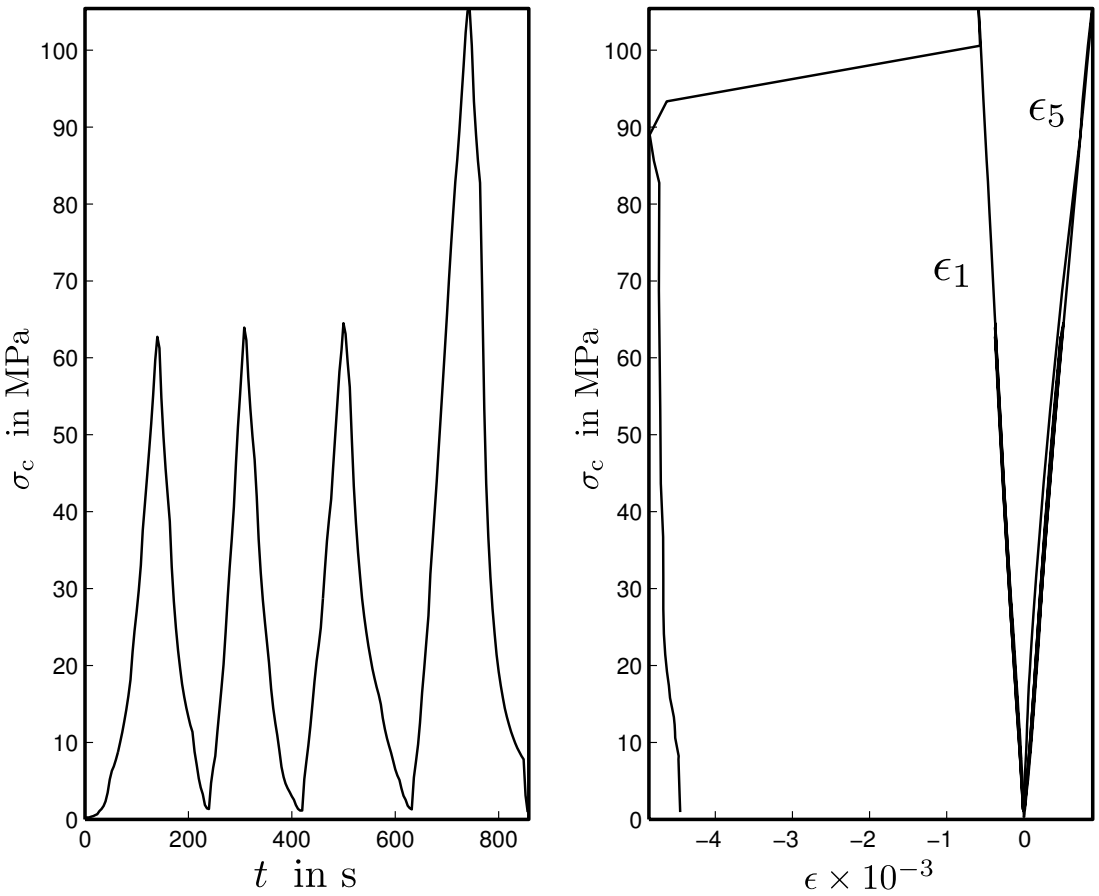

FIGURE A.95: Plots of time and deformations *vs.* vertical stress of sample 06MA

A.4.4 Specimen 06MB

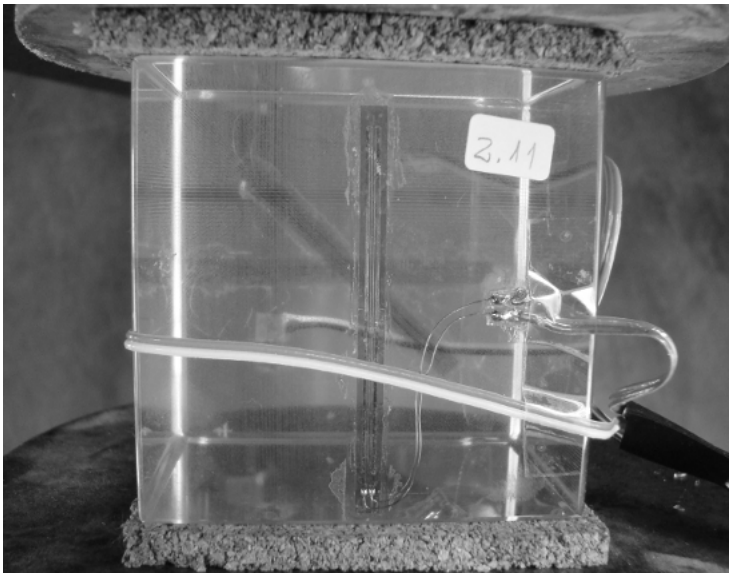

FIGURE A.96: Sample 06MB before testing

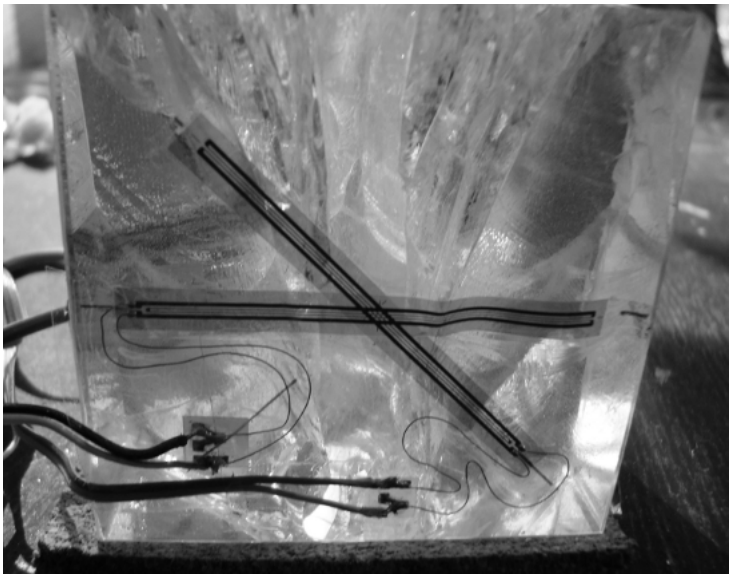

FIGURE A.97: Sample 06MB after testing

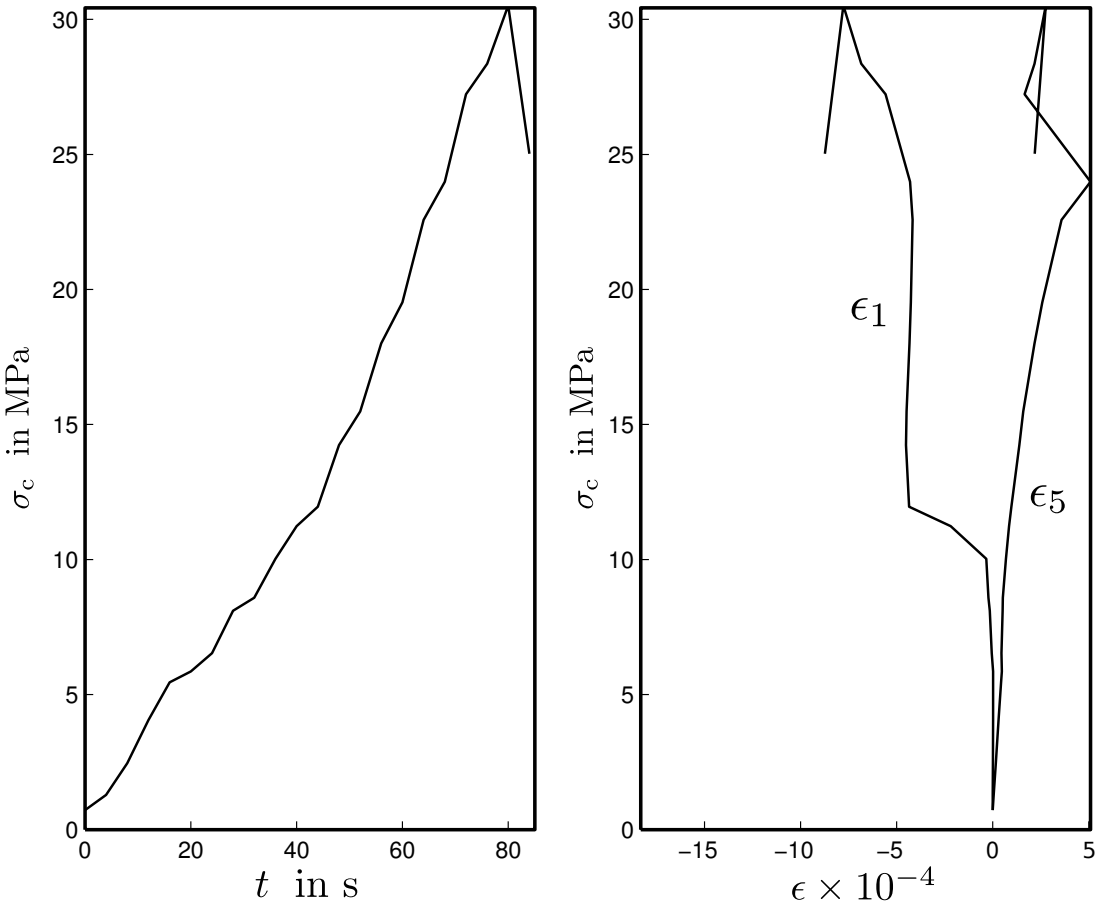

FIGURE A.98: Plots of time and deformations *vs.* vertical stress of sample 06MB

A.4.5 Specimen 06MC

FIGURE A.99: Sample 06MC before testing

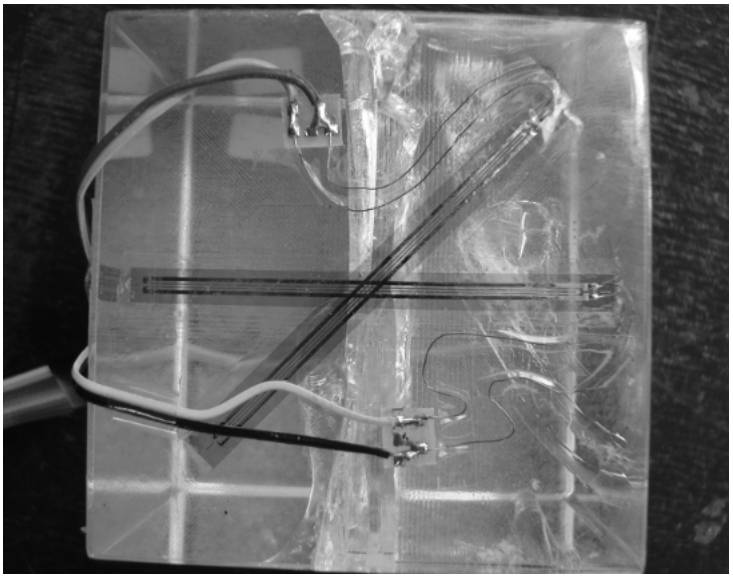

FIGURE A.100: Sample 06MC after testing

A.4.6 Specimen 18MA

FIGURE A.101: Sample 18MA before testing

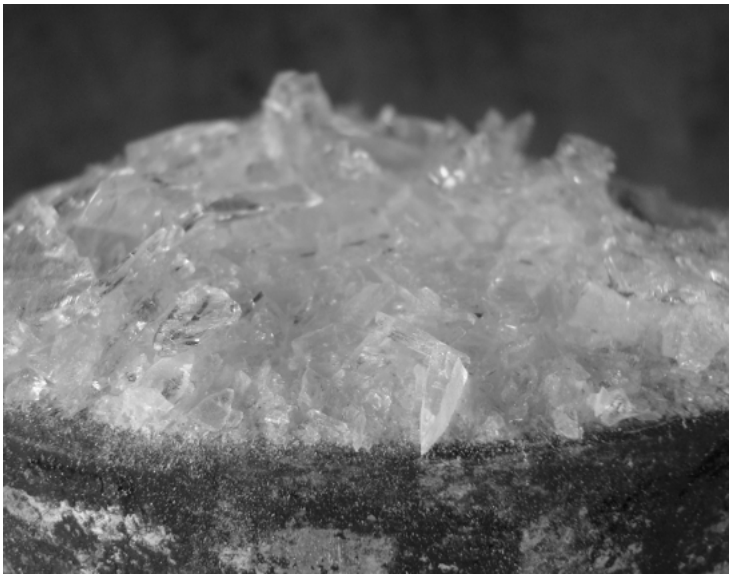

FIGURE A.102: Sample 18MA after testing

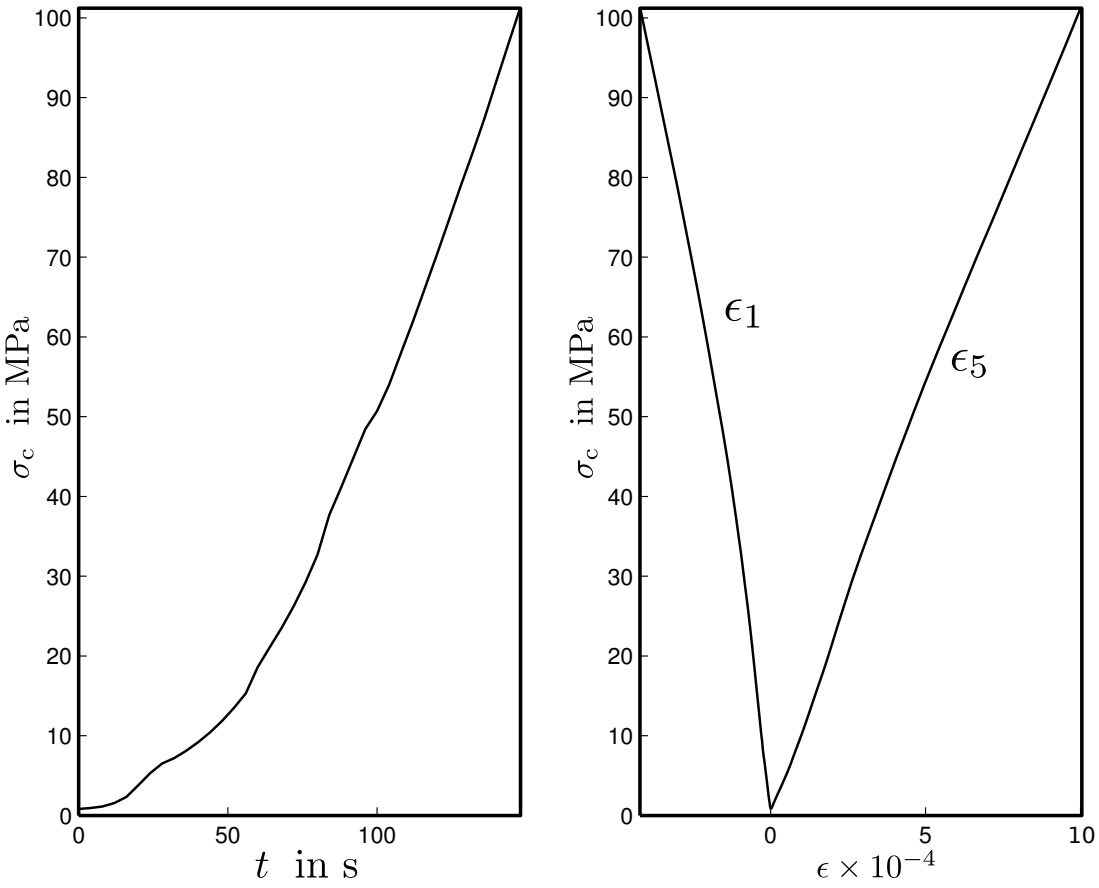

FIGURE A.103: Plots of time and deformations *vs.* vertical stress of sample 18MA

A.4.7 Specimen 18MB

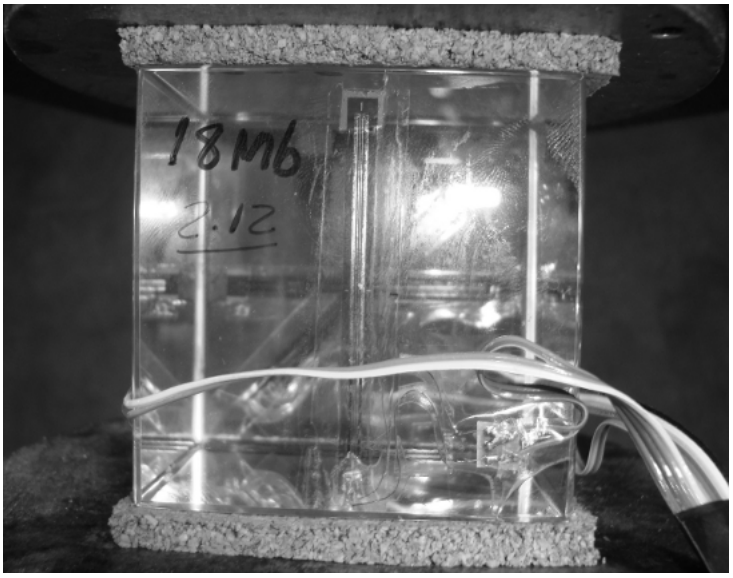

FIGURE A.104: Sample 18MB before testing

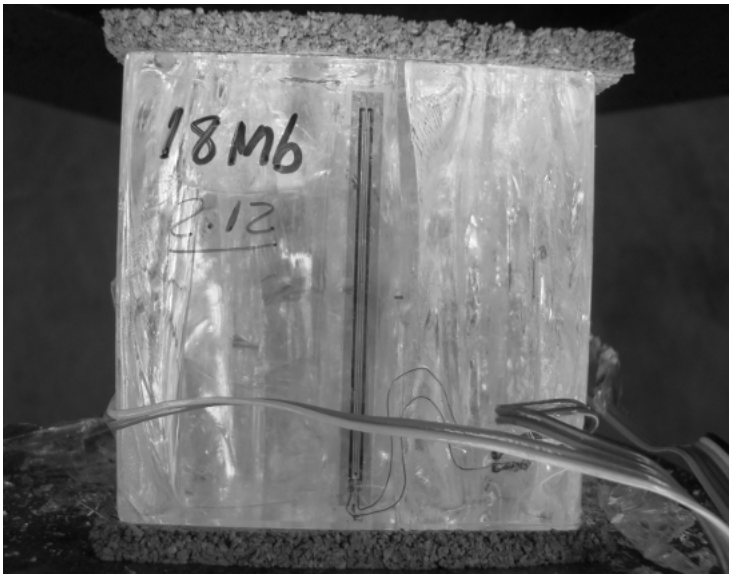

FIGURE A.105: Sample 18MB after testing

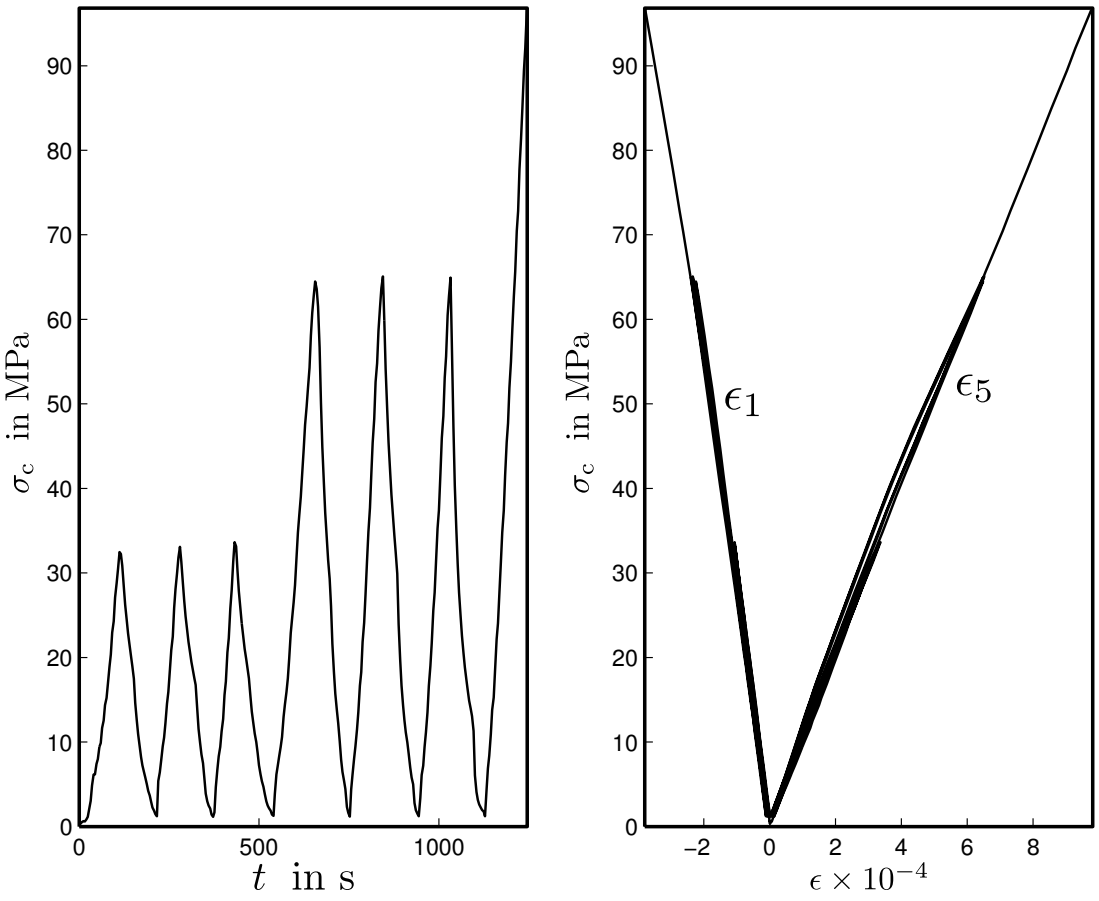

FIGURE A.106: Plots of time and deformations *vs.* vertical stress of sample 18MB

A.4.8 Specimen 18MC

FIGURE A.107: Sample 18MC after testing

Appendix B

SQL Statements for Initial Data Processing

In this appendix it will explained the data manipulation by using a data base manager as is POSTGRESQL® and the SQL language.

The main rough data base of the measurements of this research is stored in table `testedsamples`. In order to make the queries about these data, one require to use this table; but specially, it will be used to create the initial data processing data base, which will be stored in a new table called here as `testsresults`. Type in the POSTGRESQL® shell `\dt-` in order to see if this table have been created properly.

B.1 Developing the Relational Data Base

The relational data base manager program used for this task was the POSTGRESQL® 8.4.9 for i486–PC–Linux–GNU (Debian 4.4.5–8). Instructions for installing this open source software can be found in their respective web page and it depends on the operational system you are using.

In this research the following procedure was undertook successfully to install this software:

- install the program with the `aptitude` program by typing as administrator (i.e. root–user

or also named super–user) `aptitude install postgresql postgresql-client postgresql-doc pgadmin3 phppgadmin plpgsql` and close the shell;

- open a new shell again as administrator;
- maintained as administrator, enter to the program as POSTGRESQL® user with `su postgres`;
- enter to the initial and by–default template by typing `psql template1`;
- create an user with `CREATE USER user WITH PASSWORD 'userPassword';`;
- create a new database with `CREATE DATABASE databaseName;`;
- give all the privileges in the new created database to the user, with `GRANT ALL PRIVILEGES ON DATABASE databaseName TO user;`;
- exit from the template and as POSTGRESQL® user with `\q`;
- exit the shell as administrator with `exit`;
- in a new shell, this time as an user shell, enter to the new created database by writing `psql databaseName`, there you can create the tables and relations to be part of the database.

The relational data base of this research required create two tables:

- a parent table that contains all the samples general data measured during laboratory (here: `samplesForTesting`);
- a child table that contains common information for all samples (here: `materialEtchType`).

In POSTGRESQL® the creation process requires to digitize the following statements at the command shell: for the parent table ...

```
CREATE TABLE samplesForTesting (
numericalID        int        primary key                          ,
laboratoryTempID   varchar(9)                                      , --The name that was
    given for laboratory tests
materialEtchType   varchar(4) references materialEtchType(etchtype),
northLength        real[5]                                         , --Side length of the
     sample on north direction
eastLength         real[5]                                         , --Side length of the
     sample on east direction
nadirLength        real[5]                                         , --Side length of the
     sample on nadir direction
```

```
soundPropTimeNadir real                                                , --Sound wave time
    propagation in the nadir direction lenght in mili seconds
dryWeigth          real                                                , --Dry weigth of the
    sample in grams
fabricationDate    date                                                , --Date of sample
    fabrication (etching process)
testDate           date                                                  --Date of sample
    testing
);
```

and for the child table ...

```
CREATE TABLE materialEtchType (
  etchType       varchar(4)  primary key,  --
  description    varchar(60)            ,  --description of the class
  totalNumEtches int                       --Number of total etches at the sample
);
```

The data insertion is done, respectively for the parent and child tables, by using —for example— the following two SQL sentences:

```
INSERT INTO samplesfortesting (numericalID, laboratoryTempID, materialEtchType,
    northLength, eastLength, nadirLength, soundPropTimeNadir, dryWeigth, fabricationDate,
     testDate) VALUES ('39', '090VA', 'VN90', '{68.52, 68.53, 68.53, 68.54, 68.56}',
    '{69.15, 69.20, 69.21, 69.19, 69.22}', '{68.46, 68.45, 68.37, 68.29, 68.20}', '12.5',
     '811.45', '07/05/2011', '22/07/2011' );

INSERT INTO materialEtchType VALUES ('DS60', 'Blanck glass with discontinuities inclined
    at 60 grades', '1807176');
```

Some queries may be possible when all data is in the data base, for example, if someone wants know what are the unidimensional statistics of all measured dry weights, type:

```
SELECT AVG(dryWeigth) FROM samplesfortesting;
SELECT STDDEV(dryWeigth) FROM samplesfortesting;
SELECT MAX(dryWeigth) FROM samplesfortesting;
SELECT MIN(dryWeigth) FROM samplesfortesting;
```

In the preceded Appendix, it was shown how this database can be connected to a known programming language for engineers (i.e. MATLAB®), for further calculations and post–data–processing. Now, in the following sections, one will see some examples of the usefulness of SQL language to perform queries and simple initial calculations.

B.2 All Samples

I order to view the names of all the samples tested in this research, type the following query:

```
SELECT laboratorytempid AS sample_Id FROM testedSamples ORDER BY laboratorytempid;
```

Then you will have in the display the following list:

```
 sample_id
-----------
 000DA
 000DB
 000DC
 000VA
 000VB
 000VC
 00MA
 00MB
 00MC
 030DA
 030DB
 030DC
 030VA
 030VB
 030VC
 045DB
 045DC
 045VA
 045VB
 045VC
 060DA
 060DB
 060DC
 060VA
 060VB
 060VC
 06MA
 06MB
 06MC
 090DA
 090DB
 090DC
 090VA
 090VB
 090VC
 18MA
 18MB
 18MC
 SGA
 SGB
 SGC
 SGD
(42 filas)
```

B.3 Mean Dimensions

If one wants to list the mean dimensions of all samples, type the following query:

```
SELECT * FROM allSamplesAvgLengths
```

. . . and one will see the following table:

```
 sample_id | n_avg | e_avg | d_avg
-----------+-------+-------+-------
 000DA     | 68.84 | 69.14 | 68.66
 000DB     | 68.82 | 68.67 | 68.41
 000DC     | 68.67 | 68.60 | 69.03
 000VA     | 70.03 | 69.17 | 67.08
 000VB     | 69.16 | 67.39 | 69.58
 000VC     | 68.01 | 67.31 | 68.74
 00MA      | 68.57 | 69.04 | 68.92
 00MB      | 69.23 | 69.22 | 68.60
 00MC      | 69.47 | 68.48 | 66.56
 030DA     | 68.71 | 69.01 | 69.10
 030DB     | 68.49 | 68.57 | 68.02
 030DC     | 67.82 | 67.77 | 68.21
 030VA     | 69.26 | 69.45 | 69.82
 030VB     | 68.05 | 68.05 | 68.40
 030VC     | 68.94 | 67.89 | 68.63
 045DB     | 68.35 | 68.51 | 68.58
 045DC     | 68.01 | 68.89 | 68.99
 045VA     | 70.00 | 67.41 | 69.20
 045VB     | 68.66 | 68.48 | 67.63
 045VC     | 68.04 | 69.15 | 69.02
 060DA     | 68.34 | 68.25 | 68.24
 060DB     | 68.13 | 68.96 | 68.33
 060DC     | 69.32 | 68.72 | 68.72
 060VA     | 68.57 | 68.50 | 68.09
 060VB     | 69.33 | 70.13 | 68.06
 060VC     | 68.60 | 68.01 | 67.93
 06MA      | 68.71 | 68.80 | 68.70
 06MB      | 68.17 | 69.49 | 68.32
 06MC      | 68.61 | 68.47 | 68.45
 090DA     | 68.30 | 68.62 | 69.60
 090DB     | 69.32 | 68.79 | 68.97
 090DC     | 68.23 | 68.04 | 68.28
 090VA     | 68.54 | 69.19 | 68.35
 090VB     | 68.06 | 67.67 | 68.23
 090VC     | 67.57 | 68.08 | 67.94
 18MA      | 68.26 | 67.49 | 67.70
 18MB      | 68.53 | 67.72 | 68.00
 18MC      | 68.24 | 68.02 | 68.39
 SGA       | 68.60 | 69.15 | 66.48
 SGB       | 68.06 | 67.77 | 67.72
 SGC       | 67.32 | 68.12 | 68.62
 SGD       | 68.37 | 68.66 | 68.54
(42 filas)
```

The `allSamplesAvgLengths` view was created by typing:

```
CREATE VIEW allSamplesAvgLengths AS
  SELECT anyAlias.sample_Id AS sample_Id,
       CAST( AVG(anyAlias.northLengthData) AS decimal(4,2) ) AS n_avg,
       CAST( AVG(anyAlias.eastLengthData)  AS decimal(4,2) ) AS e_avg,
       CAST( AVG(anyAlias.nadirLengthData) AS decimal(4,2) ) AS d_avg
  FROM
    (
     SELECT laboratoryTempID AS sample_Id,
          unnest(northLength) AS northLengthData,
          unnest(eastLength) AS eastLengthData,
          unnest(nadirLength) AS nadirLengthData
     FROM testedSamples
    ) AS anyAlias
  GROUP BY anyAlias.sample_Id
  ORDER BY anyAlias.sample_Id ASC;
```

After the view creation, it is not necessary to re–create it, if some data is actualized. This view adds the new changes each time you call the view.

B.4 Sound Propagation Time and Dry Weight

Type `SELECT * FROM allSamplesSoundTimeDryWeigth;` in order to view all the sound propagation times and dry weights measured in this research. By doing so, one will have the following display:

```
 sample_id |  ts  |   ws
-----------+------+--------
 000DA     | 12.5 | 818.33
 000DB     | 12.5 | 810.48
 000DC     | 12.5 | 814.78
 000VA     | 12.5 | 816.49
 000VB     | 12.5 | 813.43
 000VC     | 12.5 | 789.13
 00MA      | 12.5 | 825.57
 00MB      | 12.5 | 826.78
 00MC      | 12.5 | 795.07
 030DA     | 12.5 | 820.02
 030DB     | 12.5 | 797.02
 030DC     | 12.5 | 792.01
 030VA     | 12.5 | 825.75
 030VB     | 12.5 |  793.3
 030VC     | 12.5 | 813.59
 045DB     | 12.5 | 806.69
 045DC     | 12.5 |    809
 045VA     | 12.5 | 819.48
 045VB     | 12.5 | 795.97
 045VC     | 12.5 | 817.16
 060DA     | 12.5 | 799.71
```

```
 060DB     | 12.5 | 806.75
 060DC     | 12.5 | 820.31
 060VA     | 12.5 | 801.18
 060VB     | 12.5 | 828.81
 060VC     | 12.5 | 794.47
 06MA      | 12.5 | 815.84
 06MB      | 12.5 | 813.66
 06MC      | 12.5 | 806.65
 090DA     | 12.5 | 818.16
 090DB     | 12.5 | 825.21
 090DC     | 12.5 | 793.78
 090VA     | 12.5 | 811.45
 090VB     | 12.5 | 789.36
 090VC     | 12.5 | 782.28
 18MA      | 12.5 | 784.83
 18MB      | 12.5 | 790.12
 18MC      | 12.5 | 796.66
 SGA       | 12.5 | 791.76
 SGB       | 12.5 | 785.26
 SGC       | 12.5 | 792.61
 SGD       | 12.5 |  805.8
(42 filas)
```

The above mentioned view was created by typing:

```
CREATE VIEW allSamplesSoundTimeDryWeigth AS
  SELECT
       laboratoryTempID AS sample_Id,
       soundPropTimeNadir AS ts,
       dryWeigth AS ws
  FROM testedSamples
  ORDER BY laboratorytempid ASC;
```

B.5 Input Variables for Index Properties

The following view resumes the samples dimensions, the propagation velocities and the samples weights. In order to see that, type:

```
SELECT * FROM allSamplesIndexPropsInputs;
```

And one will have on the display the following result:

```
 sample_id | n_avg | e_avg | d_avg |  ts  |   ws
-----------+-------+-------+-------+------+--------
 000DA     | 68.84 | 69.14 | 68.66 | 12.5 | 818.33
 000DB     | 68.82 | 68.67 | 68.41 | 12.5 | 810.48
 000DC     | 68.67 | 68.60 | 69.03 | 12.5 | 814.78
 000VA     | 70.03 | 69.17 | 67.08 | 12.5 | 816.49
```

```
 000VB     | 69.16 | 67.39 | 69.58 | 12.5 | 813.43
 000VC     | 68.01 | 67.31 | 68.74 | 12.5 | 789.13
 00MA      | 68.57 | 69.04 | 68.92 | 12.5 | 825.57
 00MB      | 69.23 | 69.22 | 68.60 | 12.5 | 826.78
 00MC      | 69.47 | 68.48 | 66.56 | 12.5 | 795.07
 030DA     | 68.71 | 69.01 | 69.10 | 12.5 | 820.02
 030DB     | 68.49 | 68.57 | 68.02 | 12.5 | 797.02
 030DC     | 67.82 | 67.77 | 68.21 | 12.5 | 792.01
 030VA     | 69.26 | 69.45 | 69.82 | 12.5 | 825.75
 030VB     | 68.05 | 68.05 | 68.40 | 12.5 |  793.3
 030VC     | 68.94 | 67.89 | 68.63 | 12.5 | 813.59
 045DB     | 68.35 | 68.51 | 68.58 | 12.5 | 806.69
 045DC     | 68.01 | 68.89 | 68.99 | 12.5 |    809
 045VA     | 70.00 | 67.41 | 69.20 | 12.5 | 819.48
 045VB     | 68.66 | 68.48 | 67.63 | 12.5 | 795.97
 045VC     | 68.04 | 69.15 | 69.02 | 12.5 | 817.16
 060DA     | 68.34 | 68.25 | 68.24 | 12.5 | 799.71
 060DB     | 68.13 | 68.96 | 68.33 | 12.5 | 806.75
 060DC     | 69.32 | 68.72 | 68.72 | 12.5 | 820.31
 060VA     | 68.57 | 68.50 | 68.09 | 12.5 | 801.18
 060VB     | 69.33 | 70.13 | 68.06 | 12.5 | 828.81
 060VC     | 68.60 | 68.01 | 67.93 | 12.5 | 794.47
 06MA      | 68.71 | 68.80 | 68.70 | 12.5 | 815.84
 06MB      | 68.17 | 69.49 | 68.32 | 12.5 | 813.66
 06MC      | 68.61 | 68.47 | 68.45 | 12.5 | 806.65
 090DA     | 68.30 | 68.62 | 69.60 | 12.5 | 818.16
 090DB     | 69.32 | 68.79 | 68.97 | 12.5 | 825.21
 090DC     | 68.23 | 68.04 | 68.28 | 12.5 | 793.78
 090VA     | 68.54 | 69.19 | 68.35 | 12.5 | 811.45
 090VB     | 68.06 | 67.67 | 68.23 | 12.5 | 789.36
 090VC     | 67.57 | 68.08 | 67.94 | 12.5 | 782.28
 18MA      | 68.26 | 67.49 | 67.70 | 12.5 | 784.83
 18MB      | 68.53 | 67.72 | 68.00 | 12.5 | 790.12
 18MC      | 68.24 | 68.02 | 68.39 | 12.5 | 796.66
 SGA       | 68.60 | 69.15 | 66.48 | 12.5 | 791.76
 SGB       | 68.06 | 67.77 | 67.72 | 12.5 | 785.26
 SGC       | 67.32 | 68.12 | 68.62 | 12.5 | 792.61
 SGD       | 68.37 | 68.66 | 68.54 | 12.5 |  805.8
(42 filas)
```

The upper mentioned view was created by typing the following query:

```
CREATE VIEW allSamplesIndexPropsInputs AS
    SELECT alias2.sample_Id,
           CAST( alias2.n_avg AS decimal(4,2) ),
           CAST( alias2.e_avg AS decimal(4,2) ),
           CAST( alias2.d_avg AS decimal(4,2) ),
           alias1.ts,
           alias1.ws
    FROM  allSamplesSoundTimeDryWeigth AS alias1, allSamplesAvgLengths AS alias2
    WHERE alias2.sample_Id = alias1.sample_Id
    ORDER BY alias2.sample_Id ASC;
```

B.6 Index Properties

Index properties were calculated by using also the SQL language incorporated in the POSTGRESQL® program, and the results was stored in a new view. The SQL command used for that was the following one:

```
CREATE VIEW allSamplesIndexPropsOutputs AS
    SELECT sample_id,
       CAST( n_avg *e_avg *d_avg *power(1000,-3) AS decimal(6,5) ) AS volume_m3,
       CAST( n_avg *e_avg *power(1000,-2) AS decimal(6,4) ) AS neArea_m2,
       CAST( ws /1000 *9.81 /1000 /(n_avg *e_avg *d_avg) *power(1000,3) AS decimal(4,1) )
     AS unitWeight_kN_m2,
       CAST( d_avg *power(10,-3) /ts *power(10,6) AS decimal(4,0) ) AS nadirPropVel_m_s1
    FROM allSamplesIndexPropsInputs
    ORDER BY sample_id ASC;
```

Once typing `SELECT * FROM allSamplesIndexPropsOutputs;`, one have the following display:

```
 sample_id | volume_m3 | nearea_m2 | unitweight_kn_m-3| nadirpropvel_m_s1
-----------+-----------+-----------+------------------+-------------------
 000DA     |   0.00033 |    0.0048 |             24.6 |              5493
 000DB     |   0.00032 |    0.0047 |             24.6 |              5473
 000DC     |   0.00033 |    0.0047 |             24.6 |              5522
 000VA     |   0.00032 |    0.0048 |             24.7 |              5366
 000VB     |   0.00032 |    0.0047 |             24.6 |              5566
 000VC     |   0.00031 |    0.0046 |             24.6 |              5499
 00MA      |   0.00033 |    0.0047 |             24.8 |              5514
 00MB      |   0.00033 |    0.0048 |             24.7 |              5488
 00MC      |   0.00032 |    0.0048 |             24.6 |              5325
 030DA     |   0.00033 |    0.0047 |             24.6 |              5528
 030DB     |   0.00032 |    0.0047 |             24.5 |              5442
 030DC     |   0.00031 |    0.0046 |             24.8 |              5457
 030VA     |   0.00034 |    0.0048 |             24.1 |              5586
 030VB     |   0.00032 |    0.0046 |             24.6 |              5472
 030VC     |   0.00032 |    0.0047 |             24.8 |              5490
 045DB     |   0.00032 |    0.0047 |             24.6 |              5486
 045DC     |   0.00032 |    0.0047 |             24.6 |              5519
 045VA     |   0.00033 |    0.0047 |             24.6 |              5536
 045VB     |   0.00032 |    0.0047 |             24.6 |              5410
 045VC     |   0.00032 |    0.0047 |             24.7 |              5522
 060DA     |   0.00032 |    0.0047 |             24.6 |              5459
 060DB     |   0.00032 |    0.0047 |             24.7 |              5466
 060DC     |   0.00033 |    0.0048 |             24.6 |              5498
 060VA     |   0.00032 |    0.0047 |             24.6 |              5447
 060VB     |   0.00033 |    0.0049 |             24.6 |              5445
 060VC     |   0.00032 |    0.0047 |             24.6 |              5434
 06MA      |   0.00032 |    0.0047 |             24.6 |              5496
 06MB      |   0.00032 |    0.0047 |             24.7 |              5466
 06MC      |   0.00032 |    0.0047 |             24.6 |              5476
 090DA     |   0.00033 |    0.0047 |             24.6 |              5568
 090DB     |   0.00033 |    0.0048 |             24.6 |              5518
 090DC     |   0.00032 |    0.0046 |             24.6 |              5462
```

```
 090VA      |   0.00032 |    0.0047 |             24.6 |              5468
 090VB      |   0.00031 |    0.0046 |             24.6 |              5458
 090VC      |   0.00031 |    0.0046 |             24.6 |              5435
 18MA       |   0.00031 |    0.0046 |             24.7 |              5416
 18MB       |   0.00032 |    0.0046 |             24.6 |              5440
 18MC       |   0.00032 |    0.0046 |             24.6 |              5471
 SGA        |   0.00032 |    0.0047 |             24.6 |              5318
 SGB        |   0.00031 |    0.0046 |             24.7 |              5418
 SGC        |   0.00031 |    0.0046 |             24.7 |              5490
 SGD        |   0.00032 |    0.0047 |             24.6 |              5483
(42 filas)
```

B.7 Maximum Force and Strength

To create the maximum force and strength views, one used the following two SQL command:

```
CREATE VIEW allSamplesMaxAxialForce AS
SELECT anyAlias1.sample_Id,
       CAST( MAX(anyAlias1.axialForceData) AS decimal(8,1) ) AS max_axialForce_kg
FROM
  (
  SELECT laboratorytempid AS sample_Id,
         unnest(testAxialForce1) AS axialForceData
  FROM testedSamples
  ) AS anyAlias1
GROUP BY anyAlias1.sample_Id
ORDER BY anyAlias1.sample_Id ASC;

CREATE VIEW allSamplesMaxAxialStrength AS
SELECT alias1.sample_Id,
       alias1.max_axialForce_kg,
       CAST( alias1.max_axialForce_kg *9.81 /power(10,6) /alias2.neArea_m2 AS decimal
    (4,1) ) AS max_axialStress_MPa
FROM allSamplesMaxAxialForce AS alias1, allSamplesIndexPropsOutputs AS alias2
WHERE alias1.sample_Id =alias2.sample_Id
ORDER BY alias1.sample_Id ASC;
```

In order to see the resulting view, type `SELECT * FROM allSamplesMaxAxialStrength;`, and the following display will emerge:

```
 sample_id | max_axialforce_kg | max_axialstress_mpa
-----------+-------------------+---------------------
 000DA     |           59186.5 |               121.0
 000DB     |           85169.3 |               177.8
 000DC     |           76552.9 |               159.8
 000VA     |          107863.0 |               220.4
 000VB     |           63798.6 |               133.2
 000VC     |           30417.1 |                64.9
 00MA      |           26456.4 |                55.2
```

```
 00MB      |           30686.3 |               62.7
 030DA     |           70114.2 |              146.3
 030DB     |           82437.5 |              172.1
 030DC     |           69070.8 |              147.3
 030VA     |          110104.0 |              225.0
 030VB     |           15502.1 |               33.1
 030VC     |          112717.0 |              235.3
 045DB     |          106188.0 |              221.6
 045DC     |           83832.3 |              175.0
 045VA     |           69302.7 |              144.7
 045VB     |           86312.8 |              180.2
 045VC     |           93121.7 |              194.4
 060DA     |           75972.5 |              158.6
 060DB     |           82495.7 |              172.2
 060DC     |           83444.8 |              170.5
 060VA     |           84684.8 |              176.8
 060VB     |           50202.7 |              100.5
 060VC     |          115801.0 |              241.7
 06MA      |           50511.0 |              105.4
 06MB      |           14579.9 |               30.4
 06MC      |           41305.9 |               86.2
 090DA     |           48102.9 |              100.4
 090DB     |          105292.0 |              215.2
 090DC     |           50164.2 |              107.0
 090VA     |          110455.0 |              230.5
 090VB     |           79416.9 |              169.4
 090VC     |           77113.9 |              164.5
 18MA      |           47467.2 |              101.2
 18MB      |           45406.6 |               96.8
 18MC      |           59996.8 |              127.9
 SGA       |          130103.0 |              271.6
 SGB       |           30205.6 |               64.4
 SGC       |           69302.7 |              147.8
 SGD       |           45830.2 |               95.7
(41 filas)
```

Here, data that does not have values are ignored (e.g. data of sample 00MC). Therefore, only 41 items are displayed, rather than the 42 items displayed, as it was shown in the above queries.

B.8 SQL Functions for Measurements Readings

Until here, it was performed simple SQL queries. But in the fields `time1_s`, `strain1_`, `strain2_`, ..., `strain5_`, and `force1_kgf`, values are not properly transformed to the required units for analysis:

- time data is originally stored relative to a time different from the initial value, therefore need to be transformed relative to the first value;

- strains are in $\mu m/m$, therefore should be transformed to strains by multiplying by 10^{-6};
- forces are in kg–force and should be divided by the transverse area of the corresponding sample and expressed in MPa.

In order to do those transformations, one should first create SQL functions.

B.8.1 Transforming to relative time

The SQL function used to transform the time relative to the first time–reading is the following one:

```
CREATE OR REPLACE FUNCTION time2reltime( real[] )
  --Calculates the relative, to the first reading, time array (any unit)
  --from an array that contents absolute time values
  --Input(s):
  --Absolute time one-dimensional array ($1);
  --Output(s):
  --One-dimensional array of relative times.
  RETURNS SETOF real[] AS
$BODY$
SELECT array(
          SELECT
             $1[i] -$1[array_lower($1,1)]
          FROM generate_series( array_lower($1,1), array_upper($1,1) ) AS g(i)
) AS result;
$BODY$
LANGUAGE SQL;
```

B.8.2 Transforming from $\mu m/m$ to m/m

The SQL function used to transform $\mu m/m$ to m/m, and relative to the first reading is the following one:

```
CREATE OR REPLACE FUNCTION milistrain2strain( real[] )
  --Calculates the relative, to the first reading, strain array (adimensional)
  --from an array that contents absolute strain values in microstrains.
  --Input(s):
  --Absolute strain one-dimensional array in microstrains ($1);
  --Output(s):
  --One-dimensional array of relative strains adimensional.
  RETURNS SETOF real[] AS
$BODY$
SELECT array(
```

```
          SELECT
             CAST( ($1[i] -$1[array_lower($1,1)]) *10^(-6) AS real )
          FROM generate_series( array_lower($1,1), array_upper($1,1) ) AS g(i)
) AS result;
$BODY$
LANGUAGE SQL;
```

B.8.3 Transforming from force and area to stress

The SQL function used to transform force and area to stress values is the following one:

```
CREATE OR REPLACE FUNCTION force2stressmks( real[], real )
  --Calculates the stress in mks units (i.e. MPa) of a force in kg that
  --is acting against a surface expressed in m2.
  --Input(s):
  --Force one-dimesioinal array in kg ($1);
  --Area of the surface in m2 ($2).
  --Output(s):
  --One-dimensional array of stresses in MPa.
  RETURNS SETOF double precision[] AS
$BODY$
SELECT array(
 SELECT $1[i]  /$2 *9.81 *10^(-6)
 FROM generate_series( array_lower($1,1), array_upper($1,1) ) AS g(i)
 ) AS result;
$BODY$
LANGUAGE SQL;
```

B.9 The Pre–Processed Data Base

The measured data was stored —as mentioned above— in a table named `testedsamples`. The data was stored in that table as–is, where no pre–processing was performed. Now, it will be created a new table where all data will be stored, by making the transformations described in the above section by using the three just created SQL functions (i.e. `time2reltime`, `milistrain2strai`, and `force2stressmks`). The resulting table will be named `testsResults`, but in order to reach that final table some intermediate views should be created.

This first created view transforms the rough times readings to a relative time (i.e. relative to the first measurement time) for all the samples here tested. In order to do so, one used the recent created SQL function `time2reltime` in the following statement:

```
CREATE VIEW allSamplesTimeArray1 AS
```

```
SELECT alias.sample_id,
       time2reltime( alias.absTime ) AS time1_s
FROM (
     SELECT laboratorytempid AS sample_Id,
            testTimeInstance AS absTime
     FROM testedSamples
     ) AS alias;
```

Because each sample has around hundreds of measurements, for this query example listing one will show only the measurements corresponding to the 50^{th} up to the 55^{th} readings, by typing in the POSTGRESQL® shell the following:

```
SELECT sample_Id, time1_s[50:55] FROM allSamplesTimeArray1 ORDER BY sample_Id;
```

By doing so, the following display is shown:

```
 sample_id |       time1_s
-----------+---------------------
 000DA     | {49,50,51,52,53,54}
 000DB     | {49,50,51,52,53,54}
 000DC     | {49,50,51,52,53,54}
 000VA     | {49,50,51,52,53,54}
 000VB     | {49,50,51,52,53,54}
 000VC     | {49,50,51,52,53,54}
 00MA      | {49,50,51,52,53,54}
 00MB      | {49,50,51,52,53,54}
 00MC      | {}
 030DA     | {49,50,51,52,53,54}
 030DB     | {49,50,51,52,53,54}
 030DC     | {49,50,51,52,53,54}
 030VA     | {49,50,51,52,53,54}
 030VB     | {49,50,51,52,53,54}
 030VC     | {49,50,51,52,53,54}
 045DB     | {49,50,51,52,53,54}
 045DC     | {49,50,51,52,53,54}
 045VA     | {49,50,51,52,53,54}
 045VB     | {49,50,51,52,53,54}
 045VC     | {49,50,51,52,53,54}
 060DA     | {49,50,51,52,53,54}
 060DB     | {49,50,51,52,53,54}
 060DC     | {49,50,51,52,53,54}
 060VA     | {49,50,51,52,53,54}
 060VB     | {49,50,51,52,53,54}
 060VC     | {49,50,51,52,53,54}
 06MA      | {49,50,51,52,53,54}
 06MB      | {49,50,51,52,53,54}
 06MC      | {49,50,51,52,53,54}
 090DA     | {49,50,51,52,53,54}
 090DB     | {49,50,51,52,53,54}
 090DC     | {49,50,51,52,53,54}
 090VA     | {49,50,51,52,53,54}
 090VB     | {49,50,51,52,53,54}
```

```
 090VC     | {49,50,51,52,53,54}
 18MA      | {49,50,51,52,53,54}
 18MB      | {49,50,51,52,53,54}
 18MC      | {49,50,51,52,53,54}
 SGA       | {49,50,51,52,53,54}
 SGB       | {49,50,51,52,53,54}
 SGC       | {49,50,51,52,53,54}
 SGD       | {49,50,51,52,53,54}
(42 filas)
```

As can be shown, because sample 00MC was not tested, that it has an empty array.

The following SQL statements will create the views for the transformed measurements of the five strains and the axial stress.

The SQL statement that transforms the strain measurements of strain gage 1 for all samples is as follows:

```
CREATE VIEW allSamplesStrainArray1 AS
SELECT alias.sample_id,
       milistrain2strain( alias.absStrain_milistrains ) AS strain1_
FROM (
      SELECT laboratorytempid AS sample_Id,
             testStrainGage1 AS absStrain_milistrains
      FROM testedSamples
     )
AS alias;
```

The SQL statement that transforms the strain measurements of strain gage 2 for all samples is as follows:

```
CREATE VIEW allSamplesStrainArray2 AS
SELECT alias.sample_id,
       milistrain2strain( alias.absStrain_milistrains ) AS strain2_
FROM (
      SELECT laboratorytempid AS sample_Id,
             testStrainGage2 AS absStrain_milistrains
      FROM testedSamples
     )
AS alias;
```

The SQL statement that transforms the strain measurements of strain gage 3 for all samples is as follows:

```
CREATE VIEW allSamplesStrainArray3 AS
SELECT alias.sample_id,
       milistrain2strain( alias.absStrain_milistrains ) AS strain3_
FROM (
      SELECT laboratorytempid AS sample_Id,
```

```
            testStrainGage3 AS absStrain_milistrains
      FROM testedSamples
     )
AS alias;
```

The SQL statement that transforms the strain measurements of strain gage 4 for all samples is as follows:

```
CREATE VIEW allSamplesStrainArray4 AS
SELECT alias.sample_id,
       milistrain2strain( alias.absStrain_milistrains ) AS strain4_
FROM (
      SELECT laboratorytempid AS sample_Id,
             testStrainGage4 AS absStrain_milistrains
      FROM testedSamples
     )
AS alias;
```

The SQL statement that transforms the strain measurements of strain gage 5 for all samples is as follows:

```
CREATE VIEW allSamplesStrainArray5 AS
SELECT alias.sample_id,
       milistrain2strain( alias.absStrain_milistrains ) AS strain5_
FROM (
      SELECT laboratorytempid AS sample_Id,
             testStrainGage5 AS absStrain_milistrains
      FROM testedSamples
     )
AS alias;
```

Finally, the SQL statement that transforms the force measurements to stress measurements for all samples is as follows:

```
CREATE VIEW allSamplesStressArray1 AS
SELECT alias3.sample_Id,
       CAST( force2stressmks( alias3.axialForce_kgf, alias3.area_m2 ) AS decimal(6,2)[] )
     AS stress1_MPa
FROM
  (
  SELECT alias1.laboratorytempid AS sample_Id,
         alias1.testAxialForce1 AS axialForce_kgf,
         alias2.neArea_m2 AS area_m2
  FROM testedSamples AS alias1, allSamplesIndexPropsOutputs AS alias2
  WHERE alias1.laboratorytempid =alias2.sample_id
  ) AS alias3;
```

For example, if one wants to list again the stress of the corresponding data located in the interval between the 50^{th} and the 55^{th} readings, one should type the following query:

```
SELECT sample_Id, stress1_MPa[50:55] FROM allSamplesStressArray1 ORDER BY sample_Id;
```

. . . and the following result will be displayed:

```
 sample_id |              stress1_mpa
-----------+--------------------------------------
 000DA     | {7.85,7.89,7.85,8.01,8.17,8.36}
 000DB     | {10.62,11.19,11.39,11.23,11.55,12.27}
 000DC     | {26.46,27.62,28.27,29.63,30.07,30.83}
 000VA     | {5.77,6.01,6.32,6.24,6.12,6.48}
 000VB     | {14.23,14.07,14.91,15.48,15.28,15.80}
 000VC     | {15.98,17.37,17.20,18.27,19.74,19.33}
 00MA      | {8.74,8.86,9.70,9.50,10.30,10.50}
 00MB      | {1.30,1.26,1.92,1.65,2.43,2.28}
 00MC      | {}
 030DA     | {3.61,3.73,3.93,4.09,4.21,4.37}
 030DB     | {7.38,7.70,7.54,7.38,7.54,7.82}
 030DC     | {7.13,8.15,7.86,8.68,8.64,8.97}
 030VA     | {11.27,11.11,12.52,12.29,13.70,13.62}
 030VB     | {15.81,17.37,16.96,18.43,18.02,19.58}
 030VC     | {7.90,7.58,8.50,8.26,9.10,8.90}
 045DB     | {1.24,1.12,1.32,1.44,1.28,1.64}
 045DC     | {16.84,17.32,17.12,18.76,18.48,20.33}
 045VA     | {0.72,0.76,0.72,0.72,0.80,0.80}
 045VB     | {12.79,12.59,12.51,13.59,13.71,13.55}
 045VC     | {10.10,11.07,10.82,11.95,11.83,12.75}
 060DA     | {4.77,4.61,5.13,5.21,5.09,5.61}
 060DB     | {6.82,6.74,7.14,7.46,7.54,7.42}
 060DC     | {9.42,9.62,9.46,10.56,10.48,10.48}
 060VA     | {6.66,6.74,7.18,7.46,7.58,7.50}
 060VB     | {17.92,19.11,19.34,19.50,20.84,20.61}
 060VC     | {8.22,8.62,8.94,9.22,9.90,9.86}
 06MA      | {4.89,5.41,5.29,6.05,5.69,6.25}
 06MB      | {14.19,14.07,15.44,15.40,15.36,16.84}
 06MC      | {15.88,17.24,17.08,17.80,18.24,18.56}
 090DA     | {0.52,0.48,0.52,0.56,0.60,0.60}
 090DB     | {9.34,9.93,10.17,10.05,10.13,10.83}
 090DC     | {17.86,19.01,19.33,20.11,20.89,20.69}
 090VA     | {0.92,0.92,1.08,1.04,1.04,1.16}
 090VB     | {18.11,17.90,19.74,19.50,20.65,21.14}
 090VC     | {18.93,20.32,21.01,21.18,22.61,22.33}
 18MA      | {12.49,12.33,13.48,13.19,14.38,14.05}
 18MB      | {7.05,7.82,7.70,7.78,8.52,8.32}
 18MC      | {14.58,15.24,15.61,16.34,16.71,17.53}
 SGA       | {0.68,0.80,0.76,0.80,0.88,0.80}
 SGB       | {4.55,4.26,5.24,5.08,4.87,5.61}
 SGC       | {0.74,0.78,0.74,0.74,0.82,0.82}
 SGD       | {10.94,11.67,11.83,12.79,12.75,13.87}
(42 filas)
```

But until now, one created only separate views of the pre–processed values. It is necessary to join all data in one table. The procedure to do so, is to join tables twice each time. The following

SQL statements show this procedure.

```
CREATE VIEW allSamplesTimeStrain1ArrayLast01 AS
  SELECT alias0.sample_Id,
         alias0.time1_s,
         alias1.strain1_
  FROM allSamplesTimeArray1 AS alias0,
       allSamplesStrainArray1 AS alias1
  WHERE alias0.sample_id = alias1.sample_id;

CREATE VIEW allSamplesLast01Strain2ArrayLast02 AS
  SELECT alias0.sample_Id,
         alias0.time1_s,
         alias0.strain1_,
         alias1.strain2_
  FROM allSamplesTimeStrain1ArrayLast01 AS alias0,
       allSamplesStrainArray2 AS alias1
  WHERE alias0.sample_id = alias1.sample_id;

CREATE VIEW allSamplesLast02Strain3ArrayLast03 AS
  SELECT alias0.sample_Id,
         alias0.time1_s,
         alias0.strain1_,
         alias0.strain2_,
         alias1.strain3_
  FROM allSamplesLast01Strain2ArrayLast02 AS alias0,
       allSamplesStrainArray3 AS alias1
  WHERE alias0.sample_id = alias1.sample_id;

CREATE VIEW allSamplesLast03Strain4ArrayLast04 AS
  SELECT alias0.sample_Id,
         alias0.time1_s,
         alias0.strain1_,
         alias0.strain2_,
         alias0.strain3_,
         alias1.strain4_
  FROM allSamplesLast02Strain3ArrayLast03 AS alias0,
       allSamplesStrainArray4 AS alias1
  WHERE alias0.sample_id = alias1.sample_id;

CREATE VIEW allSamplesLast04Strain5ArrayLast05 AS
  SELECT alias0.sample_Id,
         alias0.time1_s,
         alias0.strain1_,
         alias0.strain2_,
         alias0.strain3_,
         alias0.strain4_,
         alias1.strain5_
  FROM allSamplesLast03Strain4ArrayLast04 AS alias0,
       allSamplesStrainArray5 AS alias1
  WHERE alias0.sample_id = alias1.sample_id;

CREATE VIEW allSamplesLast05Stress1ArrayLast06 AS
  SELECT alias0.sample_Id,
         alias0.time1_s,
```

```
        alias0.strain1_,
        alias0.strain2_,
        alias0.strain3_,
        alias0.strain4_,
        alias0.strain5_,
        alias1.stress1_MPa
  FROM allSamplesLast04Strain5ArrayLast05 AS alias0,
       allSamplesStressArray1 AS alias1
  WHERE alias0.sample_id = alias1.sample_id;
```

The final view of all these six SQL statements (i.e. `allSamplesLast05Stress1ArrayLast06`) groups all the laboratory measurements pre–processing calculations. This values are related with the sample name. For example, if one want see the data of the 55^{th} and the 56^{th} readings of all samples whose names begins with SG, one should type the following query:

```
SELECT sample_Id, time1_s[55:56], strain1_[55:56], strain2_[55:56], strain3_[55:56],
    strain4_[55:56], strain5_[55:56], stress1_MPa[55:56]
   FROM allSamplesLast05Stress1ArrayLast06 WHERE sample_Id LIKE 'SG%' ORDER BY sample_Id
    ASC;
```

By waiting for some seconds, one will have as result the following view:

```
 sample_id | time1_s |       strain1_         |       strain2_         |         strain3_
           |         strain4_          |          strain5_           |  stress1_mpa
-----------+---------+------------------------+-------------------------+------------------
--------+-------------------------+---------------------------+---------------
 SGA       | {54,55} | {2e-06,3e-06}          | {2e-06,3e-06}          | {-6e-06,-7e-06}
           | {-1.2e-05,-1.3e-05}     | {-1.4e-05,-1.6e-05}       | {0.80,0.96}
 SGB       | {54,55} | {1.801e-05,1.754e-05} | {1.896e-05,1.896e-05} | {-2.228e-05,-2.228
    e-05}   | {-5.214e-05,-5.119e-05} | {-8.815e-05,-8.626e-05}   | {5.61,5.53}
 SGC       | {54,55} | {3.79e-06,3.79e-06}   | {3.79e-06,3.31e-06}   | {-2.85e-06,-2.85e
    -06}     | {-1.138e-05,-1.09e-05}  | {-1.09e-05,-9.95e-06}     | {0.82,0.74}
 SGD       | {54,55} | {5.829e-05,5.734e-05} | {7.393e-05,7.298e-05} |
    {-0.00013839,-0.00013744} | {-4.834e-05,-4.645e-05} | {-0.00010901,-0.00010569} |
    {13.87,13.67}
(4 filas)
```

But it should be very interesting to have a complete–results table, this means to have not only the measured data of time, strains and axial stresses, but also the data of index properties and maximum strength values, which will conform the wanted `testsResults` table. For that, one should join the views previous created: `allSamplesIndexPropsOutputs`, `allSamplesMaxAxialStrength` and `allSamplesLast05Stress1ArrayLast06`; and this joining process should be done one pair each time. The processing may delay several minutes for each joining–view, and these are as follows:

```
CREATE VIEW allSamplesIdxPropOutMaxAxialStrengthLast01 AS
    SELECT aliasView1.sample_id,
           aliasView1.volume_m3,
           aliasView1.neArea_m2,
```

```
          aliasView1.unitWeight_kN_m2,
          aliasView1.nadirPropVel_m_s1,
          aliasView2.max_axialForce_kg,
          aliasView2.max_axialStress_MPa
    FROM allSamplesIndexPropsOutputs AS aliasView1, allSamplesMaxAxialStrength AS
    aliasView2
    WHERE aliasView1.sample_Id = aliasView2.sample_Id;

CREATE VIEW allsamplesReadyDataforProcessing AS
    SELECT aliasView1.sample_id,
          aliasView1.nadirPropVel_m_s1,
          aliasView1.neArea_m2,
          aliasView1.volume_m3,
          aliasView1.unitWeight_kN_m2,
          aliasView1.max_axialForce_kg,
          aliasView1.max_axialStress_MPa,
          aliasView2.time1_s,
          aliasView2.strain1_,
          aliasView2.strain2_,
          aliasView2.strain3_,
          aliasView2.strain4_,
          aliasView2.strain5_,
          aliasView2.stress1_MPa
    FROM allSamplesIdxPropOutMaxAxialStrengthLast01 AS aliasView1,
    allSamplesLast05Stress1ArrayLast06 AS aliasView2
    WHERE aliasView1.sample_Id = aliasView2.sample_Id
    ORDER BY aliasView1.sample_id ASC;

CREATE VIEW allSamplesDipInfo AS
  SELECT alias3.laboratorytempid AS sample_Id,
         alias3.materialetchType,
         alias2.discontDip
  FROM materialEtchType AS alias2, testedSamples AS alias3
  WHERE alias3.materialetchType =alias2.etchType
  ORDER BY alias3.materialetchType ASC, alias2.discontDip DESC;

CREATE TABLE testsResults AS
  SELECT   alias1.sample_id,
          alias2.materialetchType,
          alias2.discontDip,
          alias1.nadirPropVel_m_s1,
          alias1.neArea_m2,
          alias1.volume_m3,
          alias1.unitWeight_kN_m2,
          alias1.max_axialForce_kg,
          alias1.max_axialStress_MPa,
          alias1.time1_s,
          alias1.strain1_,
          alias1.strain2_,
          alias1.strain3_,
          alias1.strain4_,
          alias1.strain5_,
          alias1.stress1_MPa
  FROM allsamplesReadyDataforProcessing AS alias1, allSamplesDipInfo AS alias2
```

```
  WHERE alias2.sample_Id = alias1.sample_Id;
```

The resulting table with all data is so big to display, but it contains all the necessary data to begin any post–processing calculation. But for example, if one wants to extract all the data from samples names beginning with 045VN, but for readings 21 and 22, one should type the following SQL sentence:

```
SELECT sample_id,
       materialetchType,
       discontDip,
       nadirPropVel_m_s1,
       neArea_m2,
       volume_m3,
       unitWeight_kN_m2,
       max_axialForce_kg,
       max_axialStress_MPa,
       time1_s[21:22],
       strain1_[21:22],
       strain2_[21:22],
       strain3_[21:22],
       strain4_[21:22],
       strain5_[21:22],
       stress1_MPa[21:22]
FROM testsResults WHERE sample_id LIKE '045V%' ORDER BY sample_Id ASC;
```

Or, if one wants all the data for sample 045VA, type:

```
SELECT sample_id,
       materialetchType,
       discontDip,
       nadirPropVel_m_s1,
       neArea_m2,
       volume_m3,
       unitWeight_kN_m2,
       max_axialForce_kg,
       max_axialStress_MPa,
       time1_s,
       strain1_,
       strain2_,
       strain3_,
       strain4_,
       strain5_,
       stress1_MPa
FROM testsResults WHERE sample_Id='045VA';
```

B.10 The Post–Processing Data Input Table

Using the last created table `testsResults` one can create easily the post–processing data input table, which will be stored in the `results4analysis` table. But before obtaining the `results4analysis` table, one will obtain intermediate views.

For example, if one wants to know the ultimate strength values for all blank samples, one can type the following query, which will be stored in a new view named `materialResultArray`:

```
CREATE VIEW materialResultArray AS
  SELECT materialEtchType,
         array( SELECT max_axialStress_MPa FROM testsResults WHERE materialetchType ='
    BLNK' ) AS maxStress_MPa
  FROM testsResults WHERE materialEtchType ='BLNK' GROUP BY materialEtchType;
```

In order to see the resulting query, one types `SELECT * FROM materialResultArray;` and obtains the following result:

```
 materialetchtype |      maxstress_mpa
------------------+-------------------------
 BLNK             | {271.6,64.4,147.8,95.7}
(1 fila)
```

For maximum stress obtained at the Etched Discontinuities Samples (i.e. ED samples), one should make the following queries (and stored each one in a view if wanted):

```
CREATE VIEW discontByDipTempo AS
 SELECT materialEtchType, max_axialStress_MPa FROM testsResults WHERE materialetchType
    LIKE 'DS%';
CREATE VIEW discontByDip00 AS
  SELECT materialEtchType, array( SELECT max_axialStress_MPa FROM discontByDipTempo WHERE
     materialetchType ='DS00' ) AS maxStress_MPa FROM discontByDipTempo WHERE
    materialEtchType ='DS00'
  GROUP BY materialEtchType;
CREATE VIEW discontByDip30 AS
  SELECT materialEtchType, array( SELECT max_axialStress_MPa FROM discontByDipTempo WHERE
     materialetchType ='DS30' ) AS maxStress_MPa FROM discontByDipTempo WHERE
    materialEtchType ='DS30'
  GROUP BY materialEtchType;
CREATE VIEW discontByDip45 AS
  SELECT materialEtchType, array( SELECT max_axialStress_MPa FROM discontByDipTempo WHERE
     materialetchType ='DS45' ) AS maxStress_MPa FROM discontByDipTempo WHERE
    materialEtchType ='DS45'
  GROUP BY materialEtchType;
CREATE VIEW discontByDip60 AS
  SELECT materialEtchType, array( SELECT max_axialStress_MPa FROM discontByDipTempo WHERE
     materialetchType ='DS60' ) AS maxStress_MPa FROM discontByDipTempo WHERE
    materialEtchType ='DS60'
  GROUP BY materialEtchType;
```

```
CREATE VIEW discontByDip90 AS
  SELECT materialEtchType, array( SELECT max_axialStress_MPa FROM discontByDipTempo WHERE
     materialetchType ='DS90' ) AS maxStress_MPa FROM discontByDipTempo WHERE
    materialEtchType ='DS90'
  GROUP BY materialEtchType;
```

The same should be made for negative–etched discontinuities samples (i.e. NED samples):

```
CREATE VIEW veinByDipTempo AS
 SELECT materialEtchType, max_axialStress_MPa FROM testsResults WHERE materialetchType
    LIKE 'VN%';
CREATE VIEW veinByDip00 AS
  SELECT materialEtchType, array( SELECT max_axialStress_MPa FROM veinByDipTempo WHERE
    materialetchType ='VN00' ) AS maxStress_MPa FROM veinByDipTempo WHERE
    materialEtchType ='VN00'
  GROUP BY materialEtchType;
CREATE VIEW veinByDip30 AS
  SELECT materialEtchType, array( SELECT max_axialStress_MPa FROM veinByDipTempo WHERE
    materialetchType ='VN30' ) AS maxStress_MPa FROM veinByDipTempo WHERE
    materialEtchType ='VN30'
  GROUP BY materialEtchType;
CREATE VIEW veinByDip45 AS
  SELECT materialEtchType, array( SELECT max_axialStress_MPa FROM veinByDipTempo WHERE
    materialetchType ='VN45' ) AS maxStress_MPa FROM veinByDipTempo WHERE
    materialEtchType ='VN45'
  GROUP BY materialEtchType;
CREATE VIEW veinByDip60 AS
  SELECT materialEtchType, array( SELECT max_axialStress_MPa FROM veinByDipTempo WHERE
    materialetchType ='VN60' ) AS maxStress_MPa FROM veinByDipTempo WHERE
    materialEtchType ='VN60'
  GROUP BY materialEtchType;
CREATE VIEW veinByDip90 AS
  SELECT materialEtchType, array( SELECT max_axialStress_MPa FROM veinByDipTempo WHERE
    materialetchType ='VN90' ) AS maxStress_MPa FROM veinByDipTempo WHERE
    materialEtchType ='VN90'
  GROUP BY materialEtchType;
```

Now, one will join all views in one and stored in the `incliUltStrengthModelTests` view:

```
CREATE VIEW incliUltStrengthModelTests AS
  SELECT materialEtchType, maxStress_MPa FROM  materialResultArray
  UNION
  SELECT materialEtchType, maxStress_MPa FROM veinByDip00
  UNION
  SELECT materialEtchType, maxStress_MPa FROM veinByDip30
  UNION
  SELECT materialEtchType, maxStress_MPa FROM veinByDip45
  UNION
  SELECT materialEtchType, maxStress_MPa FROM veinByDip60
  UNION
  SELECT materialEtchType, maxStress_MPa FROM veinByDip90
  UNION
  SELECT materialEtchType, maxStress_MPa FROM discontByDip00
```

```
  UNION
  SELECT materialEtchType, maxStress_MPa FROM discontByDip30
  UNION
  SELECT materialEtchType, maxStress_MPa FROM discontByDip45
  UNION
  SELECT materialEtchType, maxStress_MPa FROM discontByDip60
  UNION
  SELECT materialEtchType, maxStress_MPa FROM discontByDip90
  ORDER BY materialEtchType;
```

And finally, one will create the wanted table with all the values in it:

```
CREATE TABLE results4analysis AS
SELECT alias1.etchType,
       alias1.discontdip,
       alias2.maxStress_MPa
FROM materialEtchType AS alias1, incliUltStrengthModelTests AS alias2
WHERE alias1.etchType = alias2.materialEtchType
ORDER BY alias1.etchType ASC;
```

In order to display the total table, put `SELECT * FROM results4analysis;` in the POSTGRESQL® shell, which will display finally the post–processing data input table:

```
 etchtype | discontdip |      maxstress_mpa
----------+------------+-------------------------
 BLNK     |            | {271.6,64.4,147.8,95.7}
 DS00     |        0.0 | {121.0,177.8,159.8}
 DS30     |       30.0 | {146.3,172.1,147.3}
 DS45     |       45.0 | {221.6,175.0}
 DS60     |       60.0 | {158.6,172.2,170.5}
 DS90     |       90.0 | {100.4,215.2,107.0}
 VN00     |        0.0 | {220.4,133.2,64.9}
 VN30     |       30.0 | {225.0,33.1,235.3}
 VN45     |       45.0 | {144.7,180.2,194.4}
 VN60     |       60.0 | {176.8,100.5,241.7}
 VN90     |       90.0 | {230.5,169.4,164.5}
```

In this Appendix was exposed some SQL statements useful to manage the data that was obtained in this research. More queries can be made within.

Appendix C

POSTGRESQL and MATLAB interaction

In this appendix it will explained how to process data from the the initial data processing data base created with POSTGRESQL® (here stored in table `results4analysis`). Post–processing sometimes require large and more complicated calculations than those used in pre–processing, therefore it is better to use a more properly programming language rather than the SQL language[1]. This proper programming language is MATLAB® , for example; which was used in this research.

I order to use such a post–processing program, as the chosen MATLAB® , it is necessary to establish a connection between this and the data base manager program that was the whole data base (i.e. in this case the POSTGRESQL® program). If such connection is not established automatically without the user manual intervention, noting was done; because the advantages in using a data base manager is lost.

In the following sections, it will explained how to perform that connection between POSTGRESQL® and MATLAB® .

C.1 Making the Connection from MATLAB® to POSTGRESQL®

Add dynamically the Java–Class file path of the JDBC driver (i.e. `org.postgresql.Driver`) in the MATLAB® path file, by tipping in this program command window:

[1] Experts in SQL programming states that any calculation could be performed in this language, which is true; but their implementation could be cumbersome, and sometimes calculation–processing times can be longer than the corresponding when using another language programming paradigm.

```
javaaddpath /usr/share/java/postgresql-9.1-901.jdbc3.jar
```

Verify that this was done, by looking at the end of the resulting view after typing:

```
javaclasspath
```

Create the connectivity structure, named here `conn2ludgertesisdb`, by using the `database` MATLAB® function and by typing:

```
conn2ludgertesisdb =database ('ludgertesisdb', 'ludger', 'ToInfinity12', 'org.postgresql.
    Driver', 'jdbc:postgresql://localhost/ludgertesisdb')
```

If the connection was established, the following message will be displayed:

```
conn2ludgertesisdb =

       Instance: 'ludgertesisdb'
       UserName: 'ludger'
         Driver: 'org.postgresql.Driver'
            URL: 'jdbc:postgresql://localhost/ludgertesisdb'
    Constructor: [1x1 com.mathworks.toolbox.database.databaseConnect]
        Message: []
         Handle: [1x1 org.postgresql.jdbc3.Jdbc3Connection]
        TimeOut: 0
     AutoCommit: 'on'
           Type: 'Database Object'
```

One can, indeed confirm the connection by typing:

```
ping(conn2ludgertesisdb)
```

After the connection was established, one can extract any value from the created data base by using SQL commands, using the `exec` MATLAB® function. In the following paragraphs, some simple examples are shown in order to make possible to use this potential approach.

C.2 Extracting Data from POSTGRESQL® to MATLAB® and *Vice Versa*

The two connectivity activities the two programs should perform is to extract the values from POSTGRESQL® objects and perform calculations in MATLAB® , and to perform calculations in POSTGRESQL® and then exporting to MATLAB® . These two activities will guarantee the interactivity of the two programs.

C.2.1 Extract the values from POSTGRESQL® and perform calculations in MATLAB®

Obtain the SQL–sentence execution structure by typing it between simple quotation marks and store it in a MATLAB® variable, say for example `cursorC`:

```
cursorC = exec(conn2ludgertesisdb, ' SELECT array_to_string(northLength, '', '') FROM
    samplesfortesting WHERE numericalID =''1'' ');
```

In this example, the SQL–sentence is:

```
SELECT array_to_string(northLength, '', '') FROM samplesfortesting WHERE numericalID
    =''1'';
```

which orders the POSTGRESQL® to convert the array–object of the column `northLength` in the table `samplesfortesting` for the row that has an identification of 1 in `numericalID`.

After that, the `cursorC` should be transformed to a MATLAB® readable format, therefore the `fetch` function is used, as follows:

```
cursorCRes =fetch(cursorC);
```

The `cursorCRes` structure is now MATLAB® readable, but it is not still a number or an array of numbers within is possible to perform calculations, because it has a lot of information field about the origin and method of extraction of the data. Among these fields, the `.Data` is that concerns to us to extract. To do so, it is necessary to set to a new variable the value of that field, as follows:

```
arrayInCellText= cursorCRes.Data;
```

This is an array of real numbers that are under simple quotations marks (so it is a chain of numbers) inside a cell. Therefore, the next step is to transform it, first to a text chain and then to a number array, by doing the following:

```
arrayInText=char(arrayInCellText);
arrayInNum=str2num(arrayInText);
```

The `arrayInMun` is now a MATLAB® numerically manipulable variable. For example, one can calculate the average value of that array by using the simple function of MATLAB® :

```
meanValue= mean(arrayInNum);
```

C.2.2 Perform calculations in POSTGRESQL® and then exporting to MATLAB®

The POSTGRESQL® program can perform any simple or complicated operation in different object types. This program is considered the most advanced open–source data base manager nowadays. In the field of our interest, one important capability of this program is that it can operate in spatial 2D and 3D objects (i.e. points, lines, polygons, circles, cubic element). But this advantages can be used by experts in programming within this program, therefore and meanwhile, the easiest manner to make complex operations for common engineers is to use MATLAB® or a similar programming language (e.g. SciLab, Octave).

Only to show how POSTGRESQL® can perform calculations, in the following paragraphs it is exposed how to obtain the same result of the upper mentioned simple example by using SQL sentences.

Obtain a cursor with the SQL sentence that makes the average calculation of values stored in an array object.

```
cursorD = exec(conn2ludgertesisdb, ' SELECT AVG(UNNEST(anyAlias)) FROM (SELECT UNNEST(
    northLength ) FROM samplesfortesting WHERE numericalID=1 ) AS anyAlias ');
```

Transform the resulting cursor to a MATLAB® readable structure:

```
cursorDRes=fetch(cursorD);
```

Extract from that structure only the desired value and store it in a variable, which is a cell of a number:

```
meanValueInCell=cursorDRes.Data;
```

Convert the cell into a number, which is the value it is look for:

```
meanValue02=cell2mat(meanValueInCell);
```

A similar result may be possible for a simple operation in a variable that is not an array and to calculated for all the data in the table.

```
cursorB = exec(conn2ludgertesisdb, 'SELECT AVG(dryWeigth) FROM
 samplesfortesting');

cursorBRes=fetch(cursorB);
meanDensity=cursorBRes.Data{1,1};
```

C.2.3 Extract the whole data from POSTGRESQL® to be read in MATLAB®

To extract the whole or at least a great part of the entire data from a data base in order to perform calculations in MATLAB® , could not be a good idea, because it can be problems of data management and data compatibility. To show this, in this paragraphs it will attempted to extract the data that make us possible to calculate the index properties of the tested samples.

First obtain the cursor with the SQL sentence that provides the entire data in the main table `samplesfortesting`.

```
cursorA = exec(conn2ludgertesisdb, 'SELECT * FROM samplesfortesting');
```

Then, convert the cursor to a MATLAB® readable structure, and :

```
cursorARes = fetch(cursorA);
wholeDataTable= cursorARes.Data
```

Under this way, we will have the following result:

```
wholeDataTable =

  Columns 1 through 4

    [ 8]    '06MB'     'ET06'    [1x1 org.postgresql.jdbc3.Jdbc3Array]
    [ 9]    '06MC'     'ET06'    [1x1 org.postgresql.jdbc3.Jdbc3Array]
    [10]    '00MA'     'ETMX'    [1x1 org.postgresql.jdbc3.Jdbc3Array]
    [11]    '00MB'     'ETMX'    [1x1 org.postgresql.jdbc3.Jdbc3Array]
    [12]    '00MC'     'ETMX'    [1x1 org.postgresql.jdbc3.Jdbc3Array]
    [13]    '000DA'    'DS00'    [1x1 org.postgresql.jdbc3.Jdbc3Array]
    [14]    '000DB'    'DS00'    [1x1 org.postgresql.jdbc3.Jdbc3Array]
    [15]    '000DC'    'DS00'    [1x1 org.postgresql.jdbc3.Jdbc3Array]
    [16]    '045DB'    'DS45'    [1x1 org.postgresql.jdbc3.Jdbc3Array]
    [17]    '045DC'    'DS45'    [1x1 org.postgresql.jdbc3.Jdbc3Array]
    [18]    '030DA'    'DS30'    [1x1 org.postgresql.jdbc3.Jdbc3Array]
    [19]    '030DB'    'DS30'    [1x1 org.postgresql.jdbc3.Jdbc3Array]
    [20]    '030DC'    'DS30'    [1x1 org.postgresql.jdbc3.Jdbc3Array]
    [21]    '060DA'    'DS60'    [1x1 org.postgresql.jdbc3.Jdbc3Array]
    [22]    '060DB'    'DS60'    [1x1 org.postgresql.jdbc3.Jdbc3Array]
    [23]    '060DC'    'DS60'    [1x1 org.postgresql.jdbc3.Jdbc3Array]
    [24]    '090DA'    'DS90'    [1x1 org.postgresql.jdbc3.Jdbc3Array]
    [25]    '090DB'    'DS90'    [1x1 org.postgresql.jdbc3.Jdbc3Array]
    [26]    '090DC'    'DS90'    [1x1 org.postgresql.jdbc3.Jdbc3Array]
    [27]    '000VA'    'VN00'    [1x1 org.postgresql.jdbc3.Jdbc3Array]
    [28]    '000VB'    'VN00'    [1x1 org.postgresql.jdbc3.Jdbc3Array]
    [29]    '000VC'    'VN00'    [1x1 org.postgresql.jdbc3.Jdbc3Array]
    [30]    '030VA'    'VN30'    [1x1 org.postgresql.jdbc3.Jdbc3Array]
    [31]    '030VB'    'VN30'    [1x1 org.postgresql.jdbc3.Jdbc3Array]
    [32]    '030VC'    'VN30'    [1x1 org.postgresql.jdbc3.Jdbc3Array]
    [33]    '045VA'    'VN45'    [1x1 org.postgresql.jdbc3.Jdbc3Array]
    [34]    '045VB'    'VN45'    [1x1 org.postgresql.jdbc3.Jdbc3Array]
```

```
  [35]     '045VC'    'VN45'    [1x1 org.postgresql.jdbc3.Jdbc3Array]
  [36]     '060VA'    'VN60'    [1x1 org.postgresql.jdbc3.Jdbc3Array]
  [37]     '060VB'    'VN60'    [1x1 org.postgresql.jdbc3.Jdbc3Array]
  [38]     '060VC'    'VN60'    [1x1 org.postgresql.jdbc3.Jdbc3Array]
  [39]     '090VA'    'VN90'    [1x1 org.postgresql.jdbc3.Jdbc3Array]
  [40]     '090VB'    'VN90'    [1x1 org.postgresql.jdbc3.Jdbc3Array]
  [41]     '090VC'    'VN90'    [1x1 org.postgresql.jdbc3.Jdbc3Array]
  [ 1]     'SGA'      'BLNK'    [1x1 org.postgresql.jdbc3.Jdbc3Array]
  [ 2]     'SGB'      'BLNK'    [1x1 org.postgresql.jdbc3.Jdbc3Array]
  [ 3]     'SGC'      'BLNK'    [1x1 org.postgresql.jdbc3.Jdbc3Array]
  [ 4]     '18MA'     'ET18'    [1x1 org.postgresql.jdbc3.Jdbc3Array]
  [ 5]     '18MB'     'ET18'    [1x1 org.postgresql.jdbc3.Jdbc3Array]
  [ 6]     '18MC'     'ET18'    [1x1 org.postgresql.jdbc3.Jdbc3Array]
  [ 7]     '06MA'     'ET06'    [1x1 org.postgresql.jdbc3.Jdbc3Array]

Columns 5 through 6

  [1x1 org.postgresql.jdbc3.Jdbc3Array]    [1x1 org.postgresql.jdbc3.Jdbc3Array]
  [1x1 org.postgresql.jdbc3.Jdbc3Array]    [1x1 org.postgresql.jdbc3.Jdbc3Array]
  [1x1 org.postgresql.jdbc3.Jdbc3Array]    [1x1 org.postgresql.jdbc3.Jdbc3Array]
  [1x1 org.postgresql.jdbc3.Jdbc3Array]    [1x1 org.postgresql.jdbc3.Jdbc3Array]
  [1x1 org.postgresql.jdbc3.Jdbc3Array]    [1x1 org.postgresql.jdbc3.Jdbc3Array]
  [1x1 org.postgresql.jdbc3.Jdbc3Array]    [1x1 org.postgresql.jdbc3.Jdbc3Array]
  [1x1 org.postgresql.jdbc3.Jdbc3Array]    [1x1 org.postgresql.jdbc3.Jdbc3Array]
  [1x1 org.postgresql.jdbc3.Jdbc3Array]    [1x1 org.postgresql.jdbc3.Jdbc3Array]
  [1x1 org.postgresql.jdbc3.Jdbc3Array]    [1x1 org.postgresql.jdbc3.Jdbc3Array]
  [1x1 org.postgresql.jdbc3.Jdbc3Array]    [1x1 org.postgresql.jdbc3.Jdbc3Array]
  [1x1 org.postgresql.jdbc3.Jdbc3Array]    [1x1 org.postgresql.jdbc3.Jdbc3Array]
  [1x1 org.postgresql.jdbc3.Jdbc3Array]    [1x1 org.postgresql.jdbc3.Jdbc3Array]
  [1x1 org.postgresql.jdbc3.Jdbc3Array]    [1x1 org.postgresql.jdbc3.Jdbc3Array]
  [1x1 org.postgresql.jdbc3.Jdbc3Array]    [1x1 org.postgresql.jdbc3.Jdbc3Array]
  [1x1 org.postgresql.jdbc3.Jdbc3Array]    [1x1 org.postgresql.jdbc3.Jdbc3Array]
  [1x1 org.postgresql.jdbc3.Jdbc3Array]    [1x1 org.postgresql.jdbc3.Jdbc3Array]
  [1x1 org.postgresql.jdbc3.Jdbc3Array]    [1x1 org.postgresql.jdbc3.Jdbc3Array]
  [1x1 org.postgresql.jdbc3.Jdbc3Array]    [1x1 org.postgresql.jdbc3.Jdbc3Array]
  [1x1 org.postgresql.jdbc3.Jdbc3Array]    [1x1 org.postgresql.jdbc3.Jdbc3Array]
  [1x1 org.postgresql.jdbc3.Jdbc3Array]    [1x1 org.postgresql.jdbc3.Jdbc3Array]
  [1x1 org.postgresql.jdbc3.Jdbc3Array]    [1x1 org.postgresql.jdbc3.Jdbc3Array]
  [1x1 org.postgresql.jdbc3.Jdbc3Array]    [1x1 org.postgresql.jdbc3.Jdbc3Array]
  [1x1 org.postgresql.jdbc3.Jdbc3Array]    [1x1 org.postgresql.jdbc3.Jdbc3Array]
  [1x1 org.postgresql.jdbc3.Jdbc3Array]    [1x1 org.postgresql.jdbc3.Jdbc3Array]
  [1x1 org.postgresql.jdbc3.Jdbc3Array]    [1x1 org.postgresql.jdbc3.Jdbc3Array]
  [1x1 org.postgresql.jdbc3.Jdbc3Array]    [1x1 org.postgresql.jdbc3.Jdbc3Array]
  [1x1 org.postgresql.jdbc3.Jdbc3Array]    [1x1 org.postgresql.jdbc3.Jdbc3Array]
  [1x1 org.postgresql.jdbc3.Jdbc3Array]    [1x1 org.postgresql.jdbc3.Jdbc3Array]
  [1x1 org.postgresql.jdbc3.Jdbc3Array]    [1x1 org.postgresql.jdbc3.Jdbc3Array]
  [1x1 org.postgresql.jdbc3.Jdbc3Array]    [1x1 org.postgresql.jdbc3.Jdbc3Array]
  [1x1 org.postgresql.jdbc3.Jdbc3Array]    [1x1 org.postgresql.jdbc3.Jdbc3Array]
  [1x1 org.postgresql.jdbc3.Jdbc3Array]    [1x1 org.postgresql.jdbc3.Jdbc3Array]
  [1x1 org.postgresql.jdbc3.Jdbc3Array]    [1x1 org.postgresql.jdbc3.Jdbc3Array]
  [1x1 org.postgresql.jdbc3.Jdbc3Array]    [1x1 org.postgresql.jdbc3.Jdbc3Array]
  [1x1 org.postgresql.jdbc3.Jdbc3Array]    [1x1 org.postgresql.jdbc3.Jdbc3Array]
  [1x1 org.postgresql.jdbc3.Jdbc3Array]    [1x1 org.postgresql.jdbc3.Jdbc3Array]
```

```
    [1x1 org.postgresql.jdbc3.Jdbc3Array]    [1x1 org.postgresql.jdbc3.Jdbc3Array]
    [1x1 org.postgresql.jdbc3.Jdbc3Array]    [1x1 org.postgresql.jdbc3.Jdbc3Array]
    [1x1 org.postgresql.jdbc3.Jdbc3Array]    [1x1 org.postgresql.jdbc3.Jdbc3Array]
    [1x1 org.postgresql.jdbc3.Jdbc3Array]    [1x1 org.postgresql.jdbc3.Jdbc3Array]

Columns 7 through 10

    [12.5000]    [813.6600]    '2011-05-07'    '2011-07-22'
    [12.5000]    [806.6500]    '2011-05-07'    '2011-07-22'
    [12.5000]    [825.5700]    '2011-05-07'    '2011-07-22'
    [12.5000]    [826.7800]    '2011-05-07'    '2011-07-22'
    [12.5000]    [795.0700]    '2011-05-07'    '2011-07-22'
    [12.5000]    [818.3300]    '2011-05-07'    '2011-07-22'
    [12.5000]    [810.4800]    '2011-05-07'    '2011-07-22'
    [12.5000]    [814.7800]    '2011-05-07'    '2011-07-22'
    [12.5000]    [806.6900]    '2011-05-07'    '2011-07-22'
    [12.5000]    [     809]    '2011-05-07'    '2011-07-22'
    [12.5000]    [820.0200]    '2011-05-07'    '2011-07-22'
    [12.5000]    [797.0200]    '2011-05-07'    '2011-07-22'
    [12.5000]    [792.0100]    '2011-05-07'    '2011-07-22'
    [12.5000]    [799.7100]    '2011-05-07'    '2011-07-22'
    [12.5000]    [806.7500]    '2011-05-07'    '2011-07-22'
    [12.5000]    [820.3100]    '2011-05-07'    '2011-07-22'
    [12.5000]    [818.1600]    '2011-05-07'    '2011-07-22'
    [12.5000]    [825.2100]    '2011-05-07'    '2011-07-22'
    [12.5000]    [793.7800]    '2011-05-07'    '2011-07-22'
    [12.5000]    [816.4900]    '2011-05-07'    '2011-07-22'
    [12.5000]    [813.4300]    '2011-05-07'    '2011-07-22'
    [12.5000]    [789.1300]    '2011-05-07'    '2011-07-22'
    [12.5000]    [825.7500]    '2011-05-07'    '2011-07-22'
    [12.5000]    [793.3000]    '2011-05-07'    '2011-07-22'
    [12.5000]    [813.5900]    '2011-05-07'    '2011-07-22'
    [12.5000]    [819.4800]    '2011-05-07'    '2011-07-22'
    [12.5000]    [795.9700]    '2011-05-07'    '2011-07-22'
    [12.5000]    [817.1600]    '2011-05-07'    '2011-07-22'
    [12.5000]    [801.1800]    '2011-05-07'    '2011-07-22'
    [12.5000]    [828.8100]    '2011-05-07'    '2011-07-22'
    [12.5000]    [794.4700]    '2011-05-07'    '2011-07-22'
    [12.5000]    [811.4500]    '2011-05-07'    '2011-07-22'
    [12.5000]    [789.3600]    '2011-05-07'    '2011-07-22'
    [12.5000]    [782.2800]    '2011-05-07'    '2011-07-22'
    [12.5000]    [791.7600]    '2011-05-07'    '2011-07-22'
    [12.5000]    [785.2600]    '2011-05-07'    '2011-07-22'
    [12.5000]    [792.6100]    '2011-05-07'    '2011-07-22'
    [12.5000]    [784.8300]    '2011-05-07'    '2011-07-22'
    [12.5000]    [790.1200]    '2011-05-07'    '2011-07-22'
    [12.5000]    [796.6600]    '2011-05-07'    '2011-07-22'
    [12.5000]    [815.8400]    '2011-05-07'    '2011-07-22'
```

It can be observed that the POSTGRESQL® array object was not recognized correctly by the interpreter of MATLAB® , and instead to have an array of values, one have an object represented by the following:

```
[1x1 org.postgresql.jdbc3.Jdbc3Array].
```

If we consult to MATLAB® : what is the type format of the object located at the fifth row and fourth column? Within the `isjava` function, one will see that the format type is a Java object but not a MATLAB® object.

```
isjava( wholeDataTable{5,4} )

ans = 1
```

By this way, one is in in problem to retrieve from the data base the data in a clean manner, and one should require create a new Java class to be used in MATLAB® , i.e. to manipulate this type of data, something that can be made easy by computer programming experts.

But, one can display in the command window of MATLAB® one field each time, by making the following artifice. For the example case, it is required to know the values of the array located at the fifth row and fourth column:

```
aValue=wholeDataTable(5,4);
aValue{1,1}

ans = {69.349998,69.440002,69.510002,69.510002,69.540001}
```

At this point, one can have the idea to copy the value shown in the command window, and paste it via the clipboard to assign a new MATLAB® variable in order to begin calculations. If so, all the automation and advantages one explained by using a data base manager will be lost, and one would return to the classical manner to manipulate the data, which is not the intention of this implementation.

C.3 Index–Properties OOP Code in MATLAB®

This section is not properly a POSTGRESQL® *vs.* MATLAB® interaction; it is an example of the OOP programming paradigm mentioned in Section 5.8.

The following code is a MATLAB® class defined to create an object where it calculates and then stores index properties variables of a determined sample. As it can be seen; the input parameters in the object being created are the sample identification; the three lengths of the sample (in m) given as a 1×3 array; and the sample mass (in g).

```
classdef cubesampleindexprops
```

```
%
%sampleObject =cubesampleindexprops( cubeSampleNumber,...
%    sideLenghtVector, weight )
%%%%%%%%%%%%%%%
%Description:
%Creates a class for a cube-sample index properties object. By giving a
%string name, the three lengths (in meters) of the sides, the weigth
%(in grams), the class will create an object of index properties that
%reports also the cube area where stress is applied (in m2), the cube
%volume (in m3) and its unit weight (in kN m-3).
%Example:
%sample01 = cubesampleindexprops( 'SGA', 0.07 *ones(1,3), 791.76 )

properties (Constant, Hidden =true)
    gravityAceleration =9.81; % gravity acceleration in m s^{-2}
end

properties (SetAccess= public)
    cubeSampleNumber= '000';   % A correlative number of the cube sample
                               % (String)
    sideLenghtVector= [1 1 1];
                               % The side lenght in meters in the
                               % x(north)-direction in a NED coordinate
                               % system (double)
                               % The side lenght in meters in the
                               % y(east)-direction in a NED coordinate
                               % system (double)
                               % The side lenght in meters in the
                               % z(nadir)-direction in a NED coordinate
                               % system (double)
    cubeWeigth= 0.0;           % mean cube weight in grams (double)
end


properties (Dependent = true)
    cubeStressedArea           % Area of the surface that will receive
                               % the uniaxial stress in m^{2}
    cubeVolume                 % Volume of thye sample in m^{3}
    cubeUnitWeight             % Unit weight of the cube in kN m^{-3}
end

methods
    % Constructor of the Cube Sample Object (CSOBJ)
    function CSOBJ =cubesample( cubeSampleNumber, sideLenghtVector,...
            cubeWeigth )
        CSOBJ.cubeSampleNumber =cubeSampleNumber;
        CSOBJ.sideLenghtVector =sideLenghtVector;
        CSOBJ.cubeWeigth = cubeWeigth;
    end

    %Function that restricts sideLenghtVector elements <=0
    function CSOBJ =set.sideLenghtVector(CSOBJ, sideLenghtVector)
        booleanTemp =sum( sideLenghtVector <= 0);
        if booleanTemp
```

```
                error('Volumen can not be less tha cero')
            end
            CSOBJ.sideLenghtVector =sideLenghtVector;
        end

        % Function that calculates the cube stressed area
        function stressedArea =get.cubeStressedArea( CSOBJ )
             stressedArea =prod( CSOBJ.sideLenghtVector(1:2) );
        end

        % Function that calculates the cube volume
        function volume =get.cubeVolume( CSOBJ )
             volume =prod( CSOBJ.sideLenghtVector );
        end

        % Function that calculates the unit weight
        function uWeight =get.cubeUnitWeight ( CSOBJ )
            CSOBJ.cubeVolume;
            uWeight =CSOBJ.cubeWeigth *CSOBJ.gravityAceleration ./...
                CSOBJ.cubeVolume *10^(-6);
        end
    end

end
```

To create the object, you should put in the command line of MATLAB® the desired name of the object and after that the input variables:

```
SGAindexPropsOBJ = cubesampleindexprops( cubeSampleNumber, sideLenghtVector, weight );
```

For example:

```
SGAindexPropsOBJ = cubesampleindexprops( 'SGA', [0.0686 0.06815 0.06648], 791.76 );
```

By typing the name of the new object `SGAindexPropsOBJ`, the following display will be shown. Observe, that the `cubeStressedArea`, the `cubeVolume`, and the `cubeUnitWeight` variables are created automatically after all input variables are introduced in the object.

```
SGAindexPropsOBJ =
  cubesampleindexprops

  Properties:
    cubeSampleNumber: 'SGA'
    sideLenghtVector: [0.0686 0.0682 0.0665]
          cubeWeigth: 791.7600
    cubeStressedArea: 0.0047
          cubeVolume: 3.1080e-04
      cubeUnitWeight: 24.9909
  Methods
```

One also can see the class that the new object belongs to, by using the `whos` or the `isa` functions (e.g. `whos SGAindexPropsOBJ; isa(SGAindexPropsOBJ, 'cubesampleindexprops');`).

With this simple short example, it can be shown that by using classes, more control is established in the generation, manipulation and storing data. Here, the three last variables of the object can not be altered unless the complete object is re–defined.

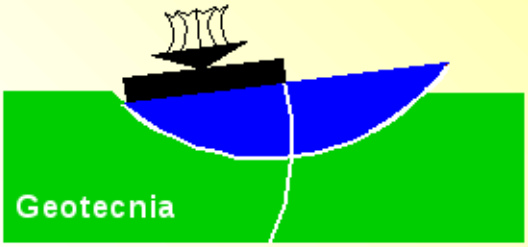

UNIVERSIDADE DE BRASÍLIA
FACULDADE DE TECNOLOGIA
Departamento de Engenharia Civil e Ambiental
Programa de Pós–Graduação em Geotecnia

DEFESA DE TESE DE DOUTORADO EM GEOTECNIA

UMA ABORDAGEM DE MODELAGEM FÍSICA QUALITATIVA DE RESISTÊNCIA PARA MACIÇOS ROCHOSOS

LUDGER OSWALDO SUÁREZ BURGOA

BANCA EXAMINADORA:

ANDRÉ PACHECO DE ASSIS, PH.D (Orientador)(ENC–UnB)
HERNÁN EDUARDO MARTINEZ CARVAJAL, DSC (ENC–UnB)
ANDRÉ LUÍS BRASIL CAVALCANTE, DSC (ENC–UnB)
JOÃO LUÍZ ARMELIN, DSC (Furnas–Electrobrás)
CARLOS ALBERTO LAURO VARGAS, DSC (EEC–UFG)

LOCAL: MINI AUDITÓRIO DO SG–12
DATA E HORA: 31/08/2012 ÀS 14:00H.

This document was created on: Friday 7th September, 2012 at 17:12.